20040224 117

REPORT DOCUMENTATION PAGE

1. AGENCY USE ONLY (Leave blank)	2. REPORT DATE May 15, 2003	3. REPORT TYPE AND DATES COVERED Technical 02/15/01 to 4/30/03

4. TITLE AND SUBTITLE: Development and Testing of the Virginia Tech Doppler Global Velocimeter	5. FUNDING NUMBERS N00014-01-1-0420
6. AUTHORS John D. Fussell and Roger L. Simpson	

7. PERFORMING ORGANIZATION NAME(S) AND ADDRESS(ES) Department of Aerospace and Ocean Engineering Virginia Polytechnic Institute and State University Blacksburg, Virginia 24061-0203	8. PERFORMING ORGANIZATION REPORT NUMBER VPI-AOE-285

9. SPONSORING/MONITORING AGENCY NAME(S) AND ADDRESS(ES) Office of Naval Research 800 N. Quincy Street Arlington, Virginia 22217	10. SPONSORING/MONITORING AGENCY REPORT NUMBER

11. SUPPLEMENTARY NOTES

12a. DISTRIBUTION/AVAILABILITY STATEMENT Unlimited	12b. DISTRIBUTION CODE

13. ABSTRACT (Maximum 200 words)

Repairs and modifications were made to a flow velocity measurement system designed to measure a planar area of unsteady three component velocities in a single realization using a velocity measurement technique referred to as Doppler Global Velocimetry (DGV). Several hardware components in the system were modified and new hardware was added. Significant improvements were made to the procedures used in acquiring DGV data as well as the procedures used in reducing the acquired DGV data. Though hardware problems were encountered, successful iodine cell calibrations were acquired and attempts were made to acquire DGV velocity data from a calibration wheel and in the wake of a 6:1 prolate spheroid. These attempts were hampered by poor performance of the Nd:YAG laser and one of the digital cameras used in this research. While the magnitudes of the velocities acquired from the calibration wheel were noticeably higher than those calculated from the angular velocity and large fluctuations were present in these reduced velocities, the general trends measured by the VT DGV system matched those calculated from the angular velocity. The attempt to acquire flow field data in the wake of a 6:1 prolate spheroid model was unsuccessful due to insufficient seed particle density in the area where data were to be obtained. The results of this research indicate that while significant improvements have been made to the system, there are still some significant problems to overcome.

14. SUBJECT TERMS Doppler Global velocimetry, planar Doppler velocimetry	15. NUMBER OF PAGES 185
	16. PRICE CODE

17. SECURITY CLASSIFICATION OF REPORT UNCLASSIFIED	18. SECURITY CLASSIFICATION OF THIS PAGE UNCLASSIFIED	19. SECURITY CLASSIFICATION OF ABSTRACT UNCLASSIFIED	20. LIMITATION OF ABSTRACT UNLIMITED

Refinement and Verification of the Virginia Tech
Doppler Global Velocimeter (DGV)

By John D. Fussell

Committee Chair: Roger L. Simpson, Aerospace and Ocean Engineering

Abstract

Repairs and modifications were made to a flow velocity measurement system designed to measure a planar area of unsteady three component velocities in a single realization using a velocity measurement technique referred to as Doppler Global Velocimetry (DGV). Several hardware components in the system were modified and new hardware was added. Significant improvements were made to the procedures used in acquiring DGV data as well as the procedures used in reducing the acquired DGV data. Though hardware problems were encountered, successful iodine cell calibrations were acquired and attempts were made to acquire DGV velocity data from a calibration wheel and in the wake of a 6:1 prolate spheroid. These attempts were hampered by poor performance of the Nd:YAG laser and one of the digital cameras used in this research. While the magnitudes of the velocities acquired from the calibration wheel were noticeably higher than those calculated from the angular velocity and large fluctuations were present in these reduced velocities, the general trends measured by the VT DGV system matched those calculated from the angular velocity. The attempt to acquire flow field data in the wake of a 6:1 prolate spheroid model was unsuccessful due to insufficient seed particle density in the area where data were to be obtained. The results of this research indicate that while significant improvements have been made to the system, there are still some significant problems to overcome.

Dedication

The presentation of this research is dedicated to
my parents Ray E. Fussell and Marguerite D. Fussell,
and to my wife Judith A. Fussell.

Acknowledgements

encouraged me to strive for excellence in everything I did. He gave me some important words to live by: "A quitter never wins and a winner never quits." I can only hope that he knew and appreciated the profound effect he had on my life. His pride in my accomplishments and his faith in my abilities meant more to me than I could ever hope to express to him. It was my sincere hope that he would be able to see all of the hard work and all of the pain and frustration I have endured in the pursuit of my dream of becoming an aerospace engineer pay off. Unfortunately, this was not to be. He passed away in April 2002. In the end what he gave me was far more valuable than the college tuition he could not afford to give me. I am very thankful for the time I had with him and for all that he taught me about life. My mother kept my dream of going to college alive in the days when I had all but given up on it. She encouraged me to dare to dream big dreams and to take some chances in order reach those dreams. I wish I could recognize by name all of my friends and co-workers who were there to give me advice or words of encouragement when I sorely needed them. I hope this global thank you will do.

Last but not least, I want to express my profound thanks to my wife, Judith Fussell. Since the day I met her she has always been there to encourage me and to love me even when I tried to make myself unlovable. She stood by me as I struggled to overcome difficulties and when my morals would not let me be satisfied with anything less than getting it right. Her faith and dedication have kept me going and inspired me to keep working and keep trying to better myself. My love for her grows deeper and stronger every day.

Table of Contents

Table of Figures

Chapter 4: Data Reduction

Chapter 5: Hardware Problems

Chapter8: Conclusions

Appendix A

Chapter 1: Introduction

Chapter 1 : Introduction

1.1 History

Since ancient times humankind has sought to learn more about how fluids flow around solid bodies. Interest in these flows has been piqued for a variety of reasons such as designing nautical vessels, designing plumbing to transport fluids over great distances, and designing flying machines. Famous names such as Aristotle, Da Vinci, and Newton, just to name a few, have considered the nature of fluid flows around solid bodies. Humankind's understanding of these flows has increased at a remarkable pace over the last 100 years through the development and implementation of such tools as the wind tunnel and computers. These tools have, in part, enabled human society to achieve feats that before the 20th century were the domain of science fiction writers and dreamers. Engineers and scientists have used these tools, in addition to a wide range of other tools, to design and improve upon airplanes, buildings, and nautical vessels as well as a wide variety of other engineered devices.[1]

Over the last 200 years scientists and engineers have spent a great deal of time thinking about and performing experiments to better understand fluid flows around bluff and "aerodynamic" bodies. Intrusive measurement devices such as Pitot tubes and hot wires have been used to measure dynamic pressures, flow velocities, and other flow properties near these bodies. Non-intrusive devices such as pressure sensitive paint and Laser Doppler Velocimeters (LDV) have also been developed and used to measure various flow properties near these bodies.[2] While the development and use of LDV marks a significant improvement in our ability to measure flow properties in a way that will not directly influence these properties through the presence of a probe within the flow being measured, LDV is

not without its disadvantages. Perhaps one of the largest disadvantages to using LDV for large scale wind tunnel experiments is the time and effort required to map out a large portion of the flow field around and behind the body of interest.[3] It would be desirable to have a non-intrusive device capable of measuring flow properties in large areas of the flow field quickly and with less effort than would be required using LDV.

1.2 Research Motivation

The purpose of this research is to develop a non-intrusive device which will measure a plane of instantaneous flow field velocities near the surface of a solid body. The primary motivation for this research is to use this device to measure flow velocities in the streamwise vortices shed in the wake of two different bodies of revolution, a 6:1 prolate spheroid model and a DARPA2 submarine model. Data gathered in the wake of the 6:1 prolate spheroid will be used to verify the performance of this new measurement system by comparing data obtained with this system to data obtained in previous tests performed with the same 6:1 prolate spheroid model. The data obtained in the wake of the DARPA2 submarine model will be used to improve performance of computational fluid dynamics flow simulations used to predict flow around full scale submarine hull shapes. This device measures a plane of flow field velocities in a single measurement realization. The device uses a measurement technique referred to as Doppler Global Velocimetry (DGV) or sometimes referred to as Planar Doppler Velocimetry (PDV).[4]

1.3 Basic Theory

The Doppler Global Velocimetry technique uses the Doppler effect to measure flow field velocities. The theory behind this technique can be described through the following equation:

$$\Delta v = \frac{v_o}{c}(\hat{a} - \hat{l}) \cdot \vec{V} \tag{1}$$

where $\Delta v = v_D - v_o$ which is the change in optical frequency of the light reflecting off of the seed particles passing through the laser sheet (v_D is the optical frequency of the Doppler shifted light and v_o is the optical frequency of the unshifted incident laser light), c is the speed of light, $\hat{a}$ is the unit vector pointing toward the direction in which the data area is being viewed, $\hat{l}$ is the unit vector pointing in the direction in which the laser light is propagating, and $\vec{V}$ is the velocity vector.[5] Figure 1.1 shows the basic setup for a single component DGV system. The vectors $\hat{a}$, $\hat{l}$, and $(\hat{a} - \hat{l})$ are shown in figure 1.1. Essentially, Δv, v_o, $\hat{a}$, and $\hat{l}$ are measured during the experiment and

equation (1) is rearranged so that it can be solved as a system of equations to determine the velocity components in the desired coordinate system.
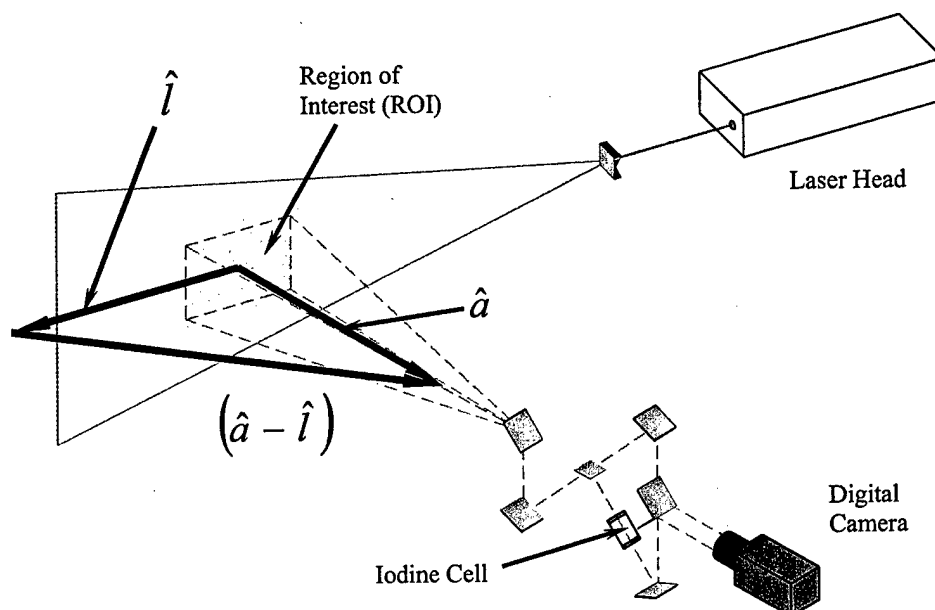
Figure 1.1 Doppler Global Velocimeter Setup

1.4 The Doppler Global Velocimetry Technique

In the Doppler Global Velocimetry technique, seed particles injected into the flow or particles naturally occurring in the flow are illuminated by a sheet of coherent, green, laser light. For a three component DGV system, a pair of images of the seed particles passing through the laser sheet are acquired from three different viewpoints using digital surveillance cameras or astronomy cameras.[6,7] One of the images from each viewpoint is used as a reference and the other image passes through a hollow glass cylinder filled with iodine gas. The hollow glass cylinder filled with diatomic iodine gas (commonly referred to as an iodine cell) acts as an optical filter since gaseous diatomic iodine has several sharp transitions from total absorption to total transmission inside the green portion of the visible light spectrum. The light intensity of each pixel in the region of interest (ROI) of the filtered view is divided by the light intensity of the corresponding pixel in the ROI of the reference view.[8]

When a frequency doubled pulsed Nd:YAG laser is used in the Doppler Global Velocimetry technique additional steps are needed to account for variations in the optical frequency of the light pulses produced by the laser. For Doppler Global Velocimetry using a frequency doubled pulsed Nd:YAG laser, the ratios of pixel intensities for each pixel location in the ROI are compared to a ratio of pixel intensities for a portion of the laser beam that is projected onto a stationary target. The

difference between the pixel intensity ratio in the region of interest and the pixel intensity ratio from the stationary target is proportional to a shift in the optical frequency of the laser light due to the Doppler effect (i.e. Δv).[9]

1.5 Mie Scattering vs. Rayleigh Scattering

The Doppler Global Velocimetry technique makes use of a physical phenomenon known as Mie scattering. Mie scattering occurs when light is scattered by particles larger than the wavelength of the light being scattered. This scattering process is generally assumed to be elastic. In other words, none of the light colliding with each particle is absorbed by the particle. Seed particles with diameters roughly between 1 μm and 10 μm, such as smoke or dust particles, can cause Mie scattering when illuminated by light in the visible spectrum. This type of light scattering is also used in some Laser Doppler Velocimetry (LDV) systems and Particle Image Velocimetry (PIV) in addition to DGV.[10] The white color of most clouds is attributed to Mie scattering since all visible wavelengths of sunlight are scattered equally by the water droplets contained in these clouds. Rain clouds appear various shades of gray because these clouds are thicker than clouds that do not produce rain and thus, less sunlight penetrates them.[11]

Another type of light scattering, known as Rayleigh scattering, has been employed by some researchers using measurement techniques very similar to the DGV technique. Rayleigh scattering occurs when light is scattered by particles smaller than the wavelength of the light being scattered. As with Mie scattering this type of light scattering is assumed to be elastic. For light in the visible spectrum, this type of scattering normally occurs with particle sizes on the order of a molecule.[12] Rayleigh scattering is responsible for the sky being blue on a sunny day. The molecules in the air scatter shorter wavelengths of light (violet and blue) more effectively than longer wavelengths of light (Red and yellow). The sky appears red at dawn and dusk because the sunlight must travel farther through the atmosphere than during the rest of the daytime, so all of the violet and blue light has been previously scattered and only the longer wavelength (red and yellow) light remains.[13]

1.6 Previous Work

1.6.1 Origin of the Doppler Global Velocimetry Technique

The Doppler Global Velocimetry technique was first introduced by Komine *et al* in 1991. The technique was presented as a method to obtain quantitative velocity information through flow visualization. They chose to use Mie scattering to acquire DGV data, because this type of scattering did not appreciably broaden the laser spectrum, unlike molecular Rayleigh scattering. The original system used a continuous-wave argon-ion laser, molecular filters containing iodine gas, and three pairs of Charge-Couple Device (CCD) video cameras which captured filtered and reference images at a rate of 30 images/second. Komine *et al.* also performed tests with an Nd:YAG laser to obtain instantaneous velocity data. The system was calibrated using a disk rotating at a known constant speed. This first DGV system was used to measure velocities in a near sonic free expanding nozzle jet.[14]

1.6.2 Improvements to the DGV Technique

Dr. Hiroshi Komine worked with James F. Meyers of NASA's Langley Research Center to refine the technique. The first DGV system assembled by Komine and Meyers was a single component system used to acquire DGV data from a disk rotating at a known constant speed. Next the single component system was used to measure flow velocities in a subsonic jet and finally the system was used to measure a portion of the flow in the wake of a 75 degree delta wing.[15]

Through these tests, and tests of the technique that followed, Meyers and other researchers began to make improvements to the technique. One of the first improvements was acquiring images of a grid of dots or squares to align the filtered and reference views. These grid images were also used to "de-warp" the acquired images so each image appeared to be looking perpendicular to the data area. This allowed views from various viewing angles to be overlaid on top of each other. Another improvement made in the technique was accounting for variations in the pixel sensitivity in the CCD arrays of the cameras used to acquire DGV data. Images called pixel sensitivity images were acquired to account for these variations.[16] The next improvement to be made to the technique was capturing "background" images to correct for ambient light, stray laser light from reflections, and dark current from the CCD array in the camera.[17]

Robert McKenzie, of NASA Ames Research Center, authored two important papers that influenced the design of the Virginia Tech DGV system. The first paper, published in 1995, discussed the measurement capabilities of a DGV system using a pulsed Nd:YAG laser. This paper documented several innovations. McKenzie's DGV system used a single 16-bit astronomy camera in place of two cameras to capture the filtered and reference images. McKenzie also monitored the mean variations in optical frequency of the laser from pulse to pulse using a pair of photodiodes and an iodine cell. In addition to these innovations McKenzie performed an extensive study on sources of uncertainties in the DGV technique. This analysis revealed that the velocity measurement uncertainty for a single realization using the DGV system described in the paper was 2 m/s (6.562 ft/s).[18] This uncertainty calculation is relevant for the Virginia Tech DGV system because the equipment and techniques used in McKenzie's DGV system were very similar to those of the initial form of the Virginia Tech system. The second paper was published in 1997. This paper introduced the idea of using a small portion of the laser beam projected into the view of one of the camera systems, used to acquire DGV data, to monitor pulse to pulse variations in the mean optical frequency of the laser light before this light is Doppler shifted. This paper also suggested using pixel binning to reduce spatial noise. Pixel binning is a form of filtering. In this technique the pixels surrounding a given pixel are used to calculate an average value for the pixel in question. McKenzie stated that 3 x 3 binning minimized excessive spatial noise while having no significant effect on the spatial resolution of the image. Again this paper showed the single realization velocity measurement uncertainty of the DGV system described in the paper to be 2 m/s (6.562 ft/s).[19]

1.6.3 Development of the Virginia Tech DGV System

Development of the Virginia Tech DGV system began in 1996. The goal of this development was to use the Virginia Tech DGV system with the Dynamic Plunge Pitch and Roll (DyPPiR) apparatus to acquire instantaneous unsteady velocity data in the wake of a DARPA2 submarine model. During the initial development phase of this program basic hardware for the system was purchased or constructed, basic software to acquire data images was written, and initial tests of the camera module optical orientation were conducted. Next, a sophisticated Windows based control program was written to perform a variety of tasks needed to acquire DGV data. Some of these tasks included: controlling the Nd:YAG laser, monitoring the temperature of the cold finger on each of the three iodine cells, acquiring and storing various correction images needed, acquiring and storing iodine cell calibration and velocity images and processing and reducing these iodine cell calibration and velocity images into DGV data. The portion of the control program used to process DGV images

into DGV data involved writing software to perform various image processing tasks such as de-warping, mirroring, image addition and subtraction, as well as using correction images to improve data quality. Once the hardware and software for the Virginia Tech three component DGV system were ready, tests were conducted to demonstrate the capabilities of the system.

The first version of the Virginia Tech three component DGV system was tested in September - October 2000 with mixed results. The capability to capture and use various correction images and the capability to acquire iodine cell calibrations was demonstrated but attempts to acquire instantaneous velocity data were unsuccessful. Several significant problems were encountered during these tests. One of the three cameras began to malfunction and was only usable for 10 to 15 minutes at a time. The system was not able to detect a Doppler shift in the laser light reflecting off of a wheel rotating at a constant angular velocity. The laser began to have problems locking on to a particular optical frequency. Also, the smoke machine, used to produce seed particles in the flow, could not produce enough seed to acquire instantaneous velocity images. These problems eventually led to the end of the first set of tests of the Virginia Tech three component DGV system.[20]

1.6.4: Recent improvements to the DGV Technique

A paper published in 2001, by Meyers *et al.* considered sources of measurement error and suggested several new improvements to reduce the single sample uncertainty of the DGV technique. The first suggestion made was to use vapor-limited iodine cells instead of cells with a cold finger. Small variations in the cold finger temperature translate to significant errors in the velocity measured by the system. In fact, the paper stated that an uncertainty of 0.1° C in the cold finger temperature resulted in an uncertainty of 3 m/s (9.843 ft/s) in velocity measurements. By using vapor limited iodine cells this uncertainty was eliminated because the number of gaseous iodine molecules remained constant as long as the body temperature of the cell was maintained above the temperature the cell was filled at.[21]

The next suggestion was to calibrate the iodine cells using a rotating disk. The previous generally accepted method used to calibrate the iodine cell determines the ratio of the filtered and unfiltered views of a white card illuminated by the diffused laser beam while varying the optical frequency produced by the Nd:YAG laser. The problem with this method was that the laser optical frequency drifts slightly from pulse to pulse. Meyers *et al* recommended using a disk rotating at a constant speed to calibrate the iodine cells. They stated that in experiments they conducted with the laser injection seeder at a constant setting, the standard deviation of the variation in laser optical

frequency was about 40 MHz. This means that using the average of a limited number of samples would not produce an acceptable uncertainty in the results. Their argument was that it is unnecessary to know the absolute optical frequency of the transition from full light transmission by the iodine cell to full light absorption if the absolute value of the optical frequency at the center of the absorption line is known. The rotating disk would produce a linear variation in the Doppler shifted optical frequencies along any vertical line on the wheel.[22] In other words, the laser light frequency recorded by the ratio of the filtered and unfiltered images of any vertical line of pixels in a de-warped view of the rotating disk will vary linearly. By measuring the ratio of the filtered and unfiltered pixel values along the vertical diameter of the rotating disk and varying the laser optical frequency in small increments these successive measurements can be pieced together to create an absorption profile. Figure 1.2 shows how the iodine cell absorption profile is constructed.[23]
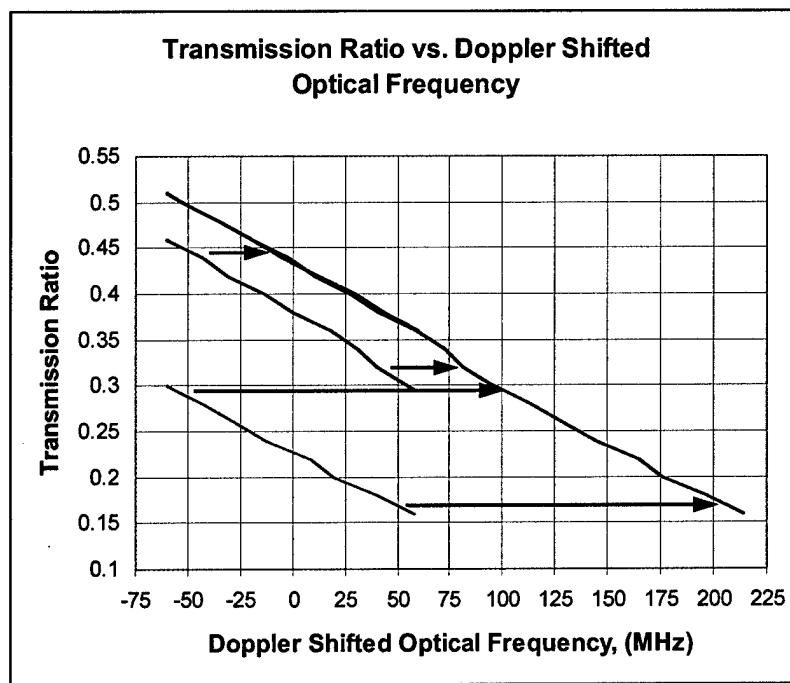
Figure 1.2: Construction of iodine cell absorption profile.[24]

Another suggestion made in this paper was to use an extra camera to monitor the temporal and spatial variations in optical frequency each laser pulse produced by the Nd:YAG laser. The paper stated that the mean optical frequency of successive laser pulses can differ by as much as 80 MHz. For a pulse with a bandwidth of 120 MHz, this variation is significant. These variations are caused by the control system in the laser dithering the rear resonator mirror to produce single frequency output. In addition to variations in the mean optical frequency of each pulse there are spatial

variations within each pulse. These variations are caused by imperfections in the Nd:YAG rods. The extra camera, used to monitor these variations, would capture images of a stationary target illuminated by each pulse of laser light used to acquire data.[25]

Other minor suggestions were also made in this paper. These suggestions ranged from the color the model should be painted to the minimum angle between the data plane and the detector to filtering data to reduce the effects of spatial and temporal measurement noise caused by laser speckle, variations in pixel sensitivity, and image to image intensity variations as well as other suggestions. They suggested painting the model and other items from which unwanted reflections might occur either flat black or flat red. They also recommended keeping the angle between the measurement plan and the detector greater than 30 degrees. The end result of all of these suggestions was to reduce velocity measurement uncertainties to 0.5 m/s for velocity measurements on a rotating wheel.[26]

1.6.5 Filtered Rayleigh Scattering

A measurement technique similar to DGV that uses the Rayleigh scattering phenomenon is called Filtered Rayleigh Scattering (FRS).[27] This technique was introduced by a group of researchers led by Dr. Richard Miles of Princeton University. This technique was originally intended to be used to improve flow visualization in situations where the signal is obscured by background scattering but has also been used to measure temperature variations in fluid flows, and measure multiple properties in fluid flows. Like the DGV technique, a molecular filter such as a glass cylinder filled with gaseous diatomic iodine and digital surveillance cameras or astronomy cameras can be used in the FRS technique. The FRS technique also uses a laser to produce a sheet of laser light which illuminates the plane in which data is to be taken. As with DGV, a frequency doubled pulsed Nd:YAG laser is often used in conjunction with the diatomic iodine molecular filter.

In the Filtered Rayleigh Scattering (FRS) technique a portion of the flow field is illuminated by a sheet of narrow linewidth laser light and light scattered by molecules passing through the laser sheet passes through a molecular filter before being captured by a detector. As with the DGV technique, the laser is tuned to an optical frequency in the middle of an absorption transition for the iodine cell so that as the optical frequency of the light is changed by reflecting off of molecules in the flow field, the intensity of the light transmitted to the detector changes. Where DGV and FRS differ is in that Rayleigh scattered light intensity is directly proportional to the density of the scattering molecules. For this reason Rayleigh scattering can be used to measure density, temperature, and pressure variations in flow fields. Filtered Rayleigh Scattering does not use the Doppler shift which

occurs when light reflects off of molecules in the flow field, unless the flow velocity is being measured in addition to thermodynamic properties. The shape and position of the spectral profile, captured by the detector, is used to measure these thermodynamic properties.[28] For more information regarding the FRS technique please see the following references: 28, 29 30 31, and 32.

Chapter 2: Hardware

Chapter 2 : Hardware

2.1 DGV Hardware

Figure 1.1 also shows some of the basic hardware used in Doppler Global Velocimeters. A laser is used to illuminate the area in which data are to be taken. The laser is fired into a lens or set of lenses to convert the laser beam into a sheet of laser light. Seed particles must be introduced into the flow. These particles must be large and abundant enough to make the portion of the laser sheet where data is to be taken visible and yet small and sparse enough not to influence the flow. The camera(s) used to acquire DGV data is housed in a camera module. A pair of images of the particles passing through the laser sheet are captured by a digital camera or a pair of digital cameras. As mentioned previously, one of these images is used as a reference and the other image passes through an iodine cell which acts as an optical frequency filter, thus capturing the magnitude of the Doppler shift of the laser light bouncing off of the moving particles, in the $(\hat{a} - \hat{l})$ direction. This chapter discusses in greater detail how this equipment is used in the Virginia Tech DGV system as well as discussing the other hardware used in this research.

Some of the new hardware used in this research included a new digital camera purchased to replace one of the original digital cameras in the system, a new calibration wheel system that was designed and built in house, new high damage tolerant laser optics, and a new smoke machine that acted as a particle seeder. While the iodine cells used in this research were not new they were modified during this research by having the cold fingers on the cells removed. The laser optics setup

was also changed during this research compared to setup used in previous tests performed with the VT DGV system.

2.2 Nd:YAG Laser and Optics

2.2.1 Laser

The laser used for Doppler Global Velocimetry can either be a constant wave laser or a pulsed laser, which emits a laser beam in the green portion of the visible spectrum. The use of constant wave lasers such as Argon-Ion lasers has been limited to time averaged data acquisition since the mechanical shutter on digital cameras open and close at a finite rate of speed usually on the order of milliseconds at best. The finite shutter speed causes the data acquired to be time averaged since digital cameras integrate the light collected while the camera shutter is open. In other words, as long as the data collection area is illuminated while the camera shutters are open the cameras collect and average data. Pulsed lasers such as the Nd:YAG laser equipped with a harmonic generator are capable of near instantaneous data acquisition since the time over which a single pulse of laser light is emitted is very brief.[34] A computer controlled shutter used in conjunction with the Nd:YAG laser allows a single high energy pulse of laser light to illuminate the data collection area during data acquisition (i.e. while the camera shutters are open).[35]

A Spectra-Physics GCR-170-10 Nd:YAG pulsed laser was used in this research to illuminate the data area. This laser emitted a pulse of laser light every 100 ms. The laser contained a harmonic generator which allowed the laser to produce two beams of laser light. One beam was an infrared beam (1064 nm wavelength) and the other beam was a green beam (532 nm wavelength). Only the green beam is used in the Virginia Tech DGV system.

The Nd:YAG laser had two operating modes. The long pulse mode was a low power mode, which was useful when aligning optics. The Q-Switch mode was a high power mode. The Q-switch mode was used during acquisition of DGV data. This mode used a device called a Q-switch to cause a large population of excited neodymium ions to build up in the YAG rod before each pulse was fired. The Q-switch also allowed the build up of ions to be quickly released causing a short burst of high intensity laser light to be emitted. When the laser operated in this mode the pulses of light emitted by the laser lasted approximately 9 ns and contained about 380 mj of energy per pulse (roughly 42.2 MW of power per pulse).[36]

The Nd:YAG laser was equipped with a seed laser. The seed laser helped the Nd:YAG laser to emit pulses of laser light over a very narrow band of optical frequencies. The seed laser was a monolithic single frequency Nd:YVO4 laser. The wavelength of the laser beam output by this laser was 1064 nm, which is the same as the output of the Nd:YAG host laser before being frequency doubled by the harmonic generator. The temperature of the seed laser and the laser diode used to pump this laser were controlled using thermoelectric coolers. The output wavelength of the seed laser could be adjusted by changing the temperature of the Nd:YVO4 seed laser. The control panel for the seed laser contained switches to change the operating configuration of the seed laser as well as outputs to monitor when the laser reset, the Q-switch build up time, the Piezoelectric voltage, and an input to change the frequency offset of the seed laser. The three outputs were used to monitor the performance of the laser. The laser reset output would send an analog signal when the laser reset. A laser reset occurred when the laser performance was not within a specified tolerance or when the Piezoelectric voltage approached the maximum allowable value. The Q-switch build up time was a voltage proportional to the time required by the Q-switch in the Nd:YAG laser to build up sufficient power to fire a pulse. The laser performance generally improved as the Q-switch build up time decreased The Piezoelectric voltage was observed using a chart recorder and it provided an additional source of information regarding the performance of the laser. This voltage would oscillate near a specific value. If the voltage about which these oscillations occurred remained fairly constant or gradually changed in a constant direction the laser was performing well. If large changes occurred in this voltage or if the general direction the voltages were proceeding in changed then this indicated that the laser performance was being degraded in some way. Large changes in the Piezoelectric voltage usually indicated that the laser had reset. The frequency offset input was used to adjust the optical frequency of the laser.[37] For more information regarding the physical principles through which Nd:YAG lasers operate and other uses for these types of lasers see reference 38.

2.2.2 Laser Optics

A JML Optical model SES16500/900 shutter was used to allow only one pulse into the data area while the digital cameras were exposed. This shutter had a 25mm aperture. Trigger delays and exposure times down to 1 millisecond could be set using the driver/timer unit purchased with the shutter. Digital signals from the control computer and a synchronizing trigger from the laser were used to open the shutter when the laser emitted a pulse.[39]

Due to the amount of energy contained in each pulse of laser light emitted by the Nd:YAG laser in Q-switch mode special high damage tolerant optics were needed to steer the laser pulses to

the location where DGV data was taken. The main laser steering mirrors and lenses all had damage tolerances substantially higher than the required 380 mJ/cm^2 for the Nd:YAG laser used in this research. The high damage tolerant optics included 8 Melles Griot 1" high damage tolerant mirrors (part # 16MFB153), a CVI Laser Corporation spherical concave lens (part # BICC-25.0-26.1-C), a CV spherical convex lens (part # BICX-25.4-34.9-C) and a CV cylindrical concave lens (part # BICX-25.4-34.9-C). The optical system used to capture a portion of the laser beam to track pulse to pulse changes in the optical frequency has been made more efficient compared to the system used in the previous version of the Virginia Tech DGV system. The previous version of the Virginia Tech DGV system used neutral density filters to split off a small portion of the laser beam. This portion of the beam passed through several more neutral density filters before being projected onto a laser reference tab within the field of view of one of the three DGV camera modules.[40] Most of the split off portion of the beam was essentially wasted. This new set of optics captured the portion of the laser light that passed through one of the main laser steering mirrors. Tests were conducted to verify that enough laser light bled through the steering mirror to be used for monitoring the variations in laser optical frequency. This was in fact found to be the case. The bleed through light was directed to a piece of opaque white Plexiglas which acted as the laser reference tab. This laser reference tab was placed so that the portion of the tab where the bleed through light was projected was in the field of view of one of the camera modules. When this camera module acquired an image of the flow field it also captured an image of the bleed through light projected on to this target. Since the target was motionless the portion of the laser beam projected on the target could be used to track the variations in optical frequency of each laser pulse. There should, in fact, be enough bleed through light that the light could be passed through an optical arrangement that would expand the beam and allow it to be used to track spatial variations within each pulse. Such an arrangement would require a fourth camera module to be added to the DGV system. This fourth camera module would be dedicated to tracking spatial and temporal changes in the laser optical frequency. Reference 41 has more information on how to incorporate this extra camera module into the DGV system.

During the tests performed in the Virginia Tech Stability Wind Tunnel, the Nd:YAG laser and laser shutter were set up on an optical table directly below the test section. The laser pulses were fired into the control room through a hole in the control room floor. Figure 2.1 shows the laser optics setup below the test section. In the control room, the optics used to fire the laser into the test section were mounted on an optical table. An assembly resembling a periscope was used to turn the laser beam so it ran horizontally above the optical table. This "periscope" was also where the bleed through light used to monitor pulse to pulse variations in the optical frequency of the laser was

captured. Figure 2.2 is a photograph of the periscope assembly. There were two distinct optical setups used in the control room. The first optical setup produced a cone of laser light used to illuminate the data plane with laser light. This setup was used during acquisition of iodine cell calibrations and velocity data from the calibration wheel. Figure 2.3 shows the laser optics setup used during iodine cell calibrations and acquisition of velocity data from the calibration wheel. The other optical setup used in the control room produced a sheet of laser light. This sheet of light was used in acquiring velocity data in the wake of the 6:1 prolate spheroid model. Figure 2.4 shows the laser optics setup used during acquisition of velocity data in the wake of the 6:1 prolate spheroid model. Figure 2.5 is a photograph of the two sets of laser optics setup in the control room of the Virginia Tech Stability Wind Tunnel.
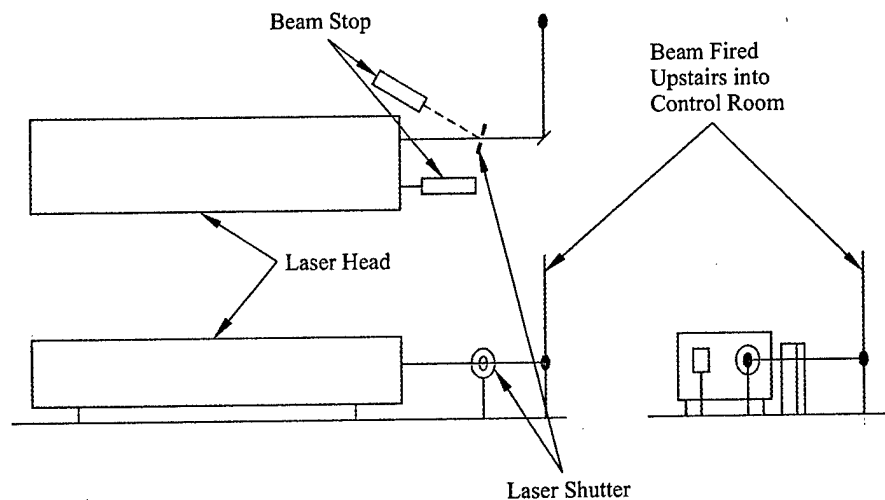
Figure 2.1: Laser optics setup below test section.
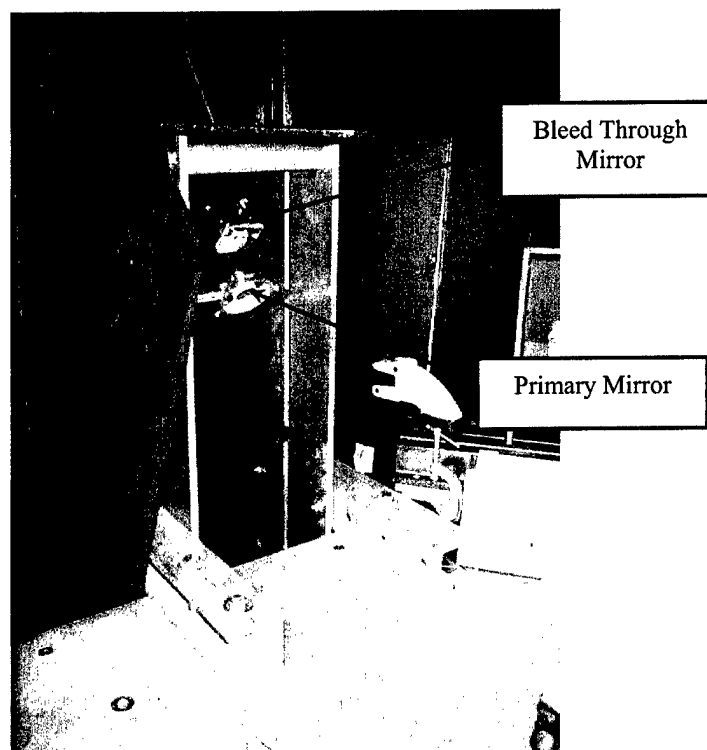
Figure 2.2: Photograph of periscope assembly.
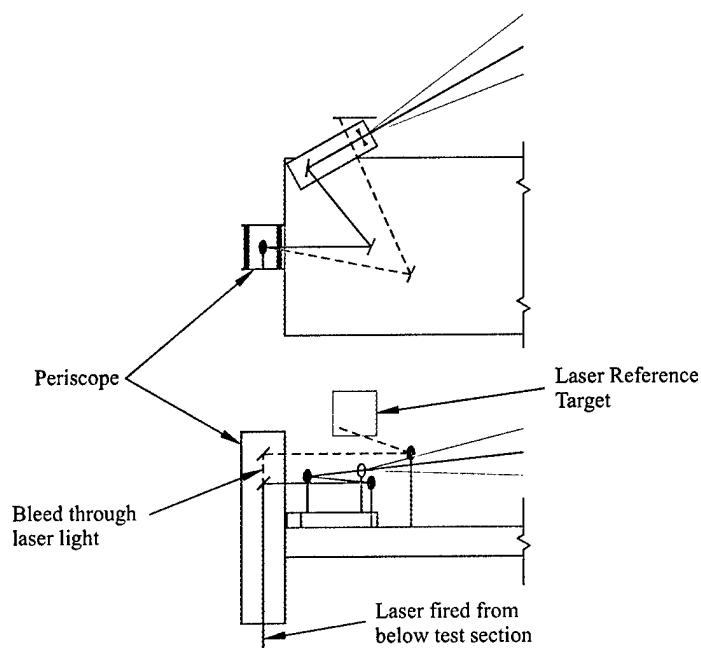
Figure 2.3: Laser optics setup for iodine cell calibrations and acquisition of velocity data from the calibration wheel.
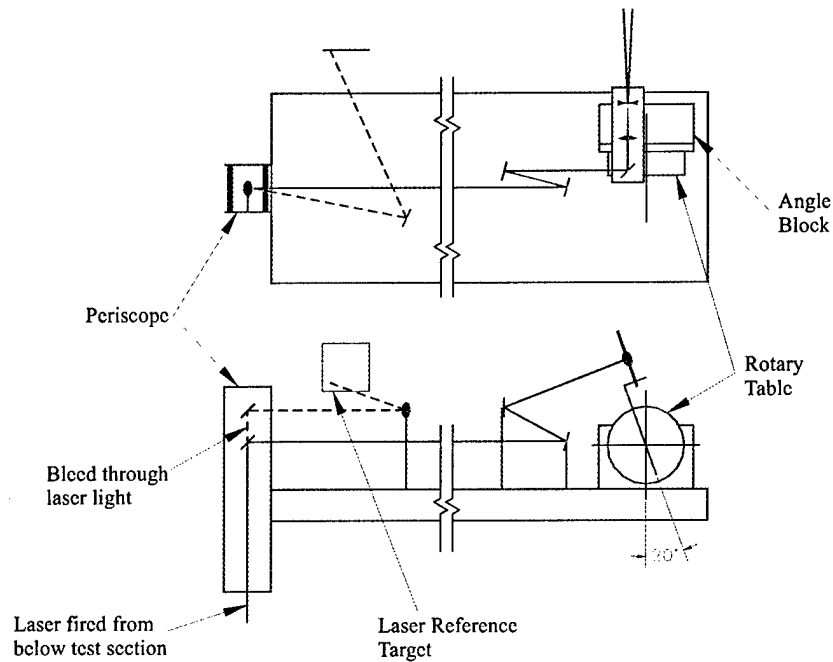
Figure 2.4: Laser optics setup for acquisition of velocity data in the wake of the 6:1 prolate spheroid model.
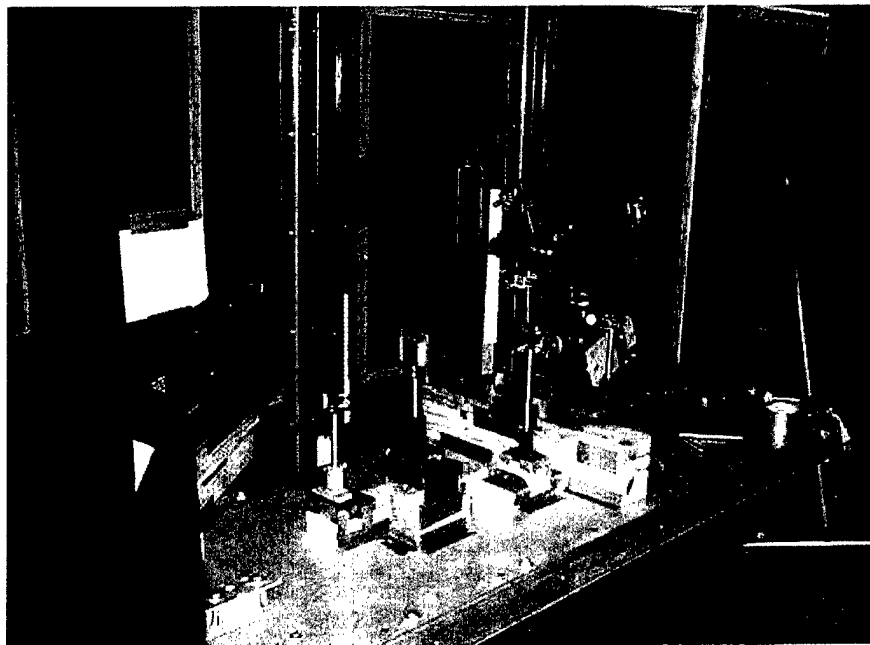
Figure 2.5: Photograph of laser optics setup in the control room of the Virginia Tech Stability Wind Tunnel.

2.3 Flow Seeding

Smoke machines and theatrical fog machines are the most common devices used to inject seed particles into large low speed (Mach number 0 – 0.3) wind tunnels for Doppler Global Velocimetry data acquisition.[42, 43, 44, 45, 46] Some important features for a smoke machine used in collecting DGV data are high volumetric flow rate, small particle sizes and the capability to produce smoke constantly. Generally it is most desirable to keep the mean particle size of the particle seeder between 0.5 to 5 μm.[47] While high volumetric flow rate is important, Meyers *et al* caution that while more seed particles will increase signal strength they also increase secondary scatter which will add uncertainty to the velocity measurement.[48] So the amount of seed/smoke used is a trade off between sufficient signal strength and secondary scatter.

A Vicount 5000 smoke machine manufactured by Corona Integrated Technologies Inc. was used to inject seed particles into the wind tunnel. This smoke machine was recommended by James Meyers of the NASA Langley Research Center.[49] The machine heated mineral oil to produce smoke and used compressed nitrogen at a pressure of 0.482600 MPa (70 psi) as a propellant.[50] The machine and rig to inject smoke into the flow were placed in the settling chamber of the Virginia Tech Stability Wind Tunnel. The nitrogen cylinder was placed in the control room of the tunnel and a hose was fed into the tunnel and to the machine. Figure 2.6 shows the machine and injection rig. The smoke volume could be adjusted using a knob inside the smoke machine or by adjusting the propellant gas pressure.[51]

Figure 2.6: Smoke machine and injection rig

The rig used to inject smoke into the wind tunnel was constructed of PVC pipe. A 76.2 mm (3 inch) diameter hose connected the injection rig to the smoke machine. The injection rig consisted of a 76.2 mm (3 inch) diameter PVC pipe which was connected to a box shaped head made of 50.8 mm (2 inch) diameter PVC pipe. The head was 90.2 cm (35 ½ inches) wide from centerline to centerline and 88.9 cm (35 inches) high from centerline to centerline. Holes spaced 38.1 mm (1.5 inches) apart were drilled into the 50.8 mm (2 inch) diameter PVC pipe to provide outlets to inject smoke into the wind tunnel. The injection rig was attached to a 38.1 mm (1.5 inch) diameter galvanized pipe which was placed vertically along the centerline of the settling chamber of the wind tunnel. The injection rig was placed so that the stream tube of smoke ran roughly through the center axis of the test section.

2.4 Camera Modules

A camera module was used to hold each of the digital cameras and the optics needed to split the image viewed by each of the cameras into a reference image and a filtered image. Figure 2.7 shows the layout of the camera module. Figure 2.8 is a dimensioned drawing of the optical arrangement inside a camera module. The image acquired by the camera is reflected off of two mirrors before encountering a beam splitter, which allows half of the image intensity to pass through, and reflects the other half of the image intensity into the iodine cell. Each of these images is reflected off of two more mirrors before the images are captured by the digital camera. Special care was taken to make sure the image paths for the reference and filtered images were the same length. The digital camera and the optics are mounted between a 9.53 mm (3/8 inch) thick aluminum plate and a 12.7 mm (1/2 inch) thick Plexiglas plate. Spacers were placed between the plates to give the module additional strength.
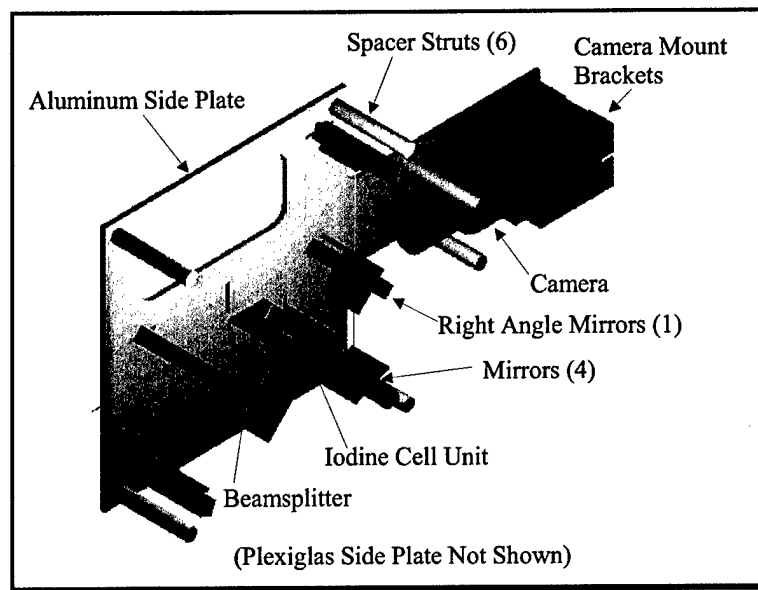
Figure 2.7: Layout of camera module (from Jones 2000)[52]
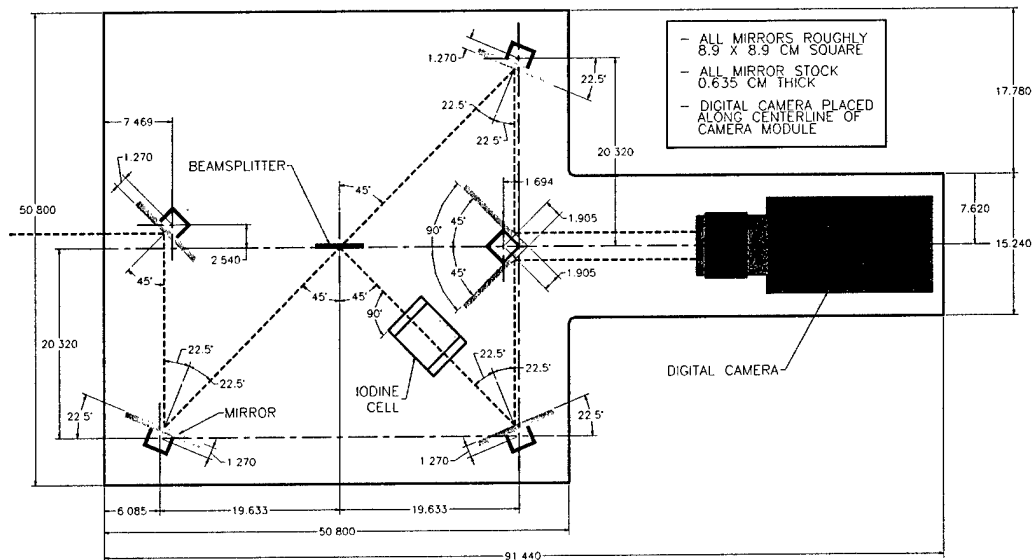
Figure 2.8: Dimensioned drawing of the optical arrangement inside a camera module

2.4.1 Digital Camera

The first DGV systems assembled used analog video cameras in conjunction with frame grabbers to acquire data.[53] While some researchers have stayed with 8-bit or 10-bit surveillance cameras others recommend using 16-bit digital astronomy cameras.[54,55] It appears the choice between these is primarily one of cost versus signal to noise ratio. The systems using 16-bit cameras generally have a higher signal to noise ratio but they can cost 10 to 28 times as much as a system

using 8-bit surveillance cameras.[56, 57, 58] Figure 2.9 shows a comparison of signal to noise ratios for various digital cameras.
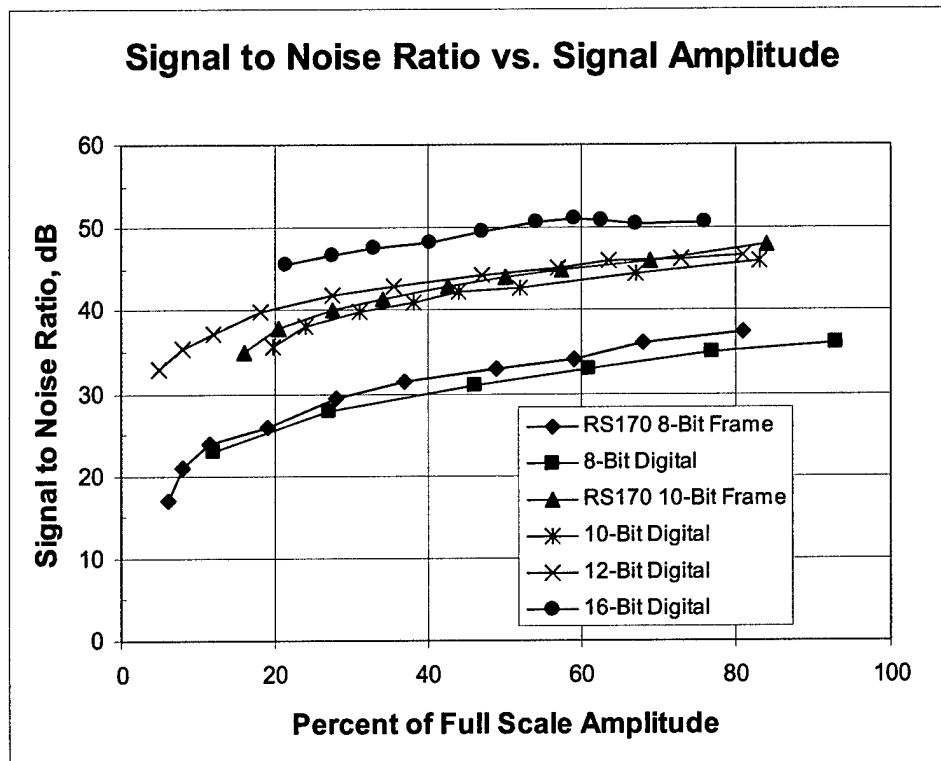
Figure 2.9: Signal to noise ratios for some digital cameras.[59]

The original Virginia Tech DGV system used three 16-bit digital cameras manufactured by Spectra-Source (1 – MCD 1000S and 2 – Orbis 16). The operation and performance of these cameras was virtually identical. One of the Orbis 16 cameras began to malfunction during the first set of DGV tests in the Virginia Tech Stability Wind Tunnel. During the research discussed in this volume the malfunctioning camera was replaced with a VersArray 16-bit camera manufactured by Roper Scientific. While the operation of this camera was somewhat different from the Spectra-Source cameras the performance was similar to the older cameras. The VT DGV control program was updated so that the new camera could be used by the VT DGV system. All of the functionality of the previous camera, before it began to malfunction, has been retained in the new camera system.

It should also be noted that the remaining Spectra-Source cameras also started to develop problems. Ice crystals began to form on the CCD array (the imaging surface) of the remaining Orbis 16 camera after it was on for roughly an hour. The camera was still usable, for the first hour that it

was on, but as section 5.3.3 will explain in greater detail, this problem led to a less than ideal solution to a problem with the images acquired by the camera modules shifting over time. During the final set of tests performed during the research discussed in this volume the MCD-1000S camera did not lock on the set point temperature required by the camera cooling system. While this did not appear to affect the performance of the camera during data acquisition the long term effects of this problem are unknown.

2.4.2 Iodine Cell

An iodine cell is essentially a hollow glass cylinder, with optical quality windows attached to the ends, and filled with iodine gas. As previously mentioned, iodine gas has some useful absorption properties for light in the green portion of the visible spectrum. Figure 2.10 shows a theoretical light absorption profile for an iodine cell over a small range of optical frequencies in the green portion of the visible spectrum. The variation in optical frequency is given in terms of the wave number. The wave number is calculated using the formula below:

$$WaveNumber = \frac{1}{\lambda} = \frac{v}{c} \qquad (2)$$

where λ is the wavelength of the light, v is the optical frequency of the light, and c is the speed of light.

A variety of different gas combinations have been used to tailor the iodine cell absorption transitions for specific uses. Researchers performing experiments in high speed flows often use cells containing a mixture of iodine and nitrogen to increase the range of optical frequencies over which a transition from full transmission to full absorption occurs.[60] Researchers performing experiments in low speed flows (Mach Numbers from 0 to 0.3) generally use iodine cells filled with pure iodine since this type of cell will have the sharpest transition between full transmission and full absorption, thus providing the best sensitivity to small variations in optical frequency.
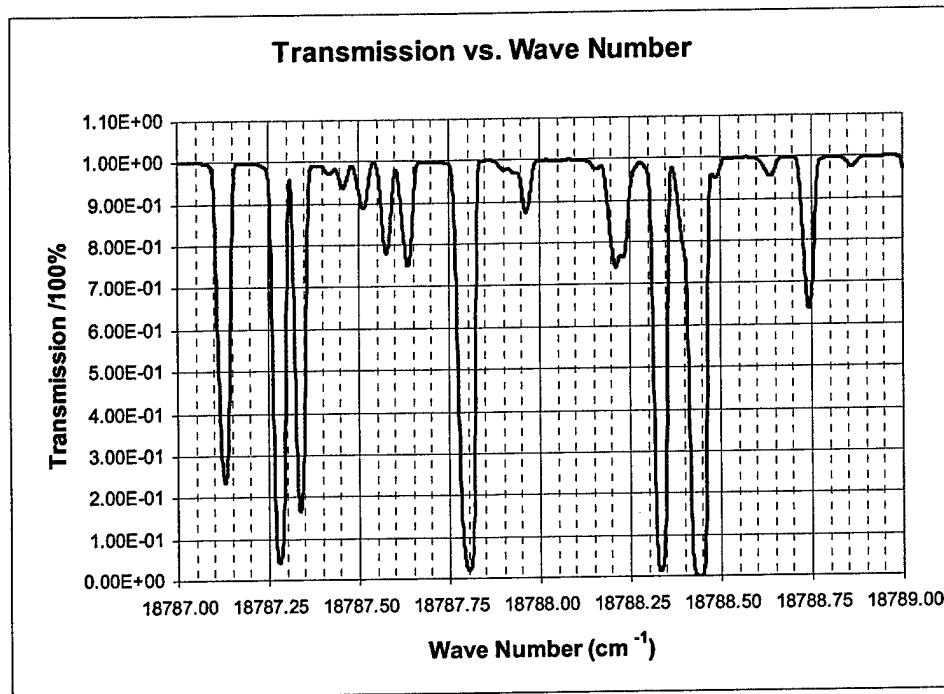
Figure 2.10: Transmission versus wave number for an iodine cell, containing pure iodine gas, at a cold finger temperature of 40 ℃.

Previous researchers using the DGV technique to perform flow velocity measurements have used iodine cells with an attachment called a cold finger. The cold finger acted as a reservoir because it contained solid crystals of iodine. As the cold finger was heated the crystals melted providing iodine gas for the body of the cell. The cold finger temperature was controlled independently from the temperature of the body of the cell. Generally the body temperature was kept considerably higher than the temperature of the cold finger so that any crystals that form in the cell form in the cold finger. An important consideration for this type of iodine cell was that the temperature of the cold finger controlled the absorption properties of the cell and therefore needed to be closely monitored. In fact a change in the cold finger temperature of 0.1℃ resulted in a change of 3 m/s in the measured velocity.[61] This sensitivity required great care to be taken in monitoring and controlling cold finger temperature in an attempt to minimize the measurement uncertainty caused by variations in the cold finger temperature.

Recently, another novel approach has been taken. A few researchers have started using "vapor limited" iodine cells.[62, 63, 64] A vapor limited iodine cell does not have a cold finger. The cell is filled with iodine gas at a specified temperature, and so long as the cell temperature is above the

temperature of the iodine gas as it was injected into the cell, no iodine crystals will form inside the cell. In addition to this, the iodine cell absorption properties will remain constant.[65]

The iodine cells previously used in the Virginia Tech DGV system had a cold finger, which contained crystallized iodine that acted as a temperature dependent reservoir. This arrangement required the cold finger temperature to be monitored very closely. The three iodine cells used in previous tests of the VT DGV system were modified to be vapor limited at temperatures above 40°C. The iodine cells were manufactured and refurbished by Opthos instruments. Each of these cells was 5.08 cm in length and 5.08 cm in diameter. The ends of the cell were sealed with ¼ wave flat windows. The windows were treated with an anti-reflective coating for light wavelengths near 532 nm. The iodine cells were filled with 99.9% pure diatomic iodine vapor and were permanently sealed to prevent the iodine vapor from escaping the cell.[66]

2.4.3 Temperature Control

Each iodine cell was wrapped with a heating mat and enclosed in an aluminum box. The aluminum box was mounted inside the camera module. An RTD, resistive temperature probe, was inserted into the aluminum box to monitor the temperature of the iodine cell body. The heating mat and RTD probe were connected to a Scientific Instruments Inc., Dyna-Sense Mk III temperature controller. This temperature controller contained a Proportional Integral Derivative (PID) control unit, which used temperatures measured by the RTD probe as feedback and turned the heating mat on and off as needed to maintain the cell body temperature near the desired body temperature. The rated temperature stability for this controller was ±0.1°C. The temperature controllers used to monitor and control the temperature of the cold fingers on the iodine cells in the previous version of the VT DGV system were eliminated from the system. The set point temperatures on the temperature controllers for the body of the iodine cells were set to keep the temperature of the iodine cells near 60°C.[67]

2.5 Calibration Wheel

The most common procedure used to test and validate DGV systems is to acquire data while viewing a disk or wheel rotating at a known angular velocity. Many researchers have used analog DC motors to drive their wheel systems and "optical tachometers" to keep track of the variations in wheel speed.[68] In fact the "optical tachometer" is really nothing more than a light source illuminating the back of the wheel which has a white line painted on it. The flash of light reflected off of the wheel when the white line passes through the beam of light is detected using a photodiode.[69] While this system may work well for some, it does not give any information about variations in wheel velocity

over the course of each revolution, thus producing a source of error in DGV measurements using the wheel and in calibrating the iodine cells if the wheel is used in the calibration procedure.

The calibration wheel system designed for the Virginia Tech DGV system contains a feedback control system to make sure the wheel speed is held constant. The calibration wheel system also has the capability to make instantaneous quantitative measurements of the wheel speed. Figure 2.11 is a diagram showing the control system architecture for the new calibration wheel system. An IBM compatible personal computer is used to write maneuver programs for the calibration wheel. These programs are downloaded to the servo motor controller (a Baldor 1-Axis Smartmove Servo Controller). The controller sends a reference voltage to the servo amplifier (Advanced Motion Controls Model #BE25A20-AC). This voltage is proportional to the current sent from the servo amplifier to the motor. An optical encoder (Hewlett Packard Model # 5640-A06) is attached to the motor to measure the position and angular velocity of the motor shaft. The signal from the encoder is used as feedback for the servo amplifier and the controller. The encoder signal can also be used by the controller to record information about the motor performance, such as wheel speed, position and following error. The motor was connected to a 304.8 mm (12 inch) long shaft through a motor coupler. The 304.8 mm (12 inch) shaft was supported by two roller bearings. A 254 mm (10 inch) diameter aluminum disk was connected to the other end of the 304.8 mm (12 inch) shaft. Sandpaper (400 grit) was applied to the side of the disk facing away from the motor. The sandpaper and outer edge of the disk were painted white. An enclosure was constructed to keep parts from flying away from the motor and shaft assembly in the event something in the motor or bearing assembly came loose or broke away. Figure 2.12 shows the calibration wheel and protective enclosure and figure 2.13 is a dimensioned drawing of the mechanical portion of the calibration wheel system inside the protective enclosure.
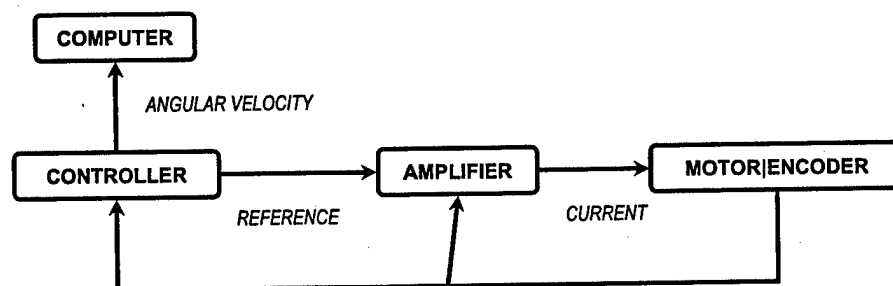
Figure 2.11: Calibration wheel control system diagram
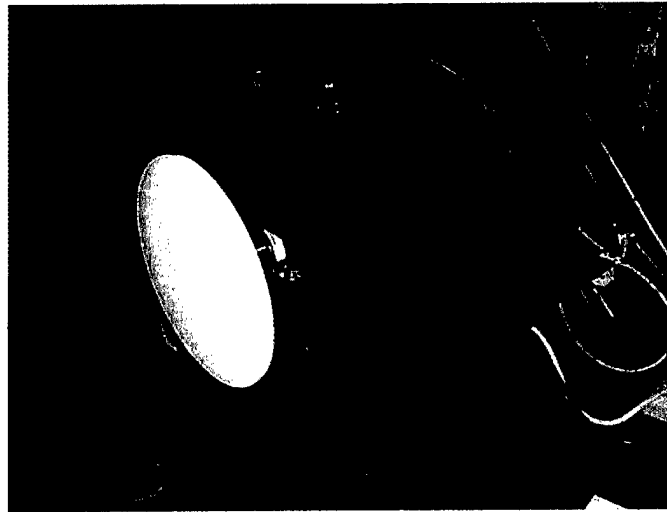
Figure 2.12: VT DGV calibration wheel
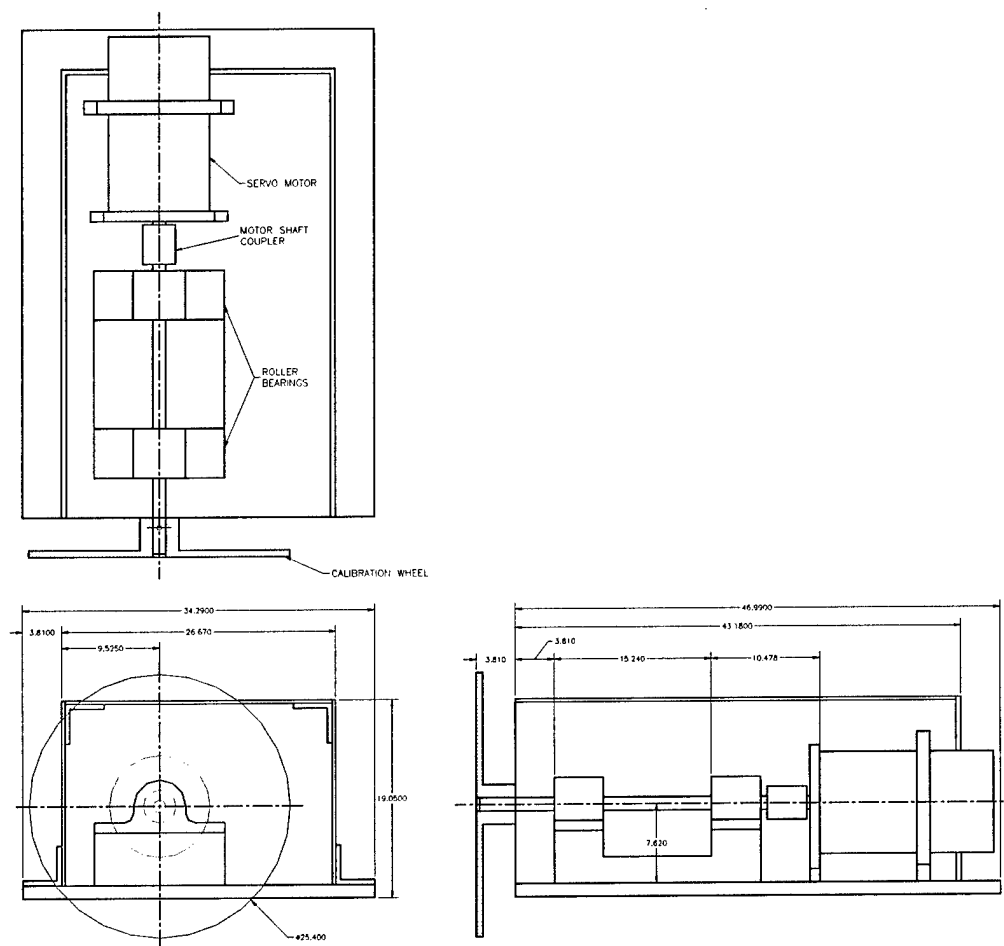
Figure 2.13: Dimensioned drawing of the mechanical portion of the calibration wheel system.

The motor controller provides two different methods for monitoring the performance of the motor. The controller can acquire and store motor velocities in an array that can be uploaded to the host computer. This capability was used to acquire an array of wheel velocity data for a series of maneuvers similar to the maneuver that will be used in calibrating the VT DGV system. Figure 2.14 shows a plot of the wheel rotation speed versus time in seconds. Data were collected at 2 millisecond intervals for 9.9 seconds, but for display purposes the plot shown in figure 2.14 contains data taken at 10 millisecond intervals. For the maneuver shown, the commanded wheel speed was 60 revolutions per second. The average wheel speed during the constant portion of the maneuver was 60.1851 revolutions per second. The standard deviation of the wheel speed measurements was 0.2207 revolutions per second. The controller can also output a voltage that is proportional to the motor velocity. This capability and the ability to store an array of velocity data were used to calibrate the wheel system.
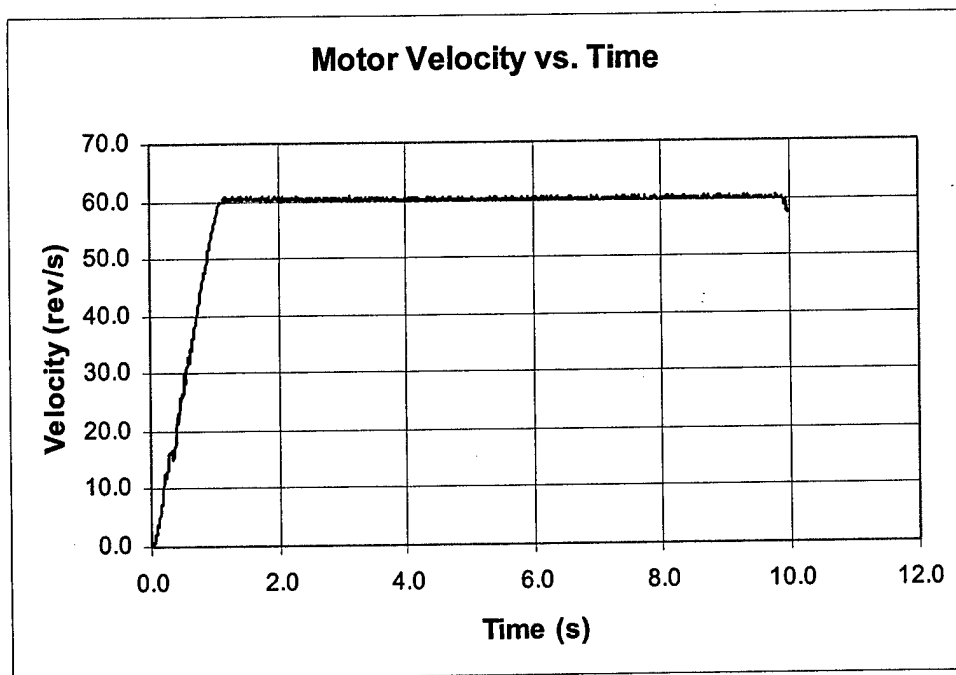
Figure 2.14: Calibration wheel test data (commanded speed: 60 rps)

2.6 Computers and Software

2.6.1 DGV Computers

Two PC compatible computers were used by the Virginia Tech DGV system. The first computer, designated DGV1, was a Pentium 160 MHz computer and contained interface cards for each of the three 16-bit digital cameras as well as a 16 channel Measurement Computing PCI-

DAS1602/16 data acquisition board. The data acquisition board was used to send digital signals from the laser shutter and to send and receive analog signals to set the optical frequency of the laser and monitor the performance of the laser. The second computer, designated DGV2, was a Celeron 700 MHz computer. This computer was used to program the calibration wheel controller and to archive DGV data files. This computer is available for use in the future to run a fourth camera module to monitor laser performance. The fourth camera module cannot be run by DGV1 because all available slots in this computer have been filled.

2.6.2 DGV Software

The DGV Control Program used to acquire and reduce DGV data was originally written by Troy Jones.[70] This Windows based program was written in Visual C++ Version 6. The program could acquire single or multiple images from any combination of the three 16-bit cameras. The user could choose whether or not to save these images and could also choose the exposure time. Images from each camera could be viewed one at a time. The program could automatically perform a variety of operations on a sequence of images. Some of these operations included: setting separate regions of interest for the filtered and reference views, setting separate regions of interest on one of the three camera views to monitor mean variations in laser optical frequency, image addition and subtraction, image division, image de-warping, image mirroring, image filtering, and applying image intensity corrections. The program could automatically acquire iodine cell calibrations and reduce the acquired data to obtain an absorption profile in terms of laser offset voltage for each of the three 16 bit cameras. It could also automatically reduce a sequence of DGV velocity images, or an average DGV velocity image to obtain a velocity field for the plane in which data was taken. This program was also used to set the power and operating mode of the Nd:YAG laser, operate the laser shutter and monitor the cold finger temperature.[71] Figure 2.15 shows the Graphic User Interface for the DGV Control Program.

Over the course of this research several changes were made to the DGV Control Program. The software used to run the malfunctioning Orbis 16 camera was replaced with software needed to run the new VersArray 16-bit camera. Since the cold fingers on the iodine cells were removed, to make the iodine cells vapor limited, portions of the program which monitored the cold finger temperature or used the temperatures obtained were disabled but left in place where possible and deleted if necessary. Software was added to turn the calibration wheel on and off from DGV1 using a digital output from the data acquisition board. The control program now has the ability to acquire voltages from the calibration wheel controller proportional to the wheel speed. This was done using

one of the analog inputs from the data acquisition board. The DGV Control Program can convert these voltages into angular velocities, and can store the voltages, standard deviations of the voltages, angular velocities, and standard deviations of the angular velocities in a file during DGV velocity data acquisition or merely sample and display the output voltage from the calibration wheel controller. Software was also added to allow the smoke machine to be turned on and off by DGV1 but this portion of the program was not used during data acquisition. Also, extensive modifications to the data reduction portion of the program were made. Some of the changes made to the data reduction algorithm included: changes to apply background and white card corrections to each image before the mean laser reference transmission ratio was calculated, the single frequency calibration function used to calculate the optical frequency from a transmission ratio was changed so that each camera module had its own frequency calibration function, the procedure used to apply the laser reference transmission ratio was changed, and the method used to calculate the wave number used as part of the data reduction procedure was changed. These changes corrected some significant problems with the data reduction procedure.
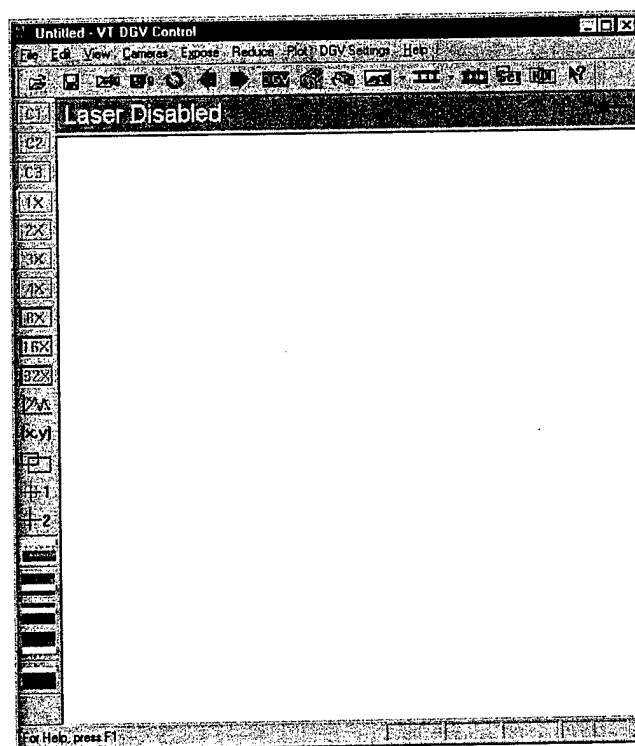
Figure 2.15: Graphic User Interface (GUI) for the Virginia Tech DGV Control Program.

A FORTRAN program written by J. N. Forkey was used to determine the theoretical absorption profile for the iodine cells.[72] This theoretical absorption profile was compared to the

profile measured during an iodine cell calibration to determine the mean optical frequency the laser was operating at for a given laser offset voltage. The iodine cell dimensions, vapor temperature, wave number range and wave number increment size were input to the program and transmission versus wave number were output by the program. More information regarding the physical principles simulated by this program and information on how this program works can be found in reference 73.

A MATLAB toolbox "Camera Calibration Toolbox for MATLAB" written by Jean Yves Bouguet, Ph.D. at California Institute of Technology, was used to determine the rotation matrix to transform the coordinate system of the data plane to the coordinate system of each camera module.[74] This was done by measuring reference points on a series of images of a checkerboard. A corner extraction program, incorporated into the toolbox, allowed the user to mouse click on an acquired image of a checkerboard near one of the box intersections and the program would automatically determine the intersection coordinates for all checkerboard intersections within the user specified region on the image. For this reason images of a checkerboard pattern were acquired to determine the rotation matrix as well as to de-warp images during the DGV data reduction procedure. The rotation matrix calculated by the toolbox was used to determine a set of Euler angles for each of the camera modules which were used in the data reduction portion of the DGV Control Program. The MATLAB toolbox used machine vision techniques to determine the rotation matrix. This toolbox was also capable of measuring and correcting for optical distortion of images captured by a digital camera. This portion of the toolbox could not be used for the camera calibration images acquired by the DGV system, because the digital cameras used in the DGV system used zoom lenses and were observing the data plane from a long distance. More information about machine vision techniques, the capabilities of this MATLAB toolbox and how to use the toolbox can be found in reference 75.

2.7 Virginia Tech Stability Wind Tunnel

The Virginia Tech Stability Wind Tunnel was used in the tests of the Virginia Tech DGV system. This tunnel has a test section that is 182.9 cm (6 feet) high by 182.9 cm (6 feet) wide and 731.5 cm (24 feet) long. The contraction ratio for the tunnel is 9:1.[76] Air is moved in the tunnel by a 600 hp D.C. motor which drives a 426.7 cm (14 foot) diameter propeller. The tunnel is capable of running at a Reynolds number per meter of 505968 (Reynolds Number per foot of 1.66×10^6) with the test section used for this experiment. The turbulence intensity in the empty test section of this tunnel is less than 0.05% and the variation of the dynamic pressure is approximately 0.05% across the test section. The vertical flow angularity in this tunnel is approximately ±1˚(previously measured through a vertical sweep of the test section). In the middle of the test section the flow angularity is

less than 0.25. The flow speed in the wind tunnel was measured using a Pitot static probe mounted in the test section. Temperature in the wind tunnel can be measured using a thermocouple, also mounted in the test section.[77]

2.8 6:1 Prolate Spheroid Model

A 6:1 prolate spheroid model was used in these tests. This model was the same model that was used by Chesnakas *et al.*[78] The model was 1.37 m long (53.9 inches) and had a maximum diameter of 0.229 m (9 inches). The model was constructed in three sections. Each section had a fiberglass skin bonded to an aluminum frame. A trip strip was placed around the circumference of the model at x/L = 0.2. This trip strip consisted of circular cylindrical posts 1.2 mm (0.047 inches) in diameter and 0.7 mm (0.028 inches) high, spaced 2.5 mm (0.098 inches) apart. Screw holes and seams between model sections were filled with red wax to smooth these irregularities out. The model had two windows which allowed optical access for an LDV system used in previous tests. These windows were covered with plastic sheeting and the entire model was painted with flat red primer. A 0.75 m (29.5 inch) sting protruded out of the rear of the model. The sting was mounted to a vertical post attached to a turntable beneath the test section floor.[79] Figure 2.16 shows the prolate spheroid model mounted in the wind tunnel test section.
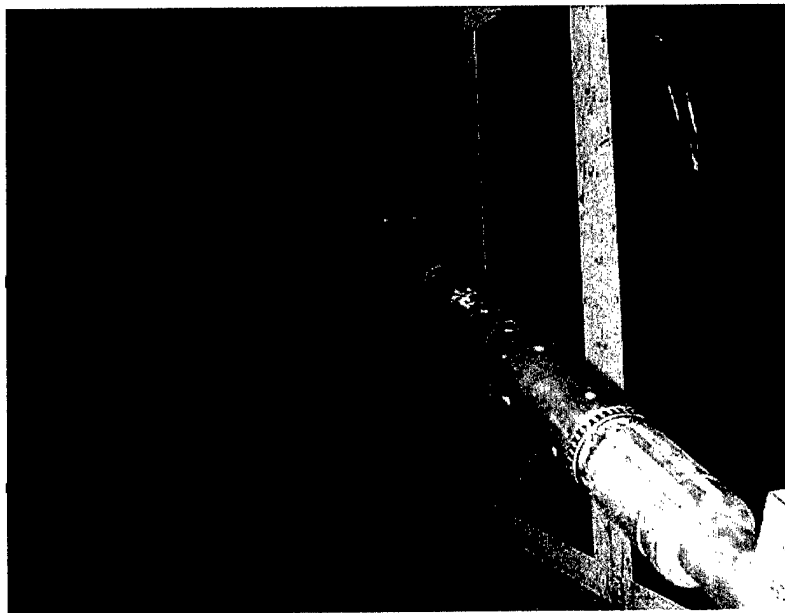
Figure 2.16: 6:1 prolate spheroid mounted in wind tunnel test section.

Chapter 3: Procedures and Techniques

Chapter 3 : Procedures and Techniques

3.1 VT DGV Procedures and Techniques

This chapter will discuss the procedures and techniques used to align the optics in each of the camera modules, calibrate and run the calibration wheel, acquire the various correction images needed to reduce raw DGV data images into DGV velocity data, acquire calibration images needed to determine the absorption characteristics of each iodine cell used in the VT DGV system, and acquire the raw DGV data images. The only significant change made during this research to the procedures used to acquire the correction, calibration, and data images was to add a procedure to acquire a series of images used in calculating Euler angles for each camera module that were then in turn used to calculate the unit vector $\hat{a}$ in equation 1. Proper alignment of the optics in the camera modules allowed the maximum image area to be used as the Regions of Interest (ROI's) while acquiring and reducing DGV data. The calibration wheel was used in this research as a way of independently verifying the performance of the VT DGV system. The VT DGV system acquired velocity data while viewing the calibration wheel as the wheel rotated at a known angular velocity. The reduced VT DGV data could then be compared to the known rectilinear velocity profile of the calibration wheel. Several different types of correction images are needed to account for various types of image imperfections inherent to the acquired data images. These imperfections occur for a variety of reasons. Two examples of image imperfections are non uniform sensitivity of the light collecting pixels in the Charge Coupled Device (CCD) inside each camera and stray ambient light collected by the cameras during data acquisition. Calibration images are needed to determine the absorption properties of the iodine cells used in the DGV system. These images can then be compared to the

theoretical absorption properties of an iodine cell of the same size and vapor pressure to determine how the absorption properties of the iodine cells vary with the optical frequency of the light passing through the cell. Once all of the correction images and calibration images have been acquired, the raw DGV data images can be acquired.

3.2 Camera Module Optics Alignment

An apparatus has been developed to align the optics inside each camera module. Proper alignment of the optics inside each module insures that the maximum viewing area is available for data collection. Figure 3.1 shows one of the camera modules during optics alignment. A Coherent© Diode Laser was used to perform the rough alignment of the optics. The diode laser was placed roughly 42 inches away from the front of the camera module. A mechanism was designed to hold and position the laser head so the beam hit the center of the first image acquisition mirror. The diode laser head was aligned so that the beam, emitted from this laser, reflected off of a mirror attached to the front edge of the camera module and back to the center of the front face of the laser head. This ensured that the beam was perpendicular to the front edge of the camera module. Next, the laser alignment mirror was removed from the front of the camera module and the laser was fired into the module toward a target placed on the lens cap of the camera. The laser beam was split by the optics inside the module and module optics were adjusted until the two beams projected on the lens cap target were equally spaced roughly 3/16 inch from a center line placed on the lens cap target. Next, the laser was turned off, the lens cap and lens cap target were removed from the camera and images were acquired of the diode laser head. The positions of the optics were adjusted until the distances from the split line between the two images to the center of the laser head on each image were equal. Finally, the positions of the optics were fine-tuned until the center of the laser head was centered horizontally in each of the fields of view.
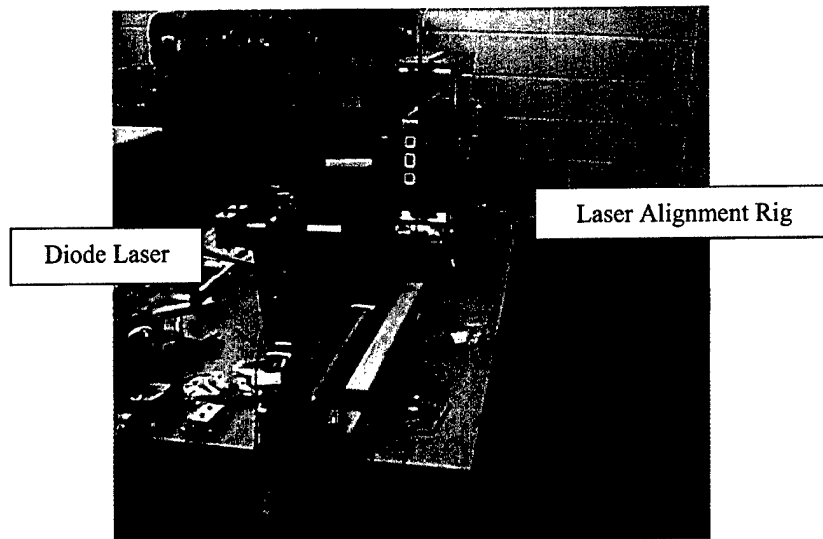
Figure 3.1: Camera module optics alignment apparatus

3.3 Calibrating the Calibration Wheel

The calibration wheel was run through a series of tests to determine the relationship between the voltage output by the Baldor Smartmove controller to the wheel speed in revolutions per second. The data needed to determine this relationship were acquired by running the wheel for 10 seconds at 5 rev/s increments from -65 rev/s to 65 rev/s as well as -66.7 rev/s and 66.7 rev/s and capturing an array of velocity data and an array of voltage data for each speed. The array of velocity data was acquired by the controller itself and then downloaded to the host computer. The voltage data were acquired by the data acquisition card in DGV1. Next the average voltage and the average motor velocity were calculated and plotted. Figure 3.2 shows a plot of the average controller output voltage versus the average wheel speed. A linear regression of these data was performed to determine an equation relating the offset voltage to the wheel speed. The plot also shows this equation relating the output voltage to the wheel speed. The equation is also given below:

$$Speed = -51.2070(Voltage) - 0.2589 \qquad (3)$$

where *Speed* is the wheel speed in rev/s and *Voltage* is the offset voltage from the controller.
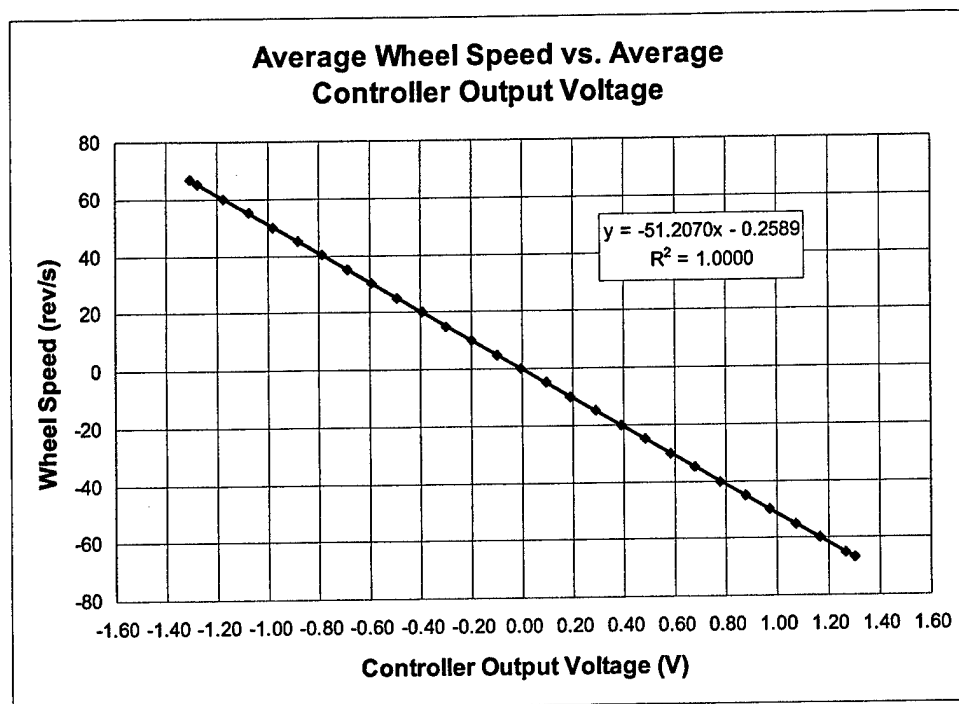
Figure 3.2: Wheel calibration plot.

3.4 Correction Images

3.4.1 Geometric Correction

Images of a dot grid or checkerboard placed in the data plane are needed when using the DGV technique. These images are used to correct for the geometric distortions that occur due to each of the camera modules viewing the data plane from a different location. During previous tests of the Virginia Tech DGV system, images of a dot grid were acquired to correct for geometric distortion. The pattern used to acquire these images was changed to a checkerboard during this research because the images of a checkerboard pattern could be directly plugged into the *"Camera Calibration Toolbox for MATLAB"*[80]. This toolbox was used to determine the viewing angles for each of the three camera modules. The checkerboard pattern was 9" x 7" in size and consisted of black and white 12.7 mm (½ inch) squares.

Prior to each iodine cell calibration or acquisition of a set of DGV velocity data, several images (between 5 and 10) of the checkerboard were acquired and averaged. The average image was used to determine the size and location of the Region of Interest (ROI) where DGV data would be collected. A warp point was selected at each of the four corners of the ROI. This region of interest appeared as a parallelogram or a trapezoid. In addition to choosing the warp points, a rectangular

region of interest proportional to the known size of the region of interest was also chosen in the Graphic User Interface of the DGV Control Program. Next the warped region of interest was mapped to the rectangular region of interest selected by the program user. This mapping is referred to as de-warping since this step removes the geometric effects of perspective from the region of interest. The reference and filtered regions of interest for each camera module were mapped separately. The region of interest for the reference view was designated Region 1 and the region of interest for the filtered view was designated Region 2. The filtered view was vertically mirrored before the warp points were selected and before the view was mapped to the corresponding rectangular region of interest. Each mapping produced an image in which the point of view appears to be perpendicular to the data plane. This type of image correction allows images acquired from multiple points of view to be overlaid on top of one another thus producing velocity data in any desired inertial reference frame. Figure 3.3 shows before and after images demonstrating the effects of mapping an image of the checkerboard to the rectangular region of interest. The selected warp points and rectangular region of interest could be saved, as part of a configuration file, for future use. More information on the techniques used to perform this mapping can be found in reference 81.

(a)   (b)
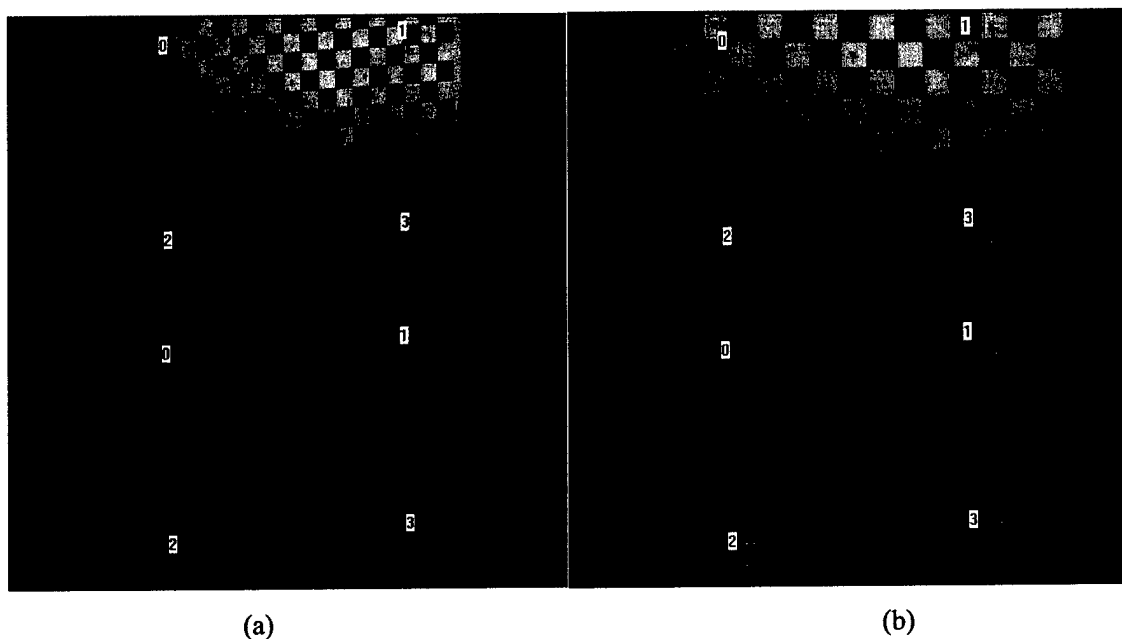
Figure 3.3: Demonstration of geometric image correction. Figure (a) shows checkerboard and warp points before mapping and figure (b) shows checkerboard after mapping.

3.4.2 Background Correction

The basic premise upon which every camera functions is that the camera collects and stores light while the shutter on the camera is open. Definable images appear through variations in light

intensity reflected off of objects in the field of view of the camera. The cameras used in the Virginia Tech DGV system also function in this way, but this principal also becomes a source of signal error because the data plane is illuminated by laser light for only a very small portion of the time the camera shutter is open. Ambient light in the area where the DGV system is being used is also collected while the camera shutters are open. Since the signal used to discern velocity in the DGV technique is the light intensity collected by each pixel in the Charge Couple Device (CCD) inside the digital cameras used by the system, this ambient light causes an error in the velocities measured by the system. The solution to this problem is straight forward. Images are collected over the same period of time and under the same lighting conditions in which velocity data will be collected but the data plane is not illuminated by the laser. These "background images" are then subtracted from the data images to account for the ambient light illuminating the area where data is being taken.

Several background images (between 5 and 20) were acquired before each iodine cell calibration was performed and before each set of velocity data was acquired. The acquired background images were averaged to calculate an average background image. This average background image was subtracted from each iodine cell calibration image and each velocity data image during data reduction. All of the background images and DGV velocity data images were acquired with all of the lights in the area turned off. The ideal background condition to acquire DGV data is complete darkness. This minimizes the effect of the background image thus providing the maximum light intensity range over which data can be collected. During DGV data acquisition in the Virginia Tech Stability Wind Tunnel, the average light intensities measured by each camera during background image acquisition were roughly: 1180 for camera module 1, 1270 for camera module 2, and 990 for camera module 3. These light intensities were out of a maximum value of 65536.

3.4.3 Pixel Sensitivity Correction

Ideally the sensitivity to light of each pixel in the Charge Couple Device (CCD) array of a camera used in a DGV system should be uniform. Unfortunately this is never the case. These variations in pixel sensitivity are a potential source of measurement error in the DGV technique so a correction is needed to account for them. The procedure used to make this correction required two different sets of images of a uniformly illuminated surface to be acquired with the lens removed from the camera. The first set of images was acquired at an illumination intensity roughly 25% of the maximum light intensity discernable by the camera. The second set of images was acquired at an illumination intensity roughly 75% of the maximum light intensity discernable by the camera. Next, a pixel sensitivity factor was calculated for each pixel in the CCD array using the following formula:

$$PS_{ij} = \frac{P_{ij}^1 - P_{ij}^2}{L_1 - L_2}$$

(4)

where PS_{ij} was the pixel sensitivity factor for the CCD pixel at row i and column j, P_{ij}^1 was the light intensity recorded by the CCD pixel at row i and column j for the higher illumination intensity (75%), P_{ij}^2 was the light intensity recorded by the CCD pixel at row i and column j for the lower illumination intensity (25%), L_1 was the average light intensity of all CCD pixels for the higher illumination intensity (75%), and L_2 was the average light intensity of all CCD pixels for the lower illumination intensity (25%). The pixel sensitivity correction is applied to an image by dividing the image by the pixel sensitivity correction image. This operation is performed by dividing the integer light intensity value for each pixel in the image being corrected by the corresponding integer light intensity value of the corresponding pixel in the pixel sensitivity correction image.[82]

The uniformly illuminated surface was created using an extension cord with an inline dimmer switch, a desk lamp, six sheets of 6.35 mm (¼ inch) thick opaque white Plexiglas, and 6 sheets of 20 bond white copy machine paper. The 6 sheets of white paper were placed between the third and fourth sheets of Plexiglas. The desk lamp was plugged into the extension cord and the Plexiglas sheets were placed against the open end of the metal shroud covering the light bulb in the lamp. The camera was placed against the other side of the Plexiglas sheets. The dimmer switch was used to adjust the intensity of the light bulb used to illuminate the Plexiglas sheets. Figure 3.4 is a drawing showing the setup used to determine the pixel sensitivity. Figure 3.5 shows the effect of the pixel sensitivity correction on an image. Figure 3.6 shows the effect of the pixel sensitivity correction on the actual pixel intensity values on row 50 of the images shown in figure 3.5.
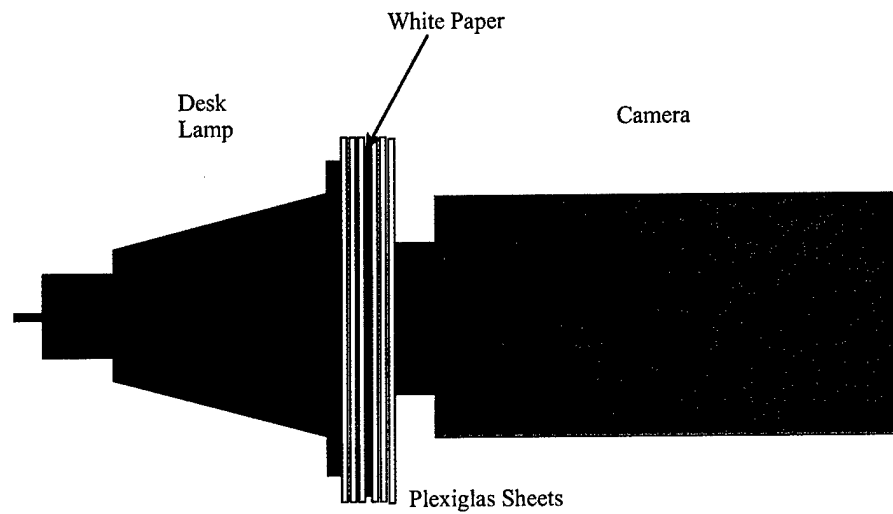
Figure 3.4: Setup used to acquire pixel sensitivity correction images.

(a)   (b)
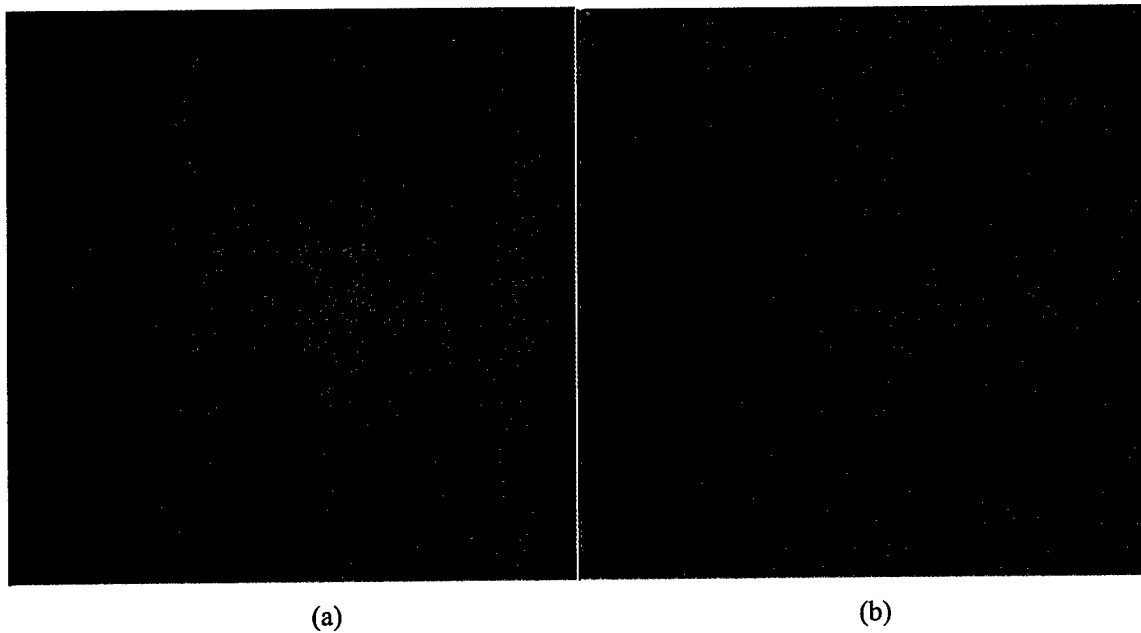
Figure 3.5: Demonstration of pixel sensitivity correction. Figure (a) shows a colorized pixel sensitivity image before correction and figure (b) shows the same image after correction.

Measured Light Intensity vs. Pixel Number for Camera 3, Row 50
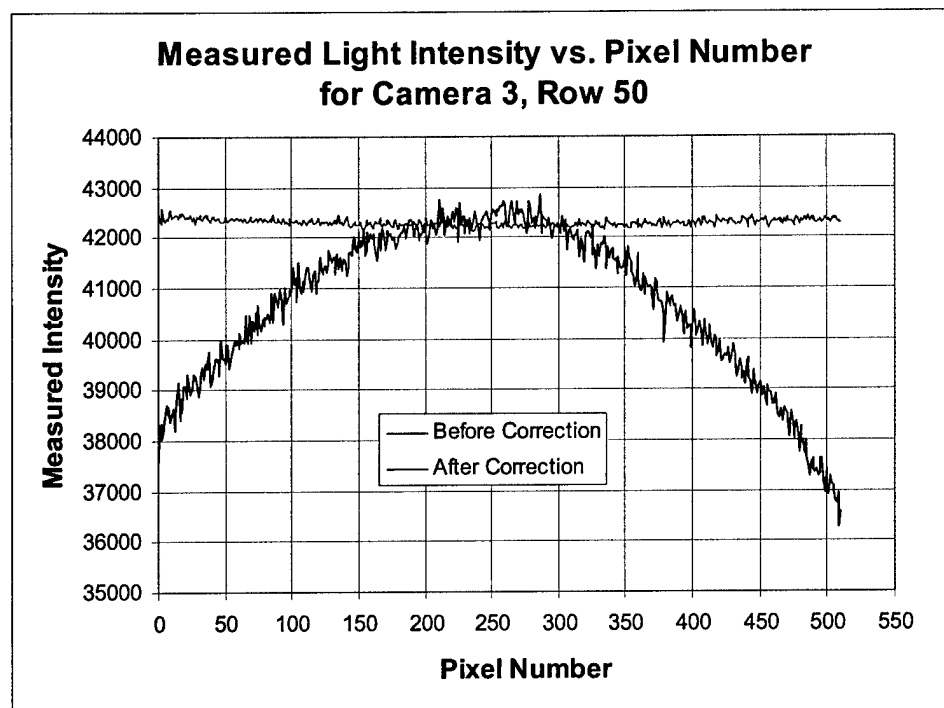
Figure 3.6: Measured light intensity versus pixel number, for row 50 of camera 3, before and after pixel sensitivity correction.

3.4.4 White Card Correction

The image passing through the iodine cell passes through two windows as well as the iodine gas inside the cell. These windows reflect and absorb a portion of the light passing through the iodine cell. The reference image does not pass through any windows and thus it does not loose the same portion of light. The end result of the loss of this reflected and absorbed light is that the ratio of the filtered and reference pixel intensities will be lower than what would be the case if the filtered image did not pass through the windows on the ends of the iodine cell. In addition to the losses due to the filtered images passing through these windows there potentially are global variations in sensitivity to light from camera to camera, so a method must be developed to correct for this as well. The procedure used to correct for these potential sources of error is called white card correction for reasons that will be explained below.

The correction used to account for the differences in light intensity recorded by each camera module due to the windows on the iodine cell and differences in the overall light sensitivity of each camera is called a white card correction because a set of images of a solid white card are acquired as part of the procedure used to perform this correction. The card is illuminated by the laser, which is fired at a constant optical frequency while the white card correction images are acquired. An iodine

cell calibration must be performed before the white card correction images are acquired, because the white card correction images must be acquired at an optical frequency where the mean transmission ratio between the filtered and reference views is at a global maximum. The physical setup used to acquire iodine cell calibration images is the same as the setup used to acquire white card correction images. Once the white card correction images are acquired and averaged to generate an average white card correction image, all of the other image corrections described above are performed. First, the average background image is subtracted from the average white card image. Next, the pixel sensitivity correction is applied to the entire image. After this step, the filtered image is vertically mirrored because prior to this the filtered image appears to be a mirror image of the reference image. Next, each warped region of interest is mapped to its corresponding rectangular region of interest. Once the two regions of interest have been de-warped, a pixel filter is applied to each region of interest. Finally, an array of white card ratios is calculated for each camera module, from the pixels in the filtered and reference regions of interest. Ideally, these ratios should all be unity, but for the reasons described in the first paragraph of this section this ratio is less than unity. The procedure used to calculate this array of white card ratios for each camera module also calculates an average white card ratio for each camera module. While the array of white card ratios and the average white card ratio for each camera module are saved in a data file the average white card ratio for the camera module to be used to monitor the laser frequency variations should be recorded by the user for later use. The white card correction is applied to an image by dividing each pixel in the image by the corresponding white card correction ratio. Figure 3.7 shows the results of an iodine cell calibration before the white card correction is applied and figure 3.8 shows the results of the same iodine cell calibration after the white card correction has been applied.
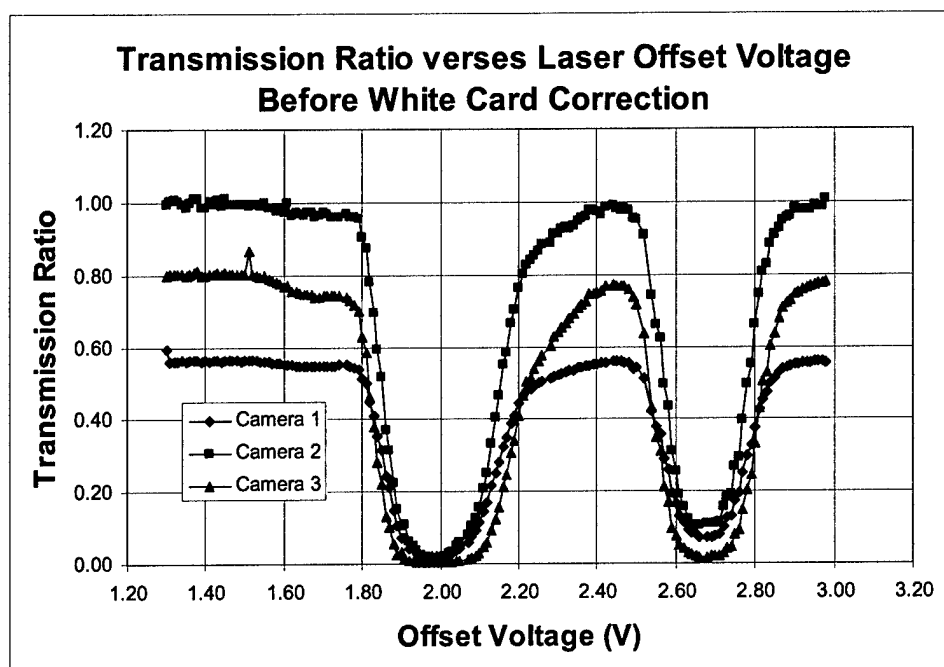
Figure 3.7: Results from iodine cell calibration before white card correction.
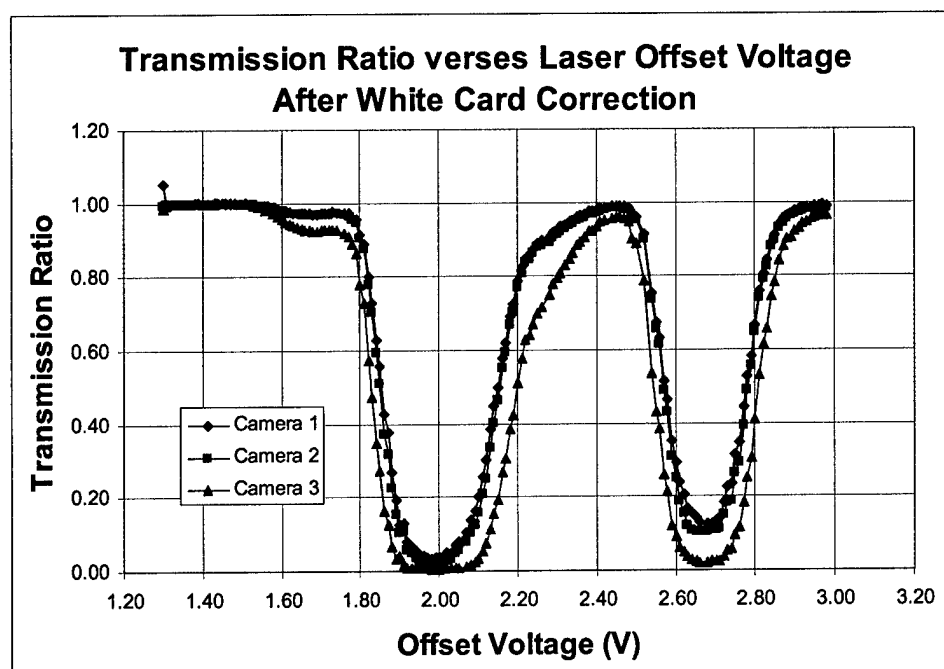
Figure 3.8: Results from iodine cell calibration after white card correction.

3.5 Camera Module Viewing Angles

The MATLAB toolbox, *"Camera Calibration Toolbox for MATLAB"*, written by Jean-Yves Bouguet, was used in previous tests of the VT DGV system to determine the camera module viewing angles needed to reduce acquired velocity data.[83] In these previous tests it was necessary to manually enter the dot center locations from the dot grid images into a data file. This data file was used by the MATLAB Toolbox to determine camera calibration parameters in addition to determining the rotation matrix needed to calculate the camera module viewing angles. To achieve the best results, a series of at least 10 different images at 10 different viewing angles should be used. Manually entering 10 sets of dot center locations took roughly 32 hours, which proved to be an unacceptable length of time for this task. A single error in data entry could prevent the toolbox from determining the viewing angles, thus making it necessary to spend precious time looking for errors. The MATLAB Camera Calibration toolbox had an automatic corner extraction program, which would automatically determine the corner locations for a series of images of a checkerboard grid. Since manually entering dot center locations was both very time consuming and error prone, the target used while acquiring dot grid images was changed from a pattern of dots to a checkerboard grid. This reduced the amount of time needed to determine the viewing angles from days to mere minutes!!

The first step in determining the viewing angles was to acquire 10 images of a checkerboard pattern from ten different viewing perspectives for each camera module. The images acquired by the DGV system cannot be directly plugged into the camera calibration toolbox so these images were exported from the DGV control program file format into the Flexible Image Transport System (FITS) file format. The FITS format images were then opened in an image viewing program provided by the manufacturer of cameras 1 and 3, Spectra Source. Once open the images were vertically mirrored and then saved in the Tag Image File (TIF) file format. The TIF images could then be used in the camera calibration toolbox. The first step in this procedure was to extract the corner locations on each of the ten images for a given camera module. This was done automatically for the most part. The user only needed to select the four outer corners of the area to be used in the camera calibration. It was important to consistently select these points in the same order and note the order in which the points were selected because the order in which the points were selected also determined the orientation of the coordinate system attached to the checkerboard pattern and hence the data plane. During this research, the points were selected in the following order: upper left corner, upper right corner, lower right corner, and finally lower left corner. This oriented the coordinate reference frame attached to the data plane in the following manner. The origin was located at the upper left corner. The positive x axis pointed down toward the lower left corner of the data plane. The positive y axis

pointed to the right toward the upper right hand corner of the data plane. Finally, the positive z axis pointed out of the data plane according to the right hand rule. The portion of the camera calibration toolbox which calculated distortion and principal point for the camera was disabled because these parameters could not be calculated because of the large distance between the camera modules and the data plane. These parameters were disabled by setting the parameters: center_optim = 0 and est_dist = (0; 0; 0; 0; 0) in the camera calibration toolbox. Once the corners were extracted for the set of images from a given camera module, and the routines to calculate distortion and principal point were disabled, the camera calibration was performed. This calibration was still able to determine quantities such as the focal point and pixel error.

Once the calibration was performed, the geometric correction image from which the viewing angles were to be determined was opened and the corners for that image were extracted using the same procedure described above. Next, the extrinsic properties of this image were calculated. These properties included a translation vector, a rotation vector, and a rotation matrix to transform the coordinate system from the reference frame attached to the data plane to the reference frame attached to the camera module. The rotation matrix was used to determine the Euler angles associated with the coordinate transformation between the camera module reference frame and the data plane reference frame. The origin for the camera module reference frame was located at pixel 0,0 in the upper left corner of the image. The positive x axis for the camera module reference frame pointed toward the upper right corner of the image along the top row of image pixels. The positive y axis for the camera module reference frame pointed toward the lower left hand corner of the image along the first column of image pixels on the left side of the image. The positive z axis pointed in the direction the camera was viewing according to the right hand rule. The rotation matrix had the following form:

$$R = \begin{bmatrix} r_{11} & r_{12} & r_{13} \\ r_{21} & r_{22} & r_{23} \\ r_{31} & r_{32} & r_{33} \end{bmatrix} \tag{5}$$

Assuming the rotation was a 3, 2, 1 (z, y, x) rotation, values in this matrix would have the following form:

$$R = \begin{bmatrix} \cos\theta_y \cos\theta_z & \cos\theta_y \sin\theta_z & -\sin\theta_y \\ (\sin\theta_x \sin\theta_y \cos\theta_z - \cos\theta_x \sin\theta_z) & (\sin\theta_x \sin\theta_y \sin\theta_z - \cos\theta_x \cos\theta_z) & \sin\theta_x \cos\theta_y \\ (\cos\theta_x \sin\theta_y \cos\theta_z - \sin\theta_x \sin\theta_z) & (\cos\theta_x \sin\theta_y \sin\theta_z - \sin\theta_x \cos\theta_z) & \cos\theta_x \cos\theta_y \end{bmatrix} \tag{6}$$

Therefore, the value in $r_{11} = \cos\theta_y \cos\theta_z$, the value in $r_{12} = \cos\theta_y \sin\theta_z$ and so on. The value of the Euler angle θ_y was determined using r_{13} as follows:

$$\theta_{y1} = -\sin^{-1}(r_{13}) \tag{7}$$

or

$$\theta_{y2} = \pi - \sin^{-1}(r_{13}) \tag{8}$$

Equation 7 was derived from the fact that arcsine is periodic with a range of $\pi/2$. These two angles were used to determine four possible values for θ_z using r_{12}:

$$\theta_z = \begin{bmatrix} \dfrac{\sin^{-1}(r_{12})}{\cos\theta_{y1}} & \pi - \dfrac{\sin^{-1}(r_{12})}{\cos\theta_{y1}} \\ \dfrac{\sin^{-1}(r_{12})}{\cos\theta_{y2}} & \pi - \dfrac{\sin^{-1}(r_{12})}{\cos\theta_{y2}} \end{bmatrix} \tag{9}$$

The same procedure was used to determine four possible values for θ_x using r_{23}:

$$\theta_x = \begin{bmatrix} \dfrac{\sin^{-1}(r_{23})}{\cos\theta_{y1}} & \pi - \dfrac{\sin^{-1}(r_{23})}{\cos\theta_{y1}} \\ \dfrac{\sin^{-1}(r_{23})}{\cos\theta_{y2}} & \pi - \dfrac{\sin^{-1}(r_{23})}{\cos\theta_{y2}} + \pi \end{bmatrix} \tag{10}$$

The four sets of angles were compared to the remaining values in the matrix R to determine which sets were possible Euler angles for the rotation matrix R. Generally two of the sets of angles did not match the other values in R and the two remaining sets matched the other values in R. The two sets that matched had the same angular displacement but the rotation was in opposite directions so either set of angles would have worked in the DGV data reduction program. The set of smaller Euler angle values was generally chosen to be used in the data reduction program.

An additional step was needed to correct for a difference in the orientation of the reference frame attached to the data plane by the calibration toolbox and the orientation of this frame desired for the DGV data reduction program. The following rotations were added to the Euler angles to account for this difference:

$$\theta_x = \theta_x' - \pi \tag{11}$$

$$\theta_y = -\theta_y' \tag{12}$$

$$\theta_z = \theta_z' - \frac{\pi}{2} \tag{13}$$

where θ_x, θ_y, and θ_z are the corrected Euler angles, and θ_x', θ_y', and θ_z' are the Euler angles directly from the rotation matrix output by the calibration toolbox. Another adjustment was also

Refinement and Verification of the Virginia Tech Doppler Global Velocimeter (DGV)   46

needed because the rotation matrix output by the camera calibration toolbox was for a coordinate transformation from the data plane reference frame to the camera reference frame. The desired coordinate transformation is from the camera reference frame to the data plane reference frame. The direction of the transformation can be changed by multiplying each of the Euler angles calculated above by -1. This puts the Euler angles into the final form needed to input them into the VT DGV data reduction procedure.

3.6 Iodine Cell Calibration

The manufacturer of the Nd:YAG laser used in this research provided an easy way to change the optical frequency for the laser. A DC offset voltage could be sent to the laser to vary the optical frequency. Unfortunately the range of frequencies and the actual optical frequency associated with a given offset voltage varied depending on the operating conditions, such as ambient temperature, in the area where the laser was being fired and the settings for various adjustments on the seed laser inside the Nd:YAG host laser. The successful use of the DGV technique depended on a specific transmission ratio calculated from the reference and filtered views of a given camera module being associated with a specific optical frequency. Therefore, each of the camera modules was calibrated to determine the relationships between the transmission ratio, offset voltage, and the optical frequency of the light captured by the camera module. The procedure used to acquire these "iodine cell calibrations", as they are often called, will be described in the rest of this section.

The first two steps in acquiring iodine cell calibration data were to acquire geometric and background images for each of the camera modules being calibrated. The checkerboard pattern used to acquire the geometric correction images was illuminated by a desk lamp. For the background images, the laser was turned on and enabled so a beam was produced, but the beam was diverted to a beam dump instead of being directed into the data area. Every effort was made to eliminate any other possible light sources while these images were being acquired and while the iodine cell calibration was being performed. This was done to maximize the dynamic range of the camera modules. The pixel sensitivity of each camera did not need to be measured prior to each iodine cell calibration or DGV data acquisition so this procedure assumes that the pixel sensitivity was determined prior to performing each iodine cell calibration. Another objective of the iodine cell calibration was to determine the offset voltage where the transmission ratio calculated from the reference and filtered views of each camera was at a maximum value so this offset voltage could be used when the white card correction images were acquired. Once the geometric and background correction images were acquired and averaged, the average geometric correction images were used to determine the warp

points and rectangular regions of interest for each camera module. The data area selected by the warp points was the same for all of the camera modules used in the calibration. This data area was the same size and covered the same area where DGV data was to be collected. All of the rectangular regions of interest for the camera modules used to acquire the iodine cell calibration were also the same size. This was done so the data area associated with the size of a pixel would be the same for all of the camera modules. During this research these rectangular regions of interest were each 350 pixels wide and 250 pixels high. The size of the data area used in this research was 0.1778 m x 0.127 m (7 inches x 5 inches).

Once the geometric and background correction images were acquired and the warp points and rectangular regions of interest were selected the system was prepared to acquire an iodine cell calibration. The offset voltage was set to the starting voltage for the calibration. The laser needed to be run at this offset voltage for about 5 minutes so the laser could settle on the commanded optical frequency. This length of time was only needed when the offset voltage was set to the starting voltage, because this usually was a large change in the optical frequency. The laser could lock on to a commanded optical frequency faster if the commanded optical frequency was close to the optical frequency the laser was previously operating at. Next, the laser beam was steered through a set of optics to form a cone of laser light which was used to illuminate the target. The target was the front surface of the calibration wheel if wheel data was to be acquired. The target was a flat plate covered with 600 grit sandpaper and painted white for the cases where flow data was to be acquired. Next, the range of offset voltages to be scanned during the calibration and the number of increments desired for the calibration were set in the DGV control program. Once these values had been set the calibration was started.

The DGV control program used the voltage range and number of increments to determine the needed change in offset voltage between the increments. An image was acquired by each of the camera modules being calibrated at each voltage increment. The user could select the length of time the program paused between acquiring images. This was important because the laser required a few seconds to lock on to the new commanded optical frequency after the offset voltage was changed. Usually, the control program was set up to wait approximately 12 to 15 seconds after the offset voltage was changed before acquiring the calibration image. The actual number of images acquired was n+1 where n was the number of increments since the first image from each camera module was acquired at the starting offset voltage. The number of images acquired for an iodine cell calibration depended on the size of the voltage range over which the calibration was being conducted and the

desired resolution. A general rule of thumb was to use 50 images for every 0.5 volts. This could be, and was, stretched to as few as 25 images for every 0.5 volts but this sacrificed calibration resolution. Figure 3.9 is a drawing which shows the setup of the DGV system in the Virginia Tech Stability Wind Tunnel during an iodine cell calibration and during calibration wheel velocity data acquisition. The procedure used to reduce the iodine cell calibration images will be discussed in Chapter 4.
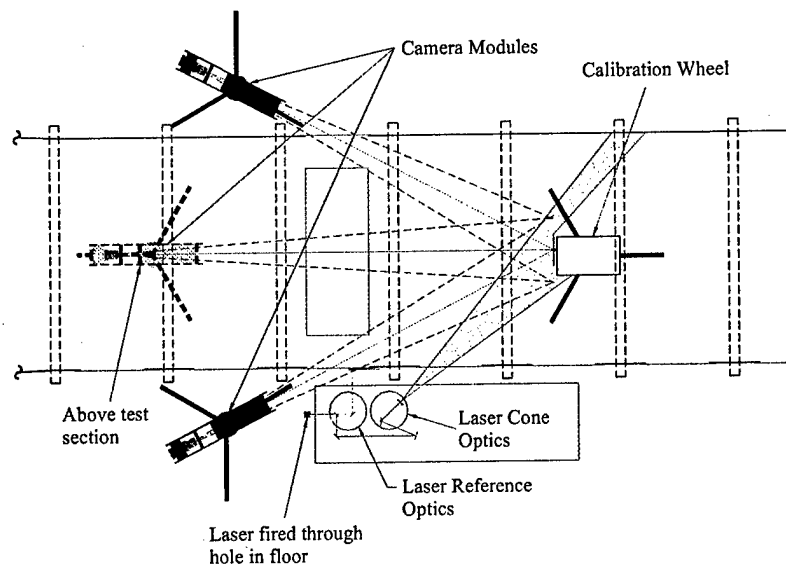
Figure 3.9: DGV system setup in the Virginia Tech Stability Wind Tunnel. This setup was used to acquire iodine cell calibrations and calibration wheel velocity data.

The main drawback to this technique for calibrating the camera modules was that the calibrations were quite time consuming. The normal size of a calibration scan was between 150 and 200 increments. A 151 point scan (150 increments) required roughly 1 hour and 15 minutes to acquire all of the calibration images. The degree to which the calibration was successful was not known until all of the calibration images had been acquired and reduced. Also, a single calibration did not provide enough information to determine all of the information needed to use the DGV system to acquire velocity data. Usually large, coarse scans were used to determine the location of interesting absorption features. Next, large scans over a more narrow offset voltage range were used to identify specific absorption characteristics. These scans used the rule of thumb described above to determine the number of increments to be used. Finally, a scan of roughly 100 images over a small voltage range (roughly 0.5 volts usually) was used to calculate the relationship between transmission ratio from each camera module and optical frequency. The problem with the length of time required to perform an iodine cell calibration was compounded by other problems with the Nd:YAG laser performance and with two of the 16-bit digital cameras used in the VT DGV system. The problems

with the laser and the digital cameras will be discussed in greater detail in Chapter 5. The end result of the laser and camera problems in addition to the length of time required to perform an iodine cell calibration was that an attempt to acquire DGV velocity data required 10 to 12 hours of work if everything worked as expected.

3.7 Calibration Wheel Data Acquisition

Once the iodine cell calibration was acquired and reduced and the white card correction ratio was determined for each camera module, the laser offset voltage was set so the transmission ratio for the camera modules was roughly 0.5 on the iodine absorption feature chosen for use in acquiring DGV velocity data. This maximized the sensitivity of each camera module to changes in optical frequency due to laser light being reflected off of a moving particle or surface. Next, the beam dump was moved into place to keep the laser beam from entering the data area. This was done so geometric and background correction images could be acquired while the laser continued to run. After these correction images were acquired the beam dump was removed and a series of 10 images were acquired by each camera module with the wheel stationary. These images were averaged to generate an average stationary wheel image for each camera module. These average images were used to determine a reference value for the transmission ratio of each camera module at the current offset voltage, as part of the DGV data reduction procedure. Next the calibration wheel was started and was allowed to run approximately 1 minute before DGV data acquisition began. A set of 50 DGV velocity images were acquired during each attempt to acquire calibration wheel data. The DGV control program waited approximately 10 seconds between each acquired image. The output voltage from the calibration wheel motor controller was acquired and averaged while each image was acquired. This voltage was used to independently measure the calibration wheel angular velocity. Three attempts were made to acquire calibration wheel data. The data from the first two attempts were judged to be unreliable because of problems with the performance of the Nd:YAG laser. The third set of calibration wheel data had the best chance of being usable so this set was closely scrutinized and reduced. The procedure used to reduce the calibration wheel data will be discussed in Chapter 4.

3.8 6:1 Prolate Spheroid Data Acquisition

Once a reliable set of calibration wheel data was acquired, an attempt was made to acquire DGV velocity data in the wake of a 6:1 prolate spheroid. This attempt required the positions and viewing angles of the camera modules to be adjusted slightly. It also required some additional laser optics to be set up to form a thin sheet of laser light perpendicular to the major axis of the prolate

spheroid at approximately 77% (1.059 m) down the length of the prolate spheroid. Figure 3.10 shows the laser optics setup used to form the laser sheet. A series of geometric and background correction images were acquired for the new camera module positions and a series of iodine cell calibrations were performed to determine the location of the iodine absorption feature to be used to acquire DGV velocity data. A special tripod was used to hold the checkerboard pattern and the solid white target plate in place where the data plane was located above the prolate spheroid. The white target was used
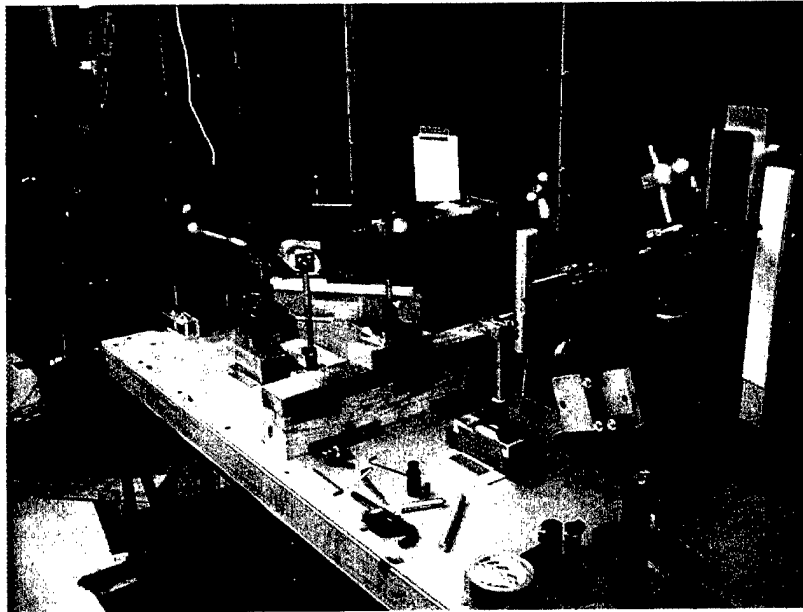
Figure 3.10: Setup for the laser optics used to form the laser sheet.

while iodine cell calibrations and white card correction images were acquired. The same optics used previously to illuminate the data plane with a cone of laser light were used while these images were acquired. Due to problems with the Nd:YAG laser, several attempts were required to acquire a usable iodine cell calibration. As was the case with the procedure used to acquire calibration wheel data, after the iodine cell calibration images and white card correction images had been successfully acquired and reduced, the laser was set to the offset voltage needed to make the mean transmission ratio, calculated from the filtered and reference views of the three camera modules, roughly 0.5. Once the laser offset voltage was set so the mean transmission ratio for each of the camera modules was roughly 0.5, a series of 10 images of the white target plate illuminated by the Nd:YAG laser was acquired. Next, the beam dump was moved into place to keep the laser beam from entering the data area and geometric correction images were acquired while the laser continued to run. Next, the tripod used to hold the checkerboard pattern and white target plate was removed from the wind tunnel test section. Once the tripod was removed, the beam stop was removed from the laser path and the laser

beam was diverted from the cone optics to the optics used to form the laser sheet in the data plane. Once the laser sheet was formed above the prolate spheroid model, the background correction images were acquired with the wind tunnel fan off and the smoke machine off. The background correction images were acquired in this way to correct for laser light reflecting off of the model and the far wall of the wind tunnel test section.[84] Next, the wind tunnel fan was started and the speed of the fan was increased until the dynamic pressure in the wind tunnel test section was 10.16 centimeters of water (4 inches of water). Once the desired dynamic pressure was reached, the smoke machine used to inject seed particles into the flow was enabled. Once the smoke machine began to inject smoke into the wind tunnel, a series of test images were acquired to see if the camera modules were capturing enough light scattered by the smoke to acquire instantaneous DGV velocity data. Unfortunately this was not the case. Images were acquired at several different fan speeds down to a dynamic pressure of 2.3 inches of water. None of the acquired images gathered enough reflected light to measure a frequency shift. The attempt to acquire DGV flow velocity data was stopped when the smoke in the wind tunnel became too thick to continue. Unfortunately, due to problems with the Nd:YAG laser and 16-bit cameras another attempt could not be made. The problems encountered with the Nd:YAG laser and the digital cameras will be discussed in greater detail in Chapter 5. Figure 3.11 is a drawing showing the setup of the VT DGV system used in the attempt to acquire DGV velocity data in the wake of a 6:1 prolate spheroid.
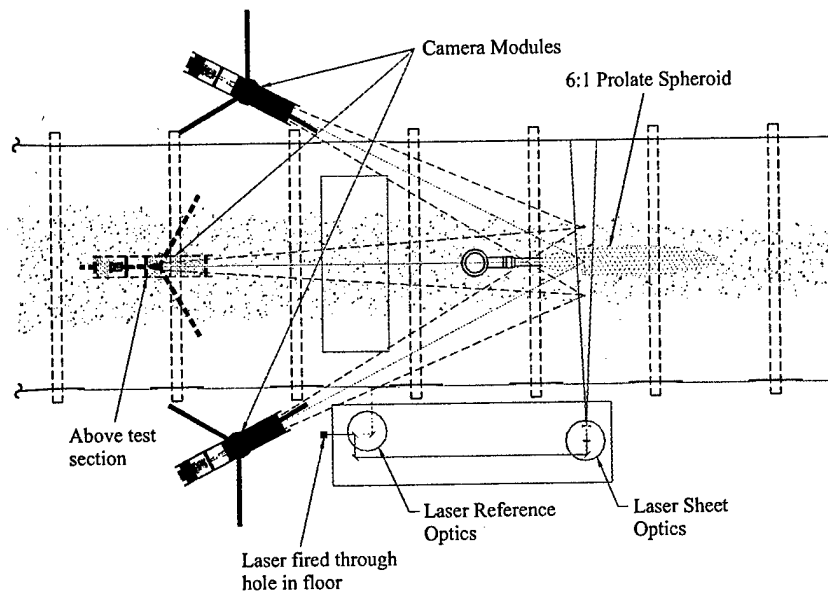
Figure 3.11: VT DGV system setup used to attempt to acquire DGV velocity data in the wake of a 6:1 prolate spheroid.

Chapter 4: Data Reduction

Chapter 4 : Data Reduction

4.1 Reducing DGV Data

Once the iodine cell calibration images or the velocity images had been acquired, these images were processed to extract the useful information they contained. The VT DGV Control Program not only contained the software needed to acquire and save the correction images, iodine cell calibration images, and velocity images, it also contained the data reduction software used to process and reduce these images. The data reduction procedure developed for the VT DGV system was assembled from several sources. A paper from James Meyers at NASA's Langley Research Center published in 1996 gave the basic procedure used to reduce DGV data.[85] Two papers from Robert McKenzie at NASA's Ames Research Center introduced the idea of using a small portion of the laser pulse to monitor pulse to pulse variations in the mean optical frequency.[86, 87] A paper from James Meyers, Joseph Lee and Richard Schwartz at NASA's Langley Research Center provided clarification in some areas as to how the data reduction procedure should proceed and also offered suggestions on how this procedure could be improved.[88] The improvements suggested by this paper were to be implemented as part of this research, but hardware problems delayed this implementation to some future date. While the procedure used to reduce the iodine cell calibration images was in some ways quite similar to the procedure used to reduce the velocity images, the end result was quite different. The desired result from the reduced iodine cell calibration was a mean transmission ratio for each image in the calibration. This mean transmission ratio was determined by calculating the average transmission ratio from the quotient of the sum of the pixel intensities of all of the pixels in the filtered view region of interest divided by the sum of the pixel intensities of all of the pixels in the

reference view region of interest. The mean transmission ratios from each image were then used to determine the relationships between transmission ratio, offset voltage and optical frequency. These relationships were used to set the laser to fire at the desired optical frequency and to relate a change in transmission ratio to a change in optical frequency. The relationship between the change in transmission ratio and the change in optical frequency was used to determine the Doppler shift in optical frequency caused by laser light being scattered by a moving particle.

A transmission ratio for each pixel in the filtered and reference regions of interest was calculated as part of the data reduction procedure used to reduce velocity data. These transmission ratios were compared to the relationship calculated from the iodine cell calibration to determine the optical frequency of the light collected at each pixel location. The relationship between transmission ratio and optical frequency for each camera module was also used to determine the actual lasar optical frequency. Next, the difference between the optical frequency of the light collected at each pixel location and the lasar optical frequency was determined. This difference was the Doppler shift caused by laser light being scattered by moving particles. The Doppler shift and the actual lasar optical frequency were used in the governing equation for the technique along with information regarding the direction of laser light propagation and the viewing angles for each camera module to convert the Doppler shifts in optical frequency into velocities. While the description above gives a rough outline of the procedures used to reduce iodine cell calibration data and velocity data, the remainder of this chapter will discuss in detail how these images were reduced as well as how and where each of the corrections described in Chapter 3 were implemented.

The data reduction program used in this research was originally written by Troy Jones as part of his M. S. thesis. Before the program was used in the current research a thorough review of the program was performed. During this review, several errors in the reduction program were located and corrected. One of the first additions made to the VT DGV data reduction program during this research was to change the procedure used to calculate the laser reference transmission ratio so the image corrections used to reduce the data images were performed before the laser reference transmission ratios were calculated. Next, the implementation of the laser reference transmission ratio was changed so that this transmission ratio was used to calculate the unshifted optical frequency of the laser pulse used to acquire the data image. The implementation of the procedures used to reduce average or active DGV data images was changed so that the laser reference transmission ratio calculated for these cases was saved for use in other areas of the data reduction procedure. The program used to calculate and implement the white card correction was changed so an average white

card correction ratio for each camera module was saved as part of the white card correction file. Finally, the procedure used to determine the wave number was changed from assuming the wave number was constant to calculating the wave number using the laser reference transmission ratio.

4.2 Reducing Iodine Cell Calibration Data

The Virginia Tech DGV Control Program contained the capability to automatically reduce an iodine cell calibration once all of the images in the calibration were acquired. The program user could also choose to reduce or re-reduce the iodine cell calibration at a later time. The control program also contained an important feature which allowed the active camera configuration, warp point locations, the sizes and locations of the rectangular regions of interest, background correction image file names, pixel sensitivity image file names, white card correction data file names, and other reduction settings for a particular iodine cell calibration or velocity set to be saved between operating sessions. These values could be saved in a configuration file which could be loaded at the beginning of a new operating session. As stated previously in this chapter, the goal of the data reduction procedure used to reduce an iodine cell calibration is to calculate a mean transmission ratio for each image from each camera used in the calibration. Once this was completed the series of mean transmission ratios could be used to determine the relationship between transmission ratio and optical frequency.

Before data reduction began, a decision had to be made regarding what, if any, image corrections were to be applied to the calibration images. The user could choose to apply any combination of these corrections desired, provided the necessary correction images were available. In addition to selecting the corrections to be applied the user could choose which images would be used to perform the correction. For a first attempt to reduce an iodine cell calibration the geometric, background, and pixel sensitivity corrections were usually used. The white card correction could not generally be applied until the offset voltage where the maximum mean transmission ratio occurred had been determined. Once this voltage was determined, white card correction images could be acquired or the iodine cell calibration images near this offset voltage could be used to calculate the white card correction for the camera module in question. Generally the 10 images around the maximum mean transmission ratio were used to determine the white card correction ratio. Once the desired image corrections and the files used to perform these corrections had been selected, the data reduction algorithm could be started.

The iodine cell data reduction algorithm processed the images from one of the camera modules at a time. In other words, the algorithm would process all of the images from a given camera module before proceeding to the images acquired by the next camera. The procedure described below assumes all of the image corrections were performed, if this was not the case the portion of the procedure pertaining to the correction that was not performed was skipped. The first step in the data reduction procedure was to load the image to be reduced into the computer's memory. Once this was completed the background image correction was performed by subtracting the background image from the calibration image. Next, the pixel sensitivity correction was performed by dividing each pixel in the image by the pixel sensitivity value for that particular pixel. Once this correction was completed the filtered view was vertically mirrored so the filtered and reference images were oriented in the same direction. After the filtered view was mirrored, the filtered and reference views were mapped to their rectangular regions of interest. Next, the white card correction was applied by dividing each pixel in the filtered rectangular region of interest by the white card ratio associated with that particular pixel. Once all of the selected image corrections had been performed, the average pixel intensities for the reference and filtered views were calculated. Next, the quotient of the average filtered pixel intensity divided by the average reference pixel intensity was calculated. This quotient was the mean transmission ratio for the image. Figure 4.1 is a chart showing the major steps in the data reduction procedure used to reduce an iodine cell calibration. This procedure was repeated for each image acquired in the iodine cell calibration.
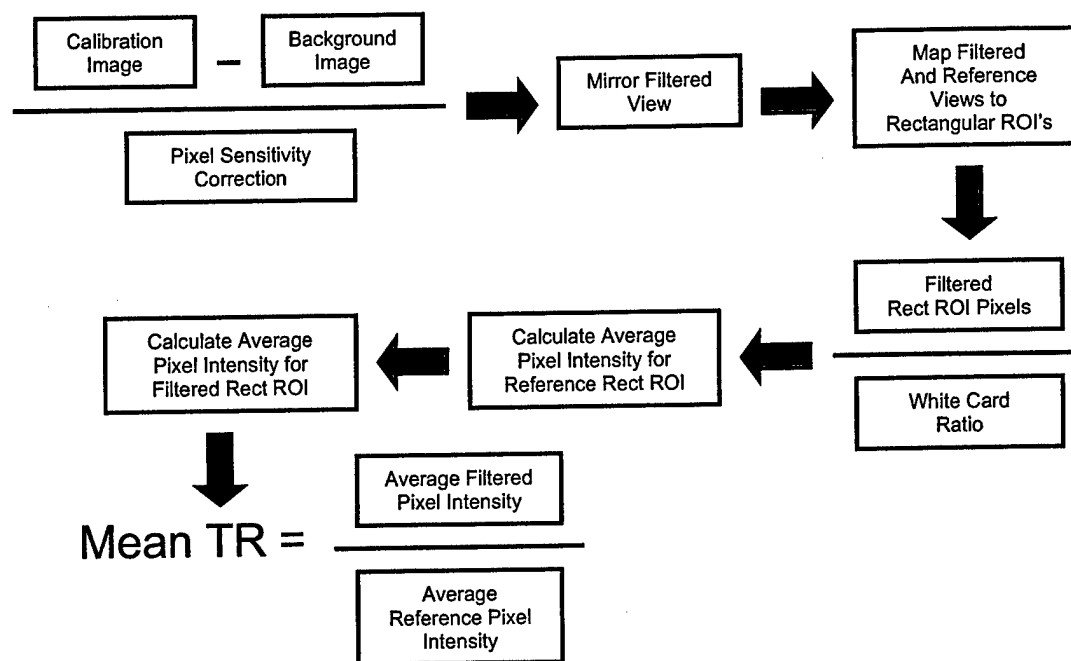
Figure 4.1: Iodine cell calibration procedure

4.3 Converting Mean Transmission Ratio into Optical Frequency

Once the offset voltage where the maximum mean transmission ratio occurred was determined, the white card correction ratio determined, and the iodine cell calibration re-reduced using the white card correction ratio, the reduced data from the iodine cell calibration could be used to determine the relationships between transmission ratio, offset voltage and optical frequency. A FORTRAN program written by J. N. Forkey was used to determine the theoretical light absorption characteristics for an iodine cell of a specified length and with a specified internal pressure.[89] The length of the iodine cells used in this research was 5.08 cm and the pressure could be determined from the "cold-finger" temperature using the following formula:

$$\log P = 9.75715 - \frac{2867.028}{T + 254.180} \tag{14}$$

where T was the "cold-finger" temperature in degrees Celsius, and P was the pressure in torr. Since the iodine cells used in this research were vapor limited and did not have a cold finger, the temperature used to calculate the pressure was the filling temperature 40° C. The range of wave numbers over which the absorption properties were to be calculated and the increment size were also input into the FORTRAN program. The program output a data file containing transmission ratios for the wave numbers in the selected range. Next, the theoretical transmission ratios were plotted and

compared to the plotted results of the iodine cell calibration. Identical features on the theoretical plot and the iodine cell calibration plot were used to determine the identity of the absorption features captured in the iodine cell calibration. Once a portion of the theoretical absorption profile was matched to the features present in the iodine cell calibration, the iodine cell calibration data was scaled and plotted with the theoretical data to determine the relationships between the offset voltage, transmission ratio, and wave number (and hence optical frequency). The equation used to convert the offset voltage to a wave number had the form:

$$HighFreq + \left(\frac{HighFreq - LowFreq}{LowVolts - HighVolts} \right) \times (Volts - LowVolts) \qquad (15)$$

where *HighFreq* and *LowFreq* were the maximum and minimum wave numbers (respectively) for the portion of the absorption profile to which the offset voltage was being scaled, *HighVolts* and *LowVolts* were the maximum and minimum offset voltages (respectively) in the iodine cell calibration being scaled, and *Volts* was the offset voltage that was being scaled. The maximum and minimum wave numbers (*HighFreq* and *LowFreq*) were adjusted until the best fit between the iodine cell calibration data and the theoretical absorption profile was achieved. Figure 4.2 shows a theoretical absorption profile with data from an iodine cell calibration overlaid on top of it. This figure
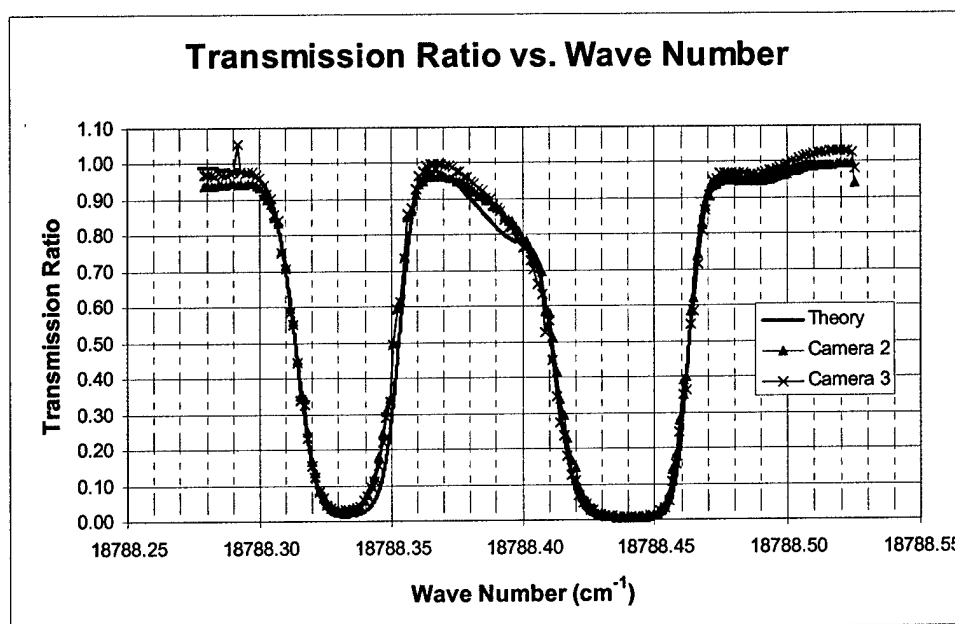
Figure 4.2: Theoretical iodine cell absorption profile with iodine cell calibration data overlaid

shows the agreement between the theoretical data and the calibration data. Once the best fit of the calibration data with the theoretical data was achieved, the portion of the calibration data inside the transition from full transmission to full absorption were re-plotted with wave number on the vertical

axis and transmission ratio on the horizontal axis. A wave number polynomial, calculated from this plot, was used by the velocity data reduction algorithm to convert measured transmission ratios into optical frequencies which could then be used to calculate velocities. The value output from wave number polynomial had units of cm^{-1}. A separate polynomial was calculated for each camera module because the transmission ratios measured by each of the camera modules differed slightly at a given offset voltage. In fact, in the iodine cell calibrations acquired prior to the final attempts to acquire calibration wheel velocity data and velocity data in the wake of the prolate spheroid model, the transmission ratios measured by camera module 3 were significantly different from the transmission ratios measured by camera modules 1 and 2. This discrepancy will be discussed in further detail in Chapter 6. Previous research indicated a fifth order polynomial would provide the best fit to the calibration data so all of the wave number polynomials calculated in this research were fifth order polynomials.[90]

4.4 Preliminary Steps for Reducing Velocity Data

The VT DGV system was designed to measure instantaneous three component velocities in a data plane within a flow field. The correction images and iodine cell calibration images were acquired and reduced by the VT DGV system for the sole purpose of making it possible to acquire and reduce velocity images. For this reason, all of the correction images discussed in Chapter 3 are optional inputs in the velocity data reduction procedure. As was stated previously, these images are used to improve the quality of the reduced velocity data. Where as the iodine cell calibrations are a critical part of the velocity data reduction procedure since these calibrations provide the relationship between transmission ratio and optical frequency.

4.4.1 Assigning the Velocity Vectors and Entering the Euler Angles

A few preliminary tasks were performed before the VT DGV Data Reduction dialog was opened and any velocity images were reduced. The first task was to assign the velocity vectors in the data plane coordinate system to the camera module. Each camera module was assigned a different velocity vector. Next, the Euler angles calculated using the *"Camera Calibration Toolbox for MATLAB"*, written by Jean-Yves Bouguet, were entered into the DGV Control Program.[91] Only two of the three Euler angles, roll and elevation, were needed to reduce the velocity data. The roll angle was the rotation about the x axis of the transformed reference frame and the elevation angle was the rotation about the y axis of the transformed reference frame. The velocity vector assignments and the entered values for the Euler angles were saved as part of the configuration file which also contained

the warp points and the sizes and locations of the rectangular regions of interest. Figure 4.3 shows the dialog box used to assign the velocity vectors to the camera modules and to enter the Euler angles.
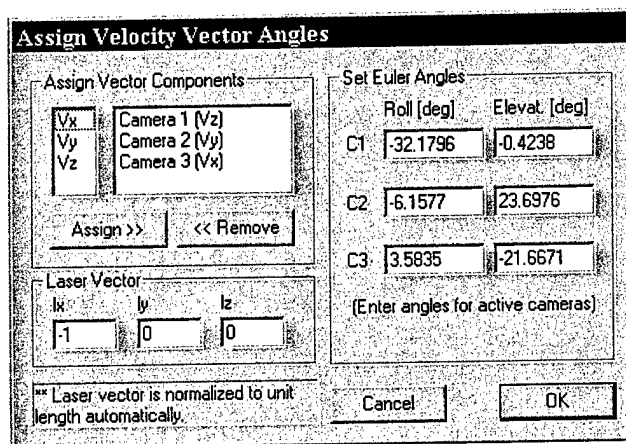
Figure 4.3: Dialog box used to assign velocity vectors to the camera modules and to enter Euler angle values for each of the camera modules.

4.4.2 Entering the Coefficients for the Frequency Calibration Functions

Next, the coefficients for the "Frequency Calibration Functions" were entered into the DGV Control Program. These functions were the wave number polynomials discussed in section 4.3. Each camera module used to acquire velocity data had its own "Frequency Calibration Function". The order of the function and the maximum and minimum transmission ratio values where the functions were valid were also entered. The coefficients, order of the polynomials, and maximum and minimum transmission ratios for each function could be saved in a file, different from the configuration file, so these values could be reloaded at the beginning of a new operating session. Figure 4.4 shows the dialog box used to enter the coefficients, order of the polynomials, and maximum and minimum transmission ratios for each function. The dialog box also had controls to save these values and to load a file containing these values. The dialog box also contained a control that allowed a reference stem temperature to be entered. This control was not used in this research because it pertained to the cold finger temperature of the iodine cells. As was discussed in Chapter 2, the iodine cells used in this research were modified to be vapor limited and the cold fingers were removed.

Figure 4.4: Dialog box used to enter the coefficient values for the "Frequency Calibration Functions",
order of the frequency calibration function polynomials, and maximum
and minimum transmission ratios for each function.

4.4.3 Laser Reference Regions of Interest

As was discussed in Chapters 1 and 2, one of the drawbacks to using an Nd:YAG laser as a light source for the DGV technique was that the mean optical frequency of the pulses emitted by the laser varied slightly from pulse to pulse. The VT DGV system accounted for these pulse to pulse variations by projecting a small portion of the laser beam to a stationary laser reference tab in the field of view of one of the camera modules. Before velocity images were reduced the laser reference regions of interest were set up in the filtered and reference views of the camera module where the laser reference tab was placed in the field of view. The first step of this process was to load the average image calculated from the images acquired of the stationary target in the data plane prior to acquiring velocity images. Only the average image for the camera module being used to monitor variations in the laser optical frequency was loaded. Once the image was loaded, the active region of interest was set to the reference view, region 1. The next step was to open the laser reference ROI dialog box. Once the dialog box was open, the user designated which camera module was being used to monitor variations in the laser optical frequency. Next, the user entered the pixel coordinates for the center of the laser reference ROI in the active region of interest, in this case region 1. The center

of the laser reference ROI was placed roughly in the center of the area where the bleed through laser light hit the laser reference tab. Once the location of the center of the laser reference ROI was entered into the dialog box the size of the laser reference ROI was selected so that the entire ROI fit inside the spot of laser light from the laser reference tab. Once this was done the active region of interest was changed to the filtered view, region 2, and the center of the laser reference ROI was selected using the same criteria used for the reference view. The size of the laser reference ROI in the filtered view was automatically set to be the same as the laser reference ROI in the reference view. The laser reference ROI dialog box also displayed the average laser reference transmission ratio and the uncertainty of the transmission ratio calculated using the selected size and locations of the laser reference ROI's. Once the laser reference ROI's were set up, the background correction, pixel sensitivity correction, and pixel filtering for the camera module could be performed, if these image corrections were to be performed during velocity data reduction, in which case the new value for the laser reference transmission ratio would be recorded for later use.

4.5 Setting Critical Values in the VT DGV Data Reduction Dialog

Once these tasks were completed, the data reduction dialog could be opened and the final preparations for data reduction could be made. Figure 4.5 shows the VT DGV Control Program data reduction dialog box. The data reduction dialog box contained options to determine what data would be reduced, how the data would be filtered, if a laser reference transmission ratio was to be used as part of the data reduction, if a filter based on the Q-switch build up time was to be used to determine which images within a sequence of images were processed and which images were skipped, and how the pixels in the rectangular region of interest would be scaled into "real world" units such as meters, feet, or inches, among other options. The dialog box also provided useful information on which image corrections were to be performed as part of the data reduction procedure and which data images were going to be used in the data reduction. The rest of this sub-section will discuss how the values entered into the data reduction dialog box were determined.

4.5.1 Setting the Reduction Mode

The VT DGV Control Program provided three different "Reduction Mode" options to select the velocity images to be reduced. The "Sequence" option would reduce a sequence of velocity images and output an average velocity profile for each of the camera modules used to acquire the velocity images. The control program also provided an option where the average velocity profiles could be transformed into velocities in the x, y, and z directions for the coordinate frame attached to data plane or left in the "natural" coordinate system, velocities in the $(\hat{a} - \hat{l})$ direction, for each
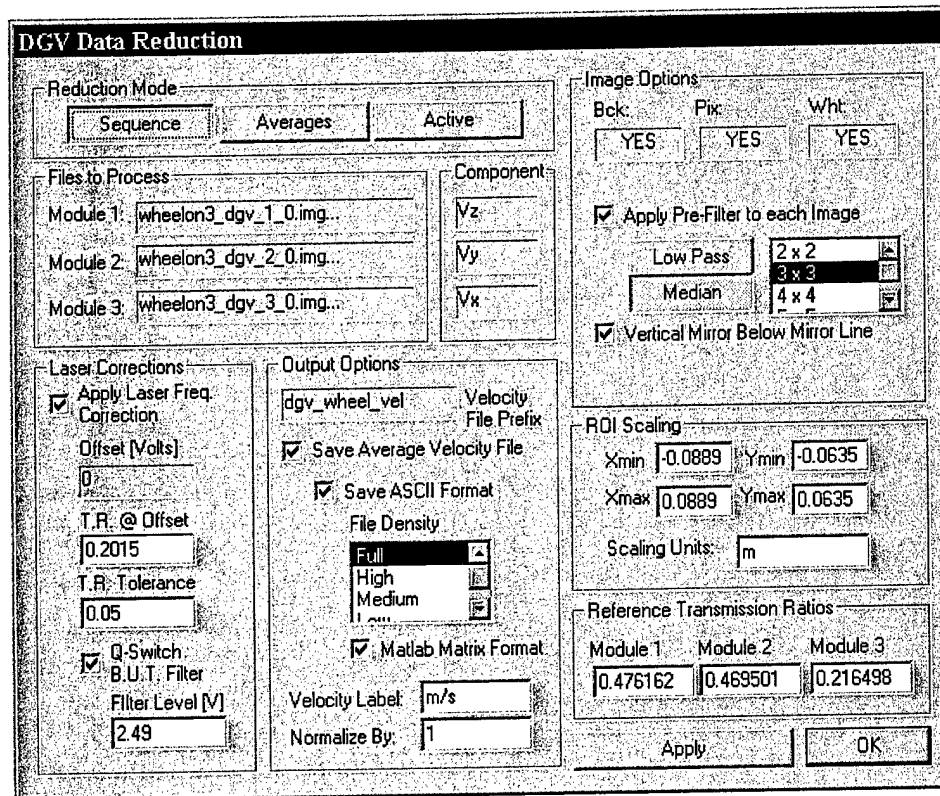
Figure 4.5: VT DGV Control Program data reduction dialog box.

camera. The "Average" option was used to reduce the average images for each of the cameras used to acquire a sequence of velocity data images. These average images were determined by calculating the average values for the pixel intensity of each pixel in an image over a sequence of images. The user had the capability to manually choose which images would be used to calculate the average image. This capability was a very useful tool because while the control program could filter an image sequence based on the Q-switch build up time, the program could not filter an image sequence based on whether the Nd:YAG laser reset while a velocity image was being acquired. The "Active" option was used to reduce the images currently displayed in the parent window of the VT DGV Control Program, and hence currently loaded into computer memory. This option provided the capability to reduce a single data acquisition realization. In other words, this option allowed a single image from each of the camera modules used to acquire velocity data to be reduced.

4.5.2 Pixel Filtering

The data reduction dialog box also provided options to select whether a pixel filter would be applied to the velocity images and to choose the type of pixel filter to be applied. Pixel filtering was used primarily to reduce the effects of laser speckle on the acquired images. It also reduced the

effects of small alignment errors between the filtered and reference views of a given image.[92] This was the type of filtering recommended by Robert McKenzie to reduce spatial noise, as discussed in Chapter 1.[93] There were two major types of pixel filters available in the VT DGV Control Program, a low pass filter and a median filter. Both types of filter used an area process called a convolution. In a low-pass filter convolution, the pixels in a predetermined area, referred to as a neighborhood, around a pixel being filtered, including the pixel being filtered, are multiplied by a value from a convolution kernel, essentially a matrix of weighting factors. Next, the sum of the weighted values in the neighborhood is calculated and the intensity value for the pixel being filtered is replaced with this sum. The standard size of the neighborhood and convolution kernel for the low-pass filters incorporated into the VT DGV Control Program was 3 x 3 pixels. The median filters included in the VT DGV Control Program operated by looking at the pixel intensity values for the pixels in the neighborhood of the pixel being filtered and determining what the median pixel intensity value was and assigning that value to the pixel being filtered. The performance of the median filter could be changed by changing the size of the neighborhood used to determine the median pixel intensity value. The neighborhood sizes for the median filter set up within the VT DGV Control Program were 2 x 2, 3 x 3, 4 x 4, and 5 x 5 pixels.[94] The low-pass and median filtering algorithms used in the control program can be found in reference 95. The pixel filter used for reducing data from this research was a low-pass filter with a 3 x 3 pixel neighborhood. All of the weighting values used in this filter were set to 1/9. This filter was chosen because it was the filter recommended by McKenzie.[96]

4.5.3 Laser Frequency Correction and Q-Switch Build Up Time Filtering

The VT DGV data reduction dialog box provided options regarding whether a laser frequency correction would be applied. If a laser frequency correction was to be applied, a reference value for the laser reference transmission ratio and a tolerance were entered in text boxes in the dialog box. The reference value and tolerance were used to filter a sequence of velocity images by rejecting images where the laser reference transmission ratio was outside of the maximum or minimum allowable values. If the laser reference correction was performed as part of the data reduction procedure for average or active images, the reference value and tolerance were not used to filter out images where the laser reference transmission ratio was outside of the maximum and minimum allowable values. In addition to being used to filter out images outside of the desired tolerance, the reference transmission ratio was used to establish a relationship between the laser reference transmission ratio and the transmission ratios measured by the camera modules for the regions of interest where velocity data were acquired. This relationship will be discussed in greater detail later in this chapter. Depending on what image corrections were performed during the reduction of the

velocity data, either the laser reference transmission ratio calculated at the end of section 4.4.3 could be directly entered into the data reduction dialog box, (if the white card correction was not being performed), or the laser reference transmission ratio calculated at the end of section 4.4.3 was divided by the average white card ratio, for the laser reference camera module, calculated at the end of section 3.4.4, and the resulting value was entered in the data reduction dialog box. The tolerance value was determined by trial and error. The final tolerance value used in the data reduction procedure was 0.05. It would have been desirable to decrease this tolerance further but problems with the Nd:YAG laser made it necessary to use this value.

An option to filter a sequence of velocity images by rejecting images acquired when the Q-switch build up time voltage was above a user selectable level was also included within the laser frequency correction portion of the data reduction dialog box. The procedure used to determine the cut off point for these Q-switch build up time voltages was to manually look through the laser monitoring file where the average Q-switch build up time and the laser reset condition were recorded for each velocity image acquired. The larger Q-switch build up time voltages and the corresponding reset conditions for these voltages were noted. If the Q-switch build up time voltage was significantly larger than most of the other Q-switch build up time voltages or if there appeared to be a correlation between a larger Q-switch build up time voltage and the laser resetting this was used as the cut off value.

4.5.4 Saving the Reduced Data

The VT DGV data reduction dialog box also included options so the user could determine if and how the reduced data would be saved. If the reduced data was to be saved the user had the option to save the data in ASCII format, otherwise the data would only be saved in binary format. Also, the user could select the file density. The file density determined the spatial resolution of the data contained in the data file. As the file density decreased, the number of data points within the data file also decreased. The user also had the option to save the reduced data in a format that could be used by MATLAB to plot the data. In this format the data were saved in between three and five different data files depending on how many camera modules were used to acquire velocity data. The x coordinate for each data point in the reduced data was contained in one file. The y coordinate for each data point in the reduced data was contained in another file. Finally the velocity data for each camera module was contained in a separate data file. The data reduction dialog box also contained a pair of text boxes which were used to designate the units for the velocities contained in the data file(s)

and to enter a scaling factor which could be used to convert the velocity data from the standard units of meters per second into whatever units were desired by the user.

The next option included in the VT DGV data reduction dialog box allowed the dimensions and units for the data area to be entered. This was done by entering the minimum and maximum values for the x and y coordinates in the data area and the data area units. The minimum and maximum values for the x and y coordinates were used to scale the pixels in the reduced data into "real world" units such as meters, feet, or inches. All of the data planes in this research were scaled to units of meters.

4.5.5 Reference Transmission Ratios for the Camera Modules

Finally, the VT DGV data reduction dialog box contained text boxes where a reference transmission ratio for each camera module could be entered. The images acquired of the stationary target just prior to acquiring velocity data images, were used to calculate these reference transmission ratios. As described in sections 3.7 and 3.8, a series of 10 images were acquired of the stationary calibration wheel or a solid white target plate, (depending on whether calibration wheel data or flow data were to be acquired), illuminated by the Nd:YAG laser at the same offset voltage to be used while velocity data images were acquired. Average images calculated from these images were used to calculate the reference transmission ratios entered in the data reduction dialog box. Once the average stationary image from each camera module used to acquire velocity data images was loaded, the image corrections to be applied to the velocity data images as part of the data reduction procedure were applied to the average stationary image from each camera module. If all of the image corrections were to be performed, the corrections were applied as follows. First, the background image was subtracted from the average stationary image. Next, the pixel sensitivity correction was applied to the average stationary image by dividing each pixel in the average stationary image by its pixel sensitivity value. Once the pixel sensitivity correction was applied, the filtered view was vertically mirrored. After the filtered view was mirrored, the reference and filtered views were mapped to their rectangular regions of interest. Next, the pixel filter was applied to the filtered and reference rectangular regions of interest. Finally, the average transmission ratio for the image was calculated and assigned to the reference value, for the camera from which the image was taken, using the "Brightness Levels" menu option in the reduce menu of the VT DGV Control Program. This procedure was repeated for each of the camera modules used to acquire velocity data images. Once all of the needed options had been selected and all of the required values had been entered into the data reduction dialog box, the velocity data reduction procedure could be started.

4.6 Reducing DGV Velocity Data

4.6.1 Laser Reference Transmission Ratio

If the laser frequency correction was to be applied to the velocity images being reduced, the laser reference transmission ratio was calculated before these images were reduced. The first step of this calculation was to load the velocity image(s) from the camera module being used to monitor the laser optical frequency. If a sequence of velocity images was being reduced, the images were loaded and processed one at a time. Once the velocity image was loaded, the image corrections and pixel filter chosen to be applied to the velocity images were applied. The first correction to be applied was the background correction. This correction was applied by subtracting the selected background image for the camera module from the velocity data image. Next, the pixel sensitivity correction was performed by dividing each pixel in the velocity data image by its pixel sensitivity factor. Once the pixel sensitivity correction had been applied, the chosen pixel filter was applied as described in section 4.5.2. After the pixel filter had been applied, the average of the pixel intensities for the pixels inside the laser reference ROI of the reference view was calculated. Next, the average of the pixel intensities for the pixels inside the laser reference ROI of the filtered view was calculated. Next, the white card correction was applied to the average pixel intensity from the filtered view by dividing the average pixel intensity value from the filtered view by the average white card correction ratio for the camera module being used to calculate the laser reference transmission ratio. Once the white card correction had been applied the average value of the pixel intensities in the filtered view, adjusted with the while card correction, was divided by the average value of the pixel intensities in the reference view. This ratio was the laser reference transmission ratio for the image. Figure 4.6 is a chart showing the procedure used to calculate the laser reference transmission ratio. For the average velocity image reduction mode case and the active velocity image reduction mode case this ratio was just saved for later use.
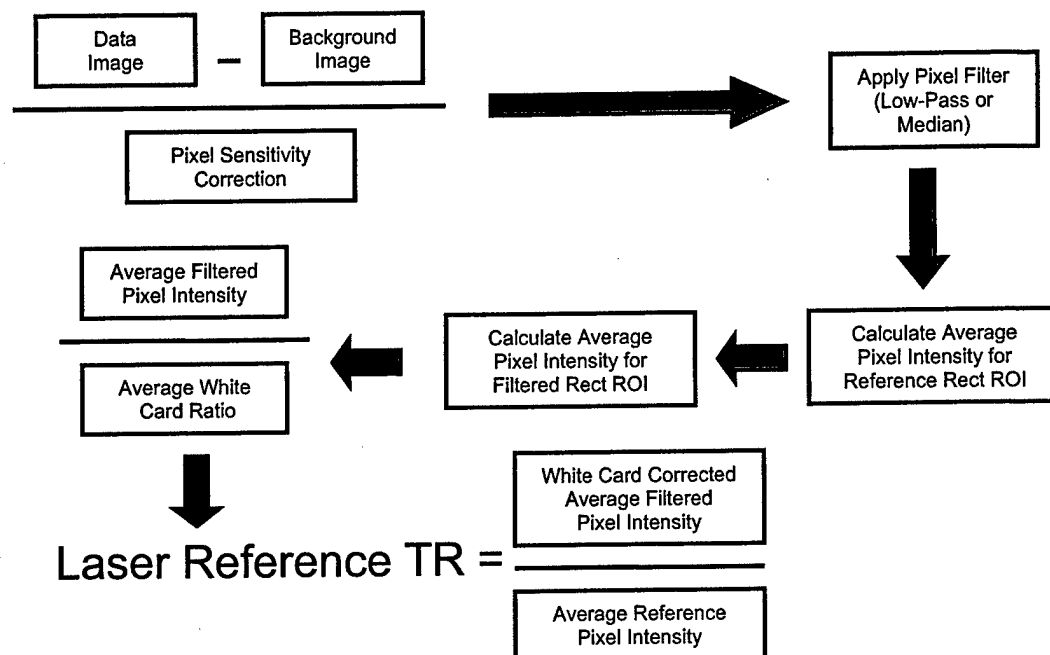
Figure 4.6: Procedure used to calculate laser reference transmission ratio

For the sequence velocity image reduction mode case, the transmission ratio and the Q-switch build up time for the velocity image were evaluated to see if the image would be processed. Once the laser reference transmission ratio for the image had been calculated it was compared to the maximum and minimum allowable values for this transmission ratio calculated from the laser reference transmission ratio and tolerance entered into the data reduction dialog box. If the actual laser reference transmission ratio was outside of the maximum and minimum allowable values the image was skipped during the velocity data reduction procedure. Next, the Q-switch build up time voltage for the image was checked. If the Q-switch build up time voltage was above the maximum value set in the data reduction dialog box the image was skipped during the velocity data reduction procedure. The laser reference transmission ratio for the images that passed the transmission ratio test and the Q-switch build up time voltage test were saved and an average laser reference transmission ratio for these images was calculated for later use.

4.6.2 Calculating Transmission Ratios for the Velocity Data

Once the laser reference transmission ratio(s) had been calculated, the velocity data images were processed and a transmission ratio for each pixel in the filtered and reference rectangular regions of interest was calculated. The procedure used to process the velocity images was very similar to the procedure used to reduce the iodine cell calibration data. All of the velocity images from a given

camera module were processed before the images from the next camera module were processed. The procedure used to process a velocity image was as follows. The procedure described below assumes that all of the image corrections were applied and a pixel filter was also applied to the velocity image. As was the case in previous data reduction procedures, the first step was to load the image to be processed into computer memory. Once the image was loaded, the background correction was applied to the image by subtracting the background image, for the particular camera module from which the velocity image was acquired, from the velocity image. Next, the pixel sensitivity correction was performed by dividing each pixel in the velocity image by the corresponding pixel sensitivity factor. Once the background correction and pixel sensitivity corrections had been performed, the filtered view in the velocity image was vertically mirrored so the filtered and reference views were oriented in the same direction. After the filtered view was mirrored, the filtered and reference views were mapped to their respective rectangular regions of interest. Next, the pixel filter selected by the user was applied as described in section 4.5.2. After the pixel filter had been applied the white card correction was performed on the pixels in the filtered region of interest by dividing each pixel in the filtered region of interest by the white card ratio calculated for that particular pixel. Next, each pixel in the filtered rectangular region of interest was divided by its corresponding pixel in the reference rectangular region of interest and the results stored in a computer buffer. For the "Average" reduction mode and the "Active" reduction mode the procedure moved on to the next camera module, but for the "Sequence" reduction mode the above procedure was repeated and the transmission ratios calculated for the next image were added to the transmission ratios calculated for the previous image. The procedure was repeated until all of the images in the sequence, from the camera module being processed, that passed the transmission ratio filter and Q-switch build up time filter, were processed and each pixel buffer location contained the sum of all of the transmission ratios calculated for that particular pixel. After all of the images from a particular camera module had been processed the sum of the transmission ratios for a given pixel in the data area was divided by the number of images processed for the particular camera module, thus calculating an average transmission ratio for the pixel. Figure 4.7 is a chart showing the basic procedure used to process velocity data images to obtain a transmission ratio at each pixel location. An array of transmission ratios was stored in computer memory for each camera module used to acquire velocity images. These arrays were used later in the data reduction procedure to first calculate the change in optical frequency at each pixel location which were then used to calculate the velocity at each pixel location.

Data Image − Background Image

Pixel Sensitivity Correction

Mirror Filtered View

Map Filtered and Reference Views to Rectangular ROI's

Apply Pixel Filter to Reference and Filtered Rectangular ROI's

Filtered View Rect ROI Pixels

White Card Ratio

$$\text{Pixel TR} = \frac{\text{Filtered Pixel Intensity}}{\text{Reference Pixel Intensity}}$$

Repeat for Each Pixel in the Data Area
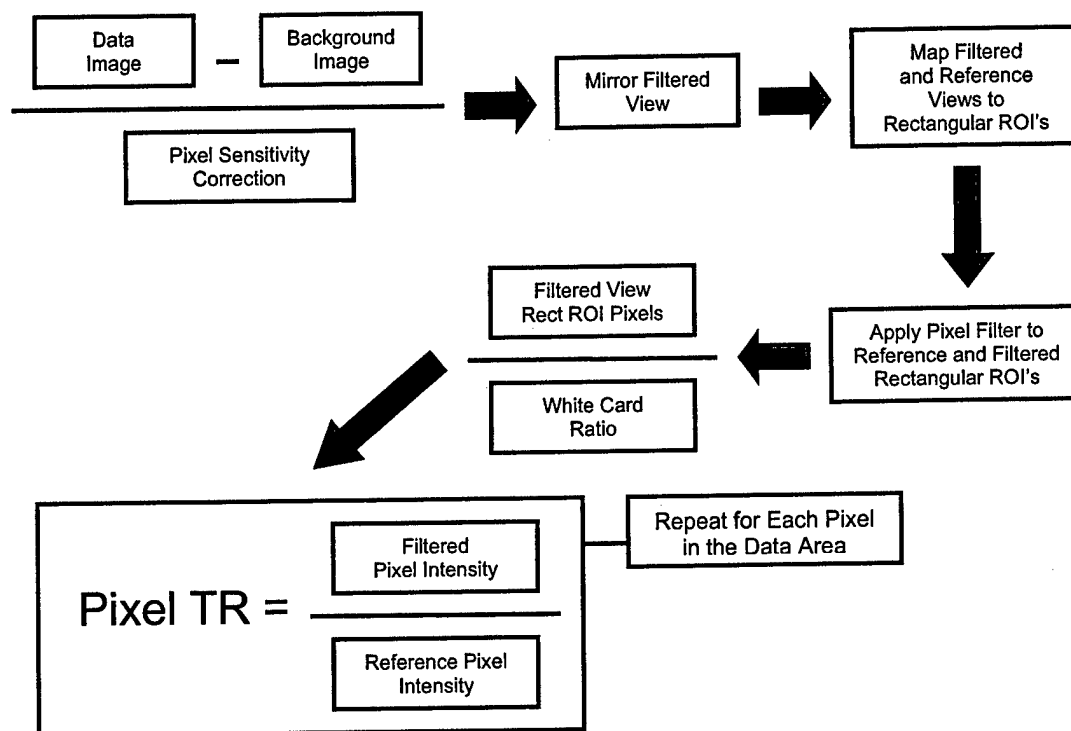
Figure 4.7: Procedure used to calculate transmission ratio for the pixels in the data area.

4.6.3 Converting Transmission Ratio into a Change in Optical Frequency

Once transmission ratios had been calculated for each pixel in the data plane and from each camera module used to acquire velocity images, these transmission ratios could be converted to a change in optical frequency. There were two major paths this conversion could take depending on whether the laser frequency correction option was selected. If this option was not selected, the reference transmission ratio, calculated at the end of section 4.5.5, for the camera module was used to calculate the wave number for the laser pulse before it was shifted through the Doppler effect. The wave number for the laser pulse was calculated by inserting the calculated transmission ratio into the frequency calibration function for the camera module from which the velocity image being reduced was acquired. Next, the function was solved for the wave number. Calculating the wave number in this way would not account for pulse to pulse variations in the optical frequency of each laser pulse.

If the laser frequency correction option was selected, the laser reference transmission ratio, calculated in section 4.6.1, the reference transmission ratio, calculated at the end of section 4.5.5, for each camera module, and the reference value for the laser reference transmission ratio, calculated in section 4.5.3, were used to calculate the wave number of the laser pulse before it was shifted through

the Doppler effect. A relationship between the laser reference transmission ratio and the reference transmission ratio for each camera module was needed because even when all of the image corrections were performed on the images from each camera module there were differences in the transmission ratio measured by each camera module for the stationary target plane illuminated by the same laser pulse. This relationship was established by calculating the difference between the reference transmission ratio calculated for each camera module and the reference value of the laser reference transmission ratio. After this relationship was established, the laser reference transmission ratio was added to the difference between the reference transmission ratio calculated for the camera module and the reference value for the laser reference transmission ratio. This value was used to calculate the wave number for the laser pulse before it was shifted through the Doppler effect. The wave number for the laser pulse was calculated by inserting the calculated transmission ratio into the frequency calibration function for the camera module from which the velocity image being reduced was acquired. Next, the function was solved for the wave number.

Once the wave number for the laser pulse was calculated, the wave number for each pixel in the data area was calculated and then the change in optical frequency was calculated. The wave number for each pixel in the data area was calculated by inserting the transmission ratio for the pixel into the frequency calibration function for the camera module from which the velocity image being reduced was acquired and then solving the function for the wave number. Next, the difference between the wave number for the pixel and the wave number of the laser pulse was calculated. This difference was then converted into a change in optical frequency by multiplying the change in wave number by 100 x speed of light (299792458 m/s). Finally, the change in optical frequency was saved in the computer buffer that previously held the transmission ratio for the pixel. The procedure described in this section was repeated for the pixel buffers from each camera module used to acquire velocity images.

4.6.4 Calculating Wave Number

The wave number for the laser pulse must be calculated for use in the governing equation of the DGV technique which will be used to calculate velocities from the change in optical frequency calculated in the previous section. In the previous version of the DGV Control Program the wave number was assumed to be constant. In reality this is not the case since the wave number is a function of the wavelength and wavelength is proportional to the optical frequency of the light emitted by the laser. As was the case in the previous section, the procedure used to calculate the wave number used in the DGV governing equation depended on whether the laser frequency

correction was performed. If the laser frequency correction was not performed, the reference transmission ratio, calculated at the end of section 4.5.5, for each of the camera modules used to acquire velocity images was used to calculate the wave number. Each reference transmission ratio was plugged into the frequency calibration function corresponding to the camera module from which the reference transmission ratio was acquired, and the function was solved for the wave number. Next, the average of the wave numbers from the camera modules used to acquire velocity images was calculated and this value was saved and used as the wave number in the governing equation for the DGV technique to solve for velocity. This procedure did not account for pulse to pulse variations in the optical frequency of the laser beam. The only way to account for these variations was to make use of the laser frequency correction.

If the laser frequency correction was performed, the laser reference transmission ratio, calculated in section 4.6.1, the reference transmission ratio, calculated at the end of section 4.5.5, for each camera module, and the reference value for the laser reference transmission ratio, calculated in section 4.5.3, were used to calculate the wave number of the laser pulse before it was shifted through the Doppler effect. The same procedure described in section 4.6.3 was used to calculate the relationship between the reference value of the laser reference transmission ratio and the reference transmission ration for each camera module. Once this was done the laser reference transmission ratio, calculated for the velocity images being reduced, was added to the difference between the reference transmission ratio calculated for the camera module and the reference value for the laser reference transmission ratio. Next, the wave number for the laser pulse was calculated by inserting the calculated transmission ratio into the frequency calibration function for the camera module from which the velocity image being reduced was acquired. Next, the function was solved for the wave number. This procedure was repeated for each of the camera modules used to acquire the velocity images. Once the wave numbers for all of the camera modules used to acquire velocity images had been calculated the average of these wave numbers was calculated and this average wave number was saved and used as the wave number in the governing equation for the DGV technique to solve for velocity.

4.6.5 Calculating Velocity from the Change in Optical Frequency

Once the transmission ratio at each pixel in the data area had been converted into a change in optical frequency, the governing equation for the DGV technique could be used to calculate the velocity at the pixel location. The governing equation for the DGV technique was given in Chapter 1

but for the purpose of this discussion it is rewritten below. The governing equation for the DGV technique is:

$$\Delta \nu = \frac{\nu_o}{c}(\hat{a} - \hat{l}) \cdot \vec{V} \tag{1}$$

where $\Delta \nu = \nu_D - \nu_o$ which is the change in optical frequency of the light reflecting off of the seed particles passing through the laser sheet (ν_D is the optical frequency of the Doppler shifted light and ν_o is the optical frequency of the unshifted incident laser light), c is the speed of light, $\hat{a}$ is the unit vector pointing toward the direction in which the data area is being viewed, $\hat{l}$ is the unit vector pointing in the direction in which the laser light is propagating, and $\vec{V}$ is the velocity vector. In the previous two subsections of this chapter the procedures used to calculate the change in optical frequency, $\Delta \nu$, and the wave number ν_o/c were described. Section 3.5 described the procedure used to calculate the Euler angles for the transformation from the coordinate system reference frame attached to the data plane to the coordinate system reference frame attached to the camera. These Euler angles can be used to calculate, $\hat{a}$, the unit vector pointing toward the direction in which the data area is being viewed. Once this vector has been calculated, all that remains is to determine the vector $\hat{l}$, rearrange governing equation, and solve for the velocity vector $\vec{V}$. The discussion below assumes that all three camera modules are being used and three components of velocity are being calculated. The procedure used to calculate one or two components of velocity follow a similar line of reasoning.

Determining the vectors $\hat{a}$ and $\hat{l}$ will be considered together. The vector $\hat{a}$ is a unit vector pointing from the data plane toward the camera module viewing the data plane. As mentioned above, this vector can be calculated using the Euler angles since the z axis in the coordinate reference frame attached to the camera module points away from the camera toward the data plane. So the $\hat{a}$ vector in the camera module coordinate system is essentially:

$$\{\hat{a}\}_2 = \left\{ \begin{array}{c} 0 \\ 0 \\ -1 \end{array} \right\}_2 \tag{16}$$

where $\hat{a}_2$ is the $\hat{a}$ vector in the camera module coordinate system. Using the Euler angles calculated in section 3.5, the $\hat{a}$ vector can be transformed into the data plane coordinate system using rotation matrix of the form:

$$T_{12} = \begin{bmatrix} \cos\theta_y \cos\theta_z & \cos\theta_y \sin\theta_z & -\sin\theta_y \\ (\sin\theta_x \sin\theta_y \cos\theta_z - \cos\theta_x \sin\theta_z) & (\sin\theta_x \sin\theta_y \sin\theta_z - \cos\theta_x \cos\theta_z) & \sin\theta_x \cos\theta_y \\ (\cos\theta_x \sin\theta_y \cos\theta_z - \sin\theta_x \sin\theta_z) & (\cos\theta_x \sin\theta_y \sin\theta_z - \sin\theta_x \cos\theta_z) & \cos\theta_x \cos\theta_y \end{bmatrix} \quad (17)$$

The transformed $\hat{a}$ vector is calculated using the following equation:

$$\{\hat{a}\}_1 = T_{12} \{\hat{a}\}_2 \tag{18}$$

After the transformation has been performed the $\hat{a}$ vector in the data plane coordinate system has the form:

$$\{\hat{a}\}_1 = \begin{Bmatrix} \sin\theta_y \\ -\sin\theta_x \cos\theta_y \\ -\cos\theta_x \cos\theta_y \end{Bmatrix}_1 \tag{19}$$

This form of the vector $\hat{a}$ was used to solve for the velocities in the data plane. Each camera module had its own $\hat{a}$ vector since each camera module viewed the data plane from a different location.[85]

The vector $\hat{l}$ did not require such a transformation because this vector is generally expressed in the data plane coordinate system. This vector did not vary from camera module to camera module. For the purposes of this discussion, the laser vector is assumed to have the form:

$$\{\hat{l}\}_1 = \begin{Bmatrix} l_x \\ l_y \\ l_z \end{Bmatrix}_1 \tag{20}[86]$$

Now that the form of the $\hat{a}$ and $\hat{l}$ vectors have been determined, the governing equation for each of the camera modules can be expressed in the following form:

$$\Delta v_1 = \frac{v_o}{c} \left[\begin{Bmatrix} \sin\theta_{y1} \\ -\sin\theta_{x1} \cos\theta_{y1} \\ -\cos\theta_{x1} \cos\theta_{y1} \end{Bmatrix}_1 - \begin{Bmatrix} l_x \\ l_y \\ l_z \end{Bmatrix}_1 \right] \cdot \begin{Bmatrix} V_x \\ V_y \\ V_z \end{Bmatrix}_1 \tag{21}$$

$$\Delta v_2 = \frac{v_o}{c} \left[\left\{ \begin{matrix} \sin\theta_{y2} \\ -\sin\theta_{x2}\cos\theta_{y2} \\ -\cos\theta_{x2}\cos\theta_{y2} \end{matrix} \right\}_1 - \left\{ \begin{matrix} l_x \\ l_y \\ l_z \end{matrix} \right\}_1 \right] \cdot \left\{ \begin{matrix} V_x \\ V_y \\ V_z \end{matrix} \right\}_1 \tag{22}$$

$$\Delta v_3 = \frac{v_o}{c} \left[\left\{ \begin{matrix} \sin\theta_{y3} \\ -\sin\theta_{x3}\cos\theta_{y3} \\ -\cos\theta_{x3}\cos\theta_{y3} \end{matrix} \right\}_1 - \left\{ \begin{matrix} l_x \\ l_y \\ l_z \end{matrix} \right\}_1 \right] \cdot \left\{ \begin{matrix} V_x \\ V_y \\ V_z \end{matrix} \right\}_1 \tag{23}$$

These three equations form a system of three equations in three unknowns. This system of equations can be expressed as follows:

$$\left\{ \begin{matrix} \Delta v_1 \\ \Delta v_2 \\ \Delta v_3 \end{matrix} \right\} = \frac{v_o}{c} \begin{bmatrix} \sin\theta_{y1} - l_x & -\sin\theta_{x1}\cos\theta_{y1} - l_y & -\cos\theta_{x1}\cos\theta_{y1} - l_y \\ \sin\theta_{y2} - l_x & -\sin\theta_{x2}\cos\theta_{y2} - l_y & -\cos\theta_{x2}\cos\theta_{y2} - l_y \\ \sin\theta_{y3} - l_x & -\sin\theta_{x3}\cos\theta_{y3} - l_y & -\cos\theta_{x3}\cos\theta_{y3} - l_y \end{bmatrix} \cdot \left\{ \begin{matrix} V_x \\ V_y \\ V_z \end{matrix} \right\}_1 \tag{24}[87]$$

A system of equations of the form:

$$\{b\} = A\{x\} \tag{25}$$

where $\{b\}$ is a vector of results, A is a matrix of coefficients, and $\{x\}$ is a vector of unknowns can be solved for $\{x\}$ in the following manner:

$$\{x\} = A^{-1}\{b\} \tag{26}$$

where A^{-1} is the inverse matrix of A. The system of equations shown in equation 24 can be placed into the same form as equation 25 and thus solved using equation 26. All that is needed is to calculate the inverse matrix of A. Consider a three by three matrix of the form:

$$A = \begin{bmatrix} a_{11} & a_{12} & a_{13} \\ a_{21} & a_{22} & a_{23} \\ a_{31} & a_{32} & a_{33} \end{bmatrix} \tag{27}$$

The first step in calculating the inverse of A is to calculate the determinate of A. The determinate of A is calculated as follows:

$$\det A = a_{11}(a_{22}a_{33} - a_{32}a_{23}) - a_{12}(a_{21}a_{33} - a_{31}a_{23}) + a_{13}(a_{21}a_{32} - a_{31}a_{22}) \qquad (28)$$

Next the value for each term in the inverse matrix can be calculated as follows:

$$a_{11}^{-1} = \frac{1}{\det A}(a_{22}a_{33} - a_{32}a_{23}) \qquad (29)$$

$$a_{21}^{-1} = \frac{1}{\det A}(-a_{21}a_{33} + a_{31}a_{23}) \qquad (30)$$

$$a_{31}^{-1} = \frac{1}{\det A}(a_{21}a_{32} - a_{31}a_{22}) \qquad (31)$$

$$a_{12}^{-1} = \frac{1}{\det A}(-a_{12}a_{33} + a_{32}a_{13}) \qquad (32)$$

$$a_{22}^{-1} = \frac{1}{\det A}(a_{11}a_{33} - a_{31}a_{13}) \qquad (33)$$

$$a_{23}^{-1} = \frac{1}{\det A}(-a_{11}a_{32} + a_{31}a_{12}) \qquad (34)$$

$$a_{13}^{-1} = \frac{1}{\det A}(a_{12}a_{23} - a_{22}a_{13}) \qquad (35)$$

$$a_{23}^{-1} = \frac{1}{\det A}(-a_{11}a_{23} + a_{21}a_{13}) \qquad (36)$$

$$a_{33}^{-1} = \frac{1}{\det A}(a_{11}a_{22} - a_{21}a_{12}) \qquad (37)[88]$$

Now that the inverse matrix has been calculated the system of equations shown in equation 24 can be solved. The matrix A and the inverse matrix A^{-1} were only calculated once during the data reduction procedure since the values in these matrices did not change. The values in the inverse matrix A^{-1} were used to solve a system of equations, in the form shown in equation 26, for the V_x, V_y, and V_z velocity components at each pixel location in the data area.

The data reduction algorithm in the VT DGV Control Program also provided the capability to calculate the velocity at each pixel value in the data plane in the "natural" coordinate system for the camera module. For this coordinate system, $(\hat{a} - \hat{l}) = 1$, so:

$$V_1 = \Delta v_1 \frac{c}{v_o} \tag{38}$$

$$V_2 = \Delta v_2 \frac{c}{v_o} \tag{39}$$

$$V_3 = \Delta v_3 \frac{c}{v_o} \tag{40}$$

These equations would be solved at each pixel location in the data plane and for each camera module used to acquire velocity images.

Chapter 5: Hardware Problems

Chapter 5 : Hardware Problems

5.1 VT DGV System Performance

The purpose of this chapter is to discuss some of the hardware problems encountered in the history of the VT DGV system and, in particular, the hardware problems encountered during this research. The reason this chapter is included in this report is because the hardware problems encountered with the VT DGV system were extensive and ultimately led to less than desirable results being obtained by the system when the velocity images were acquired and reduced. Two major hardware problems have plagued the VT DGV system since the first full tests of the system were performed in September-October 2000. These problems are with the Nd:YAG laser and with the 16-bit digital cameras. The Nd:YAG laser has proven to be an unreliable light source for the system. The laser has had optical frequency locking problems since the test of the system performed in 2000. Another problem that has plagued the system is a lack of reliability in the 16-bit digital cameras used by the system. The cameras have had problems with ice crystals forming on the imaging surface, problems with image quality degrading over time, and problems with insufficient cooling for the CCD array in the camera head. In addition to these two problems a problem with the camera modules moving over time while DGV data images were being acquired was detected. When the VT DGV system operates trouble free, the potential of the system becomes obvious, but unfortunately these moments of trouble free operation have been few and far between.

5.2 Nd:YAG Laser

Problems with the Nd:YAG laser were the primary reason why both the VT DGV system tests in 2000 and the tests discussed in this research stopped short of success. The success of the system depends on its capability to measure changes in optical frequency through changes in the transmission ratio calculated from images acquired by the camera modules. Within this constraint, the laser needs to provide a stable source of light for the camera modules to acquire. If the optical frequency of the laser pulses emitted by the laser suffer from large drifts or jumps away from the optical frequency specified by the user, the images acquired by the system will not provide usable data that can be reduced. Also, if the laser cannot regularly fire laser pulses containing the narrow band of optical frequencies needed by the system to calculate the changes in optical frequency due to the Doppler effect, the images acquired by the system will not provide usable data that can be reduced. With this having been said, the stability of the Nd:YAG laser is critical to the performance of the DGV system, and because of this, a great deal of time was spent trying to understand the possible causes of degradation in the performance of the Nd:YAG laser.

5.2.1 Initial Problems

Troy Jones discussed in his M.S. Thesis some of the problems encountered with the Nd:YAG laser during the system tests performed in September-October 2000.[97] The primary problem encountered with the laser was that toward the end of these tests the laser fired multi-mode pulses more often than it fired usable pulses. A multi-mode pulse is a laser pulse containing a wide range of optical frequencies compared to the normal narrow band of optical frequencies contained in a properly seeded laser pulse. Data images acquired when the data area was illuminated by a multi-mode pulse were unusable because the Doppler shift in the optical frequency of the reflected light was overpowered by the variations in the optical frequency of the unshifted multi-mode laser pulse. Attempts were made to improve the performance of the laser at Virginia Tech, but when no significant improvement occurred the decision was made to send the laser back to the manufacturer for repairs and refurbishment.[98]

5.2.2 Laser Damage

The repairs conducted at Spectra-Physics required roughly 6 months before the laser was ready to be shipped back to Virginia Tech. The laser was thoroughly cleaned, defective parts were replaced, and a factory quality alignment and checkout of the laser was performed before the laser was shipped back to Virginia Tech. When the shipping crates containing the laser arrived, they were damaged. Upon opening the crates it became apparent that whatever damaged the crates also

damaged the outer case of the laser head. Further investigation by a repair technician from Spectra-Physics revealed no apparent damage to the components inside the laser head, but the laser was in need of realignment. Another two months and three service visits passed before the laser was realigned and the performance of the laser was verified. Once the laser was realigned and the proper performance of the laser was verified by researchers at Virginia Tech and the repair technician from Spectra-Physics, the laser was integrated back into the VT DGV system and it was used for preliminary tests of the new laser optics purchased for use with the Nd:YAG laser. It should be noted, however, that it is possible that the damage to this laser could possibly have caused some or all of the problems that occurred with the Nd:YAG laser during the research discussed in this report.

5.2.3 Problems with Iodine Cell Calibrations

The first iodine cell calibrations performed with the Nd:YAG laser, after it returned from the factory, occurred in early July 2002. These initial iodine cell calibrations were used to evaluate the performance of the Nd:YAG laser as well as trying to locate iodine absorption features that could be used for acquiring velocity images. These calibrations also gave the user the opportunity to gain some experience in operating the VT DGV system. The quality of the first 5 calibrations performed in the first two days of testing was very encouraging. None of the acquired images in these first calibrations appeared to contain an image acquired while the laser was in a reset condition or an image acquired while a multi-mode pulse was being fired. Over the course of two iodine cell calibrations acquired on the third day of testing all of this changed. These calibrations showed a sudden degradation in the performance of the Nd:YAG laser. For example, the Q-switch build up time voltage for the images acquired during the first five calibrations was around 1.9 volts. By the end of the third day of testing, this voltage was up to around 2.9 volts. There was no obvious reason for this sudden change in laser performance. The offset voltage range where these calibrations were acquired was in the same general area where the first five calibrations were performed. No changes had been made to the laser or to the other equipment used in the room where these tests were being performed.

5.2.4 Attempts to Improve Laser Performance

The first attempt that was made to diagnose and fix the problems with the sudden degradation in laser performance was to make a small adjustment to the mirrors in the laser head that steered the seed laser beam into the host laser cavity. This caused the Q-switch build up time voltage to decrease slightly but the best reduction that could be achieved was from a voltage of roughly 2.9 volts to a voltage of roughly 2.6 volts. While this improved the Q-switch build up time voltage the laser

continued to perform poorly and a usable iodine cell calibration could not be acquired. At this point some additional diagnostic equipment was brought in. A 500 MHz oscilloscope, a photodetector, and a chart recorder were brought in to attempt to diagnose the problem with the laser further. The oscilloscope and the photodetector were used together to "look" at the quality of the laser pulses produced by the laser. The chart recorder was used to monitor the variations in the Q-switch build up time voltage and the Piezoelectric voltage outputs from the control panel of the seed laser. It was soon learned that when the Nd:YAG laser was performing well, the shape of the trace on the oscilloscope would remain nearly constant from pulse to pulse. If the laser was not performing well, the shape of the trace on the oscilloscope would vary considerably from pulse to pulse. When the laser was performing correctly, the Piezoelectric voltage measured by the chart recorder would oscillate around a specific voltage and this voltage would slowly change with time until the Piezoelectric voltage came within 0.5 volts of the maximum allowable value. At this point the laser would reset. After the laser had run for roughly 30 minutes this voltage changed so gradually that the laser could run for hours without approaching the 0.5 volt tolerance to the maximum Piezoelectric voltage, when the laser was performing correctly. When the chart recorder was connected to the Piezoelectric voltage output from the seed laser control panel, this voltage varied wildly indicating that the laser was resetting very frequently, roughly every 10 to 20 seconds.

The next attempt to fix the problem with the performance of the laser was to replace the coaxial cable connecting the data acquisition card to the Q-switch build up time output on the seed laser control panel. During attempts to diagnose the problem with the laser, the performance of the laser appeared to significantly improve when the original cable was disconnected from the laser. An important fact to note here is that the cables used to connect the laser reset condition, Q-switch build up time, and laser offset voltage input were special high impedance cables. The impedance in these cables was significantly higher than the impedance in the other coaxial cables used in the VT DGV System. These cables were specially made after stability problems occurred with the Nd:YAG laser during Troy Jones' research. These stability problems were traced back to the lower impedance coaxial cables connecting the Nd:YAG laser to the DGV control computer. A new cable for the Q-switch build up time was made and installed between the data acquisition card and the seed laser control panel. While this change did improve the performance of the laser, reduced the Q-switch build up time to roughly 2.4 volts, and caused frequency with which the laser reset to decrease considerably, the laser performance was still not as reliable as desired. Also during this time it was thought that the control cable between the laser power supply and one of the serial ports on the DGV control computer might have a loose connection so this cable was replaced with a new control cable.

Next, some of the settings on the seed laser were adjusted to try to improve the laser performance. The procedure used to adjust these settings was found in the Spectra-Physics Model 6300 and Model 6350 Instruction Manual.[99] This was the operation manual for the seed laser inside the Nd:YAG laser. The procedures that were tried were to adjust the frequency overlap of the laser and the procedure to optimize the adjustment of the trim settings. The procedures did not appear to significantly improve the performance of the laser.

At this point it was observed that the laser would frequently reset when the heater in one of the temperature controllers used to control the temperature of the iodine cells turned on. This observation was curious because the temperature controllers were in no way connected to the laser or the DGV control computer used to control the laser and monitor the performance of the laser. It was determined that there must be some RF signal being emitted by the controller and amplified through the cables between the temperature controllers and the camera modules that housed the iodine cells. This RF signal was reduced by placing ferrite toridal cores on each end of the cable.

5.2.5 Spectra Physics Service Calls

While much was learned from all of these attempts and the performance of the laser did significantly improve after all of these changes were made, the performance of the laser was still erratic. The performance of the laser fluctuated from day to day. So, a service call was placed with Spectra-Physics. During the service call the flash lamp optics were cleaned and the laser was realigned. During this alignment the service technician noticed that the laser would drift out of frequency lock and begin to fire multi-mode pulses. The technician believed that either the Marx Bank or the Piezo driver in the laser was going bad and this was what caused the sudden change in laser performance. The Marx Bank essentially controlled the frequency output of the seed laser. The Piezo driver was essentially a motor that adjusted the position of the high reflector at the back end of the host laser. Another service call was scheduled because the Marx Bank and the Piezo driver needed to be ordered from Spectra-Physics. This second service call was made about three weeks after the first call. It was determined that the Piezo driver was what caused the erratic laser performance. The driver was replaced and the laser was realigned and tuned. Within days of this second service call the laser performance degraded back to where it was before the first call so the repair technician returned again and determined that one of the connectors to the new Piezo driver was defective so the driver was replaced with a new driver. The technician also suggested that the harmonic generator crystal inside the harmonic generator should be adjusted regularly to maintain

maximum power output for the green beam emitted by the laser.[100] While the equipment needed to measure the power output directly was not available while the Nd:YAG laser was being used as part of the VT DGV system, the change in power could be measured indirectly by observing the change in the signal from the photodetector and oscilloscope.

5.2.6 Laser Problems Continue

After the third service call from Spectra-Physics, the VT DGV system was set up in the Virginia Tech Stability Wind Tunnel and prepared to acquire calibration wheel data and flow field data in the wake of a 6:1 prolate spheroid model. While iodine cell calibrations were being acquired, another problem with the Nd:YAG laser was detected. The laser began to have problems with resetting frequently and firing multi-mode pulses. The procedures to adjust the frequency overlap of the laser and to optimize the adjustment of the trim settings, described in the Spectra-Physics Model 6300 and Model 6350 Instruction Manual, were performed again to try to fix these problems.[101] These procedures were more successful than when they were tried previously.

Unfortunately, another problem was discovered shortly after these problems were fixed. This problem revealed itself through the iodine cell absorption profiles inexplicably moving up to 2 volts between iodine cell calibrations. The first attempt to deal with this problem was to let the laser fire continuously for an hour or more before attempting to acquire iodine cell calibration data. This was done because a paper from James Meyers, Joseph Lee and Richard Schwartz at NASA's Langley Research Center suggested that the optical frequency variations within a pulse from a Nd:YAG laser decreased as the laser warmed up over several hours.[102] While this did appear to help the laser performance some, the problems with large shifts in the optical frequency of the laser remained. Next, the temperature of the cooling water in the internal cooling system for the laser was monitored. Repair technicians from Spectra-Physics suggested that the problem with the optical frequency changing with time may be related to changes in the cooling water temperature. Once the laser had warmed up for roughly one hour, the water temperature was roughly 86.5° F and remained within a range of ±0.5° F over a 6 hour period. According to the repair technician from Spectra-Physics, the cooling water temperature was supposed to be roughly 100° F.[103] A fan blowing air through a radiator and a temperature sensor in the water reservoir in the power supply of the laser were connected to a control system that was supposed to vary the fan speed to maintain the water temperature at this specified value. A strobotac was used to monitor the speed of the fan to see if the fan speed changed. The fan speed remained constant the entire time the fan speed was monitored.

This suggested that part of this control system was malfunctioning. Unfortunately, this was not realized until very late in the wind tunnel entry and while every effort was made to get a new temperature sensor and control system for the cooling system, the shipment of these parts was delayed and the parts were not received until after the system had been removed from the wind tunnel. After the tunnel entry, the temperature sensor and the control system were replaced and the proper operation of the fan system used to control the water temperature was verified, but the problems with large shifts in the optical frequency of the laser continued.

A problem with the interaction between the Nd:YAG laser and the calibration wheel system was also detected when the images acquired of the rotating calibration wheel were reduced. Over half of these images were acquired while the laser was in a reset condition. There was only one image acquired while the laser was reset in the iodine cell calibration performed just prior to acquiring the calibration wheel images. The most likely cause of the frequent resets during the acquisition of the calibration images was that the calibration wheel was emitting an RF signal of some type that disrupted the performance of the Nd:YAG laser. This problem along with the problem of the optical frequency shifting will have to be investigated further in the future.

The problems with the Nd:YAG laser described above indicate that work needs to be performed to gain a better understanding of how variations in operating conditions where the laser is used affect the performance of the laser. Other researchers have also indicated the importance of operating conditions on the performance of the Nd:YAG laser but most of these reports discuss this in the context of placing the laser in an area where the temperature varies up to 30 degrees and in an area where the laser is directly exposed to air moving through a wind tunnel.[104] It appears from experience gained in this research that temperature and pressure variations much smaller than those discussed previously in literature can have a profound effect on the performance of the Nd:YAG laser. Minimizing these variations should improve the reliability of the Nd:YAG laser performance. Other considerations to possibly improve the performance of the Nd:YAG laser include reducing possible sources of RF signals and reducing exposure to vibration since previous experience indicates both of these factors can have a profound effect on the performance of the laser.

5.3 16-Bit Digital Cameras

Several problems have occurred with the 16-bit cameras used in the VT DGV system. While these problems have not prevented data images from being acquired, they have complicated the procedure used to acquire correction and data images, and potentially reduced the quality of the data

acquired with the VT DGV system. The first problem encountered with one of the 16-bit cameras was when the camera in camera module 3 began to form ice on the CCD array after the camera had been on for roughly one hour. This problem occurred during the research conducted by Troy Jones. The camera was returned to the manufacturer, Spectra-Source, where it was repaired and returned to Virginia Tech. Shortly thereafter, Spectra-Source was bought by another company who decided not to provide support for Spectra-Source's cameras. During the tests of the VT DGV system performed in September and October 2000, another 16-bit camera began to malfunction. The quality of the images acquired by this camera began to degrade after the camera had been on for roughly 10 minutes.[105] This camera was also manufactured by Spectra-Source, and since the camera could not be serviced, it was replaced with a Roper Scientific VersArray 16-bit camera with the same type of CCD array contained in the other two 16-bit cameras in the VT DGV system.

5.3.1 Problems with Camera 3

Shortly after testing for the research discussed in this report began, the Spectra-Source camera that had previously had problems with ice crystals forming on the CCD array started to have problems with ice crystals forming on the CCD array again. Since repairing this camera was not an option, and since money was not available to replace this camera with a new camera, the procedures used to acquire images with the VT DGV system were adapted so the system could be run until ice crystals began to form on the CCD array of this camera. The system could be run for roughly one hour and then the cameras had to be turned off for roughly 30 minutes so the ice crystals would melt. The result of this solution was that it took 12 hours or more to acquire correction images, iodine cell calibrations and velocity data in a single day. Combining this problem with the problems with the Nd:YAG laser meant that a large number of very time consuming iodine cell calibrations were required before calibration wheel or flow field data could be acquired. In addition to the icing problem with this camera, the shutter on this camera began to occasionally stick during image acquisition. This caused a portion of the captured image to be over exposed. Also, the absorption profiles, acquired during tests of the VT DGV system in the Virginia Tech Stability Wind Tunnel, by this camera module, were significantly different from the absorption profiles acquired by the other two camera modules. It is possible that the difference in these absorption profiles could have been caused by a malfunction in this camera.

5.3.2 Problems with Camera 1

In addition to the problem described above, the other remaining Spectra-Source camera started to have problems maintaining the operating temperature needed by the CCD array to operate

properly. This problem appeared toward the end of the wind tunnel entry and there was no immediate effect from this problem detected during these tests. The image quality from this camera appeared to be as good as that of the new Roper Scientific camera, so the Spectra-Source camera continued to be used to the end of the wind tunnel tests. This problem could however prove significant in the future.

5.3.3 Camera Module Movement

As preparations for conducting the first set of preliminary tests of the improved DGV system progressed it became apparent that there was a problem with the camera modules moving on their tripods while data was being taken. This movement translated to a shift in the image acquired of more than 3.18 mm (1/8 inch) over the course of 3 hours. This problem could potentially cause serious problems during DGV data reduction. Images, acquired over several hours, could not be averaged since the warp points used to map the filtered and reference views to their rectangular regions of interest would have moved over the time during which the images were acquired. Over two months were spent trying to diagnose and cure this problem. The tests performed indicated that the tripods were most likely the largest contributor to this problem so the tripods were checked to make sure there wasn't something loose on them. Steps were taken to make sure the feet on the tripod were not moving or that vibration was causing the problem. Tests were also performed to see if air currents were causing the problem. The camera modules were also checked to make sure nothing was loose inside the modules. Once all of these items were checked, a set of camera module supports were designed and constructed. Unfortunately these supports did not entirely eliminate this problem but they have provided some help in stabilizing the camera modules and have reduced the magnitude of the image shifts by roughly ⅓. The most likely cause of this phenomenon is either the cooling fans in the cameras are causing a slight torque in the tripod/camera support system or thermal expansion inside the cameras is causing the camera to move slightly. The solution used was to track the movement of the camera modules by acquiring dot grid images at regular intervals (roughly every 30 minutes) and adjusting the points used to map the reference and filtered views to their rectangular ROI's as the modules moved. A future solution may be to turn the cameras on and let them sit for an hour and a half to two hours before acquiring images since it appears that the images will move only so far and then will stabilize. This solution wasn't used is because of the problems with the Spectra-Source camera that formed ice crystals on the CCD array.

Chapter 6: Results and Discussion

Chapter 6 : Results and Discussion

6.1 Background

The tests performed as part of this research were the second attempt to demonstrate the Virginia Tech DGV system could perform as a viable flow velocity measurement system. As was the case in the first attempt to verify the performance of the VT DGV system, this attempt was marginally successful. As was mentioned in Chapter 5, the acquisition and reduction of iodine cell calibrations, calibration wheel velocity data, and flow field velocity data were complicated by hardware problems with the Nd:YAG laser and the digital cameras. Because of these problems, a disproportionately large number of iodine cell calibrations were acquired before an attempt was made to acquire velocity images. Also as a result of these problems, two sets of calibration wheel data were acquired only to find that the data images were not usable because the iodine absorption features had moved after the iodine cell calibration scan used to calculate the frequency calibration function was completed. A method was developed to adjust the optical frequency of the laser so the desired unshifted mean transmission ratio was achieved. While the performance of the system was less than desirable, the system was capable of detecting changes in the optical frequency of light due to the Doppler effect.

6.2 Iodine Cell Calibration Results

A series of iodine cell calibrations were performed prior to attempting to acquire velocity data images from the calibration wheel or in the wake of the 6:1 prolate spheroid. The procedure followed in

acquiring these calibrations was to first acquire a scan over a large range of offset voltages to determine the location of the iodine absorption features of interest and then acquire a scan over a smaller range of voltages to obtain a high resolution plot of the absorption feature to be used to acquire velocity data. The implementation of this procedure was complicated by the problems with the Nd:YAG laser and the digital cameras. Several attempts were required to obtain a successful large range scan and short range scan back to back, because the iodine absorption features frequently moved during the scan or between scans. The procedure described in section 4.2 was used to reduce the images acquired during each calibration. Figure 6.1 is a plot of five iodine cell calibration scans illustrating the movement of the iodine absorption features between scans. The mean transmission ratios acquired by camera module 2 during a series of iodine cell calibrations are shown in this figure.
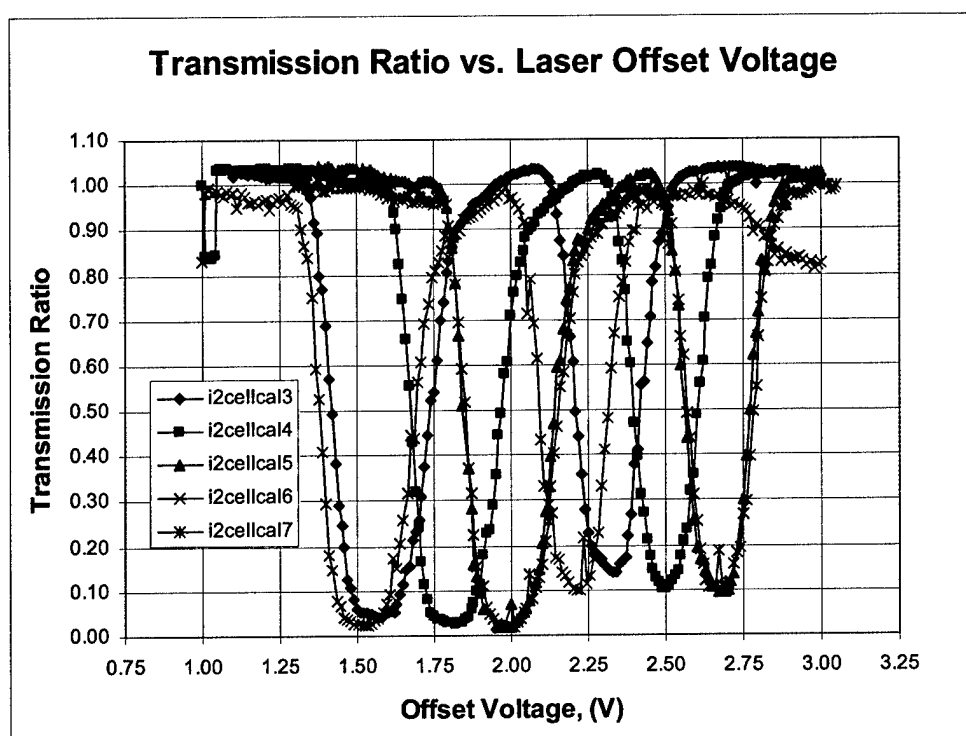
Figure 6.1: Movement of iodine absorption features between iodine cell calibration scans

Chapter 5 discusses some of the attempts made to correct this problem with the Nd:YAG laser. The laser and camera problems eventually led to attempts to decrease the length of time needed to acquire an iodine cell calibration. The decision was made to trade calibration resolution for time, so the number of calibration images acquired over a given voltage was significantly decreased. This allowed a calibration over a large voltage range to be acquired in less time than was required when

the rule of thumb of 50 images for every 0.5 volts was employed. Eventually, roughly 25 to 30 images for every 0.5 volts was used as a rule of thumb for acquiring a calibration. This allowed the correction images and calibration to be acquired without having to turn off the cameras to prevent ice crystals from forming in camera 3. While this did not eliminate the problem with the absorption features moving, iodine cell calibrations could be acquired faster and improved the chances of locating the desired absorption feature in time to acquire velocity images. Figure 6.2 is a plot showing mean transmission ratios acquired by camera module 2 during a later series of iodine cell
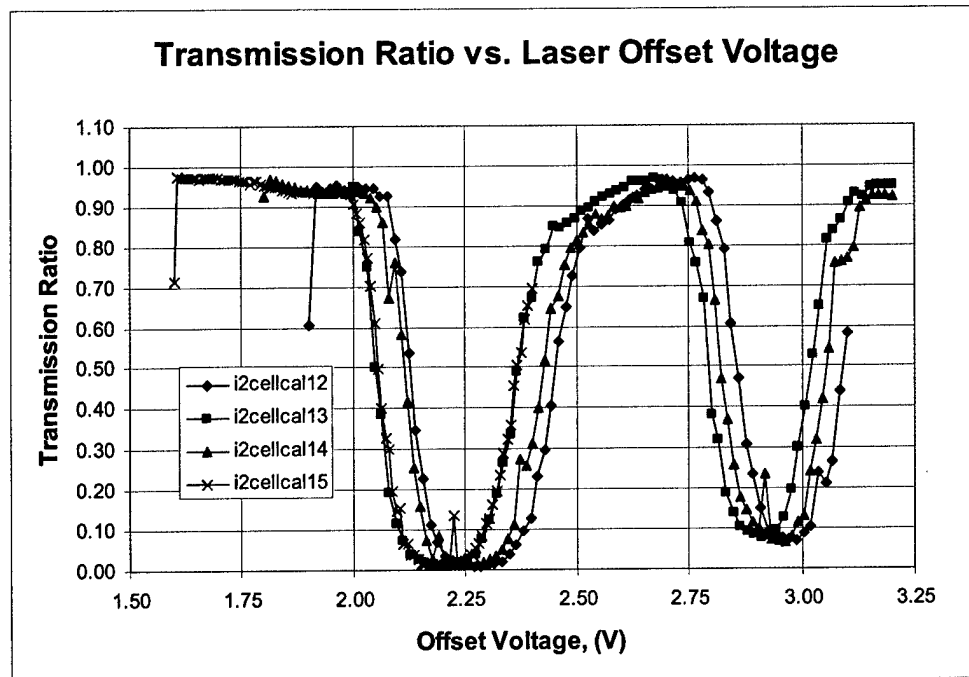
Figure 6.2: Lower resolution iodine cell calibrations.

calibrations. The calibration designated i2cellcal15 in this figure was acquired just prior to the third attempt to acquire velocity data images of the calibration wheel. This calibration was used to calculate the frequency calibration functions used to reduce the acquired calibration wheel velocity images. Figure 6.3 shows two of the iodine cell calibrations acquired just prior to the attempt to acquire velocity data in the wake of the 6:1 prolate spheroid. If velocity data images had been successfully acquired in the wake of the prolate spheroid, the calibration designated i2cellcal18 in figure 6.3 would have been used to calculate the frequency calibration functions used to reduce these velocity images.
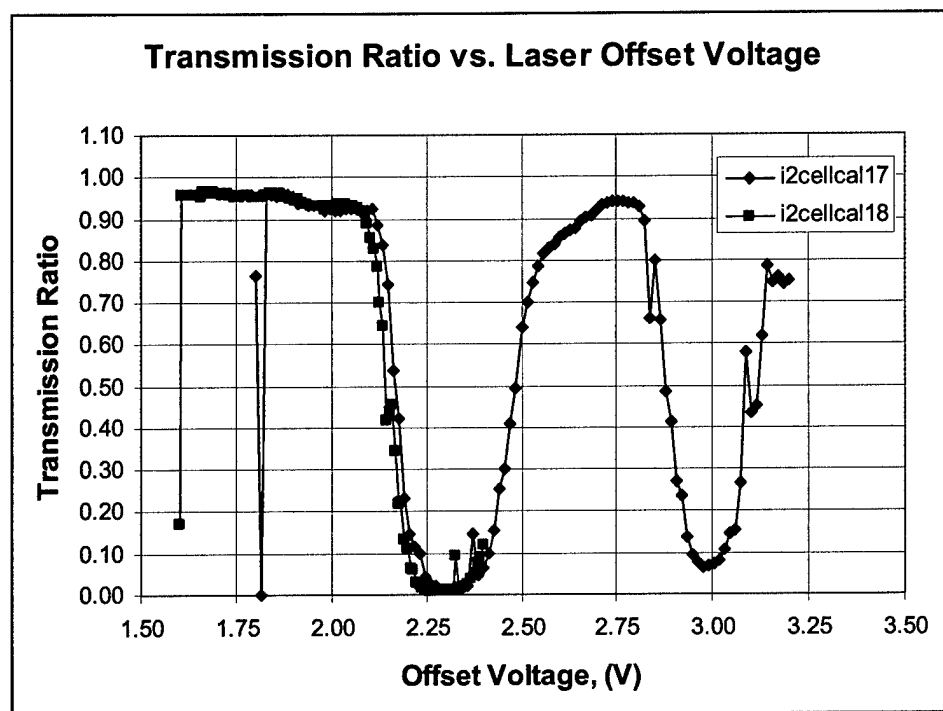
Figure 6.3: Iodine cell calibrations acquired prior to attempting to acquire velocity data images in the wake of the 6:1 prolate spheroid.

6.3 Background for Calibration Wheel Results

As was mentioned in section 6.1, three attempts were made to acquire velocity data from the calibration wheel. Only the images acquired in the third attempt were usable. During the first attempt to acquire calibration wheel data, the absorption features moved so the velocity images were acquired at an optical frequency where the transmission ratio was near its maximum value for the absorption feature being used. In the second attempt, the iodine absorption feature moved so the velocity images were acquired near the minimum transmission ratio for the absorption feature being used. As figures 6.1 and 6.2 demonstrate, there were plateaus and valleys where the maximum and minimum transmission ratios occurred. Data acquired near the maximum or minimum transmission ratio for a particular absorption feature are unreliable because the transmission ratio is not very sensitive to changes in optical frequency in these regions. Ideally, velocity data should be acquired midway between the maximum and minimum transmission ratios of a given absorption feature.

While no solution to the problem of the absorption features moving was found, a method for adjusting the offset voltage was developed so the transmission ratios measured by the camera modules were roughly midway between the maximum and minimum transmission ratios, for the absorption feature. In this method the offset voltage was set to the value believed to be where the mid

point of the absorption feature was located. Next, an image was acquired of the motionless calibration wheel or a solid white target, and the mean transmission ratio for each camera module was calculated. After the transmission ratio for each camera module was calculated the offset voltage was adjusted and the procedure repeated until the mean transmission ratios from each camera module were roughly halfway between the maximum and minimum transmission ratios for the absorption feature. There were, however, two major problems with this technique. First, there was no guarantee that the desired absorption feature was in fact the absorption feature being used to set the transmission ratios. Second, this procedure required time to perform. If more than 10 to 15 minutes was required to set the offset voltage so the desired transmission ratio was achieved, the problem with one of the digital cameras forming ice crystals on the CCD array would interfere with the acquisition of velocity data.

6.4 Calibration Wheel Reduction Settings

Before the calibration wheel data was reduced, the procedures described in 3.5, 4.3, 4.4, and 4.5 were performed to calculate values needed for the data reduction procedure. These values included the Euler angles for each of the camera modules, frequency calibration function for each camera module, reference mean transmission ratio for each camera module, reference value for the laser reference transmission ratio, and the unit vector in the direction of laser propagation. Each of these values will be discussed in the subsections below.

6.4.1 Euler Angles for Camera Modules

The procedure from 3.5 was used to determine the Euler angles for each of the camera module. The rotation matrices and Euler angles output by the camera calibration toolbox were as follows:

Camera Module 1 (Above test section):

$$R_1 = \begin{bmatrix} -0.021466 & 0.999742 & -0.007396 \\ 0.846103 & 0.022107 & 0.532561 \\ 0.532587 & 0.005174 & -0.846359 \end{bmatrix} \Rightarrow \begin{Bmatrix} 147.8204° \\ 0.4238° \\ 91.2306° \end{Bmatrix} \tag{41}$$

Camera Module 2 (Port side of test section):

$$R_2 = \begin{bmatrix} 0.022546 & 0.915402 & 0.401909 \\ 0.992868 & -0.067577 & 0.098220 \\ 0.117071 & 0.396828 & -0.910397 \end{bmatrix} \Rightarrow \begin{Bmatrix} 173.8423° \\ -23.6976° \\ 91.4109° \end{Bmatrix} \tag{42}$$

Camera Module 3 (Starboard side of test section):

$$R_3 = \begin{bmatrix} -0.013766 & 0.929243 & -0.369213 \\ 0.846103 & 0.022107 & -0.058087 \\ 0.532587 & 0.005174 & 0.927528 \end{bmatrix} \Rightarrow \begin{Bmatrix} 183.5835° \\ 21.6671° \\ 90.8481° \end{Bmatrix} \quad (43)$$

It should be noted that problems were experienced with determining the Euler angles for camera module 2. When the Euler angles calculated from the rotation matrix output by the calibration toolbox were used to calculate a rotation matrix, the some of the terms in the calculated matrix did not match the values in the matrix output by the toolbox. The maximum deviation between the values in the calculated matrix and the values in the matrix output by the toolbox was 0.049. Attempts were made to correct for this difference by changing the images used to calculate the rotation matrix but these attempts had no significant effect on the rotation matrix output by the calibration toolbox. The signs and magnitudes of the Euler angles calculated from the rotation matrix output by the toolbox matched estimates made of the Euler angles made while the VT DGV system was in the wind tunnel so these values were used in the data reduction. The additional rotations described in section 3.5 were performed on the Euler angles calculated from the rotation matrices output by the camera calibration toolbox. The Euler angles input into the data reduction were as follows:

Camera Module 1 (Above test section):

$$\theta_1 = \begin{Bmatrix} 32.1796° \\ 0.4238° \\ -1.2306° \end{Bmatrix} \quad (44)$$

Camera Module 2 (Port side of test section):

$$\theta_2 = \begin{Bmatrix} 6.1577° \\ -23.6976° \\ -1.4109° \end{Bmatrix} \quad (45)$$

Camera Module 3 (Starboard side of test section):

$$\theta_3 = \begin{Bmatrix} -3.5835 \\ 21.6671 \\ -0.8481 \end{Bmatrix} \quad (46)$$

6.4.2 Frequency Calibration Functions

The procedure described in section 4.3 was used to calculate the frequency calibration function for each camera module. Figure 6.4 is a plot of the white card corrected iodine cell calibration used to calculate the functions. Notice that the calibrations from camera modules 1 and 2 overlay each other nicely but the calibration from camera module 3 is significantly different from the

Transmission Ratio vs Laser Offset Voltage
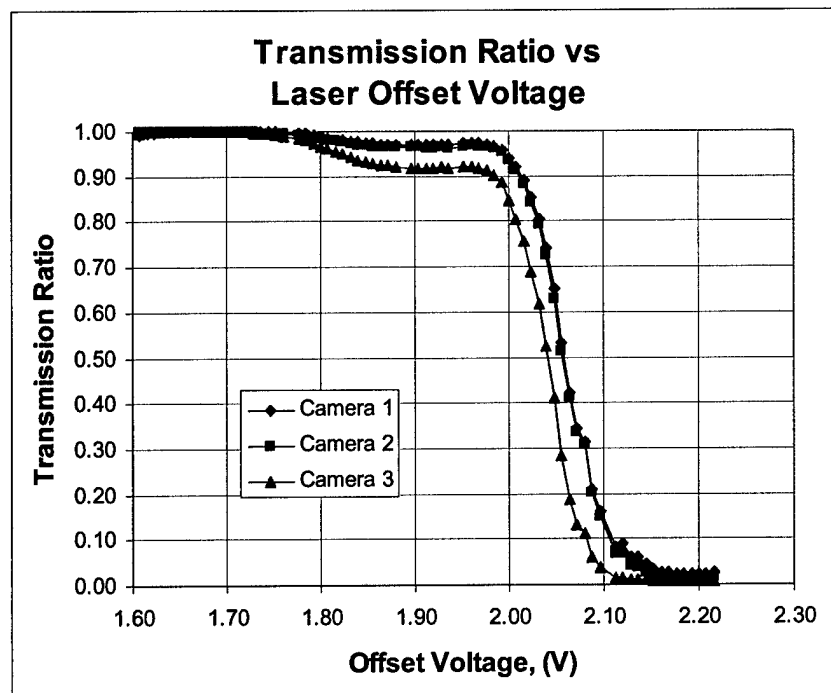
Figure 6.4 Iodine cell calibration

other two. This was the case for all of the iodine cell calibrations performed in the Virginia Tech Stability Wind Tunnel. There are several possible explanations for this difference. The first possible explanation for the difference in the calibrations from camera modules 1 and 2 and that of camera module 3 is that the iodine cell in camera module 3 could have been filled at a temperature different from the temperature at which the cells in camera modules 1 and 2 were filled. Figure 6.5 shows how filling temperature affects the absorption properties of an iodine cell. While the plot in figure 6.5 shows a very similar trend to that observed in figure 6.4, if the iodine cell in camera module 3 was in fact filled at a different temperature this problem would have been noticed in laboratory tests of the
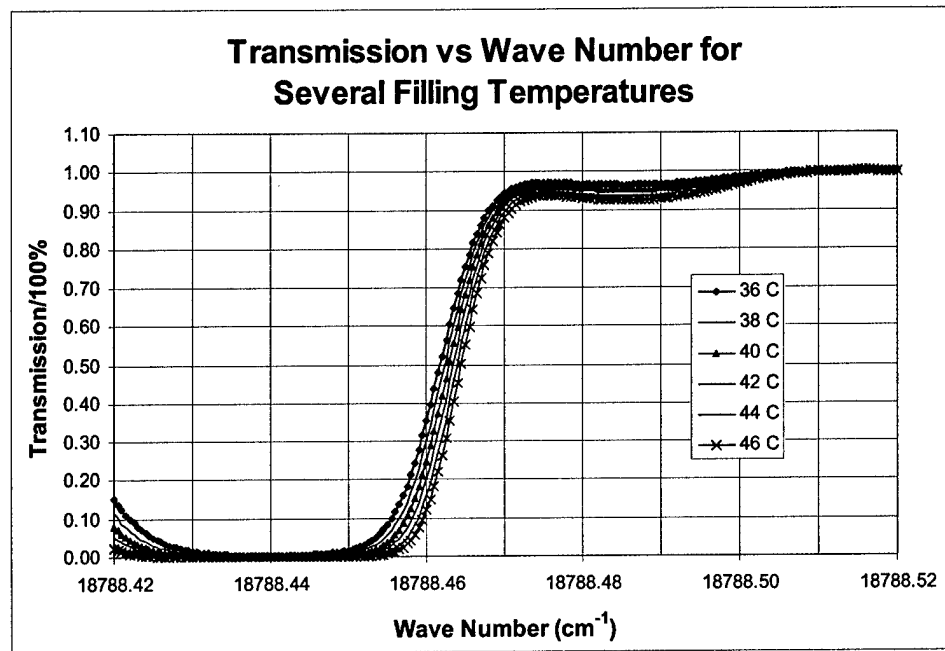
Figure 6.5: Effects of filling temperature on iodine cell absorption properties

system prior to testing the system in the wind tunnel. Another possible explanation is that camera module 3 viewed the data plane through the same Plexiglas panel through which the laser was fired. It is possible that the laser light passing through the Plexiglas panel could have had this effect on the calibration results obtained by camera module 3. The significant difference in the iodine cell calibration results made it necessary to have a separate frequency calibration function for each camera module. This would be desirable even if there wasn't a significant difference between the calibration results of the camera modules, because there are usually small differences in the calibration results obtained by each of the camera modules. The procedure described in section 4.3 was used to calculate the 5th order frequency calibration functions and to produce the plot shown in figure 6.6. The calculated frequency calibration functions were as follows:

Camera Module 1(Above test section):

$$y = 0.0371x^5 - 0.0567x^4 + 0.0540x^3 - 0.0501x^2 + 0.0364x + 18788 \qquad (47)$$

Camera Module 2 (Port side of test section):

$$y = 0.0046x^5 + 0.0449x^4 - 0.0681x^3 + 0.0195x^2 + 0.0018x + 18788 \qquad (48)$$

Camera Module 3 (Starboard side of test section):

$$y = 0.1889x^5 - 0.4897x^4 + 0.5066x^3 - 0.2509x^2 + 0.0676x + 18788 \qquad (49)$$

where y is the optical frequency, in the form of the wave number, and x is the transmission ratio. The coefficients for these functions were input into the dialog box shown in figure 4.4.
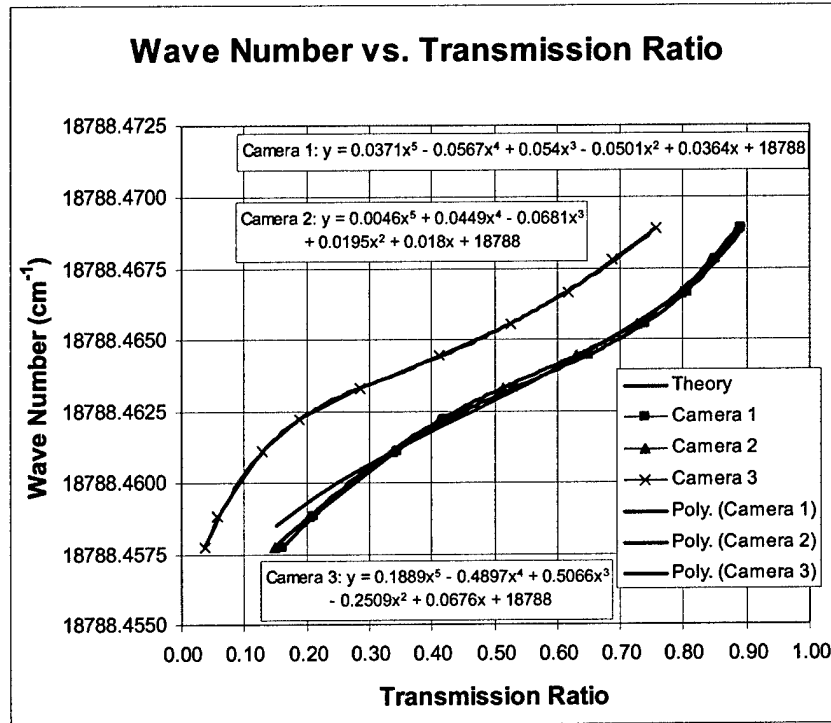
Figure 6.6: Plot of scaled iodine cell calibration results, theoretical absorption profile, and trend lines from frequency calibration functions.

6.4.3 Reference Transmission Ratios

The procedures described in sections 4.4.3, 4.5.3, and 4.5.5 were used to calculate the reference value for the laser reference transmission ratio and the reference transmission ratio for the each camera module. Camera module 3 was used to monitor variations in the optical frequency of the pulses output by the Nd:YAG laser. The reference value for the laser reference transmission ratio was 0.201773. The reference transmission ratio for camera module 1 was 0.474961. The reference transmission ratio for camera module 2 was 0.468240. The reference transmission ratio for camera module 3 was 0.218878, significantly less than the reference transmission ratios from camera modules 1 and 2. The difference in the reference value for the laser reference transmission ratio and reference transmission ratio from camera module 3 compared to those calculated for camera modules

1 and 2 was expected. This difference occurred for the same reasons the iodine cell calibrations acquired by camera module 3 were significantly different from those acquired by camera modules 1 and 2.

6.4.4 Laser Propagation Vector

There was some question about the direction of the laser propagation unit vector used to reduce the calibration wheel velocity images. It was known that for the cases where DGV data was acquired in a flow field, this unit vector was in the same plane as the data plane. Should this also be the case for the calibration wheel data, even though the laser was not being used to produce a sheet of laser light in the same plane as the data plane? Average images were calculated from the images acquired of the moving calibration wheel. These average images were used to reduce the calibration wheel images using two substantially different laser propagation vectors. The first vector was in the same plane as the data plane. The second vector was an estimate of the true laser propagation unit vector. This estimate was based on the Euler angles calculated for camera module 3. The orientation of this camera module was close to the direction the laser was fired to produce the cone of laser light used to illuminate the calibration wheel. Ideally, the reduced velocities measured in the z direction should be zero since the calibration wheel rotated in the x-y plane of the coordinate frame attached to the data plane. The velocities measured in the z direction were inspected for the two different laser propagation vectors to see if one approached the ideal condition where $V_z = 0$. Figure 6.7 is a contour plot of velocity in the z direction for the case where the laser propagation vector was taken to be in the data plane. Figure 6.8 is a plot of velocity in the z direction for the case where the estimate of the true laser propagation vector was used. By comparing the results shown in these plots, it was determined that the correct laser propagation unit vector to use in the data reduction procedure was the true laser propagation unit vector. The magnitudes of the velocities contained in the plot where the velocity vector was taken to be in the data plane are significantly higher than those in the plot where the real laser propagation vector was used. For the third set of calibration wheel data acquired in the Virginia Tech Stability Wind Tunnel the estimated laser propagation unit vector was:

$$l = \begin{Bmatrix} -0.5000 \\ -0.0604 \\ 0.8639 \end{Bmatrix} \tag{50}$$

In the future, a technique should be developed to accurately measure the laser propagation unit vector for both the cases where calibration wheel data is to be acquired and where velocity data in a flow field is to be acquired.
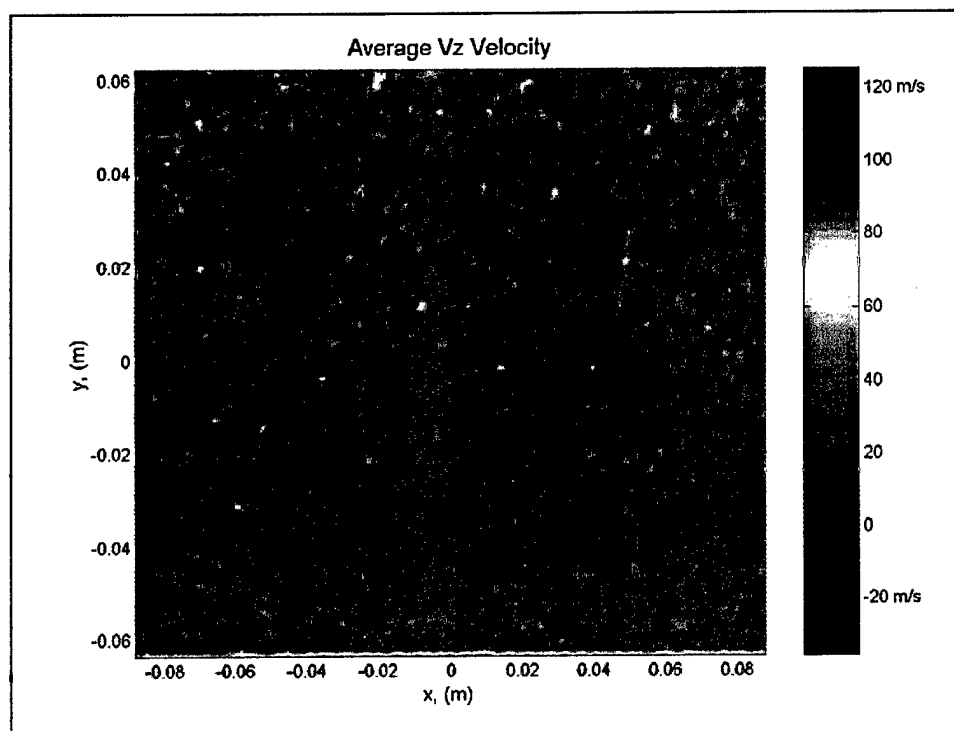
Figure 6.7: Contour plot of Vz velocity for the case where the laser propagation unit vector was taken to be in the same plane as the data plane
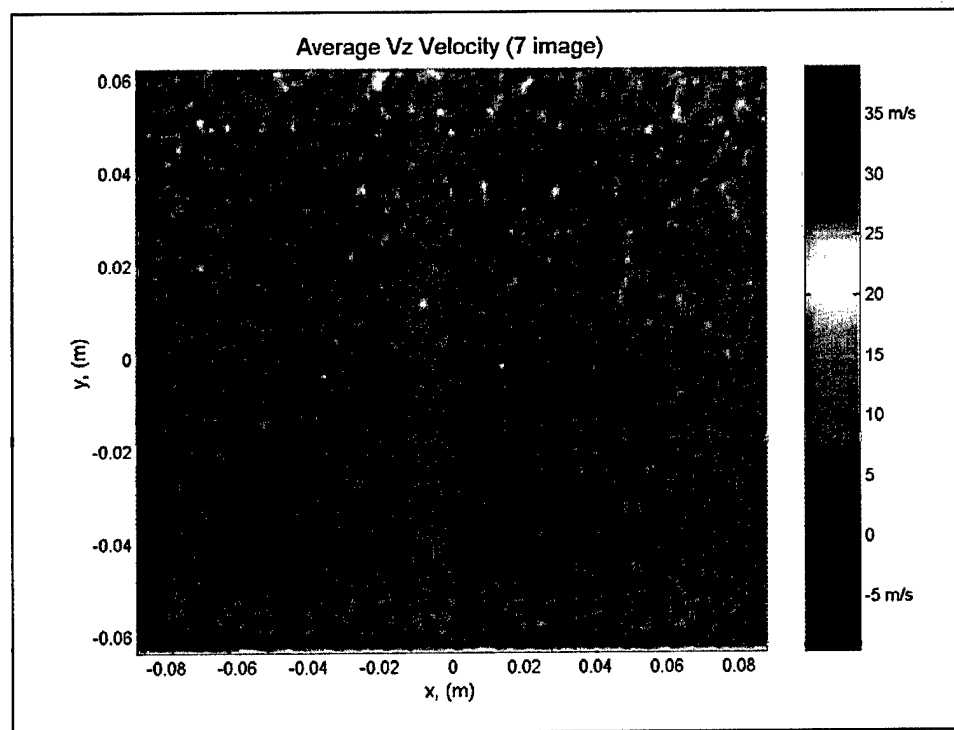
Figure 6.8: Contour plot of Vz velocity for the case where the laser propagation unit vector was taken to be the true laser propagation unit vector.

6.4.5 VT DGV setup used to acquire calibration wheel velocity data

Now that the Euler angles for each of the camera modules and the direction of the laser propagation vector have been determined, the complete setup of the VT DGV system used to acquire velocity data from the calibration wheel can be shown. This subsection contains a series of figures showing the setup of the VT DGV system used to acquire velocity data from the calibration wheel in the Virginia Tech Stability Wind Tunnel. This subsection also contains a figure showing the coordinate system attached to the data plane. This figure also shows the size and location of the data area on the calibration wheel. These figures are intended to clarify how the VT DGV system was setup in the Virginia Tech Stability Wind Tunnel during acquisition of velocity data from the calibration wheel as well as providing a visual reference for the discussion of the results from these tests.

Figure 6.9 is a drawing showing a plan view of the VT DGV setup in the Virginia Tech Stability Wind Tunnel with the Euler angles about the y axis for each of the camera modules and the laser propagation vector labeled. This figure also provides an estimate of the distance from the front end of the camera to the data plane for the camera modules on each side of the test section. Figure 6.10 is a drawing showing the setup of the VT DGV system from the control room. This figure shows the Euler angles about the x axis for the camera module in the control room, the camera module placed on top of the test section, and the laser propagation vector. This figure also provides an estimated distance from the front end of the camera to the data plane for the camera module placed on top of the test section. Figure 6.11 is a drawing showing the Euler angle about the x axis for the camera module mounted on the side of the test section opposite from the control room.

Figure 6.12 shows the coordinate system attached to the data plane. The origin of this coordinate system was placed at the center of the calibration wheel, with the z axis pointing down the shaft used to turn the calibration wheel. The origin of this coordinate system is also located at the center of the data area. The data area was a rectangle 0.1778 meters along the x axis by 0.127 meters along the y axis.
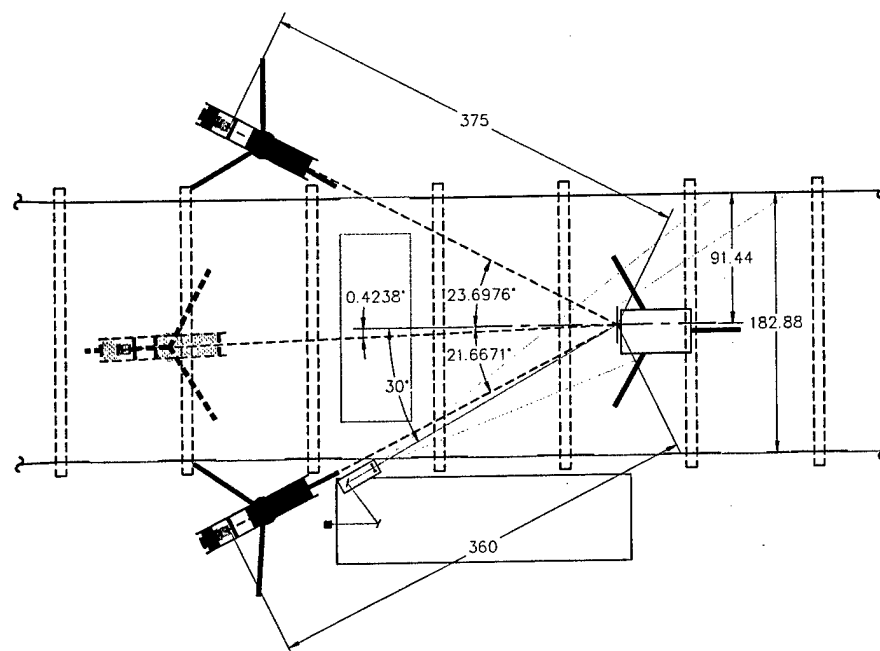
Figure 6.9: Dimensioned drawing showing the Euler angles about the y axis for each of the three camera modules and the distances from the front end of the camera to the data plane for the two camera modules mounted on the sides of the test section.
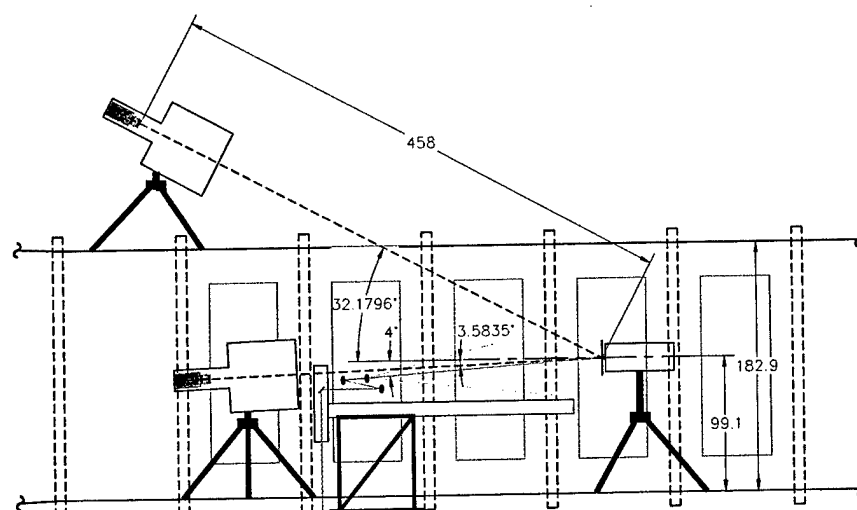
Figure 6.10: Dimensioned drawing showing the Euler angles about the x axis for the camera module in the control room and the camera module placed on top of the test section and the distance from the front end of the camera to the data plane for the camera module mounted on top of the test section.
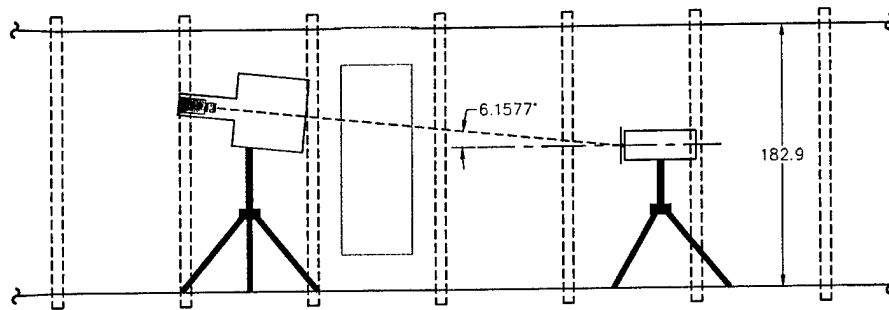
Figure 6.11: Dimensioned drawing showing the Euler angle about the x axis for the camera module placed on the side of the test section opposite to the control room.
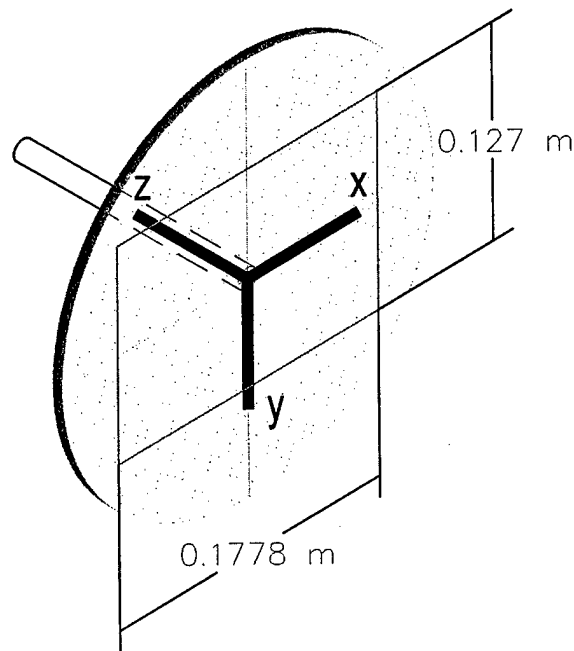
Figure 6.12: Drawing showing the orientation of the coordinate system attached to the data plane as well as the size and location of the data area.

6.5 Calibration Wheel Results

The third set of calibration wheel velocity images was acquired three days before the end of the tunnel entry scheduled to verify the performance of the VT DGV system. As mentioned previously, the two attempts made prior to this attempt were not successful because the optical frequency of the pulses output by the Nd:YAG laser had shifted out of the sensitivity range of the

iodine cell. The third set of 50 velocity images was acquired of the calibration wheel rotating at a commanded angular velocity of 50 revolutions per second. The procedure used to set the offset voltage to the laser had been adjusted to try to ensure that the optical frequency of the pulses emitted by the laser was such that the mean transmission ratio calculated by each of the camera modules was roughly 0.5. Because the light absorption properties of camera module 3 were significantly different from those of camera modules 1 and 2, this was not entirely possible. The offset voltage to the laser was set so that the mean transmission ratios measured by camera modules 1 and 2 were roughly 0.5 and this caused the mean transmission ratio measured by camera module 3 to be roughly 0.2. This decision meant that the sensitivity of camera module 3 to changes in the optical frequency due to the Doppler effect would be less than that of camera modules 1 and 2. This most likely had an effect on the quality of the data obtained from the VT DGV system in this test.

Another problem was discovered while the velocity images acquired of the calibration wheel were being reduced. An unusually large number of images were acquired while the laser was in a reset condition. Out of the 50 images acquired in this set of data, 32 images were acquired while the laser was reset. Images acquired while the laser was reset could not be used because the pulses emitted by the laser while it is reset are not the narrow bandwidth pulses needed to measure changes in optical frequency due to the Doppler effect. Only one image was acquired while the laser was reset during the 100 image iodine cell calibration acquired just prior to this attempt to acquire velocity images. The iodine cell calibrations acquired after this attempt did not have this problem either. Another interesting fact to note is that the Q-switch build up times for these images were no higher than the Q-switch build up times for the images acquired when the laser was not reset. Usually when the laser started to perform badly or when a bad pulse was fired, the Q-switch build up time would be noticeably higher than it was when the laser was performing correctly. The most likely explanation for the large number of images acquired while the laser was in a reset condition is that the calibration wheel was producing a RF signal that was picked up by the laser. Before the next attempt to acquire DGV data from the calibration wheel, this problem will have to be investigated further and a solution will have to be developed.

6.5.1 Velocity Components Calculated from the Angular Velocity

The output voltage from the motor controller was used to independently measure the angular velocity of the calibration wheel while each image was acquired. These voltages were used to calculate an average angular velocity for the images that were reduced. The average angular velocity calculated from the reduced images was 50.03 rev/s. This angular velocity was used to generate

contour plots of the x and y velocity components inside the data area. Figures 6.13 and 6.14 are contour plots showing the x and y components of velocity, respectively, calculated from the average angular velocity of the calibration wheel measured using the output voltage from the motor controller. A plot of the z component is not shown because the velocities in the z direction should all be zero.
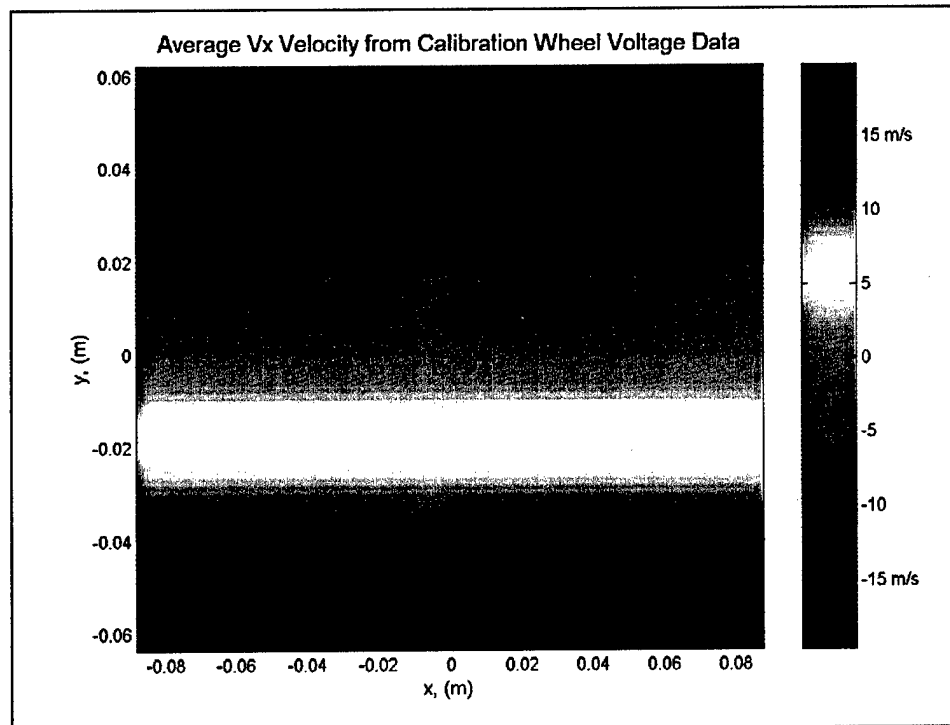
Figure 6.13: Contour plot of x velocity components calculated from average angular velocity measured using output voltage from motor controller
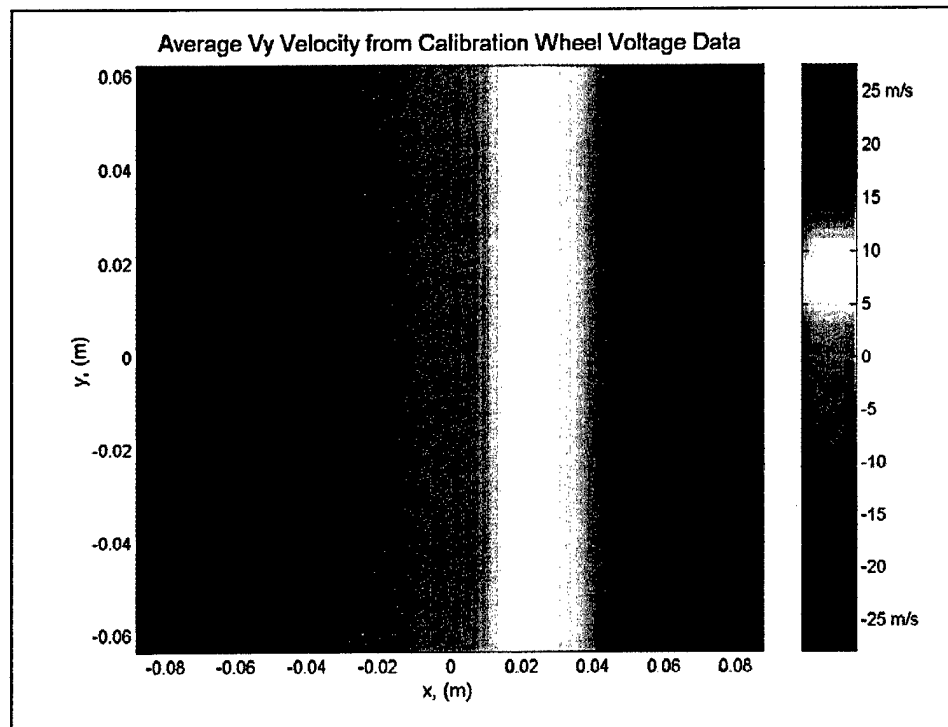
Figure 6.14: Contour plot of y velocity components calculated from average angular velocity measured using output voltage from motor controller

6.5.2 Sequence and Average Image Data Reduction

The sequence of velocity images acquired of the calibration wheel, except the images acquired while the laser was reset, were reduced using the transmission ratio and Q-switch build up time filtering options in the data reduction procedure, as described in section 4.5.3. Out of the remaining 18 images only seven sets of images passed through the transmission ratio and Q-switch build up time filtering to be reduced. These seven sets of images were used to calculate an average image for each camera module. These average images were also reduced and compared to the results of the sequence data reduction. Figures 6.15, 6.16 and 6.17 are contour plots of the average x, y and z components of velocity, respectively, calculated for the sequence of seven velocity images acquired from the calibration wheel. Figures 6.18, 6.19, and 6.20 are contour plots of the average x, y, and z components of velocity, respectively, calculated from the average images. Comparing the results from the image sequence data reduction and the average image data reduction to the plots of the x and y velocities calculated using the average angular velocity from the motor controller output voltage, the x and y velocity component plots from the data acquired by the VT DGV system show the same trends shown in figures 6.13 and 6.14. However, the magnitudes of the velocity components measured by the VT DGV system are higher than those calculated from the angular velocity of the

wheel. The most likely cause for this discrepancy is that the transmission ratios acquired by camera module 3 were closer to the minimum transmission ratio for the absorption feature being used to acquire velocity data, thus, the transmission ratios acquired by this camera module were not as sensitive to changes in optical frequency as were the transmission ratios acquired by camera modules 1 and 2. Given the problems with the optical frequency of the Nd:YAG laser drifting, as indicated by the movement of the iodine absorption features from calibration to calibration, it is also quite possible that the optical frequency of the pulses output by the Nd:YAG laser drifted such that the degradation in the sensitivity of camera module 3 was exaggerated.
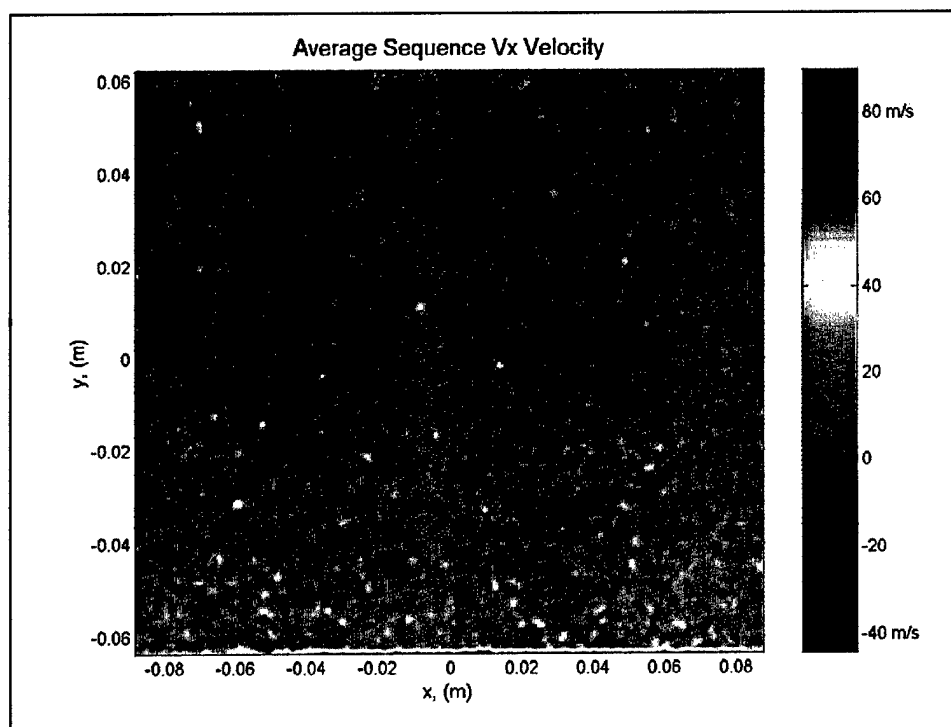
Figure 6.15: Contour plot of average x velocity components calculated by the image sequence data reduction procedure.
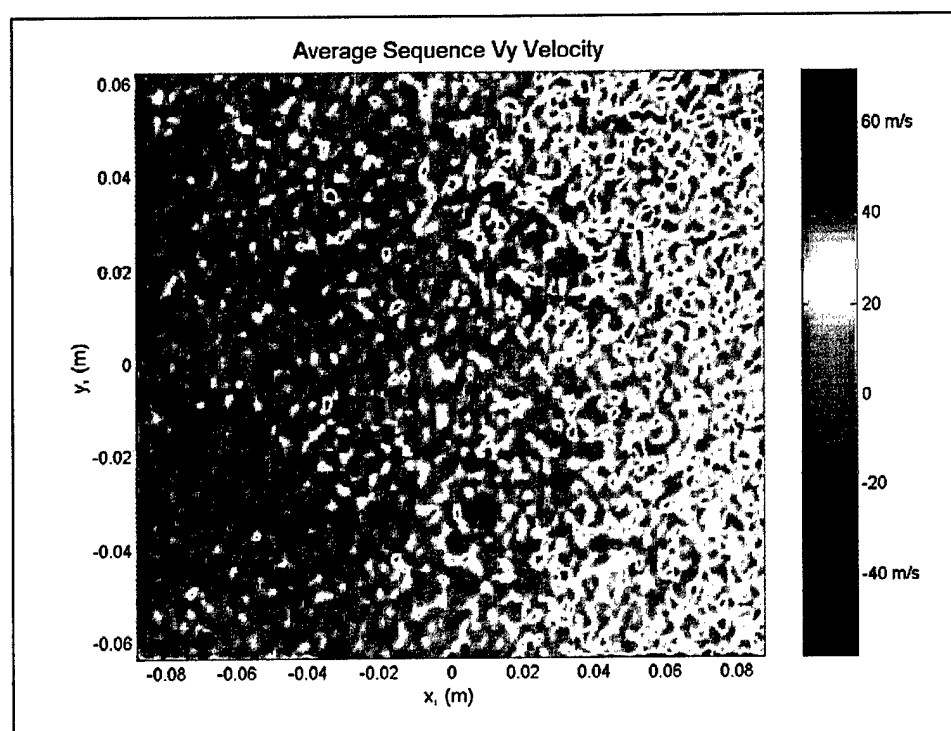
Figure 6.16: Contour plot of average y velocity components calculated by the image sequence data reduction procedure.
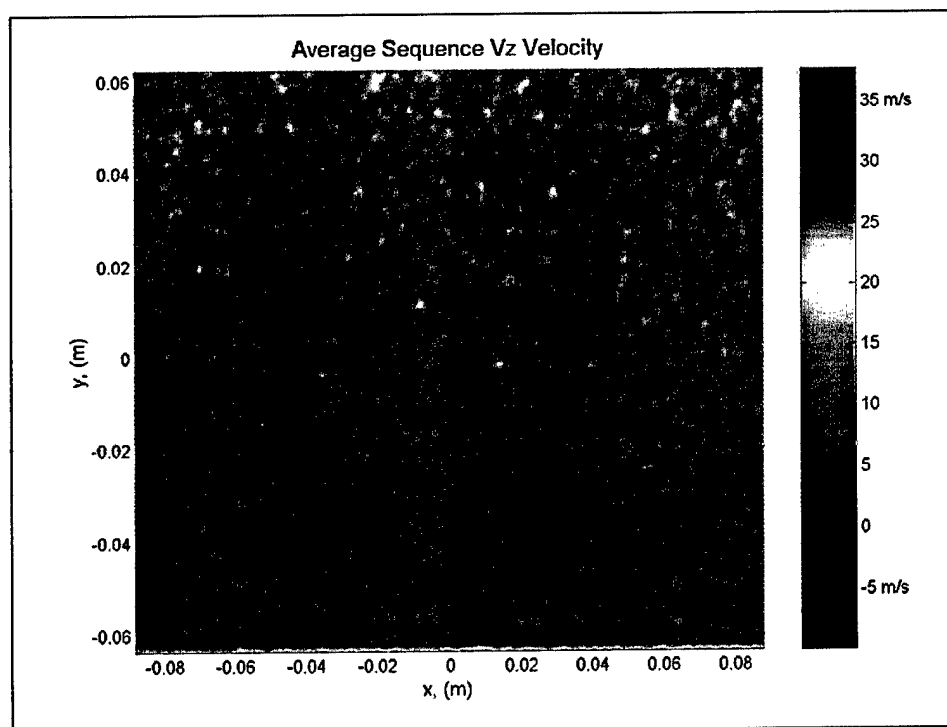
Figure 6.17: Contour plot of average z velocity components calculated by the image sequence data reduction procedure.

Figure 6.18: Contour plot of average x velocity components calculated from the average images.

Figure 6.19: Contour plot of average y velocity components calculated from the average images.

Figure 6.20: Contour plot of average z velocity components calculated from the average images.

Figures 6.21 and 6.22 show the x, y, and z velocity components along the horizontal and vertical centerlines of the calibration wheel, respectively, for the image sequence data reduction. Figures 6.23 and 6.24 show the x, y, and z velocity components along the horizontal and vertical centerlines of the calibration wheel, respectively, for the average image data reduction. These figures show that the magnitudes of the velocity components measured by the VT DGV system fluctuate considerably. There are several possible causes for these fluctuations. One possible cause for these fluctuations is spatial variations in optical frequency within each pulse used to illuminate the calibration wheel while the data image was acquired. These spatial variations could also be a contributing factor in explaining why the velocity components measured by the VT DGV system are significantly higher than the velocities calculated from the angular velocity of the wheel, but it is unlikely that these spatial variations are the major cause of this discrepancy. Another possible cause for the fluctuations in the velocity components measured by the VT DGV system is the roughness of the wheel surface. Sand paper was applied to the surface of the calibration wheel to facilitate light scattering, but it is possible the 400 grit sand paper applied to the surface was too coarse and causing shadowing to occur on the illuminated wheel surface.
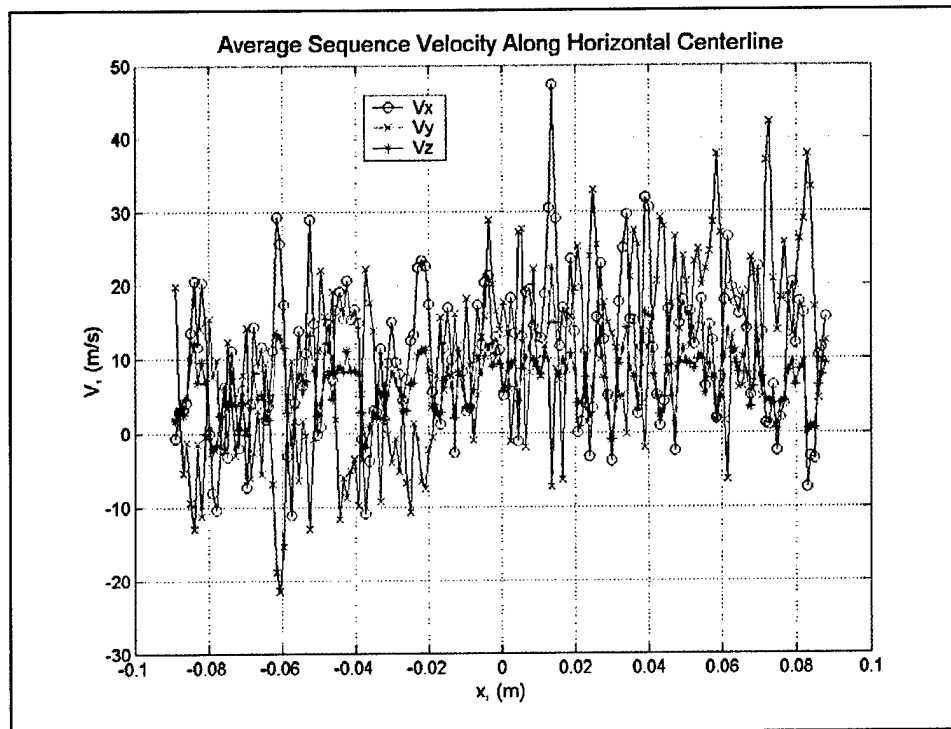
Figure 6.21: x, y, and z velocity components along the horizontal centerline of the calibration wheel, calculated during the image sequence data reduction.
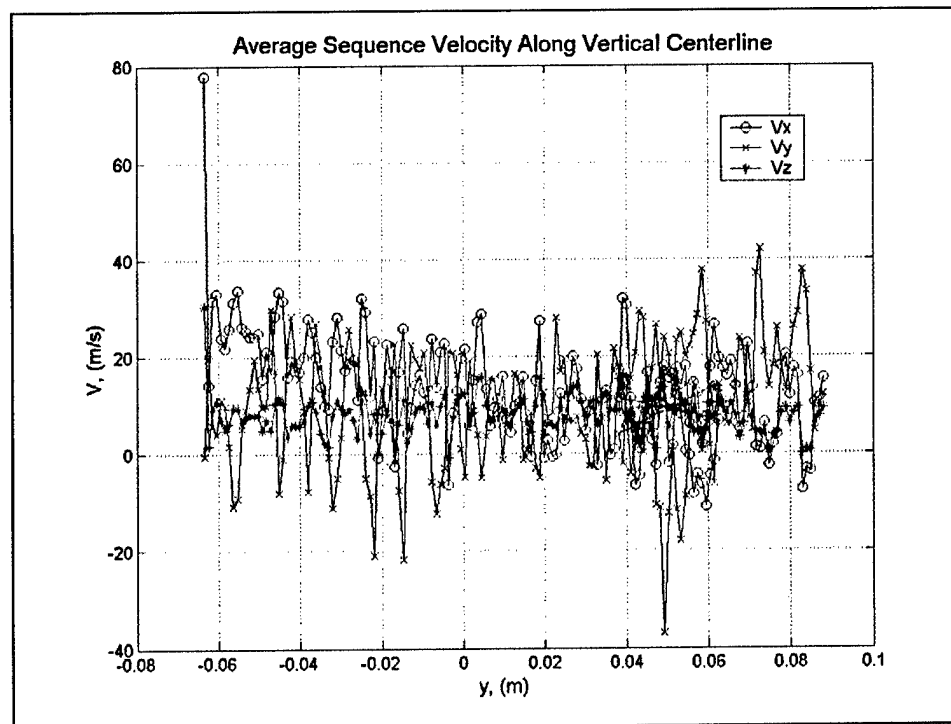
Figure 6.22: x, y, and z velocity components along the vertical centerline of the calibration wheel, calculated during the image sequence data reduction.
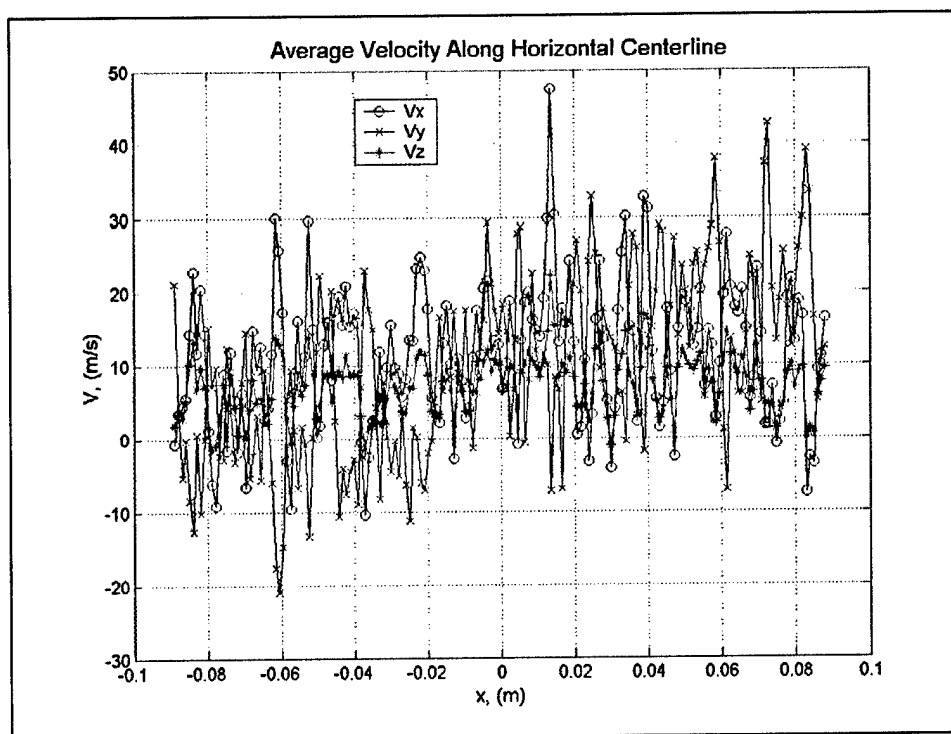
Figure 6.23: x, y, and z velocity components along the horizontal centerline of the calibration wheel, calculated during the average image data reduction.
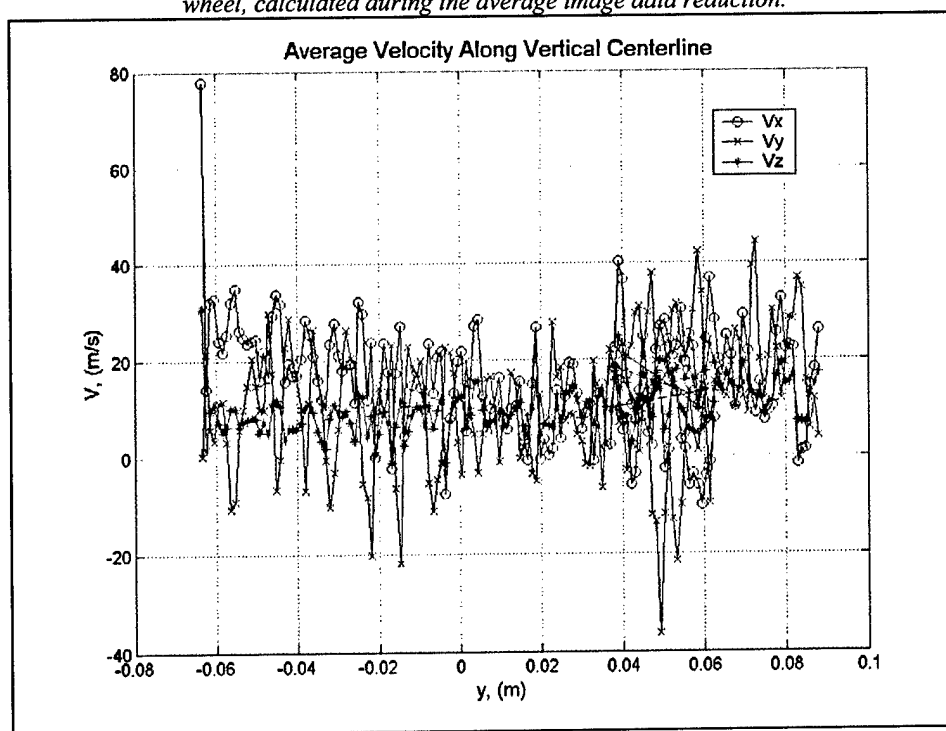
Figure 6.24: x, y, and z velocity components along the vertical centerline of the calibration wheel, calculated during the average image data reduction.

6.5.3 Individual Image Data Reduction

Because of the fluctuations observed in the results from the image sequence data reduction and the average image data reduction, and because only seven images were reduced in the image sequence data reduction and the same seven images were used to calculate the average images, each of the seven images was reduced individually. The contour plots containing the x, y, and z velocity components for each of the seven images can be found in Appendix A. Plots of the x, y, and z velocity components along the horizontal and vertical centerlines of the calibration wheel can be found in Appendix B. The contour plots and the plots of the velocity components along the vertical center line indicate that a small portion of the velocity data was lost in three of the seven images. The magnitude of the velocity components measured in these areas where data was lost was zero. The VT DGV data reduction program automatically assigns a value of zero for the transmission ratio at a particular pixel location if the pixel intensity in the reference view is zero. This prevents the program from trying to divide by zero when the transmission ratio is calculated. Also, if the transmission ratio input into the frequency calibration function is outside of the bounds set in the frequency calibration function dialog box, an optical frequency of zero is returned to the data reduction program. The data reduction program checks to see if the optical frequency is zero, if this is the case the change in optical frequency for the pixel is set to zero and hence the velocity calculated for the pixel will be zero. More than likely the problem with these images is that the transmission ratio for one of the three camera modules was outside of the maximum or minimum bounds set for calculating the optical frequency, in the region where data was lost. This theory is supported by the fact that there does not appear to be a problem with these images when they are viewed, but when they are reduced the velocities in a portion of the image are set to zero. If the pixel intensities in the reference view were zero for this region of the image it would be noticeable when the image was viewed. Because the results from these images were suspicious, another average image was calculated for each of the camera modules using the remaining four images. These new average images were reduced using the average image data reduction procedure. Figures 6.25, 6.26, and 6.27 are contour plots showing the x, y, and z velocity components for the new average images.
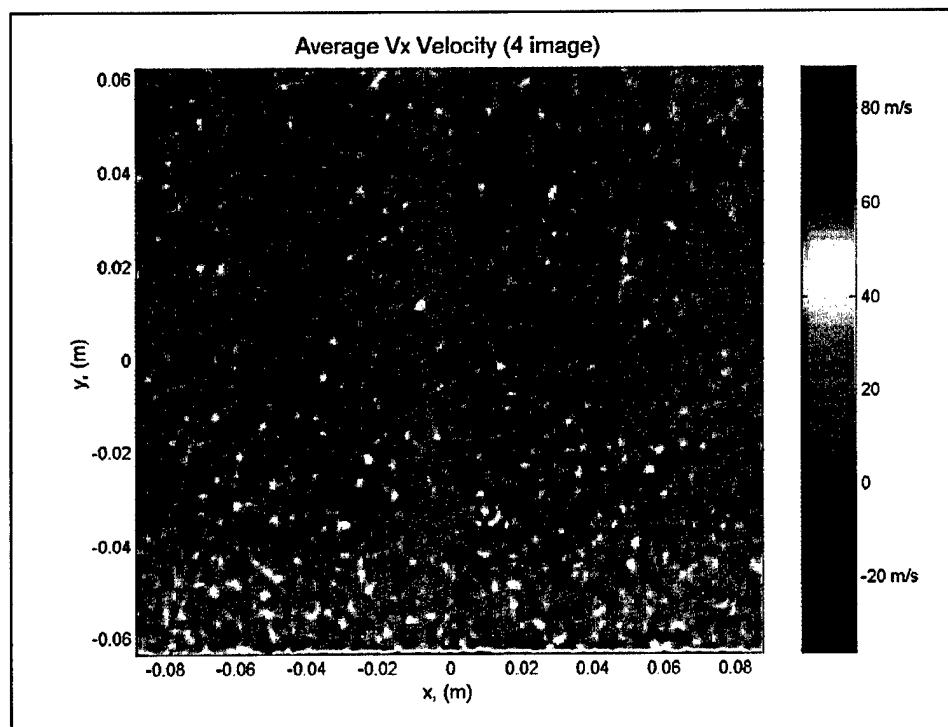
Figure 6.25: Contour plot of average x velocity components calculated from the new (4 image) average images.

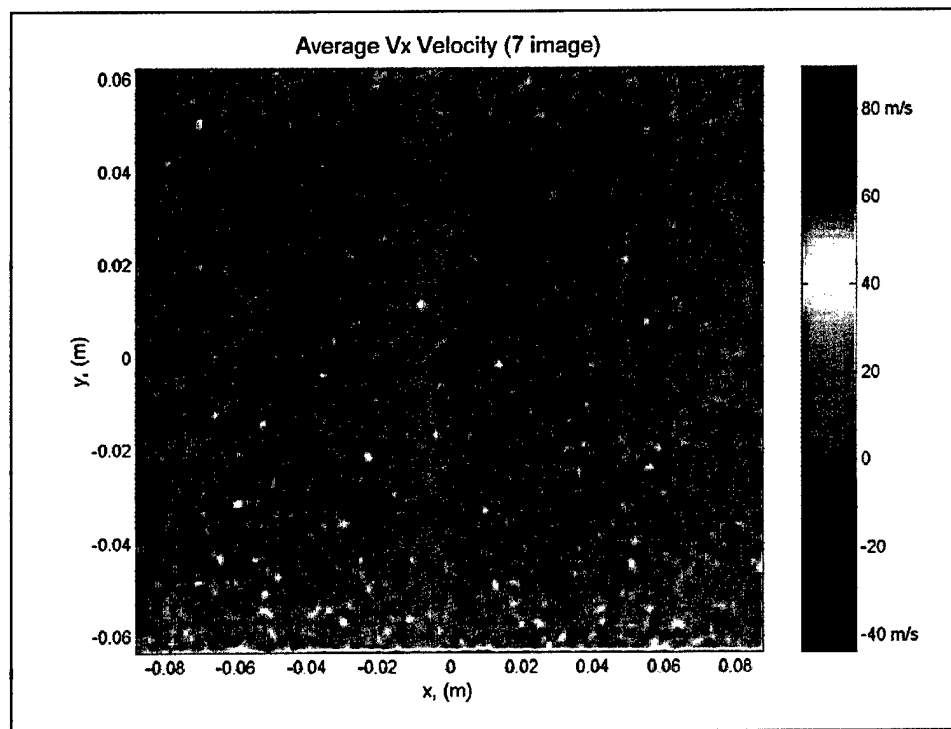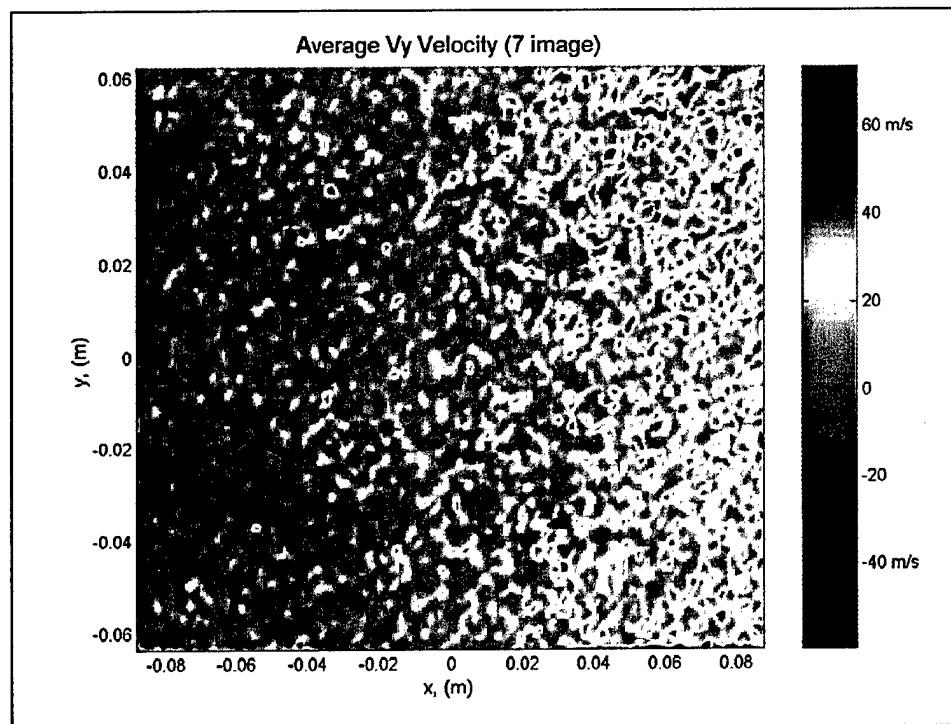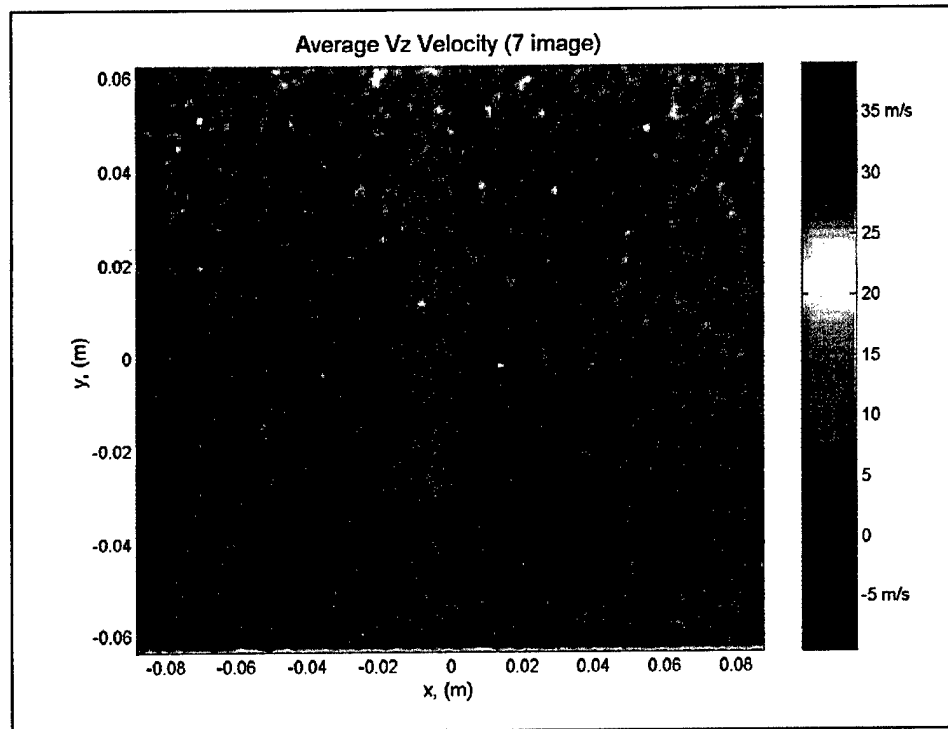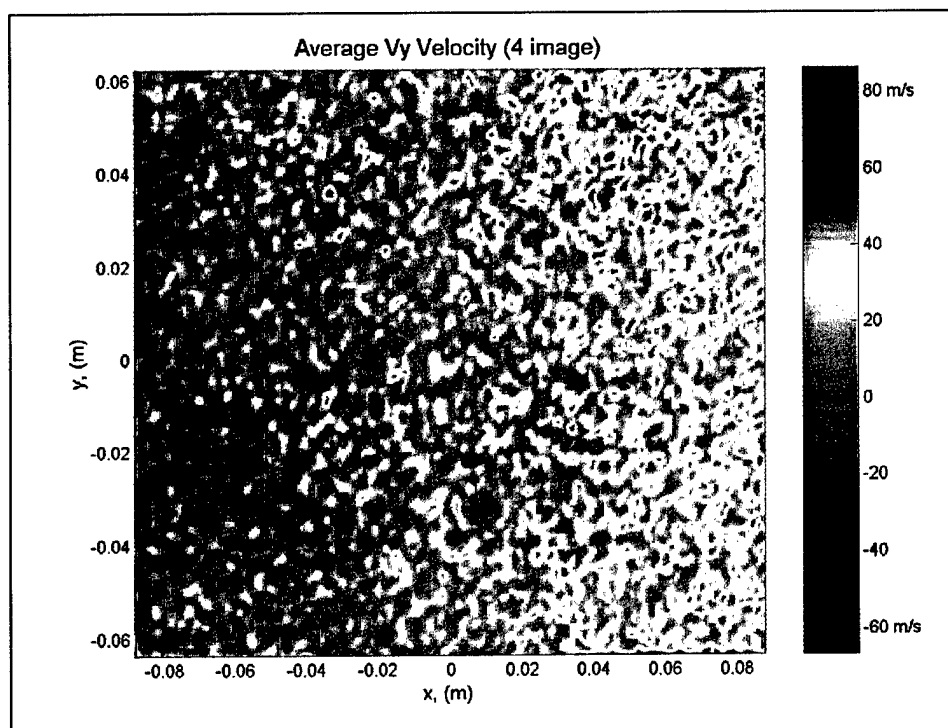*Figure 6.26: Contour plot of average y velocity components calculated from the new (4 image) average images.*
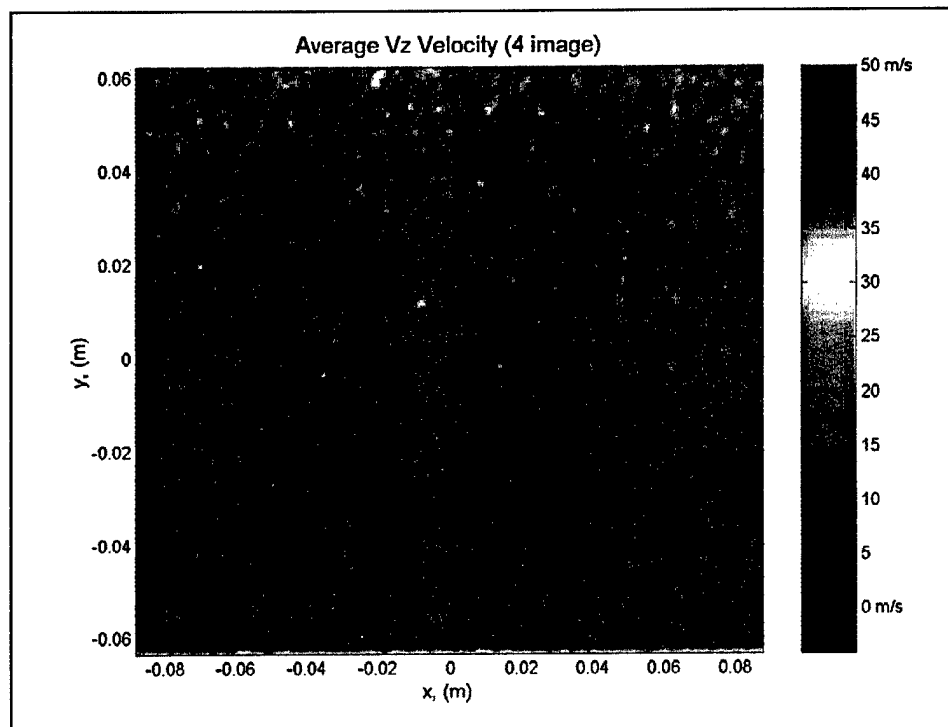
Figure 6.27: Contour plot of average z velocity components calculated from the new (4 image) average images.

Figures 6.28 and 6.29 are plots of the x velocity component along the horizontal and vertical centerlines, respectively, of the calibration wheel for the image sequence data reduction, seven image average image data reduction, four image average image data reduction and the values calculated using the seven image average angular velocity determined from the output voltage from the motor controller. Figures 6.30 and 6.31 are plots of the y velocity component along the horizontal and vertical centerlines, respectively, of the calibration wheel for the image sequence data reduction, seven image average image data reduction, four image average image data reduction and the values calculated using the seven image average angular velocity determined from the output voltage from the motor controller. Figures 6.32 and 6.33 are plots of the z velocity component along the horizontal and vertical centerlines, respectively, of the calibration wheel for the image sequence data reduction, seven image average image data reduction, four image average image data reduction and the values calculated using the seven image average angular velocity determined from the output voltage from the motor controller. Comparing the results from the three data reduction procedures, the velocities calculated by the image sequence data reduction and the seven image average data reduction closely agree, as expected. The magnitudes of the velocities calculated by the new, four image average data reduction are noticeably higher than those calculated using the other two data reduction procedures. As was indicated by the contour plots shown in figures 6.13 through 6.20, plots in figures 6.28

through 6.33 show the magnitudes of the velocities measured by the VT DGV system are generally much higher than those calculated using the angular velocity. Another important fact to note in these plots is that the plot of the x velocity component along the vertical centerline does appear to have the same trend shown in the velocities calculated from the angular velocity and the y velocity component along the horizontal centerline also appears to have the same trend shown in the velocities calculated from the angular velocity.
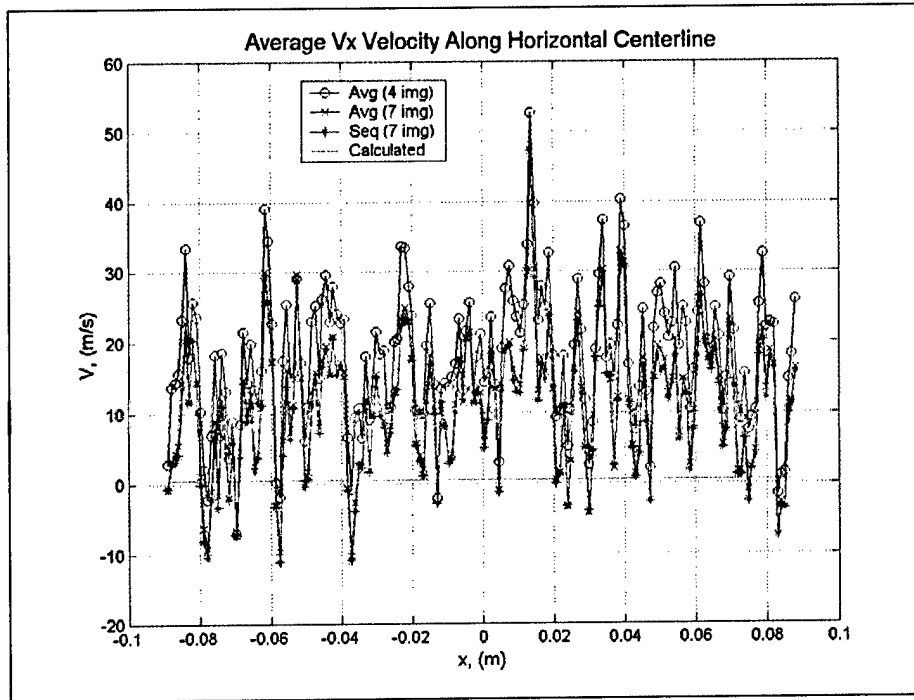
Figure 6.28: Plot of x velocity component along the horizontal centerline of the calibration wheel for the image sequence data reduction, average image data reduction, new (4 image) average image data reduction and the values calculated from the angular velocity.
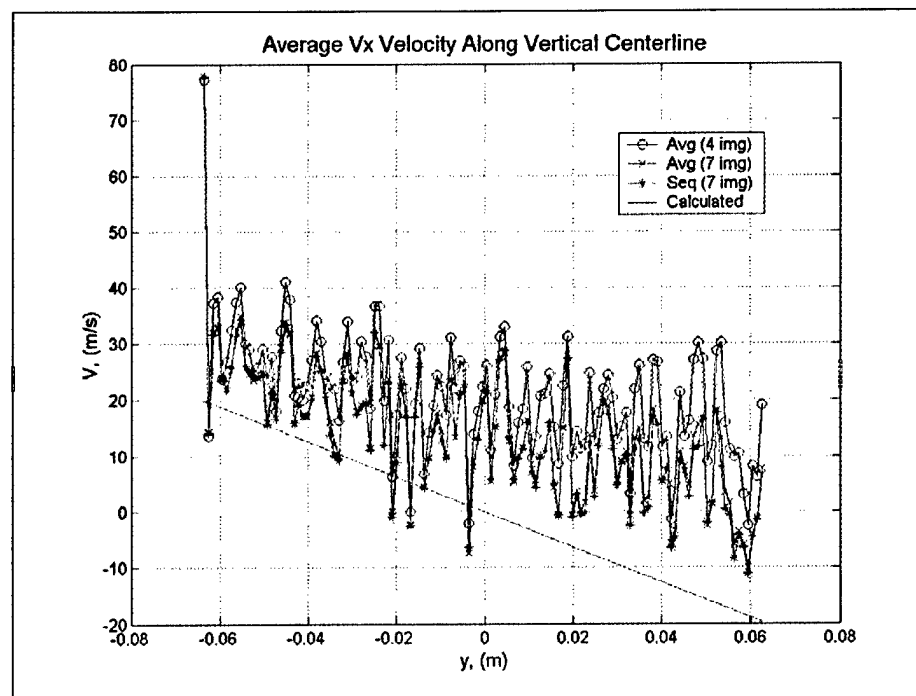
Figure 6.29: Plot of x velocity component along the vertical centerline of the calibration wheel for the image sequence data reduction, average image data reduction, new (4 image) average image data reduction and the values calculated from the angular velocity.
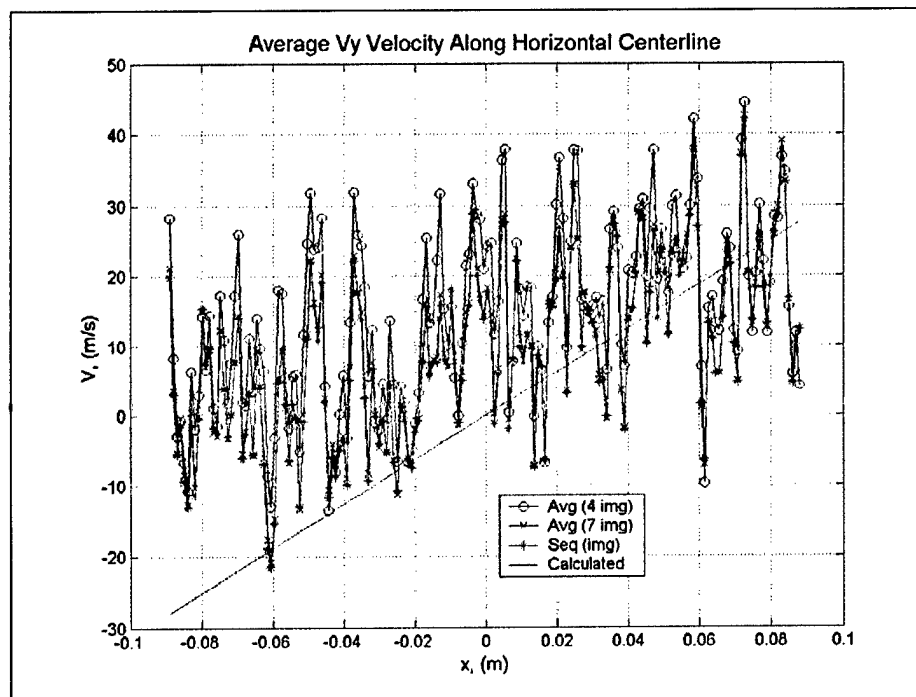
Figure 6.30: Plot of y velocity component along the horizontal centerline of the calibration wheel for the image sequence data reduction, average image data reduction, new (4 image) average image data reduction and the values calculated from the angular velocity.
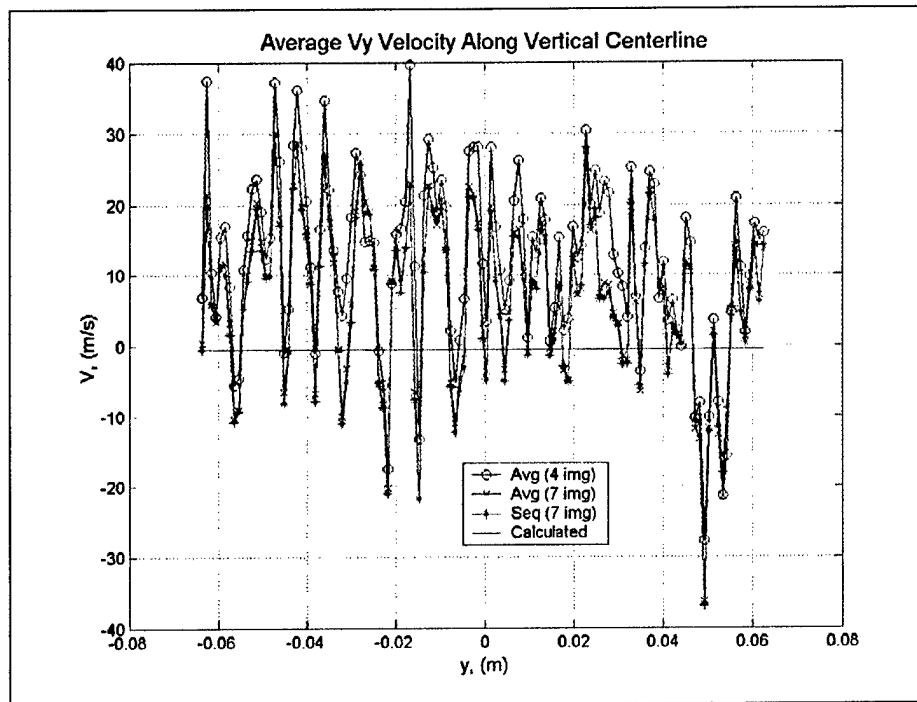
Figure 6.31: Plot of y velocity components along the vertical centerline of the calibration wheel for the image sequence data reduction, average image data reduction, new (4 image) average image data reduction and the values calculated from the angular velocity.
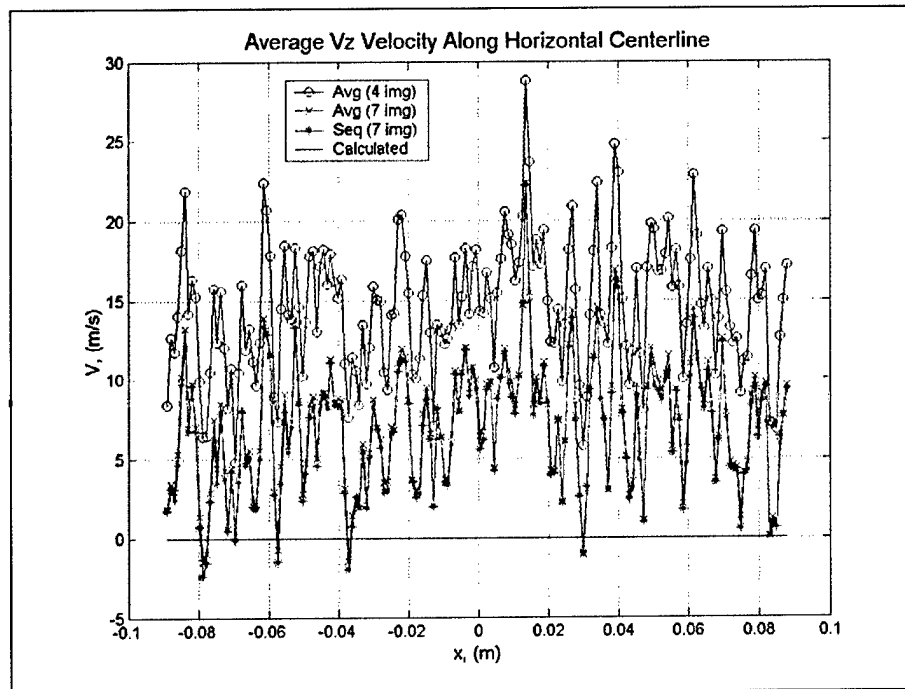
Figure 6.32: Plot of z velocity components along the horizontal centerline of the calibration wheel for the image sequence data reduction, average image data reduction, new (4 image) average image data reduction and the values calculated from the angular velocity.
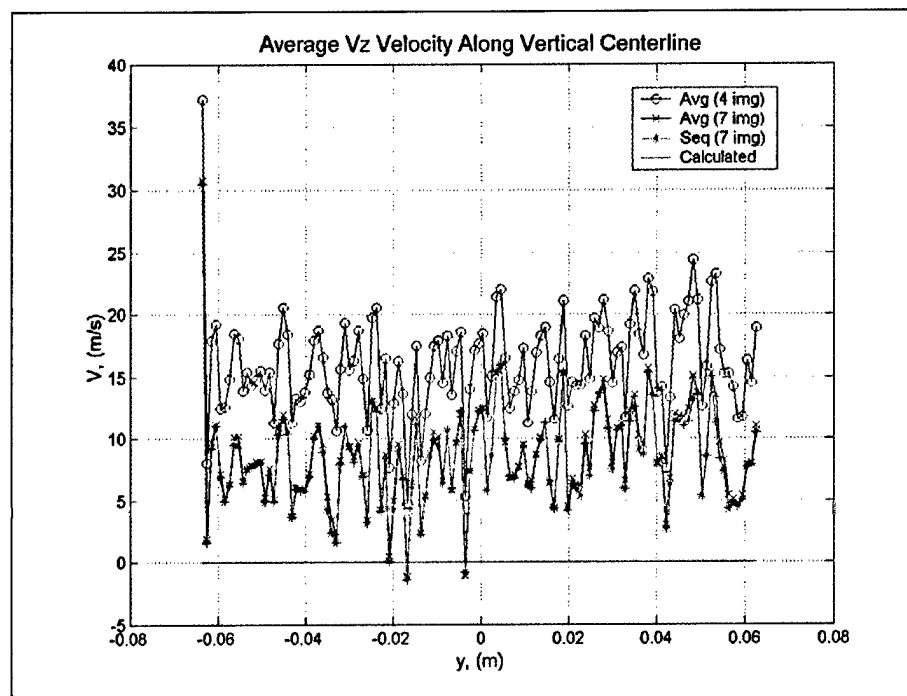
Figure 6.33: Plot of z velocity components along the vertical centerline of the calibration wheel for the image sequence data reduction, average image data reduction, new (4 image) average image data reduction and the values calculated from the angular velocity.

6.6 6:1 Prolate Spheroid Results

As was discussed in section 3.8, an attempt was made to acquire DGV data in the wake of a 6:1 prolate spheroid. The hardware problems discussed in Chapter 5 delayed this attempt until the last day of the wind tunnel entry. A full day was required to reposition the camera modules and set up the optics needed to form the laser sheet used to acquire DGV data in the flow field. Once the system setup had been adapted to acquire flow field data, four iodine cell calibrations were acquired before a usable calibration was found. Next, the correction images were acquired as described in section 3.8. Finally, the wind tunnel was started and the free stream velocity inside the test section was increased until a dynamic pressure of 4 inches of water was reached. Once the speed of the tunnel was set the smoke machine was enabled and seed particles were injected into the wind tunnel. A test image was acquired prior to an attempt to acquire a series of velocity data images. This test image did not show any measurable pattern of scattered light. The free stream velocity in the wind tunnel was decreased so the dynamic pressure was 3 inches of water and another test image was acquired. The results were the same as before, no measurable pattern of scattered light was captured by any of the camera modules. Another attempt was made at a dynamic pressure of 2.3 inches of water with the same results. This was the last attempt to be made because diffused smoke in the wind tunnel obscured the data plane. Figure 6.34 shows a false color version of one of the velocity data

images acquired by camera module 1, figure 6.35 shows a false color version of one of the data images acquired by camera module 2, and figure 6.36 shows a false color version of one of the data images acquired by camera module 3.
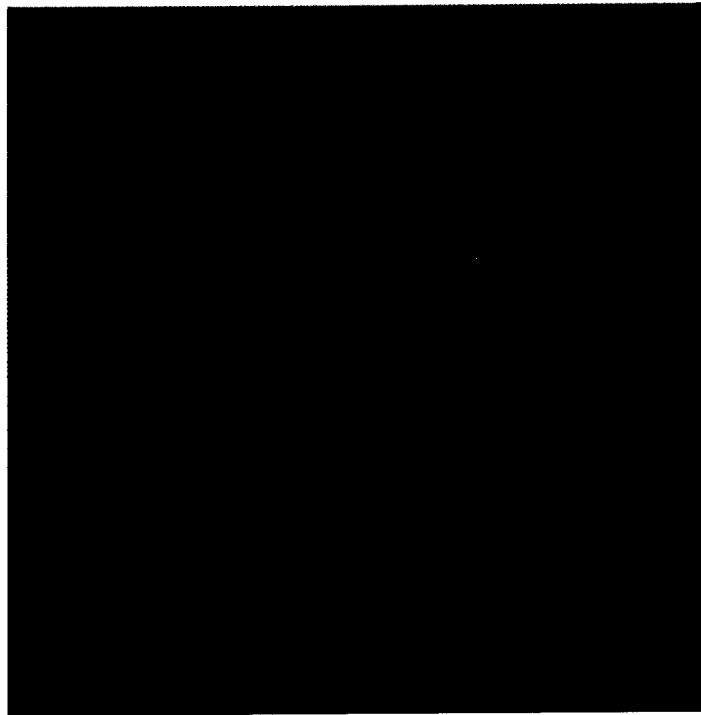
Figure 6.34: False color version of velocity data image acquired by camera module 1 of the flow in the wake of a 6:1 prolate spheroid model.
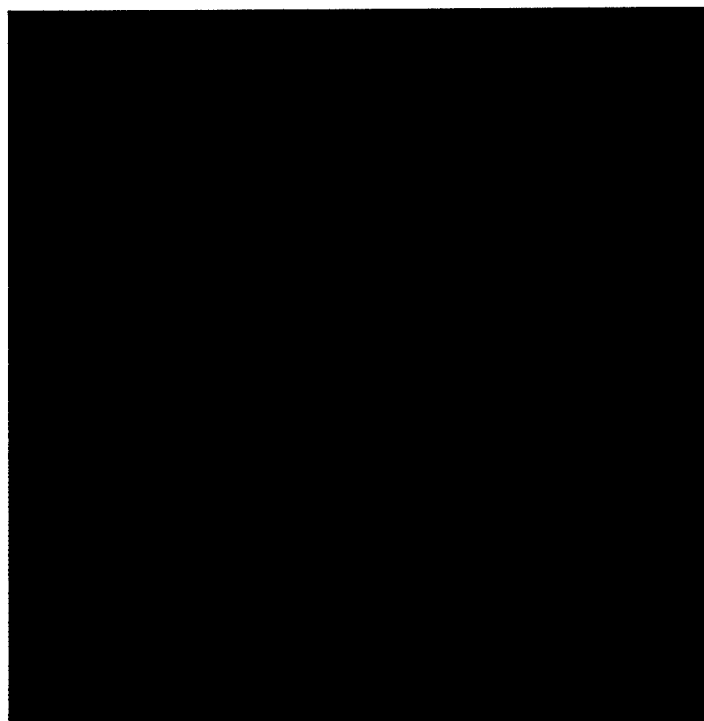
Figure 6.35: False color version of velocity data image acquired by camera module 2 of the flow in the wake of a 6:1 prolate spheroid model.
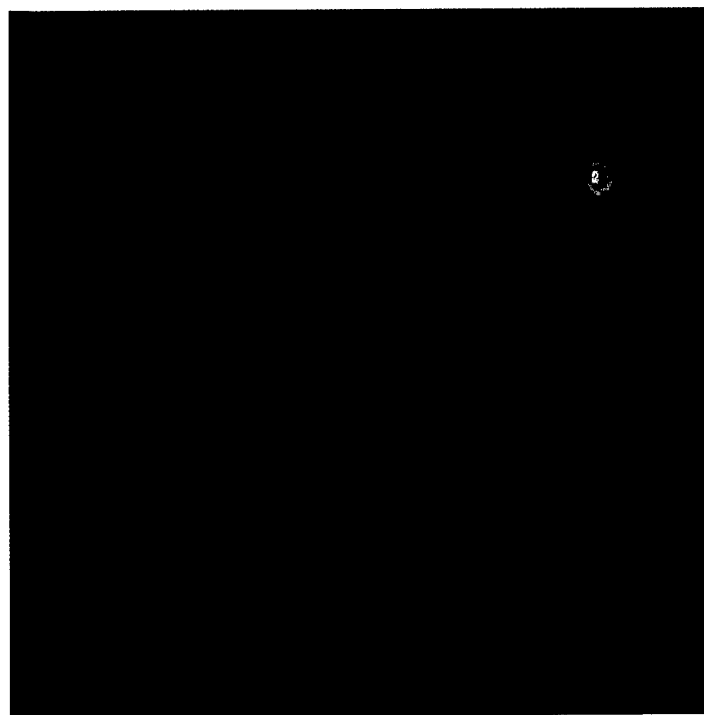
Figure 6.36: False color version of velocity data image acquired by camera module 3 of the flow in the wake of a 6:1 prolate spheroid model.

While the attempt itself was unsuccessful, some important lessons were learned. The first lesson learned is that an experiment with a flexible test schedule needs to be performed using the Nd:YAG laser, wind tunnel, smoke machine, model(s) to be tested, and one of the camera modules to try different smoke machine positions and injection methods to maximize the light scattering while minimizing the amount of smoke used. These tests would not necessarily need to be attempts to acquire DGV data. In fact, it would be advisable not to try to acquire DGV data in these attempts, but to only try to successfully acquire images of smoke particles passing through the laser sheet. This would significantly simplify the test schedule and decrease the number of tasks to be performed between attempts. The smoke machine filled the wind tunnel with smoke in a very short period of time (roughly 5 minutes) so the smoke machine appears to be capable of producing enough smoke to acquire DGV velocity images. The stream tube containing the smoke plume may have been too large and was most likely in the wrong location to acquire velocity images in the wake of the prolate spheroid. Another important lesson was that skilled and attentive help is needed when flow velocity data are to be acquired with the VT DGV system. The people who assisted with setting up the VT DGV system during this research were smart, skilled, and attentive people, but these people were not present when the attempts to acquire velocity data in the wake of the prolate spheroid were made. The VT DGV system requires at least two skilled people to acquire flow velocity images. One of these people would run the DGV control computer and acquire the images and the other person would be responsible for running the wind tunnel and smoke machine. The second person would have to pay close attention to the size and location of the smoke plume and make the person running the DGV control computer aware of any problems encountered. A third experienced person would also prove very helpful in monitoring the performance of the Nd:YAG laser until confidence in the performance of the laser is gained.

6.7 General Comments

While the performance of the VT DGV system was less than expected, some valuable lessons have been learned. Considerable time was needed to set up the VT DGV system in the wind tunnel. Future work on the system needs to address this problem by making the system easier to setup, reposition, and take down as well as addressing the hardware problems within the system. A permanent laser optics setup needs to be designed and constructed. In the previous tests of the VT DGV system as well as the tests performed in this research the laser optics were temporarily set up on a pair of optical tables. The first table was where the laser was placed and the optics on this table were used to fire the laser into the control room. The second table held the optics used to create the cone of laser light and the laser sheet. Precious time was needed to set up and adjust the laser optics.

A compact and permanent setup would save set up time and potentially eliminate some of the frequent adjustments needed during this research. Every effort was made to eliminate stray reflections from the laser optics. Covers were designed and constructed to cover the optics and eliminate these reflections. This was done for two reasons, to make the area where the system was being used safer and to also try to eliminate possible sources of "noise" in the system since the light from these stray reflections could easily be acquired by the camera modules. The background correction images may or may not be able to account for all of these stray reflections, depending on how the correction images were acquired. Special windows made of optical quality glass are needed where the laser is being fired into the test section as well as where the camera modules are placed to view the data plane. Scratches and imperfections in the Plexiglas windows degraded the uniformity in the illumination of the data area and the quality of the images acquired by the camera modules. Holes were cut into the Plexiglas panels where the laser was to pass through to prevent the laser from burning the panel and to allow the data area to be illuminated as uniformly as possible. The windows to be made for the laser to pass through will need to be made of a material capable of surviving the high power output from the laser. Also, the hardware problems with the system must be addressed aggressively. The problems with the stability of the Nd:YAG laser coupled with the problems with the digital cameras severely hampered the progress of this research and ultimately led to the poor performance of the system during the attempts to acquire velocity images. The hope of future success with the VT DGV system rests on permanently solving these hardware problems. A way must be found to stabilize the performance of the Nd:YAG laser and to make it more reliable or the laser must be replaced with a another laser, possibly another type of laser. An argon ion laser may, in fact, be a possible alternative to the Nd:YAG laser. The digital camera with the problem of forming ice crystals must be replaced. Using the system an hour at a time was not only inconvenient, it prevented this research from progressing in a timely manner and prevented other problems with the system from being diagnosed and fixed. In addition to the work described above, much work remains to be done before the system can be used in conjunction with the Dynamic Plunge Pitch and Roll (DyPPiR) apparatus. Finally, the modifications suggested in the paper published by Meyers *et al,* in 2001 and discussed in Chapter 1, need to be reviewed and where possible implemented to improve the performance of the VT DGV system. In particular, the modification needed to monitor spatial variations in the optical frequency from pulse to pulse should be implemented as soon as it is practical.[106]

Chapter 7: Uncertainty Analysis

Chapter 7 : Uncertainty Analysis

After the velocity data acquired from the calibration wheel had been reduced, an uncertainty analysis was performed to determine the uncertainty of the velocities measured by the VT DGV system. All of the uncertainties discussed in this chapter have a confidence level of 95%. In addition to determining the overall uncertainty of the data obtained from the calibration wheel, this analysis was used to determine what factors in the acquisition and reduction of the calibration wheel data led to the largest increases in uncertainty. Determining what factors led to the largest increases in uncertainty will provide guidance on what portions of the VT DGV system will require the most attention to improve the performance of this system in the future.

The software used to calculate the standard deviations in the pixel intensities for a series of data images, the uncertainties of the reference value of the laser reference transmission ratio, the uncertainty of the laser reference transmission ratio and the uncertainty of the average reference transmission ratio for camera module i, was written by Troy Jones as part of his M.S. thesis.[107] The rest of the software used in this uncertainty analysis was written as part of this research. The procedure used to conduct this analysis was adapted from one discussed in Troy Jones' M.S. thesis.[108] The procedures used to calculate the uncertainty in the wave number used to reduce the calibration wheel velocity data and to calculate the uncertainty in the Euler angles used to determine the laser propagation vector were added to the procedure discussed in Jones' thesis. While this uncertainty analysis was being performed, errors in the procedures used to calculate the uncertainty of the transmission ratios used in the data reduction procedure were located and corrected

The governing equation used to solve for velocities in the DGV technique can be expressed in the following manner:

$$\begin{Bmatrix} V_x \\ V_y \\ V_z \end{Bmatrix} = \frac{c}{v_o} \begin{bmatrix} \sin\theta_{y1} + \sin\theta_{ylas} & -\sin\theta_{x1}\cos\theta_{y1} - \sin\theta_{xlas}\cos\theta_{ylas} & -\cos\theta_{x1}\cos\theta_{y1} - \cos\theta_{xlas}\cos\theta_{ylas} \\ \sin\theta_{y2} + \sin\theta_{ylas} & -\sin\theta_{x2}\cos\theta_{y2} - \sin\theta_{xlas}\cos\theta_{ylas} & -\cos\theta_{x2}\cos\theta_{y2} - \cos\theta_{xlas}\cos\theta_{ylas} \\ \sin\theta_{y3} + \sin\theta_{ylas} & -\sin\theta_{x3}\cos\theta_{y3} - \sin\theta_{xlas}\cos\theta_{ylas} & -\cos\theta_{x3}\cos\theta_{y3} - \cos\theta_{xlas}\cos\theta_{ylas} \end{bmatrix}^{-1} \cdot \begin{Bmatrix} \Delta v_1 \\ \Delta v_2 \\ \Delta v_3 \end{Bmatrix}$$

(51)

where V_x, V_y, and V_z were the velocity components in the x, y, and z directions, respectively, c was the speed of light, v_0 was the optical frequency of the laser pulse used to acquire DGV data, θ_{x1}, θ_{x2}, and θ_{x3} were the Euler angles, about the x axis, used to calculate the unit vector pointing toward the direction from which the data area is being viewed by camera modules 1, 2, and 3 respectively, θ_{y1}, θ_{y2}, and θ_{y3} were the Euler angles, about the y axis, used to calculate the unit vector pointing toward the direction from which the data area is being viewed by camera modules 1, 2, and 3 respectively, θ_{xlas} and θ_{ylas} were the Euler angles about the x and y axes, respectively, used to calculate the laser propagation unit vector, and Δv_1, Δv_2, and Δv_3 were the changes in optical frequency measured by camera modules 1, 2, and 3 respectively. Therefore, the general equation used to calculate the uncertainty of the velocity data was:

$$\omega V_j = \sqrt{\begin{aligned} & \left(\omega\Delta f_1 \cdot \frac{\partial V_j}{\partial \Delta v_1}\right)^2 + \left(\omega\Delta f_2 \cdot \frac{\partial V_j}{\partial \Delta v_2}\right)^2 + \left(\omega\Delta f_3 \cdot \frac{\partial V_j}{\partial \Delta v_3}\right)^2 + \\ & \left(\omega\theta_{x1} \cdot \frac{\partial V_j}{\partial \theta_{x1}}\right)^2 + \left(\omega\theta_{x2} \cdot \frac{\partial V_j}{\partial \theta_{x2}}\right)^2 + \left(\omega\theta_{x3} \cdot \frac{\partial V_j}{\partial \theta_{x3}}\right)^2 + \\ & \left(\omega\theta_{y1} \cdot \frac{\partial V_j}{\partial \theta_{y1}}\right)^2 + \left(\omega\theta_{y2} \cdot \frac{\partial V_j}{\partial \theta_{y2}}\right)^2 + \left(\omega\theta_{y3} \cdot \frac{\partial V_j}{\partial \theta_{y3}}\right)^2 + \\ & \left(\omega\theta_{xlas} \cdot \frac{\partial V_j}{\partial \theta_{xlas}}\right)^2 + \left(\omega\theta_{ylas} \cdot \frac{\partial V_j}{\partial \theta_{ylas}}\right)^2 + \left(\omega WN \cdot \frac{\partial V_j}{\partial WN}\right)^2 \end{aligned}}$$

(52)

where ωV_j was the uncertainty of the jth velocity component, $\omega\Delta v_1$, $\omega\Delta v_2$, and $\omega\Delta v_3$ were the uncertainties in the change in optical frequency due to the Doppler effect, $\omega\theta_{x1}$, $\omega\theta_{x2}$, and $\omega\theta_{x3}$

were the uncertainties in the Euler angles about the x axis for the camera viewing angles, $\omega\theta_{y1}$, $\omega\theta_{y2}$, and $\omega\theta_{y3}$ were the uncertainties in the Euler angles about the y axis for the camera viewing angles, and $\omega\theta_{xlas}$, and $\omega\theta_{ylas}$ were the uncertainties in the Euler angles used to calculate the laser propagation vector. The term ωWN was the uncertainty in the calculated wave number of the laser pulse. As was discussed in Chapter 2, the wave number was defined to be v_o/c. The uncertainty of each velocity component (V_x, V_y, and V_z) was calculated at each pixel location in the data plane. The average uncertainty for each of these velocity components was also calculated.

7.1 Calculating Frequency Shift Uncertainties

Before the uncertainty of the acquired velocities could be calculated, the uncertainties on the right hand side of equation 52 had to be determined. The frequency shift uncertainties: $\omega\Delta v_1$, $\omega\Delta v_2$, and $\omega\Delta v_3$, will be considered first. The change in optical frequency due to the Doppler effect was determined by calculating the difference in the optical frequency at each pixel location in the data plane and the optical frequency of the unshifted laser beam. Both optical frequencies were calculated using the frequency calibration functions contained in equations 47 through 49. These three equations were functions of transmission ratio and so the change in optical frequency was a function of transmission ratio, as can be seen in equation 53:

$$\Delta v_i = v_i\left(TR_i\right) - v_i\left(TR_i^{ref}\right) \tag{53}$$

where $v_i\left(TR_i\right)$ was the frequency calibration function for camera module i, solved at each pixel location in the data plane, and $v_i\left(TR_i^{ref}\right)$ was the frequency calibration function solved using the laser reference transmission ratio calculated for the camera module as described in section 4.6.3. From equation 53, the equation to express the uncertainty of Δv_i was derived to be:

$$\omega\Delta v_i = \sqrt{\left(\omega TR_i \cdot \frac{\partial\Delta v_i}{\partial TR_i}\right)^2 + \left(\omega TR_i^{ref} \cdot \frac{\partial\Delta v_i}{\partial TR_i^{ref}}\right)^2} \tag{54}$$

where ωTR_i was the uncertainty of the transmission ratio calculated at each pixel location in the data area for camera module i, and ωTR_i^{ref} was the uncertainty of the laser reference transmission ratio

for camera module i.[109] The partial derivatives in this equation were determined by calculating the partial derivatives of equation 53 with respect to the transmission ratio calculated at each pixel location in the data area for camera module i and the laser reference transmission ratio for camera module i. The values for these partial derivatives were calculated using the following equations:

Camera Module 1: (Above test section)

$$\frac{\partial \Delta v_1}{\partial TR_1} = c \cdot 100 \left(0.1855(TR_1)^4 - 0.2268(TR_1)^3 + 0.162(TR_1)^2 - 0.1002(TR_1) + 0.0364\right) \quad (55)$$

$$\frac{\partial \Delta v_1}{\partial TR_1^{ref}} = -c \cdot 100 \left(0.1855\left(TR_1^{ref}\right)^4 - 0.2268\left(TR_1^{ref}\right)^3 + 0.162\left(TR_1^{ref}\right)^2 - 0.1002\left(TR_1^{ref}\right) + 0.0364\right)$$

$$(56)$$

Camera Module 2: (Port side of test section)

$$\frac{\partial \Delta v_2}{\partial TR_2} = c \cdot 100 \left(0.023(TR_2)^4 + 0.1796(TR_2)^3 - 0.2043(TR_2)^2 + 0.0390(TR_2) + 0.0018\right) \quad (57)$$

$$\frac{\partial \Delta v_2}{\partial TR_2} = -c \cdot 100 \left(0.023\left(TR_2^{ref}\right)^4 + 0.1796\left(TR_2^{ref}\right)^3 - 0.2043\left(TR_2^{ref}\right)^2 + 0.0390\left(TR_2^{ref}\right) + 0.0018\right)$$

$$(58)$$

Camera Module 3: (Starboard side of test section)

$$\frac{\partial \Delta v_3}{\partial TR_3} = c \cdot 100 \left(0.9445(TR_3)^4 - 1.9588(TR_3)^3 + 1.5198(TR_3)^2 - 0.5018(TR_3) + 0.0676\right) \quad (59)$$

$$\frac{\partial \Delta v_3}{\partial TR_3} = -c \cdot 100 \left(0.9445\left(TR_3^{ref}\right)^4 - 1.9588\left(TR_3^{ref}\right)^3 + 1.5198\left(TR_3^{ref}\right)^2 - 0.5018\left(TR_3^{ref}\right) + 0.0676\right)$$

$$(60)$$

where c was the speed of light.

7.1.1 Calculating Transmission Ratio Uncertainty

Before the uncertainty of the change in optical frequency ($\omega \Delta v_i$) could be calculated, the uncertainties ωTR_i and ωTR_i^{ref} needed to be calculated. The transmission ratio at a given pixel location (x, y) in the data area, $TR_i(x, y)$ was a function of the reference and filtered pixel intensities at that pixel location, so therefore, the uncertainty of the transmission ratio at pixel location (x, y) was calculated using the following equation:

$$\omega TR_i(x,y) = \sqrt{\left(\omega P_{filtered}(x,y) \cdot \frac{\partial TR_i(x,y)}{\partial P_{filtered}(x,y)} \right)^2 + \left(\omega P_{reference}(x,y) \cdot \frac{\partial TR_i(x,y)}{\partial P_{reference}(x,y)} \right)^2} \quad (61)$$

where $\omega P_{filtered}(x, y)$ was the uncertainty in the pixel intensity for the pixel in the filtered view at location (x, y) and $\omega P_{reference}(x, y)$ was the uncertainty in the pixel intensity for the pixel in the reference view at location (x, y). The uncertainties in the filtered and reference view pixel intensities at location (x, y) were calculated using the standard deviation in the pixel intensities over the sequence of images reduced, the number of images within the sequence of images reduced, and Student's t distribution. The uncertainties in these pixel intensities were calculated using an equation of the following form:

$$\omega P = \frac{t\sigma}{\sqrt{n}} \quad (62)$$

where t was Student's t value, σ was the standard deviation in the mean pixel intensity, and n was the number of images in the sequence of images reduced.[110] The values for the partial derivatives in equation 61 were calculated using the following equations:

$$\frac{\partial TR_i(x,y)}{\partial P_{filtered}(x,y)} = \frac{1}{P_{reference}(x,y)} \quad (63)$$

$$\frac{\partial TR_i(x,y)}{\partial P_{reference}(x,y)} = \frac{P_{filtered}(x,y)}{\left(P_{reference}(x,y)\right)^2} \quad (64)$$

7.1.2 Calculating Laser Reference Transmission Ratio Uncertainty

A similar procedure was used to calculate the uncertainty in the calculated laser reference transmission ratio for each camera module. The following equation was used to calculate the laser reference transmission ratio for each camera module:

$$TR_i^{ref} = TR_{laser \atop ROI} + \left(TR_{camera}^{ref} - TR_{laser \atop ROI}^{ref} \right) \tag{65}$$

where TR_i^{ref} was the laser reference transmission ratio for camera module i, $TR_{laser \atop ROI}$ was the average transmission ratio for the pixels inside the laser region of interest from the laser reference camera data image, TR_{camera}^{ref} was the average reference transmission ratio for camera module i, as described in subsection 4.5.5, and $TR_{laser \atop ROI}^{ref}$ was the reference value of the laser reference transmission ratio from the laser reference camera, as described in section 4.5.3. From equation 65, the following equation was derived to calculate the uncertainty in the calculated value of the laser reference transmission ratio for camera module i:

$$\omega TR_i^{ref} = \sqrt{ \left(\omega TR_{laser \atop ROI} \cdot \frac{\partial TR_i^{ref}}{\partial TR_{laser \atop ROI}} \right)^2 + \left(\omega TR_{laser \atop ROI}^{ref} \cdot \frac{\partial TR_i^{ref}}{\partial TR_{laser \atop ROI}^{ref}} \right)^2 + \left(\omega TR_{camera}^{ref} \cdot \frac{\partial TR_i^{ref}}{\partial TR_{camera}^{ref}} \right)^2 } \tag{66}$$

The transmission ratio uncertainties, $\omega TR_{laser \atop ROI}$, $\omega TR_{laser \atop ROI}^{ref}$, and ωTR_{camera}^{ref}, were calculated using a series of equations of the form shown in equations 61 through 64. The standard deviations used to calculate $\omega TR_{laser \atop ROI}$ and $\omega TR_{laser \atop ROI}^{ref}$ were calculated from the filtered and reference pixel intensities for the pixels inside the laser reference regions of interest described in section 4.4.3. The standard deviations used to calculate ωTR_{camera}^{ref} were calculated from the filtered and reference pixel intensities for the pixels inside the filtered and reference regions of interest from the reference images acquired prior to acquiring velocity data from the calibration wheel. The values for the partial derivatives in equation 66 were calculated by taking the partial derivative of equation 65 with respect to $TR_{laser \atop ROI}$, TR_{camera}^{ref}, and $TR_{laser \atop ROI}^{ref}$. The partial derivative of the laser reference transmission ratio for camera module i, with respect to the average transmission ratio for the pixels inside the laser region

of interest from the laser reference camera data image, $TR_{laser \atop ROI}$, was 1. The partial derivative of the

laser reference transmission ratio for camera module i, with respect to the reference value of the laser

reference transmission ratio from the laser reference camera, $TR_{laser \atop ROI}^{ref}$, was -1. The partial derivative

of the laser reference transmission ratio for camera module i, with respect to the average reference

transmission ratio from camera module i, TR_{camera}^{ref}, was 1. Once the uncertainty of the transmission

ratio at each pixel location in the data area and the uncertainty of the laser reference transmission ratio

had been calculated for camera module i, equation 54 could be used to solve for the uncertainty of the

change in optical frequency measured by camera module i, $\omega \Delta v_i$, could be calculated.

7.1.3 Calculating Velocity Partial Derivatives with respect to Δv

The governing equation for the DGV technique shown in equation 51 can also be expressed
in the following manner:

$$V_x = m_{11}\Delta v_1 + m_{12}\Delta v_2 + m_{13}\Delta v_3 \tag{67}$$

$$V_y = m_{21}\Delta v_1 + m_{22}\Delta v_2 + m_{23}\Delta v_3 \tag{68}$$

$$V_z = m_{31}\Delta v_1 + m_{32}\Delta v_2 + m_{33}\Delta v_3 \tag{69}$$

where

$$m_{11} = \lambda \cdot a_{11} \tag{70}$$

$$m_{12} = \lambda \cdot a_{12} \tag{71}$$

$$m_{13} = \lambda \cdot a_{13} \qquad and\ so\ on.... \tag{72}$$

The $a_{i,j}$ terms in equations 70-72 correspond to the terms in the inverse matrix shown in equation 51

and the λ term is the wavelength of the laser pulse which is equal to the reciprocal of the wave

number. Taking the partial derivatives of each velocity component with respect to Δv_i gives

the following results:

$$\frac{\partial V_x}{\partial \Delta v_1} = m_{11} = \lambda \cdot a_{11} \tag{73}$$

$$\frac{\partial V_x}{\partial \Delta v_2} = m_{12} = \lambda \cdot a_{12} \tag{74}$$

$$\frac{\partial V_x}{\partial \Delta v_3} = m_{13} = \lambda \cdot a_{13} \tag{75}$$

$$\frac{\partial V_y}{\partial \Delta v_1} = m_{21} = \lambda \cdot a_{21} \tag{76}$$

$$\frac{\partial V_y}{\partial \Delta v_2} = m_{22} = \lambda \cdot a_{22} \qquad and\ so\ on.... \tag{77}$$

Using the Euler angles calculated for each of the camera modules and the laser propagation vector calculated in Chapter 6 the values for the partial derivatives of each velocity component with respect to the change in optical frequency measured by each camera module were:

$$\begin{bmatrix} \dfrac{\partial V_x}{\partial \Delta v_1} & \dfrac{\partial V_x}{\partial \Delta v_2} & \dfrac{\partial V_x}{\partial \Delta v_3} \\ \dfrac{\partial V_y}{\partial \Delta v_1} & \dfrac{\partial V_y}{\partial \Delta v_2} & \dfrac{\partial V_y}{\partial \Delta v_3} \\ \dfrac{\partial V_z}{\partial \Delta v_1} & \dfrac{\partial V_z}{\partial \Delta v_2} & \dfrac{\partial V_z}{\partial \Delta v_3} \end{bmatrix} = \frac{1}{WN} \begin{bmatrix} 0.391437 & -1.47640 & 1.08858 \\ -1.92423 & 0.813357 & 1.03147 \\ 0.0626446 & -0.662552 & 0.0382006 \end{bmatrix} \tag{78}$$

where WN was the wave number of the pulse used to acquire velocity data.

7.2 Calculating Wave Number Uncertainty

The procedure used to calculate the uncertainty for the wave number used some of the same information used to calculate the uncertainty for the change in optical frequency, so this procedure will be discussed next. As was discussed in Chapter 2, the wave number is defined as 1/wavelength. The frequency calibration functions given in equations 47 – 49 were used to calculate the wave number for the laser pulse as well as calculating the optical frequency at each pixel location in the data area. A wave number was calculated using laser reference transmission ratio from each camera module, TR_i^{ref}. The three wave numbers were then averaged to calculate an average wave number, which was used in the data reduction procedure. Because the laser reference transmission ratio from each camera module was used in calculating the wave number used in the data reduction procedure, the equation used to calculate the uncertainty of the calculated wave number was:

$$\omega WN = \sqrt{\left(\omega TR_1^{ref} \cdot \frac{\partial WN}{\partial TR_1^{ref}}\right)^2 + \left(\omega TR_2^{ref} \cdot \frac{\partial WN}{\partial TR_2^{ref}}\right)^2 + \left(\omega TR_3^{ref} \cdot \frac{\partial WN}{\partial TR_3^{ref}}\right)^2} \qquad (79)$$

where ωWN was the uncertainty of the wave number, and ωTR_1^{ref}, ωTR_2^{ref}, and ωTR_3^{ref} were the uncertainties in the laser reference transmission ratios for camera modules 1, 2, and 3 respectively. The uncertainties ωTR_1^{ref}, ωTR_2^{ref}, and ωTR_3^{ref} were calculated as part of the procedure used to calculate the uncertainty of the changes in optical frequency, Δv_1, Δv_2, and Δv_3, (see section 7.1.2). All that was needed was to calculate the partial derivatives in equation 79. The equations used to calculate the values for these partial derivatives are given below.

Camera Module 1: (Above test section)

$$\frac{\partial WN}{\partial TR_1^{ref}} = 100\left(0.1855\left(TR_1^{ref}\right)^4 - 0.2268\left(TR_1^{ref}\right)^3 + 0.162\left(TR_1^{ref}\right)^2 - 0.1002\left(TR_1^{ref}\right) + 0.0364\right)$$

$$(80)$$

Camera Module 2: (Port side of test section)

$$\frac{\partial WN}{\partial TR_2} = 100\left(0.023\left(TR_2^{ref}\right)^4 + 0.1796\left(TR_2^{ref}\right)^3 - 0.2043\left(TR_2^{ref}\right)^2 + 0.0390\left(TR_2^{ref}\right) + 0.0018\right)$$

$$(81)$$

Camera Module 3: (Starboard side of test section)

$$\frac{\partial WN}{\partial TR_3} = 100\left(0.9445\left(TR_3^{ref}\right)^4 - 1.9588\left(TR_3^{ref}\right)^3 + 1.5198\left(TR_3^{ref}\right)^2 - 0.5018\left(TR_3^{ref}\right) + 0.0676\right)$$

$$(82)$$

The partial derivative of velocity with respect to wave number, found in equation 52, was calculated to be:

$$\begin{Bmatrix} \frac{\partial V_x}{\partial WN} \\ \frac{\partial V_y}{\partial WN} \\ \frac{\partial V_z}{\partial WN} \end{Bmatrix} = \frac{1}{WN^2} \begin{bmatrix} \sin\theta_{y1} + \sin\theta_{ylas} & -\sin\theta_{x1}\cos\theta_{y1} - \sin\theta_{xlas}\cos\theta_{ylas} & -\cos\theta_{x1}\cos\theta_{y1} - \cos\theta_{xlas}\cos\theta_{ylas} \\ \sin\theta_{y2} + \sin\theta_{ylas} & -\sin\theta_{x2}\cos\theta_{y2} - \sin\theta_{xlas}\cos\theta_{ylas} & -\cos\theta_{x2}\cos\theta_{y2} - \cos\theta_{xlas}\cos\theta_{ylas} \\ \sin\theta_{y3} + \sin\theta_{ylas} & -\sin\theta_{x3}\cos\theta_{y3} - \sin\theta_{xlas}\cos\theta_{ylas} & -\cos\theta_{x3}\cos\theta_{y3} - \cos\theta_{xlas}\cos\theta_{ylas} \end{bmatrix}^{-1} \cdot \begin{Bmatrix} \Delta v_1 \\ \Delta v_2 \\ \Delta v_3 \end{Bmatrix}$$

$$(83)$$

Inserting the Euler angles for the camera module viewing angles and the laser propagation vector calculated in Chapter 6, equation 83 becomes:

$$\begin{Bmatrix} \dfrac{\partial V_x}{\partial WN} \\[2mm] \dfrac{\partial V_y}{\partial WN} \\[2mm] \dfrac{\partial V_z}{\partial WN} \end{Bmatrix} = \dfrac{1}{WN^2} \begin{bmatrix} 0.391437 & -1.47640 & 1.08858 \\ -1.92423 & 0.813357 & 1.03147 \\ 0.0626446 & -0.662552 & 0.0382006 \end{bmatrix} \cdot \begin{Bmatrix} \Delta v_1 \\ \Delta v_2 \\ \Delta v_3 \end{Bmatrix} \qquad (84)$$

7.3 Calculating Angle Uncertainties

7.3.1 Viewing angle uncertainty

As was discussed in the M. S thesis of Troy Jones, the camera calibration toolbox used to calculate the Euler angles for each of the camera modules did not provide direct uncertainties on the extrinsic properties output by the toolbox.[111] The toolbox did output average pixel errors but these values were a measure of the accuracy of the analytical reprojection of the reference points input into the toolbox and not an indicator of the accuracy of the rotation matrix output by the program. Jones performed an iterative procedure where small perturbations to the Euler angles calculated by the toolbox were made and the change in the observation vector was calculated. From this analysis, Jones estimated the uncertainties for all of these angles to be ±0.75°, or ±0.013090 radians.[112] This uncertainty value was also used in the current uncertainty analysis.

7.3.2 Laser Propagation Vector Uncertainty

Because the laser propagation vector used to reduce the calibration wheel data was calculated from estimated Euler angles, the uncertainties for these angles are considerably higher than those calculated for the camera Euler angles. The uncertainties for the θ_{xlas} and θ_{ylas} angles used to calculate the laser propagation vector were both assumed to be ±3°, or ±0.052360 radians.

7.3.3 Partial Derivatives for the Angular Measurements

The partial derivatives of each of the velocity components with respect to each of the angular measurements used in reducing the calibration wheel data were calculated using Mathematica. Mathematica was chosen to perform these calculations because these partial derivatives were too complicated to calculate by hand and Mathematica had the ability to perform mathematical operations on symbolic expressions. The following equations were obtained from Mathematica and used in this uncertainty analysis:

$$
\begin{Bmatrix} \dfrac{\partial V_x}{\partial \theta_{x1}} \\[2mm] \dfrac{\partial V_y}{\partial \theta_{x1}} \\[2mm] \dfrac{\partial V_z}{\partial \theta_{x1}} \end{Bmatrix} = \lambda \begin{bmatrix} -0.650550 & 0.407580 & 0.333758 \\ 3.19799 & -2.00359 & -1.64070 \\ -0.104113 & 0.0652282 & 0.0534139 \end{bmatrix} \begin{Bmatrix} \Delta f_1 \\ \Delta f_2 \\ \Delta f_3 \end{Bmatrix} \tag{100}
$$

$$
\begin{Bmatrix} \dfrac{\partial V_x}{\partial \theta_{x2}} \\[2mm] \dfrac{\partial V_y}{\partial \theta_{x2}} \\[2mm] \dfrac{\partial V_z}{\partial \theta_{x2}} \end{Bmatrix} = \lambda \begin{bmatrix} 2.59546 & -1.18932 & -1.38087 \\ -1.42986 & 0.655203 & 0.760728 \\ 1.16475 & -0.533721 & -0.619681 \end{bmatrix} \begin{Bmatrix} \Delta f_1 \\ \Delta f_2 \\ \Delta f_3 \end{Bmatrix} \tag{101}
$$

$$
\begin{Bmatrix} \dfrac{\partial V_x}{\partial \theta_{x3}} \\[2mm] \dfrac{\partial V_y}{\partial \theta_{x3}} \\[2mm] \dfrac{\partial V_z}{\partial \theta_{x3}} \end{Bmatrix} = \lambda \begin{bmatrix} -1.93891 & 0.779342 & 1.04388 \\ -1.83719 & 0.738456 & 0.989113 \\ -0.0680407 & 0.0273488 & 0.0366319 \end{bmatrix} \begin{Bmatrix} \Delta f_1 \\ \Delta f_2 \\ \Delta f_3 \end{Bmatrix} \tag{102}
$$

$$
\begin{Bmatrix} \dfrac{\partial V_x}{\partial \theta_{y1}} \\[2mm] \dfrac{\partial V_y}{\partial \theta_{y1}} \\[2mm] \dfrac{\partial V_z}{\partial \theta_{y1}} \end{Bmatrix} = \lambda \begin{bmatrix} -0.150405 & 0.578270 & -0.427782 \\ 0.739364 & -2.84267 & 2.10290 \\ -0.0240704 & 0.0925450 & -0.0684613 \end{bmatrix} \begin{Bmatrix} \Delta f_1 \\ \Delta f_2 \\ \Delta f_3 \end{Bmatrix} \tag{103}
$$

$$
\begin{Bmatrix} \dfrac{\partial V_x}{\partial \theta_{y2}} \\[2mm] \dfrac{\partial V_y}{\partial \theta_{y2}} \\[2mm] \dfrac{\partial V_z}{\partial \theta_{y2}} \end{Bmatrix} = \lambda \begin{bmatrix} 0.614704 & -1.65685 & 1.38347 \\ -0.338644 & 0.912769 & -0.762163 \\ 0.275856 & -0.743531 & 0.620849 \end{bmatrix} \begin{Bmatrix} \Delta f_1 \\ \Delta f_2 \\ \Delta f_3 \end{Bmatrix} \tag{104}
$$

$$\left\{\begin{array}{c} \dfrac{\partial V_x}{\partial \theta_{y3}} \\[2mm] \dfrac{\partial V_y}{\partial \theta_{y3}} \\[2mm] \dfrac{\partial V_z}{\partial \theta_{y3}} \end{array}\right\} = \lambda \begin{bmatrix} -0.469470 & 1.77982 & -1.09069 \\ -0.444841 & 1.68645 & -1.03347 \\ -0.0164747 & 0.0624579 & -0.0382747 \end{bmatrix} \begin{Bmatrix} \Delta f_1 \\ \Delta f_2 \\ \Delta f_3 \end{Bmatrix} \qquad (105)$$

$$\left\{\begin{array}{c} \dfrac{\partial V_x}{\partial \theta_{xlas}} \\[2mm] \dfrac{\partial V_y}{\partial \theta_{xlas}} \\[2mm] \dfrac{\partial V_z}{\partial \theta_{xlas}} \end{array}\right\} = \lambda \begin{bmatrix} -0.00599899 & 0.00239674 & 0.00323139 \\ 0.131703 & -0.0526185 & -0.0709426 \\ 0.931642 & -0.372213 & -0.501835 \end{bmatrix} \begin{Bmatrix} \Delta f_1 \\ \Delta f_2 \\ \Delta f_3 \end{Bmatrix} \qquad (106)$$

$$\left\{\begin{array}{c} \dfrac{\partial V_x}{\partial \theta_{ylas}} \\[2mm] \dfrac{\partial V_y}{\partial \theta_{ylas}} \\[2mm] \dfrac{\partial V_z}{\partial \theta_{ylas}} \end{array}\right\} = \lambda \begin{bmatrix} -0.00158187 & 0.00592247 & -0.0033486 \\ 0.0347288 & -0.130023 & 0.0735158 \\ 0.245665 & -0.919759 & 0.520036 \end{bmatrix} \begin{Bmatrix} \Delta f_1 \\ \Delta f_2 \\ \Delta f_3 \end{Bmatrix} \qquad (107)$$

where λ was the wavelength, which was equal to 1/wave number. These were the last terms needed to solve equation 52 for the uncertainty of each velocity component. This procedure was different from the one used by Troy Jones to calculate these partial derivatives. He calculated these partial derivatives using a perturbation technique similar to the one he used to calculate the uncertainties in the camera Euler angles.[113]

7.4 Uncertainty Analysis Results

Figures 7.1, 7.2, and 7.3 are contour plots of the uncertainties for the velocity components in the x, y, and z directions, respectively. Figure 7.1 shows that the uncertainties for the velocity components in the x direction vary from roughly 9 m/s to 28 m/s. Figure 7.2 shows that the uncertainties for the velocity components in the y direction vary from roughly 20 m/s to 55 m/s. Figure 7.3 shows that the uncertainties for the velocity components in the z direction vary from roughly 1.5 m/s to 11.75 m/s. Given the results shown in Chapter 6, the large uncertainties shown

here were to be expected. More will be said about the primary sources of the large uncertainties shown here later in this chapter.
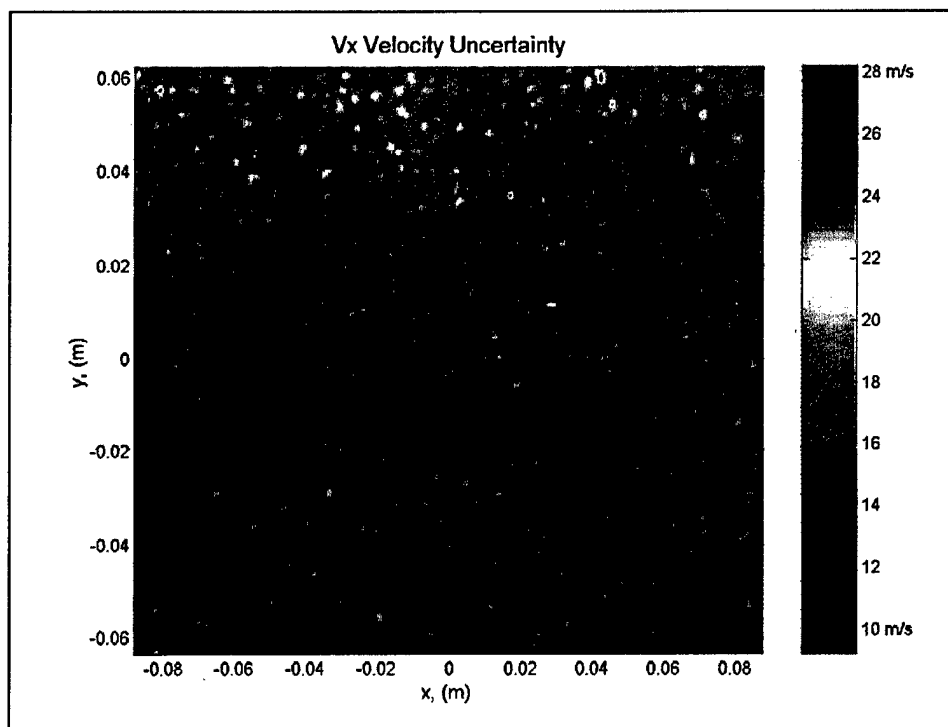

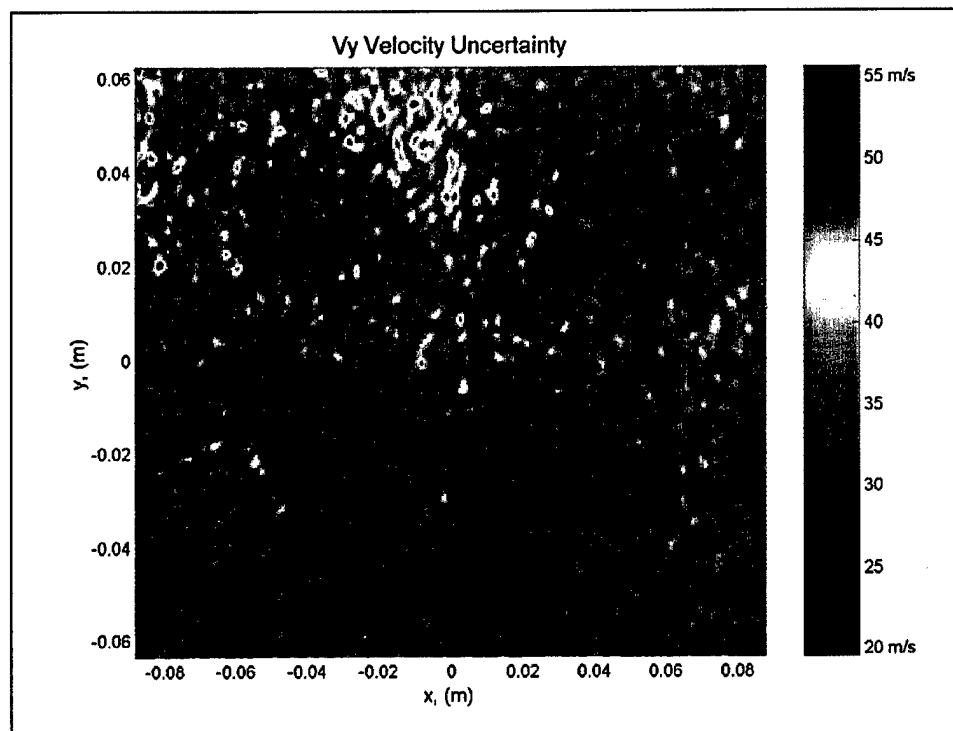Figure 7.1: Uncertainty of the velocity components in the x direction.

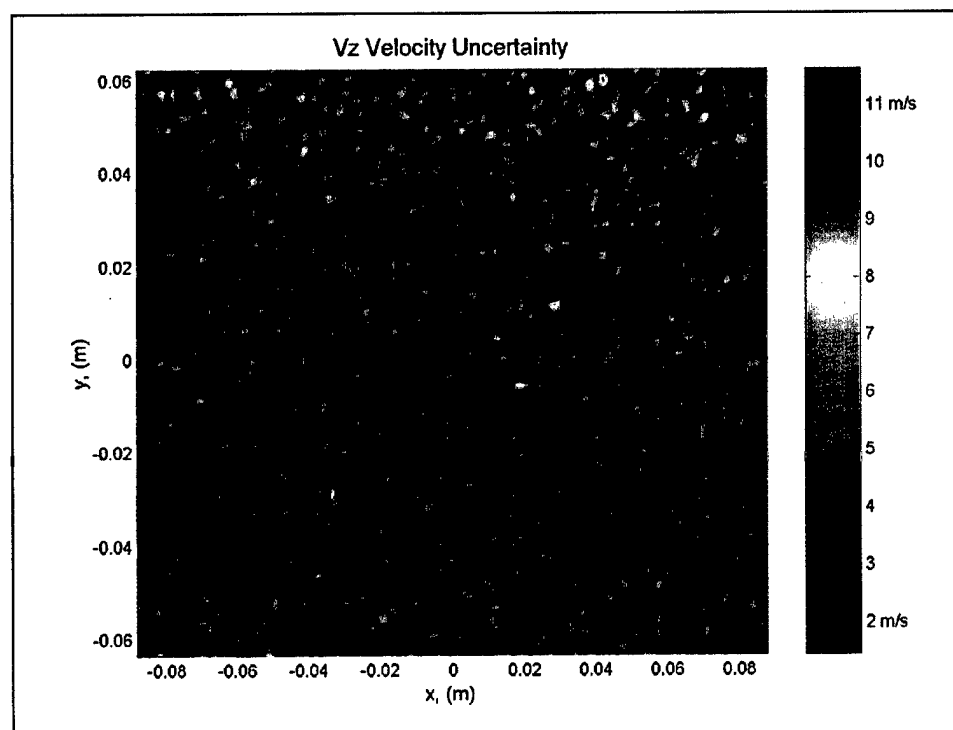*Figure 7.2: Uncertainty of the velocity components in the y direction.*

Figure 7.3: Uncertainty of the velocity components in the z direction.

Figures 7. 4 and 7.5 show the upper and lower bounds for the V_x velocity uncertainties applied to plots of the V_x velocity component measured along the vertical and horizontal centerlines of the calibration wheel. Figures 7.6 and 7.7 show the upper and lower bounds for the V_y velocity uncertainties applied to plots of the V_y velocity component along the vertical and horizontal centerlines of the calibration wheel. Figures 7.8 and 7.9 show the upper and lower bounds for the V_z velocity uncertainties applied to plots of the V_z velocity along the vertical and horizontal centerlines of the calibration wheel.

Figure 7.4: Upper and lower bounds on V_x velocity uncertainty and V_x velocity component along horizontal centerline of calibration wheel.

Figure 7.5: Upper and lower bounds on V_x velocity uncertainty and V_x velocity component along vertical centerline of calibration wheel.

Figure 7.6: Upper and lower bounds on V_y velocity uncertainty and V_y velocity component along horizontal centerline of calibration wheel.

Figure 7.7: Upper and lower bounds on V_y velocity uncertainty and V_y velocity component along vertical centerline of calibration wheel.
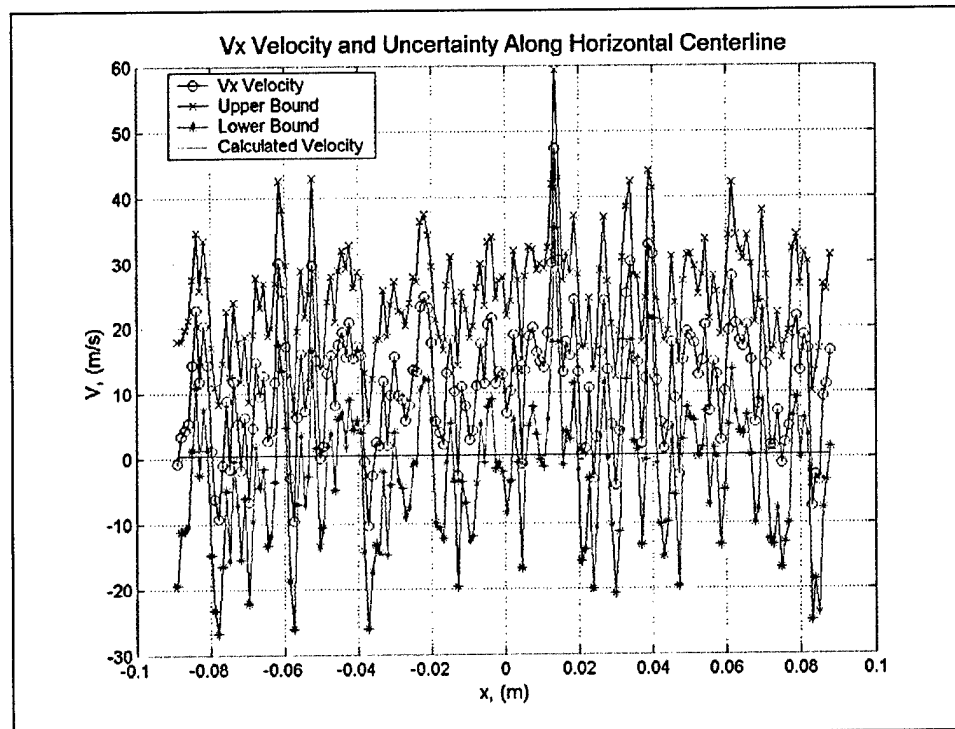

Figure 7.8: Upper and lower bounds on V_z velocity uncertainty and V_z velocity component along horizontal centerline of calibration wheel.
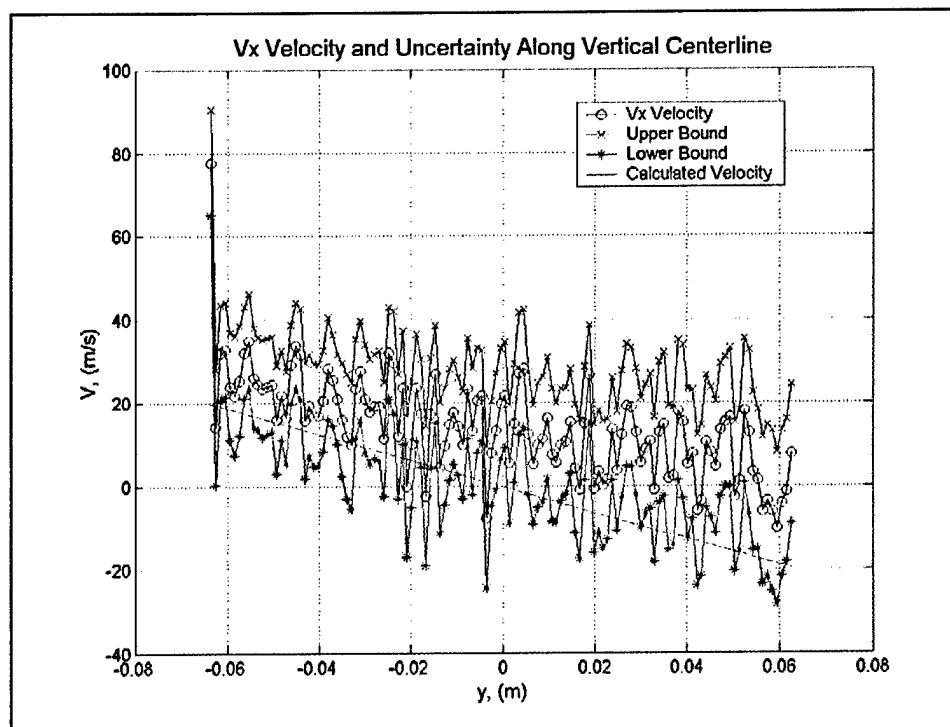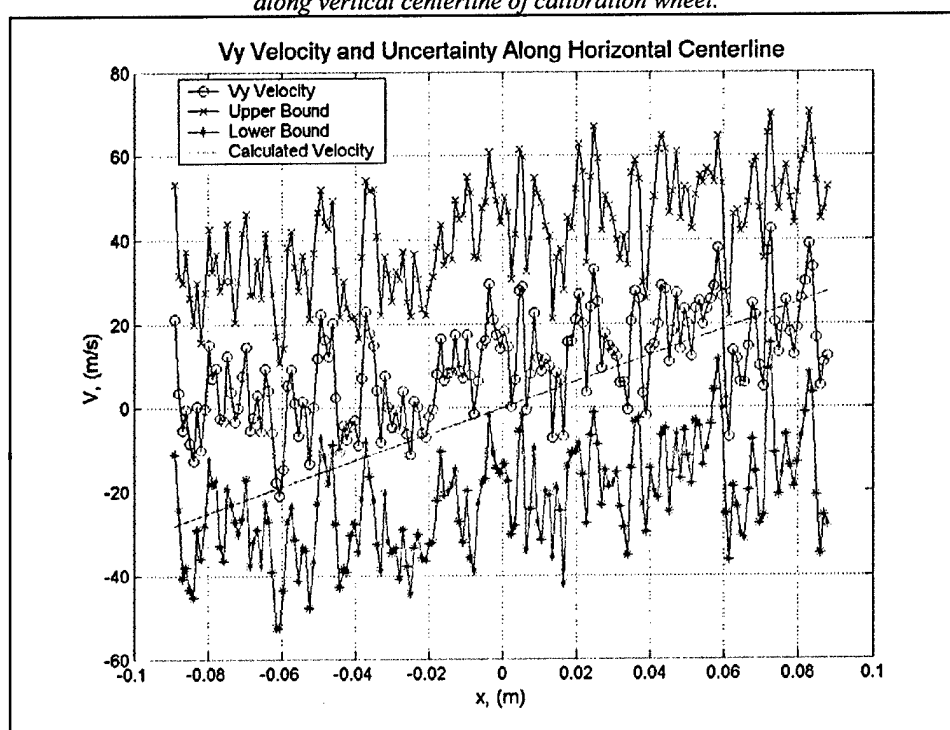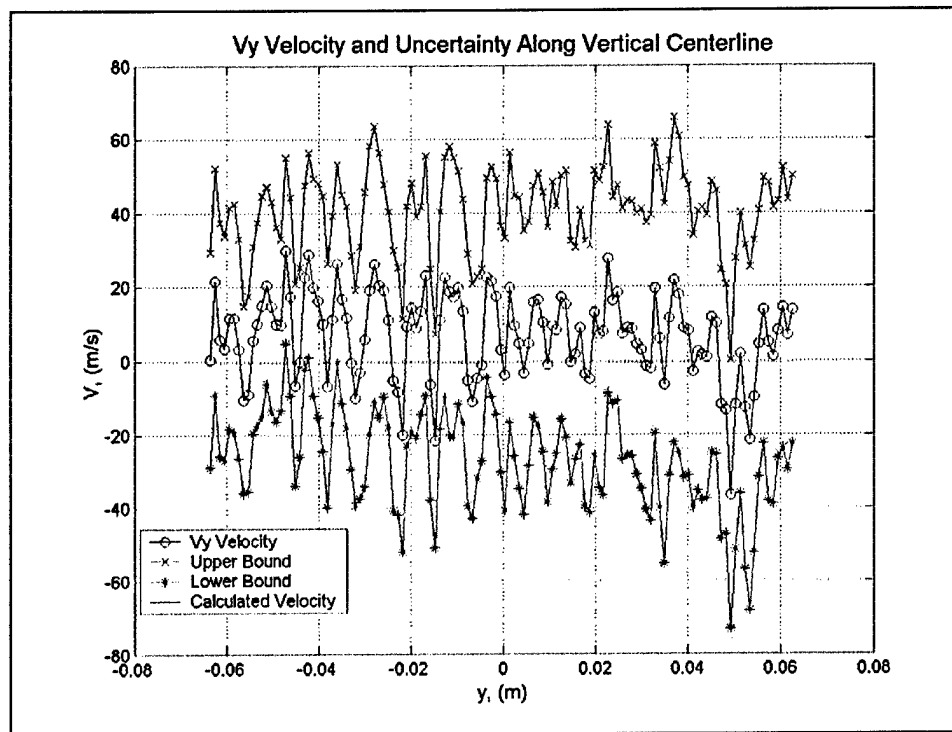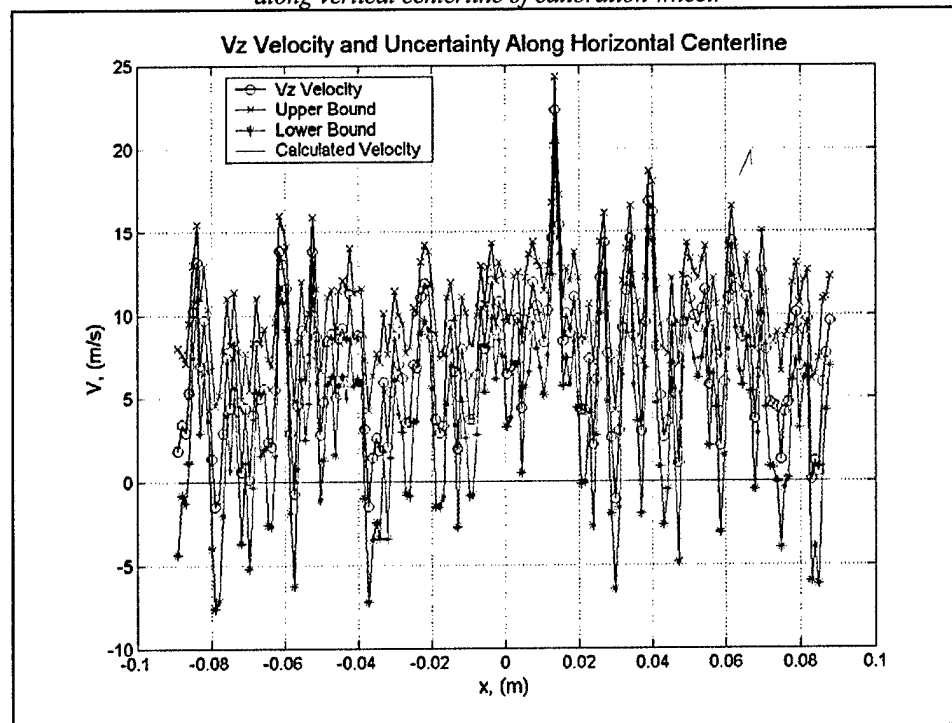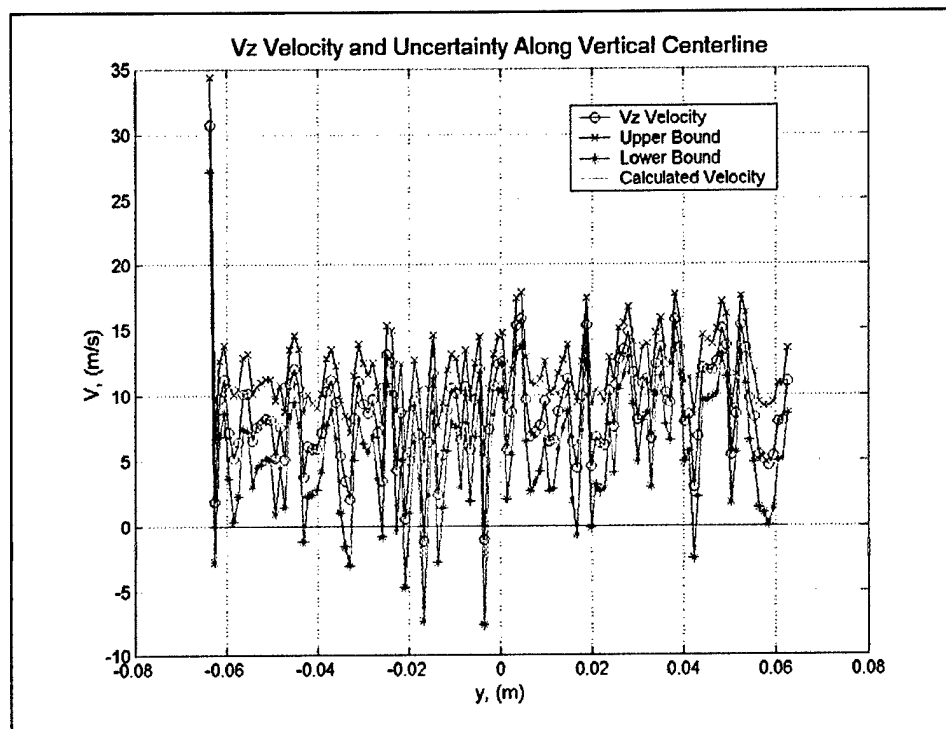
Figure 7.9: Upper and lower bounds on V_z velocity uncertainty and V_z velocity component along vertical centerline of calibration wheel.

7.5 Analysis of Uncertainty Components

An analysis of the calculated values for each term in equation 52 will reveal the largest sources of uncertainty in the measured calibration wheel velocities. Determining the largest sources of uncertainty will provide direction for where improvements can and should be made to the VT DGV system in the future. The average uncertainty for each velocity component will be calculated as part of this analysis.

7.5.1 Optical Frequency Uncertainty

The first step in calculating the average uncertainty of the measured change in optical frequency was to calculate the uncertainties in the transmission ratios TR_i and TR_i^{ref}, as was discussed in sections 7.1.1 and 7.1.2. The average uncertainty values calculated for the transmission ratios in the data area were: $\omega TR_1 = 0.08227$, $\omega TR_2 = 0.09755$, and $\omega TR_3 = 0.04229$. The average uncertainty values calculated for the laser reference transmission ratio from each camera module were: $\omega TR_1^{ref} = 0.01253$, $\omega TR_2^{ref} = 0.01255$, and $\omega TR_3^{ref} = 0.01251$. Next, the partial derivatives of the change in optical frequency with respect to the data area transmission ratios and laser reference

transmission ratios were calculated. The average values calculated for the partial derivatives of the change in optical frequency with respect to the data area transmission ratios were:

$$\frac{\partial \Delta v_1}{\partial TR_1} = 3.6511 \times 10^8 \tag{108}$$

$$\frac{\partial \Delta v_2}{\partial TR_2} = -9.5744 \times 10^7 \tag{109}$$

$$\frac{\partial \Delta v_3}{\partial TR_3} = 3.9646 \times 10^8 \tag{110}$$

The average values calculated for the partial derivatives of the change in optical frequency with respect to the laser reference transmission ratios for each camera module were:

$$\frac{\partial \Delta v_1}{\partial TR_1^{ref}} = 3.1925 \times 10^8 \tag{111}$$

$$\frac{\partial \Delta v_2}{\partial TR_2^{ref}} = -1.4999 \times 10^8 \tag{112}$$

$$\frac{\partial \Delta v_3}{\partial TR_3^{ref}} = 3.8415 \times 10^8 \tag{113}$$

Once the uncertainties for the data area and laser reference transmission ratios and the partial derivatives of the change in optical frequency with respect to the data area and laser reference transmission ratios had been calculated, the uncertainty in the measured change in optical frequency was calculated using equation 54. The following average uncertainty values were obtained: $\omega \Delta v_1 = 3.0304 \times 10^7$, $\omega \Delta v_2 = 9.5273 \times 10^6$, and $\omega \Delta v_3 = 1.7442 \times 10^7$.

Next, the partial derivatives of each velocity component with respect to the change in optical frequency measured by each camera module were calculated. The following average values for these partial derivatives were obtained:

$$\begin{bmatrix} \dfrac{\partial V_x}{\partial \Delta v_1} & \dfrac{\partial V_x}{\partial \Delta v_2} & \dfrac{\partial V_x}{\partial \Delta v_3} \\[2mm] \dfrac{\partial V_y}{\partial \Delta v_1} & \dfrac{\partial V_y}{\partial \Delta v_2} & \dfrac{\partial V_y}{\partial \Delta v_3} \\[2mm] \dfrac{\partial V_z}{\partial \Delta v_1} & \dfrac{\partial V_z}{\partial \Delta v_2} & \dfrac{\partial V_z}{\partial \Delta v_3} \end{bmatrix} = \left(1 \times 10^{-7}\right) \begin{bmatrix} 2.0835 & -7.8582 & 5.7940 \\ -10.241 & 4.3291 & 1.03147 \\ 0.33343 & -3.5265 & 0.20332 \end{bmatrix} \tag{114}$$

Once the average uncertainties in the measured change in optical frequency for each camera module and average values for the partial derivatives of each velocity component with respect to the change in optical frequency measured by each camera module had been calculated, the terms input into equation 52 were calculated. The values for these terms were as follows:

$$\left(\omega \Delta v_1 \cdot \frac{\partial V_x}{\partial \Delta v_1} \right)^2 = 39.865 \tag{115}$$

$$\left(\omega \Delta v_2 \cdot \frac{\partial V_x}{\partial \Delta v_2} \right)^2 = 56.051 \tag{116}$$

$$\left(\omega \Delta v_3 \cdot \frac{\partial V_x}{\partial \Delta v_3} \right)^2 = 102.129 \tag{117}$$

$$\left(\omega \Delta v_1 \cdot \frac{\partial V_y}{\partial \Delta v_1} \right)^2 = 963.129 \tag{118}$$

$$\left(\omega \Delta v_2 \cdot \frac{\partial V_y}{\partial \Delta v_2} \right)^2 = 17.011 \tag{119}$$

$$\left(\omega \Delta v_3 \cdot \frac{\partial V_y}{\partial \Delta v_3} \right)^2 = 3.237 \tag{120}$$

$$\left(\omega \Delta v_1 \cdot \frac{\partial V_z}{\partial \Delta v_1} \right)^2 = 1.021 \tag{121}$$

$$\left(\omega \Delta v_2 \cdot \frac{\partial V_z}{\partial \Delta v_2} \right)^2 = 11.288 \tag{122}$$

$$\left(\omega \Delta v_3 \cdot \frac{\partial V_z}{\partial \Delta v_3} \right)^2 = 0.125 \qquad (123)$$

7.5.2 Wave Number Uncertainty

Next, the wave number uncertainty was calculated using equation 79. As was discussed in section 7.2, the uncertainties of the laser reference transmission ratio for each camera module, ωTR_1^{ref}, ωTR_2^{ref}, and ωTR_3^{ref}, were calculated as part of the procedure used to calculate the uncertainty of the changes in optical frequency Δv_1, Δv_2, and Δv_3. The partial derivatives of wave number with respect to TR_1^{ref}, TR_2^{ref}, and TR_3^{ref} were calculated using equations 80-82. The following values were obtained for these partial derivatives:

$$\frac{\partial WN}{\partial TR_1^{ref}} = 1.0649 \qquad (124)$$

$$\frac{\partial WN}{\partial TR_2^{ref}} = -0.5000 \qquad (125)$$

$$\frac{\partial WN}{\partial TR_3^{ref}} = 1.2814 \qquad (126)$$

The uncertainties of the laser reference transmission ratios for each of the camera modules and the values for the partial derivatives shown in equations 124 through 126 were used to calculate the uncertainty of the wave number. The value calculated for the uncertainty of the wave number was $\omega WN = 2.1779 \times 10^{-2}$.

After the uncertainty of the wave number had been calculated, the partial derivative of each velocity component with respect to the wave number was calculated using equation 84. The calculated values for these partial derivatives were as follows:

$$\frac{\partial V_x}{\partial WN} = 5.9426 \times 10^{-6} \qquad (127)$$

$$\frac{\partial V_y}{\partial WN} = 4.8131 \times 10^{-6} \qquad (128)$$

$$\frac{\partial V_z}{\partial WN} = 5.7329 \times 10^{-6} \qquad (129)$$

Once the uncertainty of the wave number and the partial derivative of each velocity component with respect to the wave number had been calculated, the wave number term in equation 52 was calculated for each velocity component. The calculated values for these terms were:

$$\left(\omega WN \cdot \frac{\partial V_x}{\partial WN}\right)^2 = 1.6751 \times 10^{-14} \qquad (130)$$

$$\left(\omega WN \frac{\partial V_y}{\partial WN}\right)^2 = 1.0988 \times 10^{-14} \qquad (131)$$

$$\left(\omega WN \cdot \frac{\partial V_z}{\partial WN}\right)^2 = 1.5589 \times 10^{-14} \qquad (132)$$

7.5.3 Angular Measurement Uncertainty

The uncertainties in the Euler angles for each camera module and for the Euler angles used to calculate the laser propagation vector were given in sections 7.3.1 and 7.3.2 respectively. All that is needed is to calculate the partial derivatives for the velocity components with respect to each of these Euler angles. The average values calculated for the partial derivatives of each velocity component with respect to the θ_x Euler angles for the camera modules were:

$$\begin{bmatrix} \frac{\partial V_x}{\partial \theta_{x1}} & \frac{\partial V_x}{\partial \theta_{x2}} & \frac{\partial V_x}{\partial \theta_{x3}} \\ \frac{\partial V_y}{\partial \theta_{x1}} & \frac{\partial V_y}{\partial \theta_{x2}} & \frac{\partial V_y}{\partial \theta_{x3}} \\ \frac{\partial V_z}{\partial \theta_{x1}} & \frac{\partial V_z}{\partial \theta_{x2}} & \frac{\partial V_z}{\partial \theta_{x3}} \end{bmatrix} = \begin{bmatrix} 0.7505 & -10.593 & 9.811 \\ -3.698 & 5.836 & 9.297 \\ 0.1201 & -4.754 & 0.3443 \end{bmatrix} \qquad (133)$$

The average values calculated for the partial derivatives of each velocity component with respect to the θ_y Euler angles for the camera modules were:

$$
\begin{bmatrix}
\dfrac{\partial V_x}{\partial \theta_{y1}} & \dfrac{\partial V_x}{\partial \theta_{y2}} & \dfrac{\partial V_x}{\partial \theta_{y3}} \\[2mm]
\dfrac{\partial V_y}{\partial \theta_{y1}} & \dfrac{\partial V_y}{\partial \theta_{y2}} & \dfrac{\partial V_y}{\partial \theta_{y3}} \\[2mm]
\dfrac{\partial V_z}{\partial \theta_{y1}} & \dfrac{\partial V_z}{\partial \theta_{y2}} & \dfrac{\partial V_z}{\partial \theta_{y3}}
\end{bmatrix}
=
\begin{bmatrix}
-4.411 & 8.164 & -15.389 \\
21.682 & -4.498 & -14.581 \\
-0.7059 & 3.664 & -0.5400
\end{bmatrix}
\tag{134}
$$

The average values calculated for the partial derivatives of each velocity component with respect to the Euler angles used to calculate the laser propagation vector were:

$$
\begin{bmatrix}
\dfrac{\partial V_x}{\partial \theta_{xlas}} & \dfrac{\partial V_x}{\partial \theta_{ylas}} \\[2mm]
\dfrac{\partial V_y}{\partial \theta_{xlas}} & \dfrac{\partial V_y}{\partial \theta_{ylas}} \\[2mm]
\dfrac{\partial V_z}{\partial \theta_{xlas}} & \dfrac{\partial V_z}{\partial \theta_{ylas}}
\end{bmatrix}
=
\begin{bmatrix}
0.03061 & -0.05326 \\
-0.6720 & 1.169 \\
-4.754 & 8.272
\end{bmatrix}
\tag{135}
$$

Once the values for all of the partial derivatives were calculated, the angular measurement uncertainty terms in equation 52 were calculated. The average values calculated for the uncertainty terms containing the θ_x Euler angle for each of the camera modules were:

$$
\begin{bmatrix}
\left(\omega\theta_{x1}\cdot\dfrac{\partial V_x}{\partial \theta_{x1}}\right)^2 & \left(\omega\theta_{x2}\cdot\dfrac{\partial V_x}{\partial \theta_{x2}}\right)^2 & \left(\omega\theta_{x3}\cdot\dfrac{\partial V_x}{\partial \theta_{x3}}\right)^2 \\[3mm]
\left(\omega\theta_{x1}\cdot\dfrac{\partial V_y}{\partial \theta_{x1}}\right)^2 & \left(\omega\theta_{x2}\cdot\dfrac{\partial V_y}{\partial \theta_{x2}}\right)^2 & \left(\omega\theta_{x3}\cdot\dfrac{\partial V_y}{\partial \theta_{x3}}\right)^2 \\[3mm]
\left(\omega\theta_{x1}\cdot\dfrac{\partial V_z}{\partial \theta_{x1}}\right)^2 & \left(\omega\theta_{x2}\cdot\dfrac{\partial V_z}{\partial \theta_{x2}}\right)^2 & \left(\omega\theta_{x3}\cdot\dfrac{\partial V_z}{\partial \theta_{x3}}\right)^2
\end{bmatrix}
=
\left(1\times10^{-2}\right)
\begin{bmatrix}
0.009651 & 1.9227 & 1.6493 \\
0.2343 & 0.5836 & 1.4810 \\
0.000247 & 0.3873 & 0.002031
\end{bmatrix}
\tag{136}
$$

The average values calculated for the uncertainty terms containing the θ_y Euler angle for each of the camera modules were:

$$
\begin{bmatrix}
\left(\omega\theta_{y1}\cdot\dfrac{\partial V_x}{\partial\theta_{y1}}\right)^2 & \left(\omega\theta_{y2}\cdot\dfrac{\partial V_x}{\partial\theta_{y2}}\right)^2 & \left(\omega\theta_{y3}\cdot\dfrac{\partial V_x}{\partial\theta_{y3}}\right)^2 \\[2ex]
\left(\omega\theta_{y1}\cdot\dfrac{\partial V_y}{\partial\theta_{y1}}\right)^2 & \left(\omega\theta_{y2}\cdot\dfrac{\partial V_y}{\partial\theta_{y2}}\right)^2 & \left(\omega\theta_{y3}\cdot\dfrac{\partial V_y}{\partial\theta_{y3}}\right)^2 \\[2ex]
\left(\omega\theta_{y1}\cdot\dfrac{\partial V_z}{\partial\theta_{y1}}\right)^2 & \left(\omega\theta_{y2}\cdot\dfrac{\partial V_z}{\partial\theta_{y2}}\right)^2 & \left(\omega\theta_{y3}\cdot\dfrac{\partial V_z}{\partial\theta_{y3}}\right)^2
\end{bmatrix}
= \left(1\times10^{-2}\right)
\begin{bmatrix}
0.3334 & 1.1420 & 4.0579 \\
8.0552 & 0.3467 & 3.6429 \\
0.008538 & 0.2300 & 0.004996
\end{bmatrix}
\qquad (137)
$$

The average values calculated for the uncertainty terms containing the θ_{xlas} and θ_{ylas} Euler angles used to calculate the laser propagation vector were:

$$
\begin{bmatrix}
\left(\omega\theta_{xlas}\cdot\dfrac{\partial V_x}{\partial\theta_{xlas}}\right)^2 & \left(\omega\theta_{yas}\cdot\dfrac{\partial V_x}{\partial\theta_{ylas}}\right)^2 \\[2ex]
\left(\omega\theta_{xlas}\cdot\dfrac{\partial V_y}{\partial\theta_{xlas}}\right)^2 & \left(\omega\theta_{ylas}\cdot\dfrac{\partial V_y}{\partial\theta_{ylas}}\right)^2 \\[2ex]
\left(\omega\theta_{xlas}\cdot\dfrac{\partial V_z}{\partial\theta_{xlas}}\right)^2 & \left(\omega\theta_{ylas}\cdot\dfrac{\partial V_z}{\partial\theta_{ylas}}\right)^2
\end{bmatrix}
= \left(1\times10^{-2}\right)
\begin{bmatrix}
0.000257 & 0.000778 \\
0.1238 & 0.3747 \\
6.1961 & 18.76
\end{bmatrix}
\qquad (138)
$$

7.5.4 Component Contributions to Total Uncertainty

Once the average values for the individual terms in the uncertainty equation given in equation 52 were calculated, these values were used to calculate an average uncertainty for each velocity component. The average values for the uncertainty of each velocity component were: $\omega V_x = 14.076$ m/s, $\omega V_y = 32.743$ m/s, and $\omega V_z = 3.562$ m/s. The average values used in equation 52 were also used to determine how much each term contributed to the total uncertainty of the velocity measurement. Table 7.1 shows a breakdown in terms of percentage, that each term contributed to the total uncertainty for the V_x velocity component. Table 7.2 shows a breakdown in terms of percentage, that each term contributed to the total uncertainty for the V_y velocity component. Table 7.3 shows a breakdown in terms of percentage, that each term contributed to the total uncertainty for the V_z velocity component. Looking at tables 7.1, 7.2, and 7.3, the largest contributors to the total uncertainty of the V_x, V_y, and V_z velocity component are, by far, the changes in optical frequency

measured by the VT DGV system. The other uncertainties in this calculation are miniscule compared to the uncertainties in the measured changes in optical frequency.

Table 7.1: Uncertainty Contribution Percentages for V_x velocity uncertainty.

	ωV_x
Δv_1	20.12086%
Δv_2	28.29034%
Δv_3	51.54705%
WN	0.00000%
θ_{x1}	0.00005%
θ_{x2}	0.00970%
θ_{x3}	0.00832%
θ_{y1}	0.00168%
θ_{y2}	0.00576%
θ_{y3}	0.02048%
θ_{xlas}	0.00005%
θ_{ylas}	0.00005%

Table 7.2: Uncertainty Contribution Percentages for V_y velocity uncertainty.

	ωV_y
Δv_1	89.83588%
Δv_2	1.58670%
Δv_3	0.30193%
WN	0.00000%
θ_{x1}	0.00022%
θ_{x2}	0.00054%
θ_{x3}	0.00138%
θ_{y1}	0.00751%
θ_{y2}	0.00032%
θ_{y3}	0.00340%
θ_{xlas}	0.00001%
θ_{ylas}	0.00001%

Table 7.3: Uncertainty Contribution Percentages
for V_z velocity uncertainty.

	ωV_z
Δv_1	8.04532%
Δv_2	88.94762%
Δv_3	0.98498%
W/N	0.00000%
θ_{x1}	0.00002%
θ_{x2}	0.03052%
θ_{x3}	0.00016%
θ_{y1}	0.00067%
θ_{y2}	0.01812%
θ_{y3}	0.00039%
θ_{xlas}	0.00076%
θ_{ylas}	0.00076%

The results from this uncertainty analysis indicate that future work on the VT DGV system needs to focus on reducing the uncertainties in the measured changes in optical frequency. Looking at the uncertainties of the transmission ratios used to calculate the change in optical frequency for each camera module, found in section 7.5.1, the uncertainties for the transmission ratios in the data area are all over 3.5 times greater than the uncertainties of the laser reference transmission ratios for each camera module, so, the uncertainties for the transmission ratios in the data plane contributed the largest portion to the total uncertainty in the measured changes in optical frequency. The uncertainties in the transmission ratios from the data area were directly affected by the poor performance of the Nd:YAG laser and by the fact that only seven calibration wheel images were reduced. If the laser performance was more stable and if more of the calibration wheel images could have been reduced, this would have significantly reduced the uncertainties from the measured change in optical frequency.

Improving the technique used to measure the laser reference transmission ratio would also help to reduce the uncertainties of the measured changes in optical frequency. The technique used to measure the laser reference transmission ratio can be improved upon by adding a fourth camera to the VT DGV system, and using this camera to monitor the spatial and temporal variations in the laser pulses used to acquire velocity data. This improvement would be two fold. First, it would allow

spatial variations within a given laser pulse to be measured and accounted for. Adding a fourth camera would also increase the number of pixels used to calculate the laser reference transmission ratio, thus reducing the uncertainty of this value.

Chapter 8: Conclusions

Chapter 8 : Conclusions

An existing flow velocity measurement system was modified and tested during this research. The system used a measurement technique referred to as Doppler Global Velocimetry. In this technique, velocities within a planar data area are measured in a single measurement realization. The Doppler Global Velocimetry technique uses a laser to generate a sheet of laser light, cameras to view seed particles passing through the sheet of laser light and an iodine cell which acts as a molecular filter to measure the Doppler shift of the light scattered by the moving particles. The particular system discussed in this research was designed to measure three non-orthogonal velocity components and convert this data into velocity components in a desired coordinate frame. This system used discoveries by previous researchers as well as adapting the technique to the specific requirements needed for the system to operate in the Virginia Tech Stability Wind Tunnel and with the Dynamic Plunge Pitch and Roll (DyPPiR) apparatus.

The following improvements were made to the VT DGV system over the course of this research:

- Iodine cells were converted from a cold finger arrangement to vapor limited
- Malfunctioning 16-bit digital camera was replaced with a new camera
- A new calibration wheel system was designed, calibrated, and used in tests of the VT DGV system
- Improvements were made to the procedure used to measure the Euler angles for each of the camera modules

- Thorough review of data reduction procedure was made and errors were corrected
- New procedure to calculate the unshifted laser optical frequency was implemented
- New procedure to measure the wave number of the laser pulses used to acquire velocity data was developed and implemented

Several hardware problems were encountered during this research. These problems included:
- Nd:YAG laser was damaged while being shipped back to Virginia Tech after receiving service at manufacturer
- Poor performance of the Nd:YAG laser hampered every attempt to acquire iodine cell calibration images and velocity images
- Laser consistently had problems with frequently resetting and with the large changes in the optical frequency occurring over time
- Ice crystals began to form on the imaging surface of one of the three cameras after it had been on for one hour
- Positions of the camera modules moved over time
- Iodine cell calibrations acquired by one of the camera modules were offset compared to the calibrations acquired by the other two modules
- Insufficient seed particle density in the data plane prevented velocity data in the wake of the 6:1 prolate spheroid model from being acquired
- All problems still exist despite attempts to correct them

The following conclusions can be made about the calibration wheel data acquired during this research:
- Only one of the three sets of velocity data was acquired from the calibration wheel was reducible
- The same general trends present in velocities calculated from angular velocities were observed in the reduced calibration wheel data acquired from the VT DGV system
- The magnitudes of the velocities measured by the VT DGV system were generally significantly higher than those calculated from angular velocities.
- Large fluctuations were present in the velocities measured by the VT DGV system
- Poor laser performance and problems with acquired iodine cell calibrations are most likely causes of the bias in magnitudes and large fluctuations observed in the reduced calibration wheel data

- Average uncertainties for the calculated velocity components were: $\omega V_x = 14.076$ m/s, $\omega V_y = 32.743$ m/s, and $\omega V_z = 3.562$ m/s
- Largest sources of uncertainty in the calculated velocities were the changes in optical frequency calculated from the measured transmission ratios

The following suggestions were made to possibly improve the performance of the VT DGV system in the future:

- The hardware problems encountered with the VT DGV system need to be addressed.
- The problems with performance of the Nd:YAG need to be corrected or the laser needs to be replaced.
- The malfunctioning digital camera needs to be replaced.
- Modifications suggested in the paper published by Meyers *et al* in 2001 should be implemented, including adding a fourth camera module to monitor spatial and temporal variations in the laser pulses output by the laser.
- Perform additional tests to determine the best location and method for injecting seed particles into the wind tunnel
- Simplify the setup and repositioning of the system to make it easier to acquire DGV data at different locations along the model being tested.
- New windows, made of optical quality glass, need to be made for firing the laser into the test section of the Virginia Tech Stability Wind Tunnel and for the camera modules to view the data area.
- The windows for firing the laser into the test section will need to be made to withstand the high power output of the laser. Finally a method to measure the direction of laser propagation needs to be developed.

The VT DGV system has the potential to become a successful and very useful measurement tool. The value of having a system capable of instantaneously measuring a plane of velocities is obvious. The Doppler Global Velocimetry technique is still a fairly new technique and improvements continue to be made. While the results of this research were admittedly less than satisfactory, significant improvements were made to the system and a better understanding of what needs to be done to improve the performance of the system was gained.

References

References

1. Anderson, John D., A History of Aerodynamics, New York: Cambridge University Press, 1997 pp. 16,17,19-27,37-40.

2. Barlow, Jewel B., Rae, William H., and Pope, Alan, Low-Speed Wind Tunnel Testing, 3rd ed., New York: John Wiley and Sons, 1999, pp. 145-146, 154-155, 164-169.

3. Elder, Andreas, Durst, Bodo, Jordan, Martin, "Laser-Doppler Velocimetry – Principle and Application to Turbulence Measurements", Optical Measurements, Techniques and Applications, 2nd ed., Berlin: Springer, 2001, p. 113.

4. Samimy, M and Wernet, M. P., "Review of Planar Multiple-Component Velocimetry in High Speed Flows", AIAA Journal, Vol38 No 4, April 2000, pp. 554.

5. McKenzie, R. L., "Measurement Capabilities of Planar Doppler Velocimetry Using Pulsed Lasers", AIAA 95-0297, AIAA 33rd Aerospace Sciences Meeting and Exhibit, January 1995, Reno NV, p. 3.

6. Meyers, James F, and Komine, Hiroshi, "Doppler Global Velocimetry A New Way to Look at Velocity" ASME Fourth International Conference on Laser Anemometry, August 1991, Cleveland, OH, p. 4.

7. McKenzie, R. L., "Measurement Capabilities of Planar Doppler Velocimetry Using Pulsed Lasers", AIAA 95-0297, AIAA 33rd Aerospace Sciences Meeting and Exhibit, January 1995, Reno NV, p. 11.

8. McKenzie, R. L., "Measurement Capabilities of Planar Doppler Velocimetry Using Pulsed Lasers", AIAA 95-0297, AIAA 33rd Aerospace Sciences Meeting and Exhibit, January 1995, Reno NV, p. 2.

9. Meyers, James F., Lee, Joseph W, and Schwartz, Richard J., "Characterization of measurement error sources in Doppler Global Velocimetry", Measurement Science and Technology, Vol. 12, No 4, Institute of Physics Publishing, United Kingdom, 2001, p. 6.

10. Kruppa, Boris, Strube, Gernoth, and Gerlach, Christof, "Light Scattering", Optical Measurements, Techniques and Applications, 2nd ed., Berlin: Springer, 2001, pp. 100-101.

11. University of Illinois at Urbana-Champaign, Department of Atmospheric Sciences, WW2010 Project, http://ww2010.atmos.uiuc.edu/%28Gh%29/wwhlpr/mie_scattering.rxml?hret=/indexlist.rxml.

12. Kruppa, Boris, Strube, Gernoth, and Gerlach, Christof, "Light Scattering", Optical Measurements, Techniques and Applications, 2nd ed., Berlin: Springer, 2001, pp. 103-104.

13. Kruppa, Boris, Strube, Gernoth, and Gerlach, Christof, "Light Scattering", Optical Measurements, Techniques and Applications, 2nd ed., Berlin: Springer, 2001, pp. 98.

14. Komine, H, Brosnan, S.J., Litton, A.B., and Stappaerts, E.A., "Real-Time, Doppler Global Velocimetry", AIAA 91-0337, 29th Aerospace Sciences Meeting, January 2001,Reno, NV, p. 1.

15. Meyers, James, F. and Komine, Hiroshi, "Doppler Global Velocimetry, A New Way to Look at Velocity", ASME Fourth International Conference on Laser Anemometry, August 1991, Cleveland, OH, pp. 6, 7.

16. Meyers, James, F., "Doppler Global Velocimerty, The Next Generation?", AIAA-92-3897, AIAA 17th Aerospace Ground Testing Conference, July 1992, Nashville, TN, pp. 4, 5.

17. Meyers, James, F., "Development of Doppler Global Velocimetry for Wind Tunnel Testing", AIAA 94-2582, AIAA 18th Ground Testing Conference, Colorodo Springs, CO, June 1994, p. 7.

18. McKenzie, R. L., "Measurement Capabilities of Planar Doppler Velocimetry Using Pulsed Lasers", AIAA 95-0297, AIAA 33rd Aerospace Sciences Meeting and Exhibit, January 1995, Reno NV, p. 3, 4, 17.

19. McKenzie, R. L., "Planar Doppler Velocimetry for Large-Scale Wind Tunnel Applications", Paper No. 9 of the AGARD Fluid Dynamics Panel 81st Meeting and Symposium on Advanced Aerodynamic Measurement Technology, September 1997, Seattle, WA, pp. 9-3, 9-6, 9-12.

20. Jones, Troy, B, Development and Testing of the Virginia Tech Doppler Global Velocimeter (DGV), M. S. Thesis, Virginia Polytechnic Institute and State University, 2000.

21. Meyers, James F., Lee, Joseph W, and Schwartz, Richard J., "Characterization of measurement error sources in Doppler Global Velocimetry", Measurement Science and Technology, Vol. 12, No 4, Institute of Physics Publishing, United Kingdom, 2001, p. 4.

22. Meyers, James F., Lee, Joseph W, and Schwartz, Richard J., "Characterization of measurement error sources in Doppler Global Velocimetry", Measurement Science and Technology, Vol. 12, No 4, Institute of Physics Publishing, United Kingdom, 2001, p. 5.

23. Meyers, James F., Lee, Joseph W, and Schwartz, Richard J., "Characterization of measurement error sources in Doppler Global Velocimetry", Measurement Science and Technology, Vol. 12, No 4, Institute of Physics Publishing, United Kingdom, 2001, p. 5.

24. Meyers, James F., Lee, Joseph W, and Schwartz, Richard J., "Characterization of measurement error sources in Doppler Global Velocimetry", Measurement Science and Technology, Vol. 12, No 4, Institute of Physics Publishing, United Kingdom, 2001, p. 5.

25. Meyers, James F., Lee, Joseph W, and Schwartz, Richard J., "Characterization of measurement error sources in Doppler Global Velocimetry", Measurement Science and Technology, Vol. 12, No 4, Institute of Physics Publishing, United Kingdom, 2001, p. 6-7.

26. Meyers, James F., Lee, Joseph W, and Schwartz, Richard J., "Characterization of measurement error sources in Doppler Global Velocimetry", Measurement Science and Technology, Vol. 12, No 4, Institute of Physics Publishing, United Kingdom, 2001, p. 8-11.

27. Forkey, J. N., Lempert, W. R., Bogdonoff, S. M., Miles, R. B., and Russell, G., "Volumetric Imaging of Supersonic Boundary Layers using Filtered Rayleigh Scattering Background Suppression", AIAA 94-0491, AIAA 32rd Aerospace Sciences Meeting and Exhibit January 1994, Reno NV, p. 2.

28. Elliott, Gregory S., Boguszko, Martin, and Carter, Campbell, "Filtered Rayleigh Scattering: Toward Multiple Property Measurement (Invited)", AIAA 2001-0301, AIAA 39th Aerospace Sciences Meeting and Exhibit January 2001, Reno NV, p. 2 – 6.

29. Elliott, Gregory S., Boguszko, Martin, and Carter, Campbell, "Filtered Rayleigh Scattering: Toward Multiple Property Measurement (Invited)", AIAA 2001-0301, AIAA 39th Aerospace Sciences Meeting and Exhibit January 2001, Reno NV.

30. Miles, R. B. and Lempert, W.R., "Flow Diagnostics in unseeded air" AIAA Paper 90-0624, 1990

31. Forkey, J. N., Development and demonstration of Filtered Rayleigh Scattering – A laser based flow diagnostic for planar measurement of velocity, temperature and pressure., PhD Dissertation, Princeton University, New Jersey, 1996.

32. Forkey, J. N., Finkelstein N. D. Lempert, W. R., and Miles, R. B., "Demonstration and characterization of filtered Rayeigh scattering for planar velocity measurements." AIAA Journal 1996; 34: 442-448.

33. Miles, R. B., Forkey, J. N., and Lempert, W.R., "Rayleigh Scattering measurements in supersonic/hypersonic facilities" AIAA Paper 92-3894, 1992.

34. Meyers, James F., Lee, Joseph W, and Schwartz, Richard J., "Characterization of measurement error sources in Doppler Global Velocimetry", Measurement Science and Technology, Vol. 12, No 4, Institute of Physics Publishing, United Kingdom, 2001, p. 3.

35. Jones, Troy, B, Development and Testing of the Virginia Tech Doppler Global Velocimeter (DGV), M. S. Thesis, Virginia Polytechnic Institute and State University, 2000, pp. 15-16.

36. Spectra-Physics, Pulsed Nd:YAG Lasers User's Manual GCR Series.

37. Spectra-Physics, Model6300/Model 6350 Instruction Manual.

38. Herrman, Joachim, and Wilhelmi, Bernd, Lasers for Ultrashort Light Pulses, Amsterdam: North-Holland, 1987.

39. Jones, Troy, B, Development and Testing of the Virginia Tech Doppler Global Velocimeter (DGV), M. S. Thesis, Virginia Polytechnic Institute and State University, 2000, p. 15.

40. Jones, Troy, B, Development and Testing of the Virginia Tech Doppler Global Velocimeter (DGV), M. S. Thesis, Virginia Polytechnic Institute and State University, 2000, pp. 14-15.

41. Meyers, James F., Lee, Joseph W, and Schwartz, Richard J., "Characterization of measurement error sources in Doppler Global Velocimetry", Measurement Science and Technology, Vol. 12, No 4, Institute of Physics Publishing, United Kingdom, 2001.

42. McKenzie, R. L., "Measurement Capabilities of Planar Doppler Velocimetry Using Pulsed Lasers", AIAA 95-0297, AIAA 33rd Aerospace Sciences Meeting and Exhibit, January 1995, Reno NV, p. 13.

43. Meyers, James, F. and Komine, Hiroshi, "Doppler Global Velocimetry, A New Way to Look at Velocity", ASME Fourth International Conference on Laser Anemometry, August 1991, Cleveland, OH, pp. 7.

44. McKenzie, R. L. and Reinath, M. S., "Planar Doppler Velocimetry Capabilities at Low Speeds and its Application to a Full-Scale Rotor Flow (Invited)", AIAA 2000-2292, 21st AIAA Aerodynamic Measurement Technology and Ground Testing Conference, June 2000, Denver CO, p.15.

45. Mosedale, A. D., and Elliot, G. S., "Planar Doppler Velocimetry in a Large-Scale Facility", AIAA Journal 2000; 38: 1015.

46. Meyers, J. F., Fleming, G. A., Gorton, S. A., and Berry, J. D., "Instantaneous Doppler Global Velocimetry Measurements of a Rotor Wake: Lessons Learned", 9th International Symposium on Applications of Laser Technologies to Fluid Mechanics, July 1998, Lisbon, Portugal, p. 252.

47. McKenzie, R. L., "Measurement Capabilities of Planar Doppler Velocimetry Using Pulsed Lasers", AIAA 95-0297, AIAA 33rd Aerospace Sciences Meeting and Exhibit, January 1995, Reno NV, p. 13.

48. Meyers, James F., Lee, Joseph W, and Schwartz, Richard J., "Characterization of measurement error sources in Doppler Global Velocimetry", Measurement Science and Technology, Vol. 12, No 4, Institute of Physics Publishing, United Kingdom, 2001, p. 9.

49. Meyers, James, F., Personal Communication, April 2001

50. Corona Integrated Technologies Inc, "Vicount Operating Instructions"

51. Corona Integrated Technologies Inc, "Vicount Smoke Density Adjustment"

52. Jones, Troy, B, Development and Testing of the Virginia Tech Doppler Global Velocimeter (DGV), M.S. Thesis, Virginia Polytechnic Institute and State University, 2000, pp. 62.

53. Meyers, James, F. and Komine, Hiroshi, "Doppler Global Velocimetry, A New Way to Look at Velocity", ASME Fourth International Conference on Laser Anemometry, August 1991, Cleveland, OH, pp. 4-5.

54. Meyers, J. F., Fleming, G. A., Gorton, S. A., and Berry, J. D., "Instantaneous Doppler Global Velocimetry Measurements of a Rotor Wake: Lessons Learned", 9th International Symposium on Applications of Laser Technologies to Fluid Mechanics, July 1998, Lisbon, Portugal, p. 247.

55. McKenzie, R. L., "Measurement Capabilities of Planar Doppler Velocimetry Using Pulsed Lasers", AIAA 95-0297, AIAA 33rd Aerospace Sciences Meeting and Exhibit, January 1995, Reno NV, p. 17.

56. Meyers, James F., Lee, Joseph W, and Schwartz, Richard J., "Characterization of measurement error sources in Doppler Global Velocimetry", Measurement Science and Technology, Vol. 12, No 4, Institute of Physics Publishing, United Kingdom, 2001, p. 10.

57. Price Quote Roper Scientific March 2001

58. Price Quote Subtechnique Inc. June 2001

59. Meyers, James F., Lee, Joseph W, and Schwartz, Richard J., "Characterization of measurement error sources in Doppler Global Velocimetry", Measurement Science and Technology, Vol. 12, No 4, Institute of Physics Publishing, United Kingdom, 2001, p. 11.

60. Samimy, M and Wernet, M. P., "Review of Planar Multiple-Component Velocimetry in High Speed Flows", AIAA Journal, Vol38 No 4, April 2000, pp. 557-558.

61. Meyers, James F., Lee, Joseph W, and Schwartz, Richard J., "Characterization of measurement error sources in Doppler Global Velocimetry", Measurement Science and Technology, Vol. 12, No 4, Institute of Physics Publishing, United Kingdom, 2001, p. 4.

62. Samimy, M and Wernet, M. P., "Review of Planar Multiple-Component Velocimetry in High Speed Flows", AIAA Journal, Vol38 No 4, April 2000, pp. 557.

63. Elliott, Gregory S., Boguszko, Martin, and Carter, Campbell, "Filtered Rayleigh Scattering: Toward Multiple Property Measurement (Invited)", AIAA 2001-0301, AIAA 39th Aerospace Sciences Meeting and Exhibit January 2001, Reno NV, pp. 4-5.

64. Meyers, James F., Lee, Joseph W, and Schwartz, Richard J., "Characterization of measurement error sources in Doppler Global Velocimetry", Measurement Science and Technology, Vol. 12, No 4, Institute of Physics Publishing, United Kingdom, 2001, p. 4.

65. Meyers, James F., Lee, Joseph W, and Schwartz, Richard J., "Characterization of measurement error sources in Doppler Global Velocimetry", Measurement Science and Technology, Vol. 12, No 4, Institute of Physics Publishing, United Kingdom, 2001, p. 4.

66. Jones, Troy, B, Development and Testing of the Virginia Tech Doppler Global Velocimeter (DGV), M. S. Thesis, Virginia Polytechnic Institute and State University, 2000, pp. 16.

67. Jones, Troy, B, Development and Testing of the Virginia Tech Doppler Global Velocimeter (DGV), M. S. Thesis, Virginia Polytechnic Institute and State University, 2000, pp. 17.

68. Meyers, James F., Lee, Joseph W, and Schwartz, Richard J., "Characterization of measurement error sources in Doppler Global Velocimetry", Measurement Science and Technology, Vol. 12, No 4, Institute of Physics Publishing, United Kingdom, 2001, p. 2.

69. James F. Meyers, Personal Communication, August 2001

70. Jones, Troy, B, Development and Testing of the Virginia Tech Doppler Global Velocimeter (DGV), M. S. Thesis, Virginia Polytechnic Institute and State University, 2000, p. 24

71. Jones, Troy, B, Development and Testing of the Virginia Tech Doppler Global Velocimeter (DGV), M. S. Thesis, Virginia Polytechnic Institute and State University, 2000, p. 24

72. Forkey, J.N., Lempert, W. R., and Miles, R. B., "Corrected and calibrated I2 absorption model at frequency-doubled Nd:YAG laser wavelengths", Applied Optics, vol. 36, September 1997.

73. Forkey, J.N., Lempert, W. R., and Miles, R. B., "Corrected and calibrated I2 absorption model at frequency-doubled Nd:YAG laser wavelengths", Applied Optics, vol. 36, September 1997.

74. "Camera Calibration Toolbox for MATLAB" Web Site, http://newbologna.vision.caltech.edu/bouguetj/calib_doc/index.html

75. "Camera Calibration Toolbox for MATLAB" Web Site, http://newbologna.vision.caltech.edu/bouguetj/calib_doc/index.html

76. Simpson, R L., "Unsteady Aero/Hydrodynamics For Maneuvering Aircraft, Submarines, And Automobiles: Dynamic Wind Tunnel Testing In The Aerospace And Ocean Engineering Department At Virginia Tech: New Test Methodologies And Facilities", Report VPI-AOE-253, 1997, p. 1.

77. Choi, K., and Simpson, R. L., "Some Mean Velocity, Turbulence, and Unsteadiness Characteristics of the VPI &SU Stability Wind Tunnel", Report VPI-AOE-161, 1987.

78. Chesnakas, Christopher, J. Simpson, Roger, L., and Madden, Michael, M., "Three-Dimensional Velocity Measurements on a 6:1 Prolate Spheroid at 10° Angle of Attack", Report VPI-AOE-202, 1994, p. 2.

79. Chesnakas, Christopher, J. Simpson, Roger, L., and Madden, Michael, M., "Three-Dimensional Velocity Measurements on a 6:1 Prolate Spheroid at 10° Angle of Attack", Report VPI-AOE-202, 1994, p. 2.

80. "Camera Calibration Toolbox for MATLAB" Web Site, http://newbologna.vision.caltech.edu/bouguetj/calib_doc/index.html

81. Jones, Troy, B, Development and Testing of the Virginia Tech Doppler Global Velocimeter (DGV), M. S. Thesis, Virginia Polytechnic Institute and State University, 2000, pp. 27 - 28.

82. Jones, Troy, B, Development and Testing of the Virginia Tech Doppler Global Velocimeter (DGV), M. S. Thesis, Virginia Polytechnic Institute and State University, 2000, pp. 28 - 29.

83. "Camera Calibration Toolbox for MATLAB" Web Site, http://newbologna.vision.caltech.edu/bouguetj/calib_doc/index.html

84. Meyers, James, F., Personal Communication, August 2001.

85. Meyers, J., F., "Evolution of Doppler Global Velocimetry Data Processing", 8th International Symposium on Applications of Laser Technologies to Fluid Mechanics, July 1996, Lisbon, Portugal.

86. McKenzie, R. L., "Measurement Capabilities of Planar Doppler Velocimetry Using Pulsed Lasers", AIAA 95-0297, AIAA 33rd Aerospace Sciences Meeting and Exhibit, January 1995, Reno NV.

87. McKenzie, R. L., "Planar Doppler Velocimetry for Large-Scale Wind Tunnel Applications", Paper No. 9 of the AGARD Fluid Dynamics Panel 81st Meeting and Symposium on Advanced Aerodynamic Measurement Technology, September 1997, Seattle, WA.

88. Meyers, James F., Lee, Joseph W, and Schwartz, Richard J., "Characterization of measurement error sources in Doppler Global Velocimetry", Measurement Science and Technology, Vol. 12, No 4, Institute of Physics Publishing, United Kingdom, 2001.

89. Forkey, J.N., Lempert, W. R., and Miles, R. B., "Corrected and calibrated I2 absorption model at frequency-doubled Nd:YAG laser wavelengths", Applied Optics, vol. 36, September 1997.

90. Jones, Troy, B, Development and Testing of the Virginia Tech Doppler Global Velocimeter (DGV), M. S. Thesis, Virginia Polytechnic Institute and State University, 2000, pp. 33-34.

91. "Camera Calibration Toolbox for MATLAB" Web Site, http://newbologna.vision.caltech.edu/bouguetj/calib_doc/index.html

92. Jones, Troy, B, <u>Development and Testing of the Virginia Tech Doppler Global Velocimeter (DGV)</u>, M. S. Thesis, Virginia Polytechnic Institute and State University, 2000, pp. 30.

93. McKenzie, R. L., "Planar Doppler Velocimetry for Large-Scale Wind Tunnel Applications", Paper No. 9 of the AGARD Fluid Dynamics Panel 81st Meeting and Symposium on Advanced Aerodynamic Measurement Technology, September 1997, Seattle, WA, pp. 9-3, 9-6, 9-12.

94. Jones, Troy, B, <u>Development and Testing of the Virginia Tech Doppler Global Velocimeter (DGV)</u>, M. S. Thesis, Virginia Polytechnic Institute and State University, 2000, pp. 30.

95. Lindley, C., <u>Practical Image Processing in C</u>, New York, John Wiley and Sons, 1991.

96. McKenzie, R. L., "Planar Doppler Velocimetry for Large-Scale Wind Tunnel Applications", Paper No. 9 of the AGARD Fluid Dynamics Panel 81st Meeting and Symposium on Advanced Aerodynamic Measurement Technology, September 1997, Seattle, WA, pp. 9-3, 9-6, 9-12.

97. Jones, Troy, B, <u>Development and Testing of the Virginia Tech Doppler Global Velocimeter (DGV)</u>, M. S. Thesis, Virginia Polytechnic Institute and State University, 2000, p. 46

98. Jones, Troy, B, <u>Development and Testing of the Virginia Tech Doppler Global Velocimeter (DGV)</u>, M. S. Thesis, Virginia Polytechnic Institute and State University, 2000, p. 50

99. Spectra-Physics, <u>Model6300/Model 6350 Instruction Manual</u>, pp. 4-10 to 4.11, 4-12 to 4-14.

100. Coe, Michael, Personal Communication, December 2002, Spectra-Physics Repair Engineer.

101. Spectra-Physics, <u>Model6300/Model 6350 Instruction Manual</u>, pp. 4-10 to 4.11, 4-12 to 4-14.

102. Meyers, James F., Lee, Joseph W, and Schwartz, Richard J., "Characterization of measurement error sources in Doppler Global Velocimetry", <u>Measurement Science and Technology</u>, Vol. 12, No 4, Institute of Physics Publishing, United Kingdom, 2001, p. 7

103. Coe, Michael, Personal Communication, December 2002, Spectra-Physics Repair Engineer.

104. Meyers, J. F., Fleming, G. A., Gorton, S. A., and Berry, J. D., "Instantaneous Doppler Global Velocimetry Measurements of a Rotor Wake: Lessons Learned", 9th International Symposium on Applications of Laser Technologies to Fluid Mechanics, July 1998, Lisbon, Portugal, p. 251.

105. Jones, Troy, B, <u>Development and Testing of the Virginia Tech Doppler Global Velocimeter (DGV)</u>, M.S Thesis, Virginia Polytechnic Institute and State University, 2000, pp. 47.

106. Meyers, James F., Lee, Joseph W, and Schwartz, Richard J., "Characterization of measurement error sources in Doppler Global Velocimetry", <u>Measurement Science and Technology</u>, Vol. 12, No 4, Institute of Physics Publishing, United Kingdom, 2001.

107. Jones, Troy, B, <u>Development and Testing of the Virginia Tech Doppler Global Velocimeter (DGV)</u>, M. S. Thesis, Virginia Polytechnic Institute and State University, 2000, pp. 96-97.

108. Jones, Troy, B, <u>Development and Testing of the Virginia Tech Doppler Global Velocimeter (DGV)</u>, M. S. Thesis, Virginia Polytechnic Institute and State University, 2000, pp. 94-107.

109. Jones, Troy, B, <u>Development and Testing of the Virginia Tech Doppler Global Velocimeter (DGV)</u>, M. S. Thesis, Virginia Polytechnic Institute and State University, 2000, pp. 96-97.

110. Holman, J., <u>Experimental Methods for Engineers</u>, 6th ed., New York: McGraw-Hill, 1994, pp. 92-93.

111. Jones, Troy, B, <u>Development and Testing of the Virginia Tech Doppler Global Velocimeter (DGV)</u>, M. S. Thesis, Virginia Polytechnic Institute and State University, 2000, pp. 99.

112. Jones, Troy, B, <u>Development and Testing of the Virginia Tech Doppler Global Velocimeter (DGV)</u>, M. S. Thesis, Virginia Polytechnic Institute and State University, 2000, pp. 99.

113. Jones, Troy, B, <u>Development and Testing of the Virginia Tech Doppler Global Velocimeter (DGV)</u>, M. S. Thesis, Virginia Polytechnic Institute and State University, 2000, pp. 99.

Appendix A

Appendix A

The seven images to pass the transmission ratio and Q-switch build up time filters were images 14, 15, 24, 36, 38, 42, and 48. The plots contained in this appendix are contour plots of the x, y, and z velocity components for each of the images reduced.
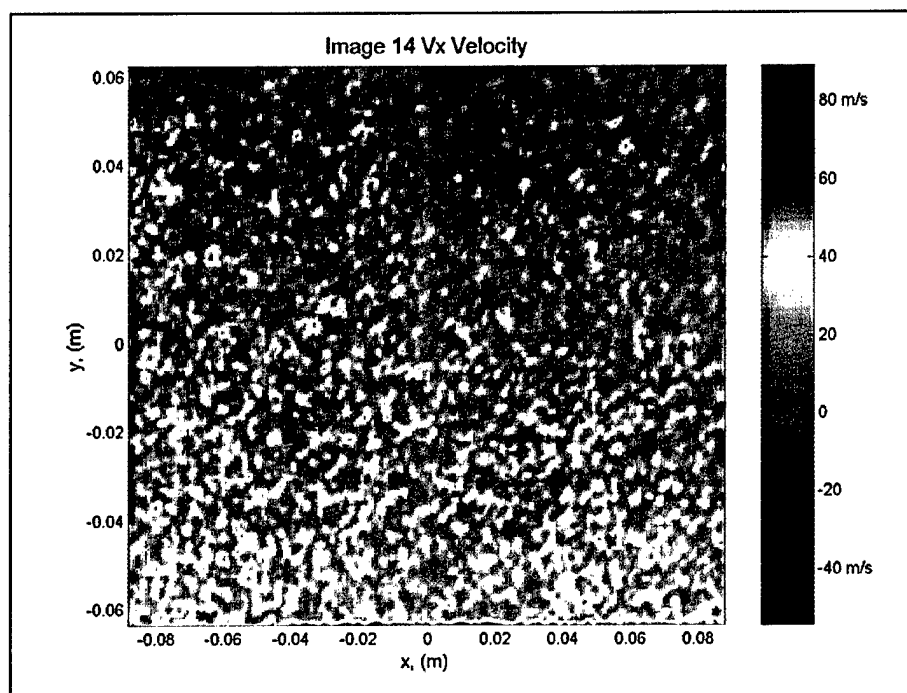
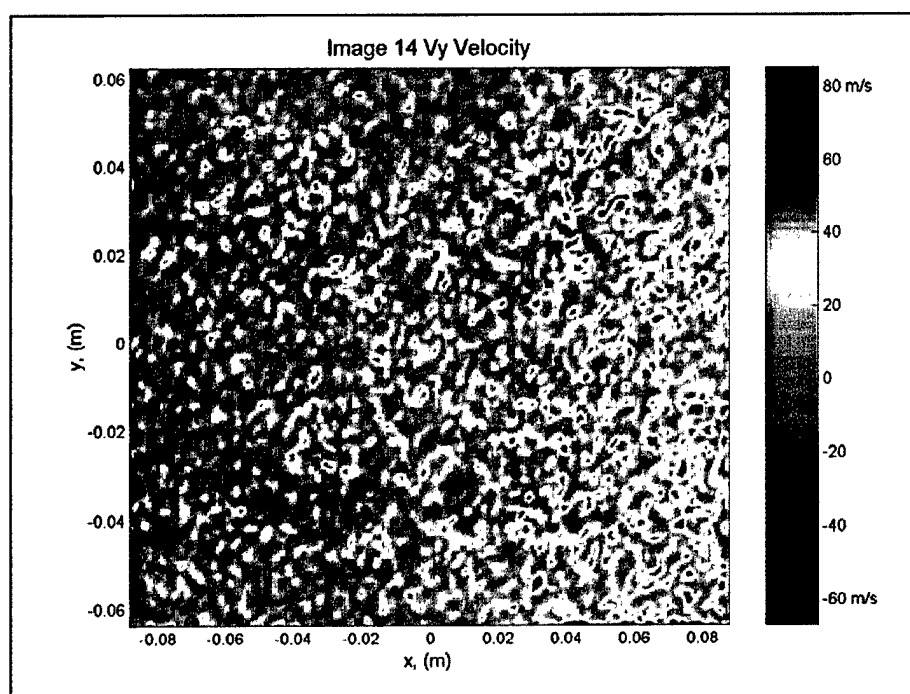*Figure A.1: Contour plot of x velocity components calculated from image 14.*

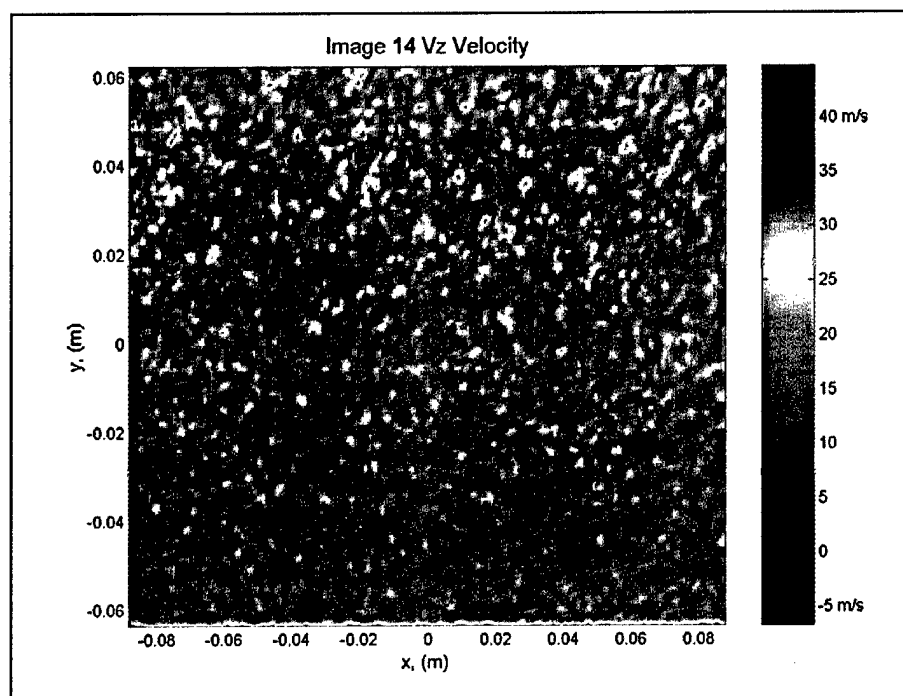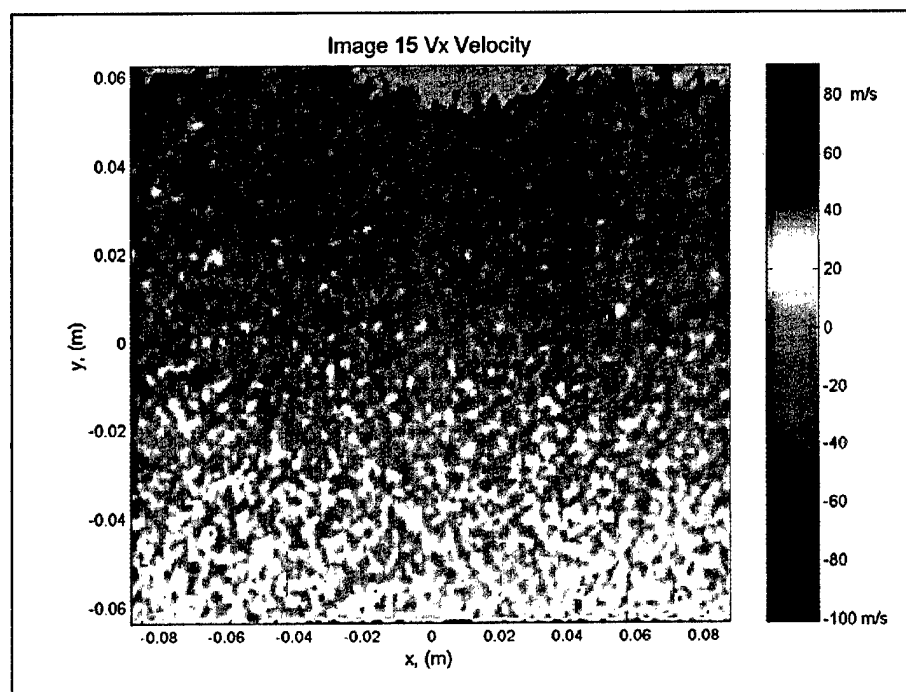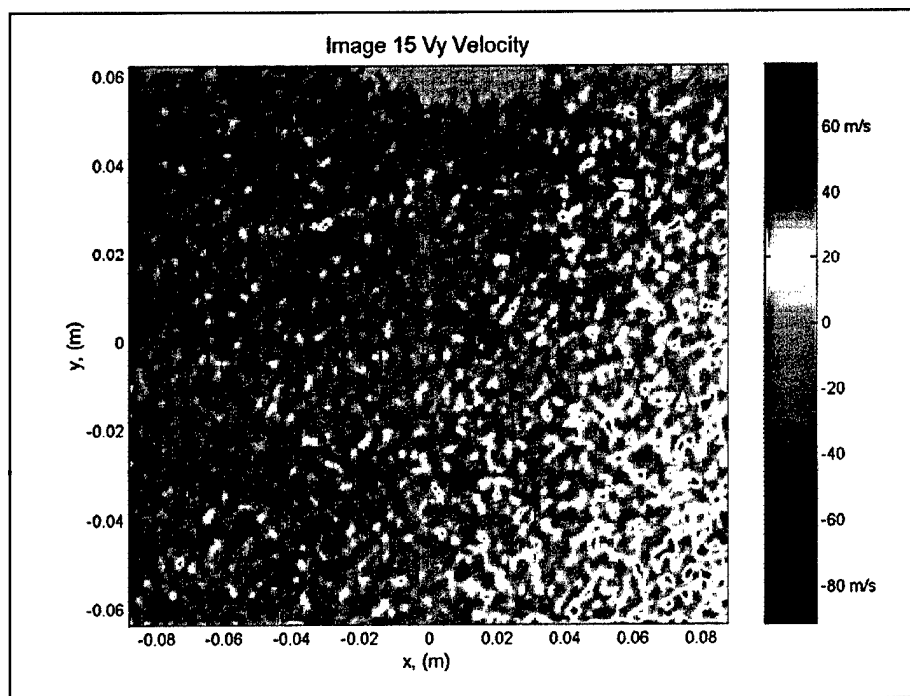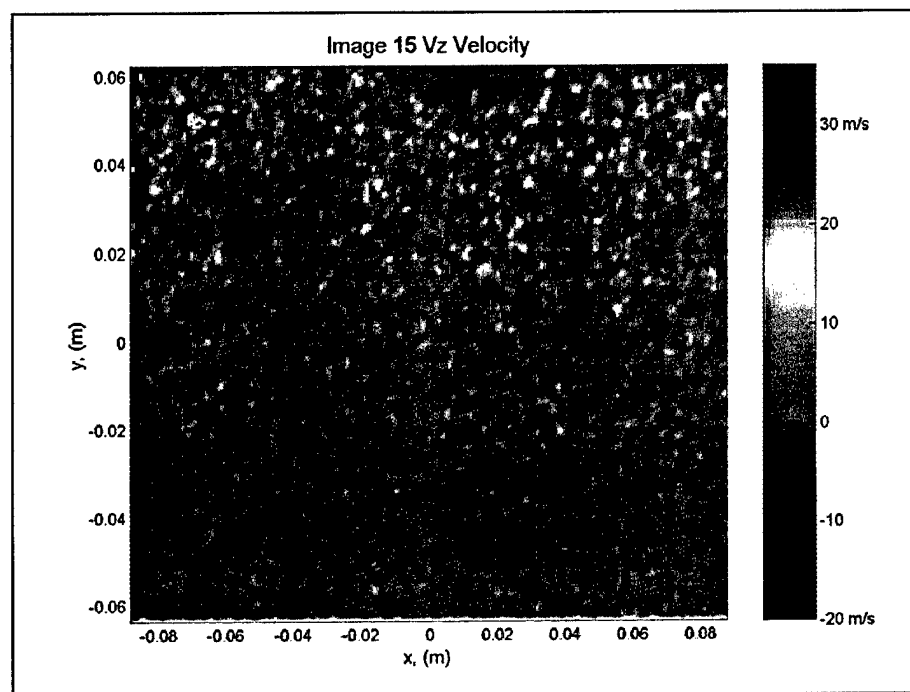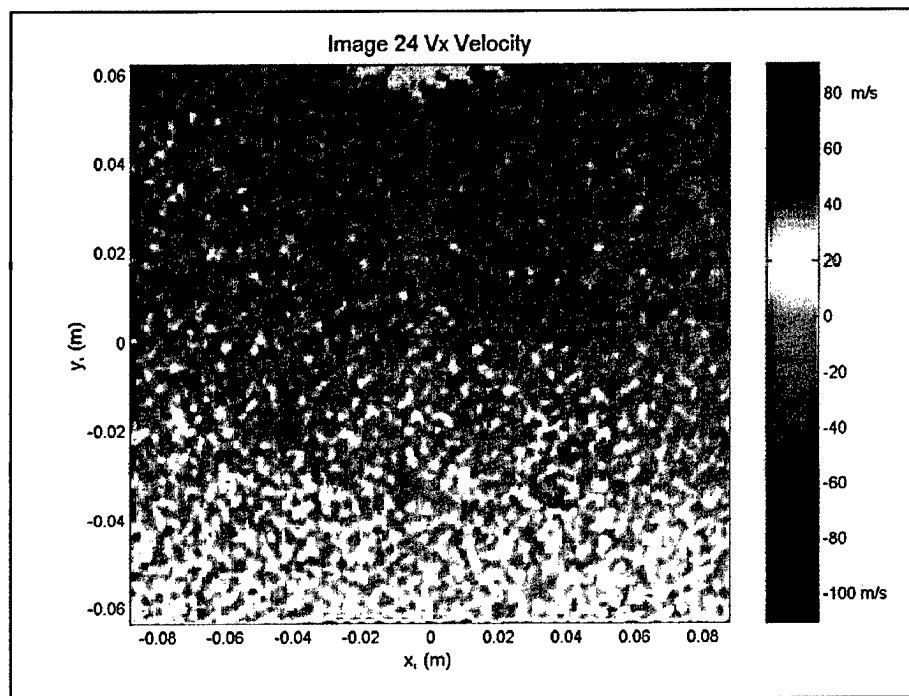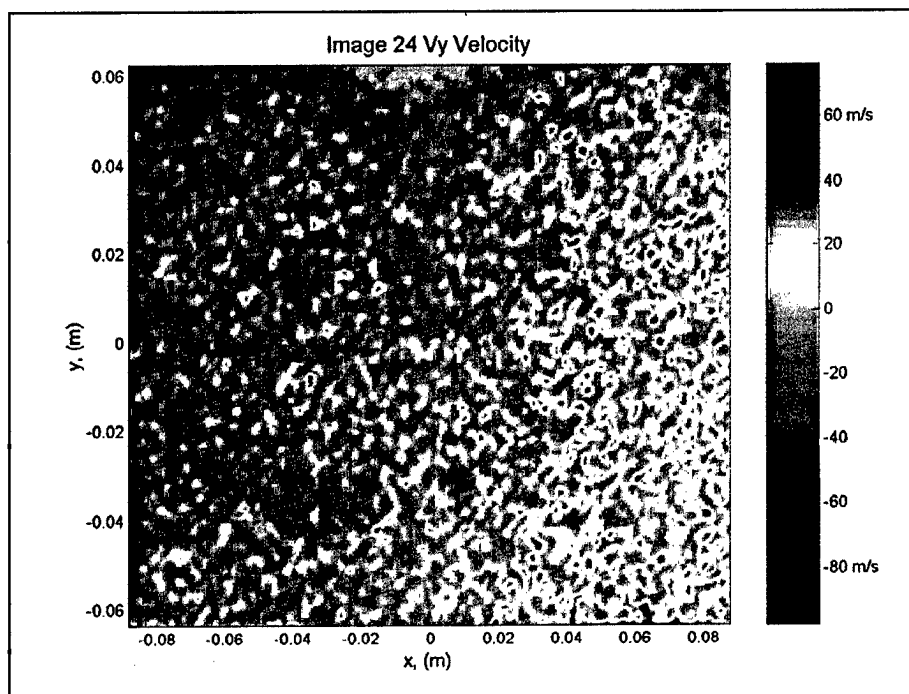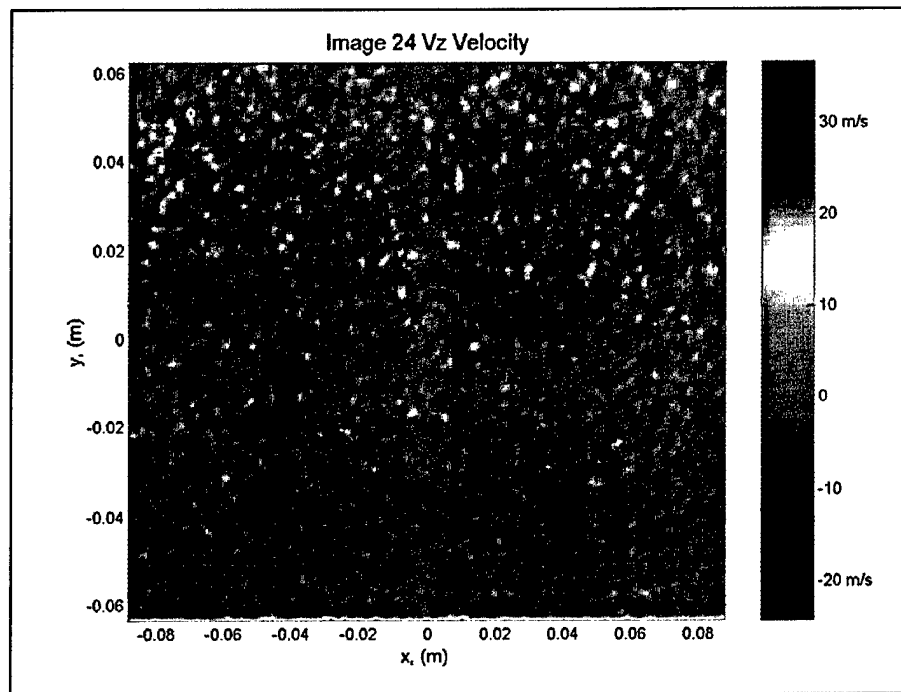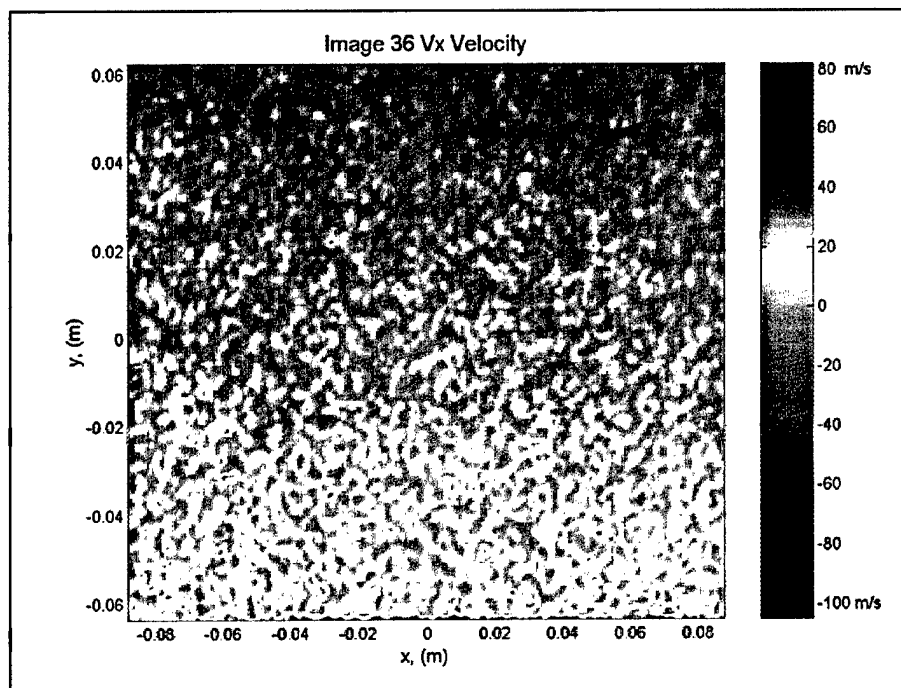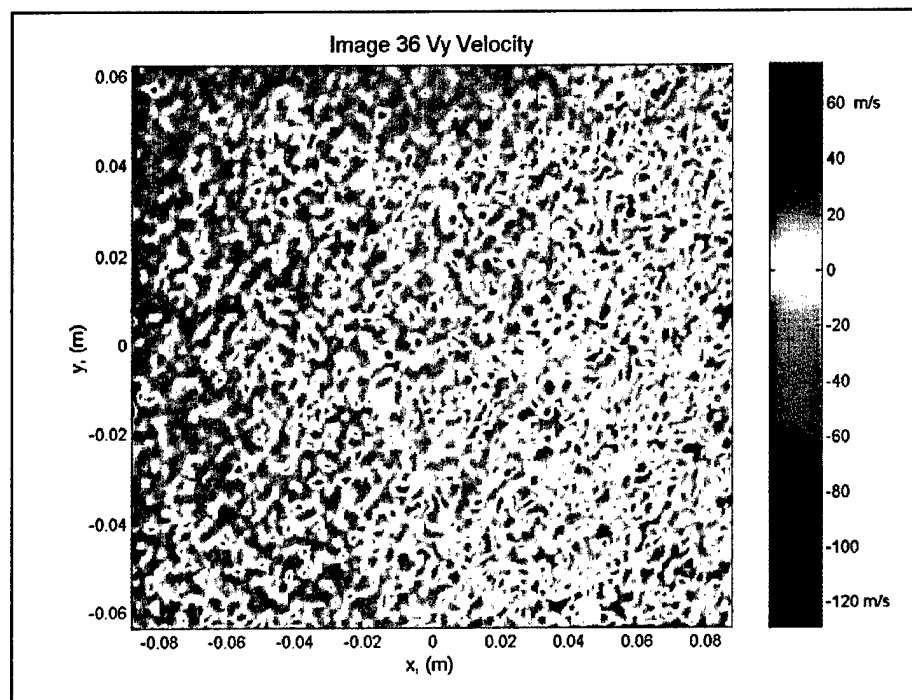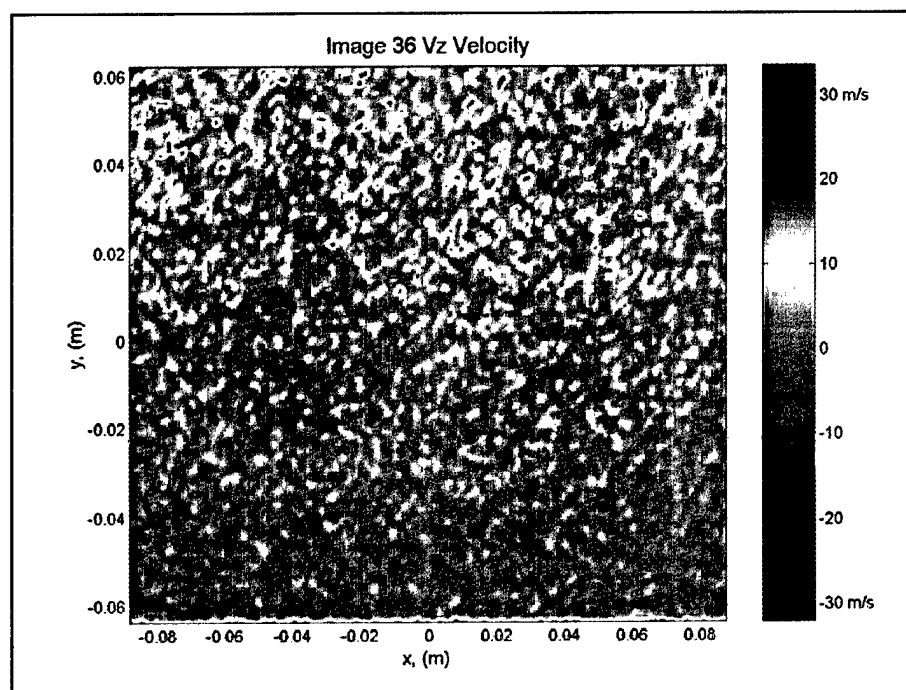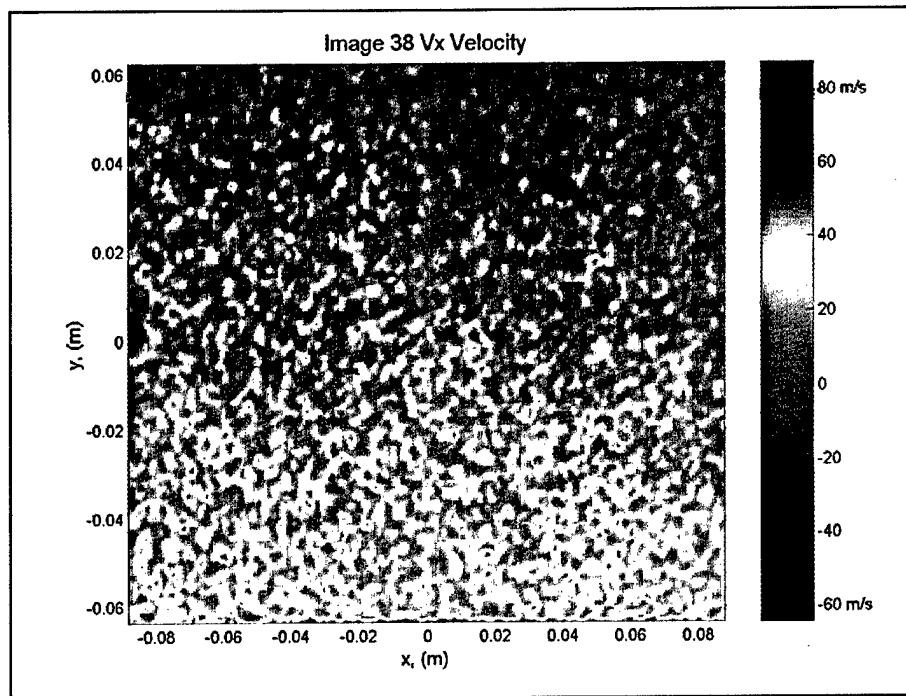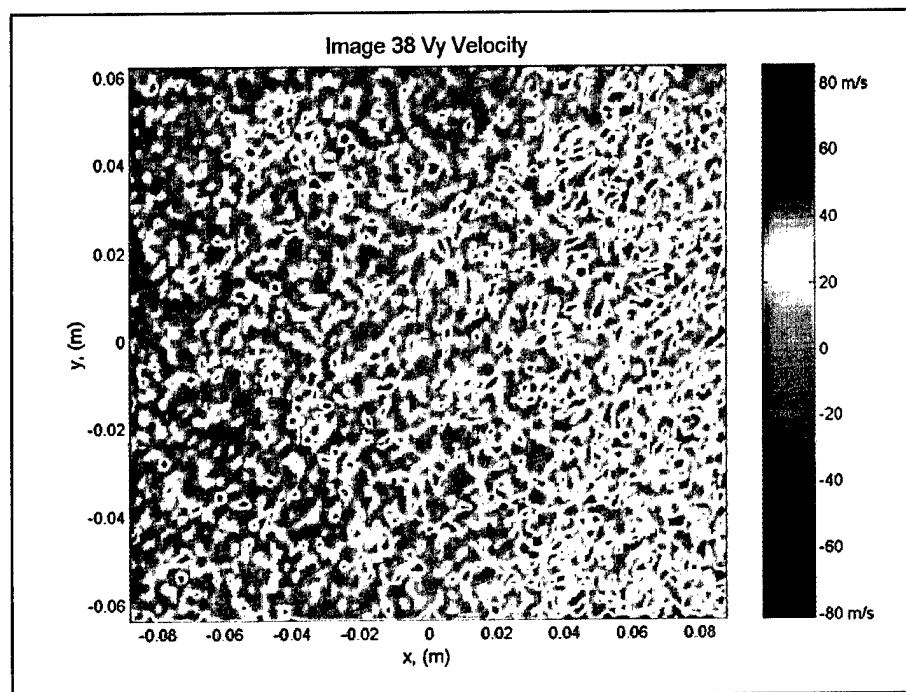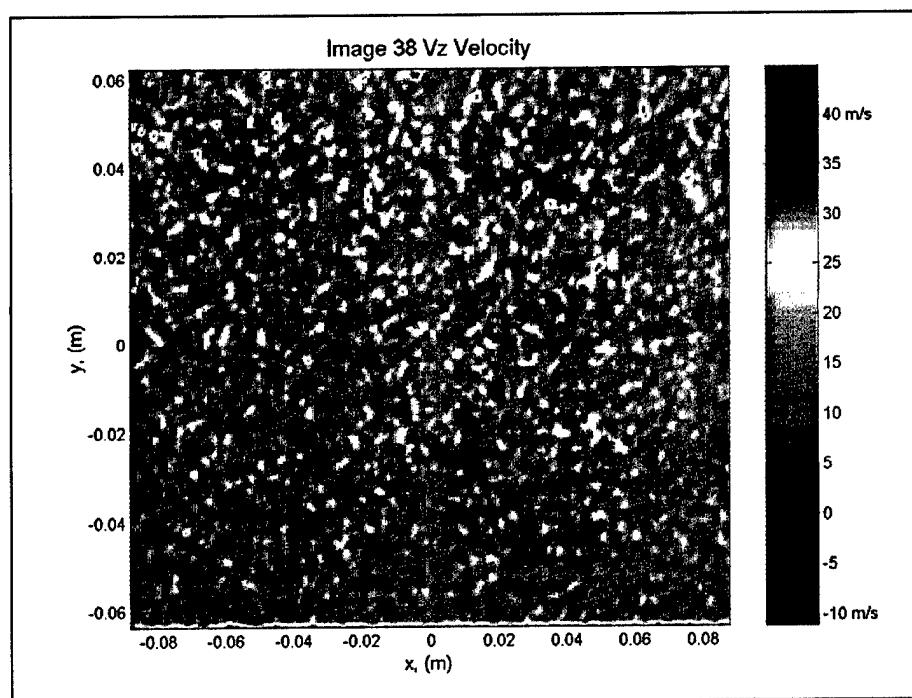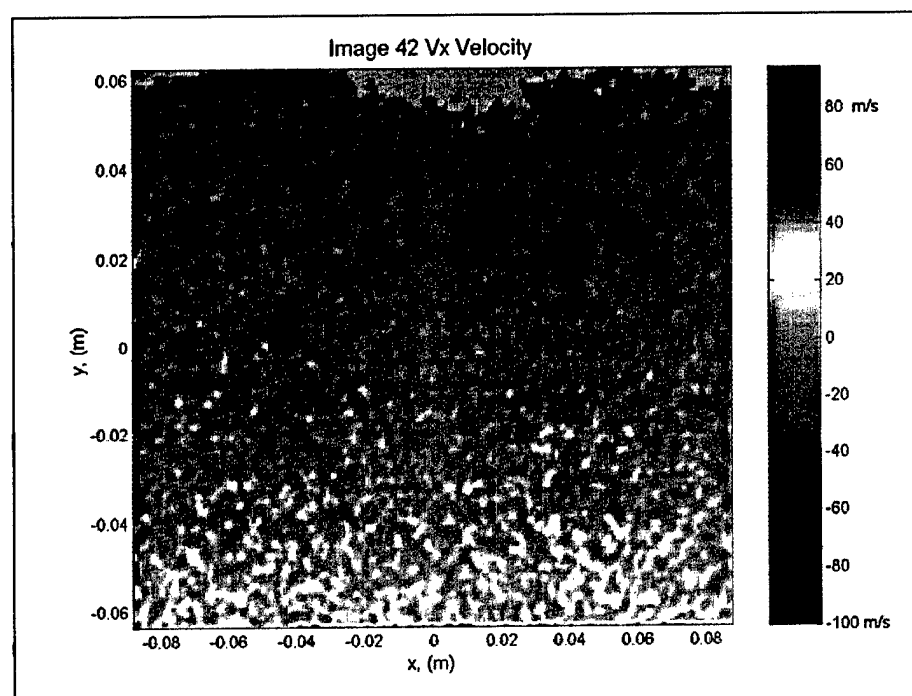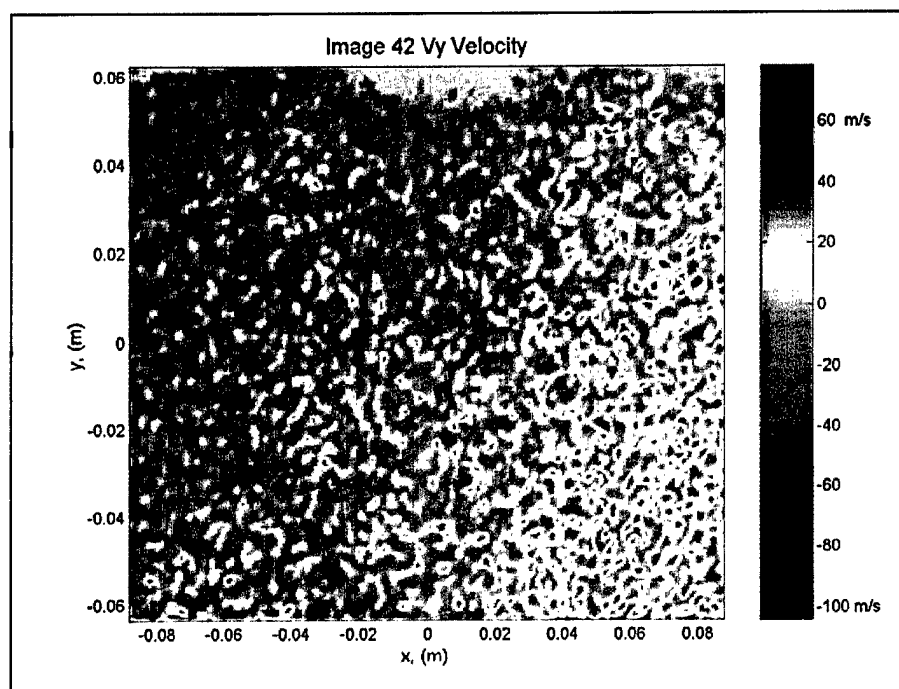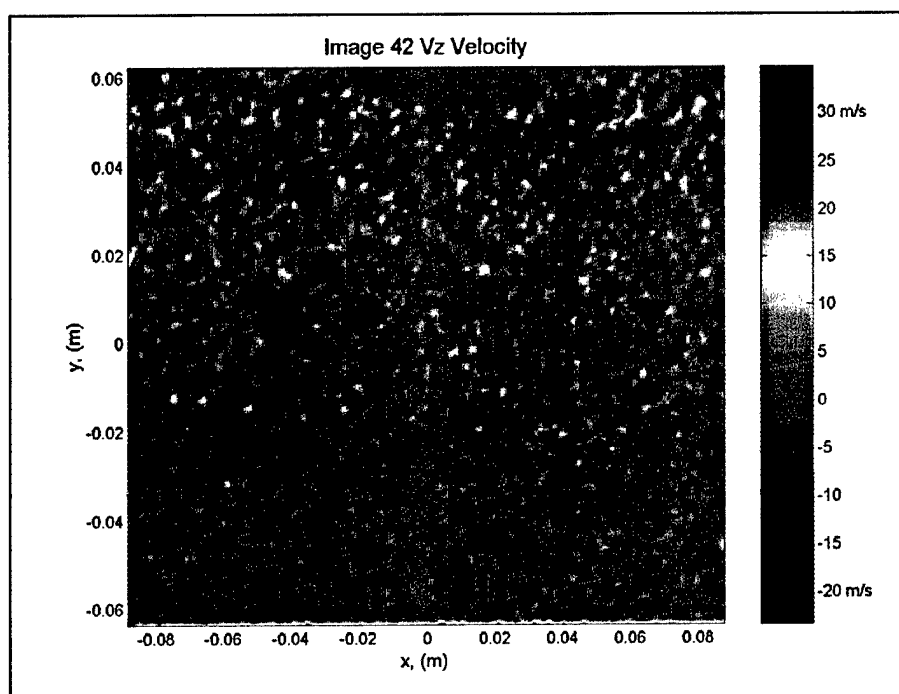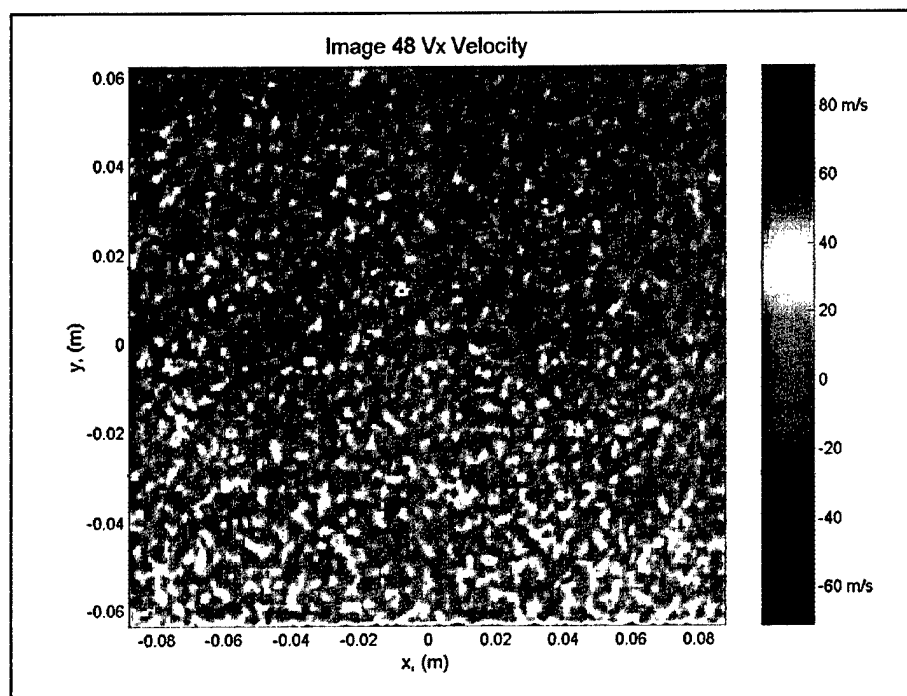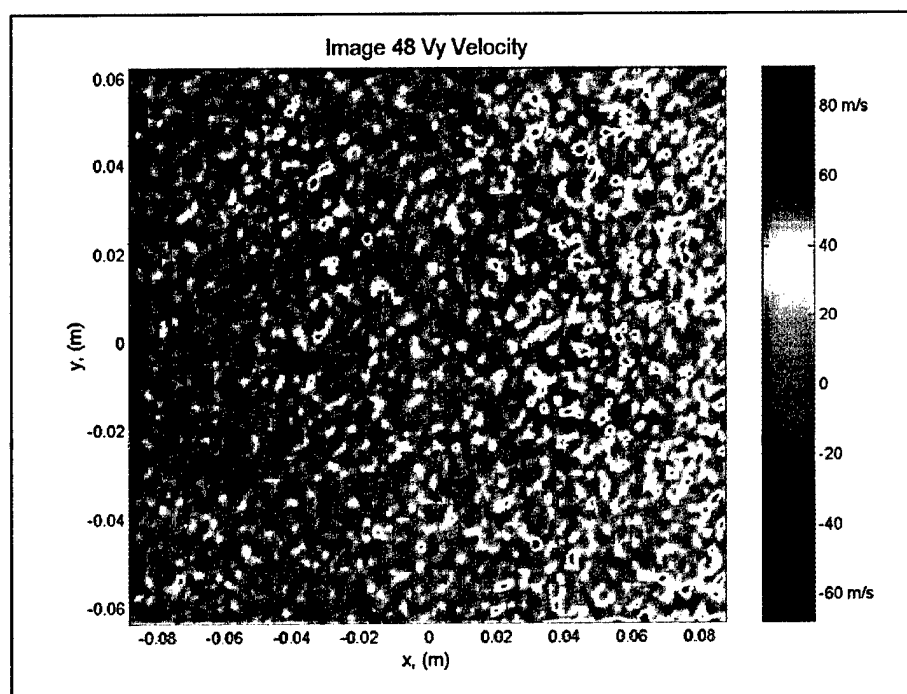*Figure A.2: Contour plot of y velocity components calculated from image 14.*

Figure A.3: Contour plot of z velocity components calculated from image 14.

Figure A.4: Contour plot of x velocity components calculated from image 15.

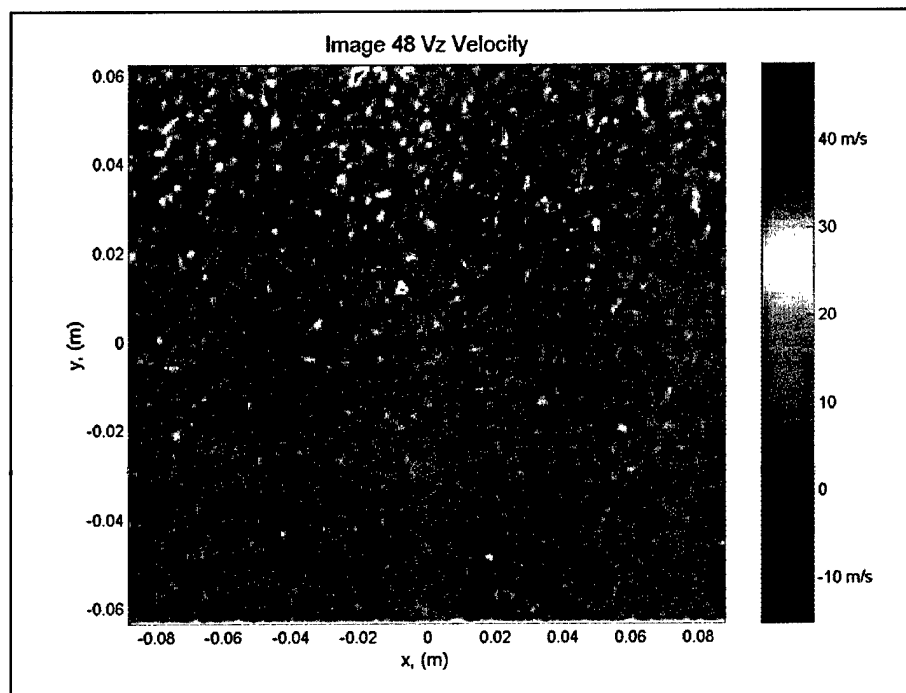*Figure A.5: Contour plot of y velocity components calculated from image 15.*

Figure A.6: Contour plot of z velocity components calculated from image 15.

Figure A.7: Contour plot of x velocity components calculated from image 24.

Figure A.8: Contour plot of y velocity components calculated from image 24.

Figure A.9: Contour plot of z velocity components calculated from image 24.

Figure A.10: Contour plot of x velocity components calculated from image 36.

Figure A.11: Contour plot of y velocity components calculated from image 36.

Figure A.12: Contour plot of z velocity components calculated from image 36.

Figure A.13: Contour plot of x velocity components calculated from image 38.

Figure A.14: Contour plot of y velocity components calculated from image 38.

Figure A.15: Contour plot of z velocity components calculated from image 38.

Figure A.16: Contour plot of x velocity components calculated from image 42.

Figure A.17: Contour plot of y velocity components calculated from image 42.

Figure A.18: Contour plot of z velocity components calculated from image 42.

Figure A.19: Contour plot of x velocity components calculated from image 48.

Figure A.20: Contour plot of y velocity components calculated from image 48.

Figure A.21: Contour plot of z velocity components calculated from image 48.

Appendix B

Appendix B

The seven images to pass the transmission ratio and Q-switch build up time filters were images 14, 15, 24, 36, 38, 42, and 48. A portion of the data was lost from three of these images, (images 15, 24, and 42). The plots contained in this appendix are grouped as follows. Data from images 15, 24, and 42 are plotted together and data from images 14, 36, 38, and 48 are plotted together. This was done so the reader could look at the data from the images used to calculate the new (4 image) average image, separately from the data from the images where a portion of the data was lost. The plots contained in this appendix show the x, y, and z velocity components, along the horizontal and vertical centerlines of the calibration wheel, for each of the seven images.
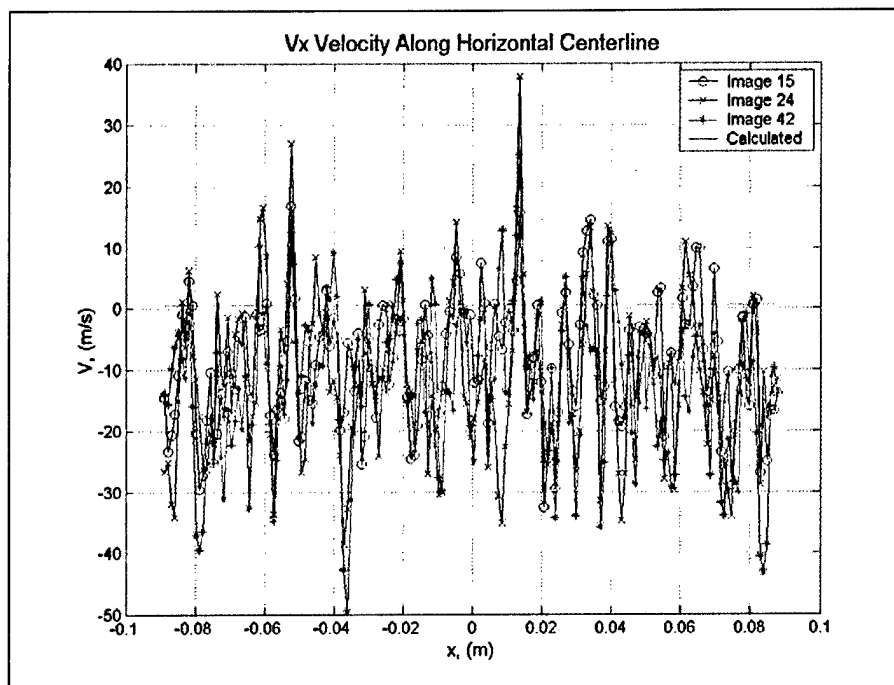
Figure B.1: x component of velocity along the horizontal centerline of the calibration wheel for images 15, 24, 42 and the values calculated from the angular velocity measured by the motor controller.
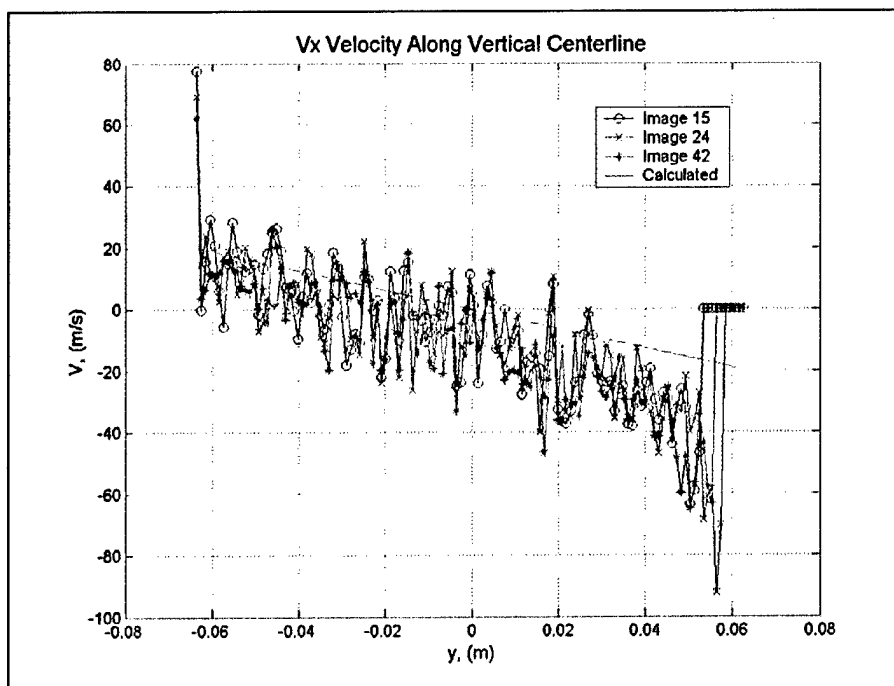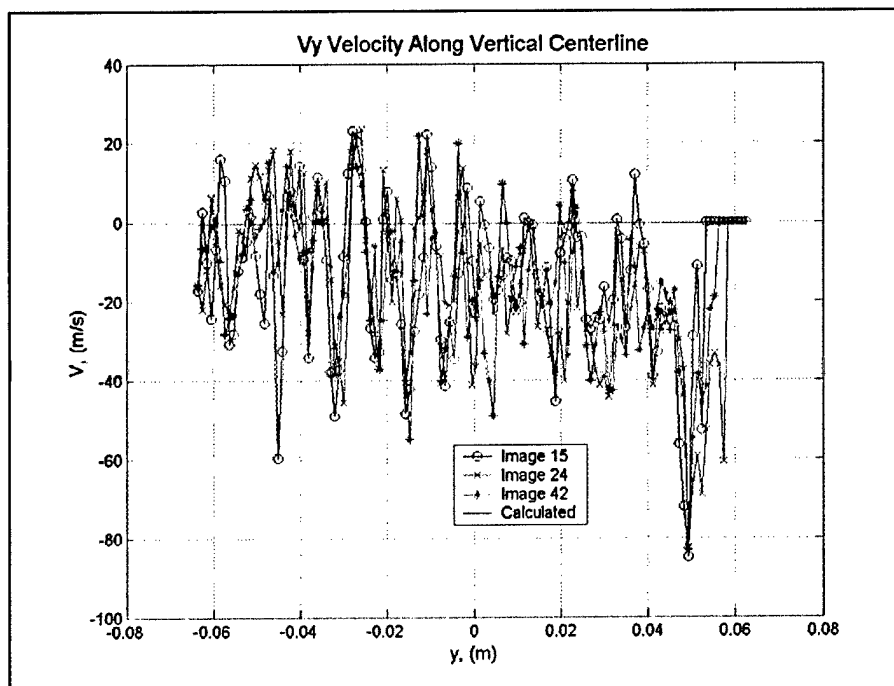

Figure B.2: x component of velocity along the vertical centerline of the calibration wheel for images 15, 24, 42 and the values calculated from the angular velocity measured by the motor controller.
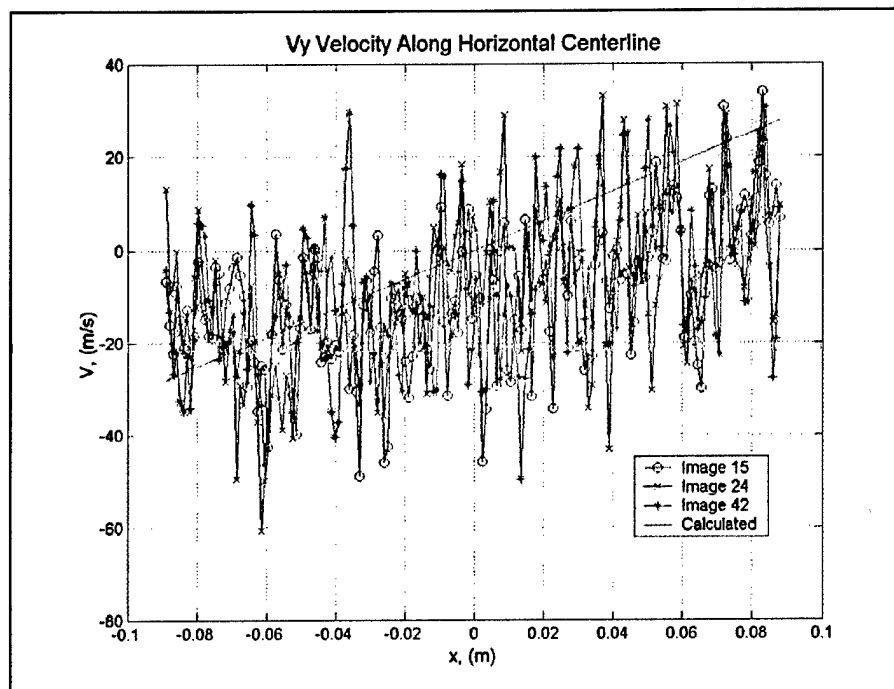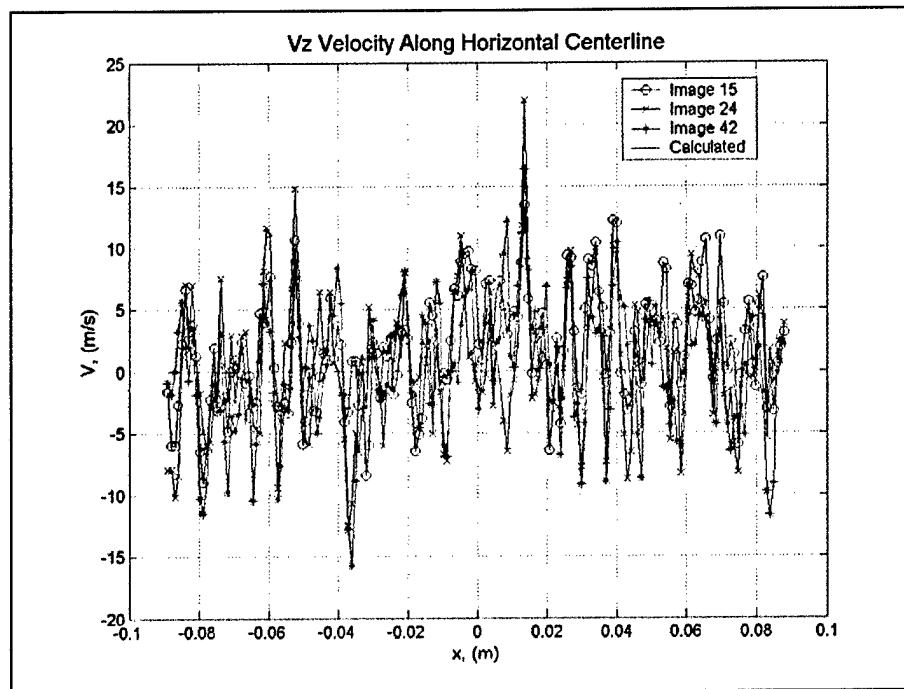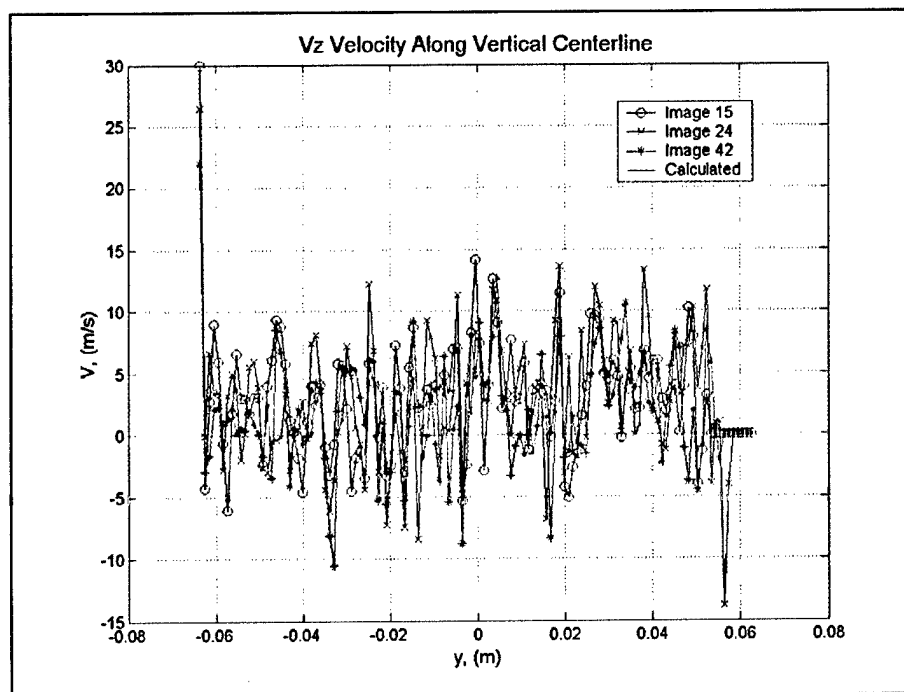
Figure B.3: y component of velocity along the horizontal centerline of the calibration wheel for images 15, 24, 42 and the values calculated from the angular velocity measured by the motor controller.

Figure B.4: y component of velocity along the vertical centerline of the calibration wheel for images 15, 24, 42 and the values calculated from the angular velocity measured by the motor controller.
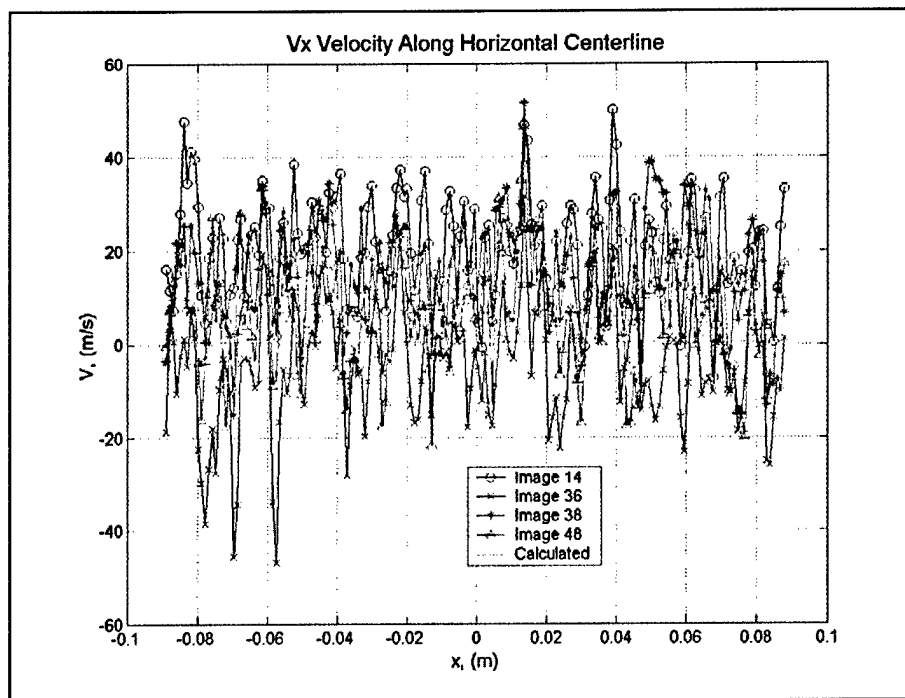
*Figure B.5: z component of velocity along the horizontal centerline of the calibration
wheel for images 15, 24, 42 and the values calculated from the
angular velocity measured by the motor controller.*

*Figure B.6: z component of velocity along the vertical centerline of the calibration
wheel for images 15, 24, 42 and the values calculated from the
angular velocity measured by the motor controller.*

Figure B.7: x component of velocity along the horizontal centerline of the calibration wheel for images 14, 36, 38, 42 and the values calculated from the angular velocity measured by the motor controller.
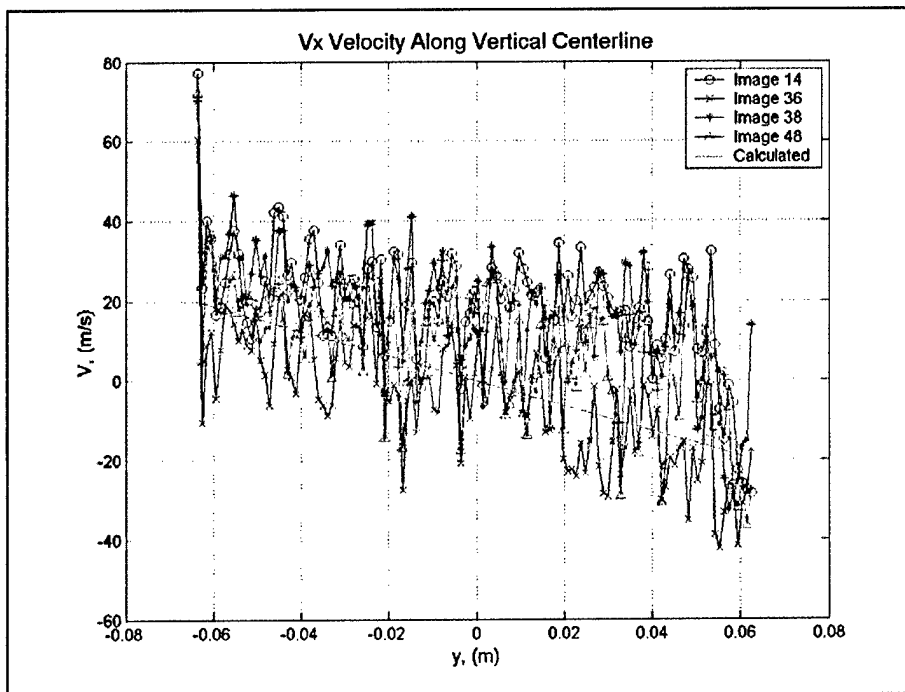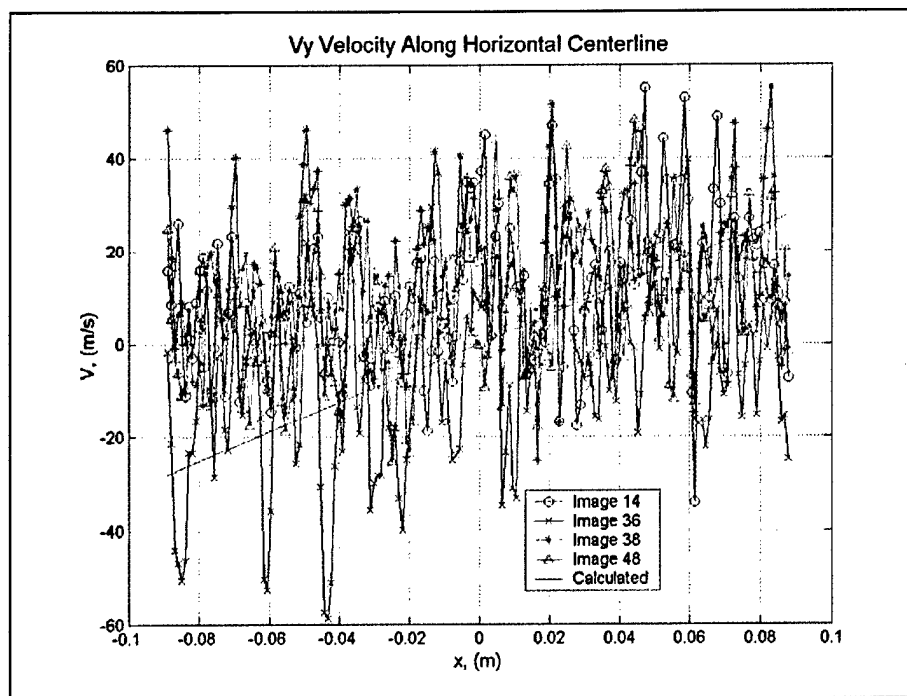

Figure B.8: x component of velocity along the vertical centerline of the calibration wheel for images 14, 36, 38, 42 and the values calculated from the angular velocity measured by the motor controller.
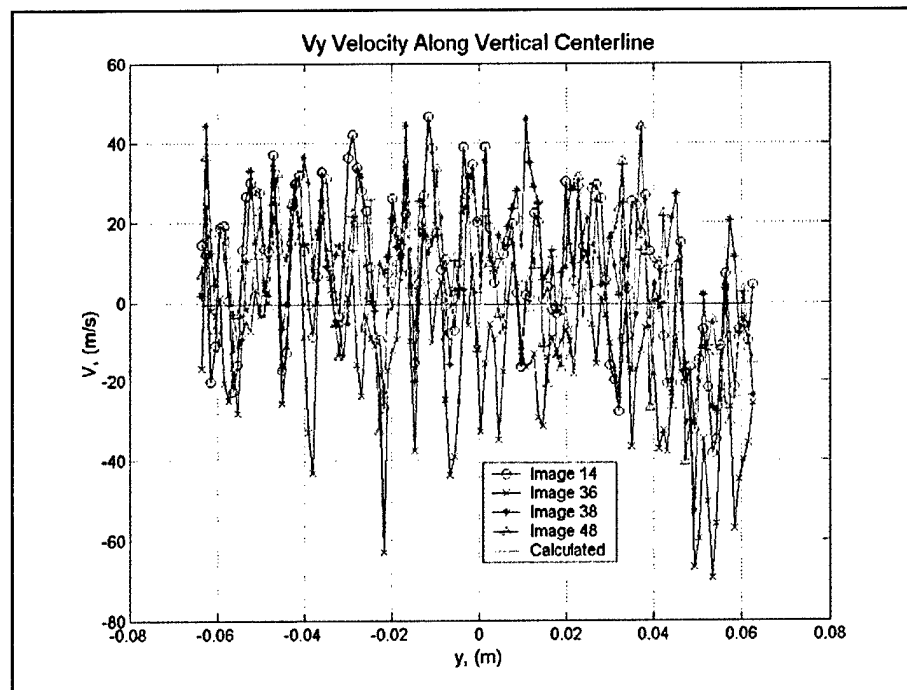
Figure B.9: y component of velocity along the horizontal centerline of the calibration wheel for images 14, 36, 38, 42 and the values calculated from the angular velocity measured by the motor controller.

Figure B.10: y component of velocity along the vertical centerline of the calibration wheel for images 14, 36, 38, 42 and the values calculated from the angular velocity measured by the motor controller.
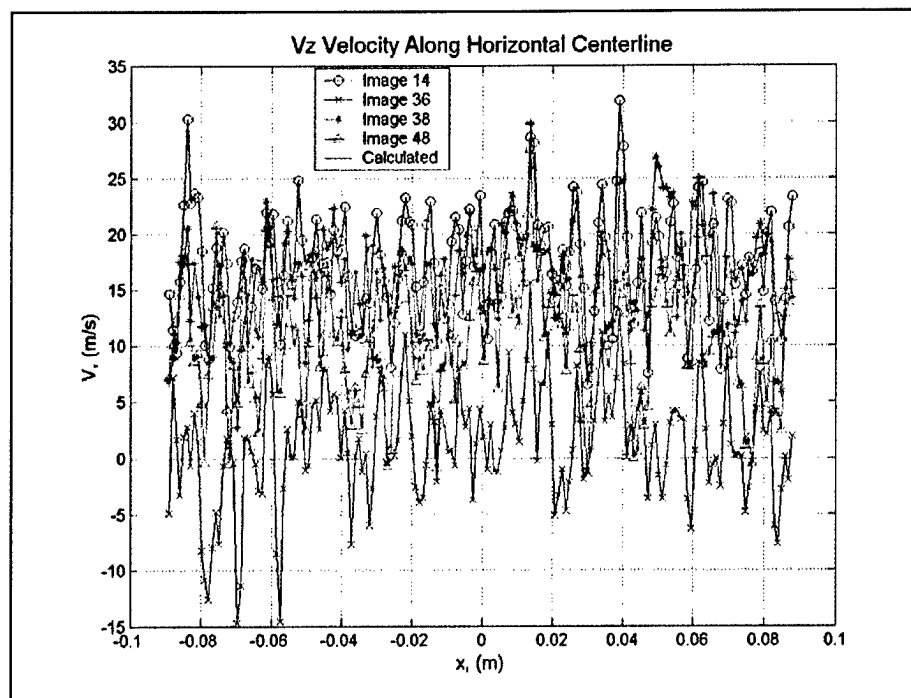
Figure B.11: z component of velocity along the horizontal centerline of the calibration wheel for images 14, 36, 38, 48 and the values calculated from the angular velocity measured by the motor controller.
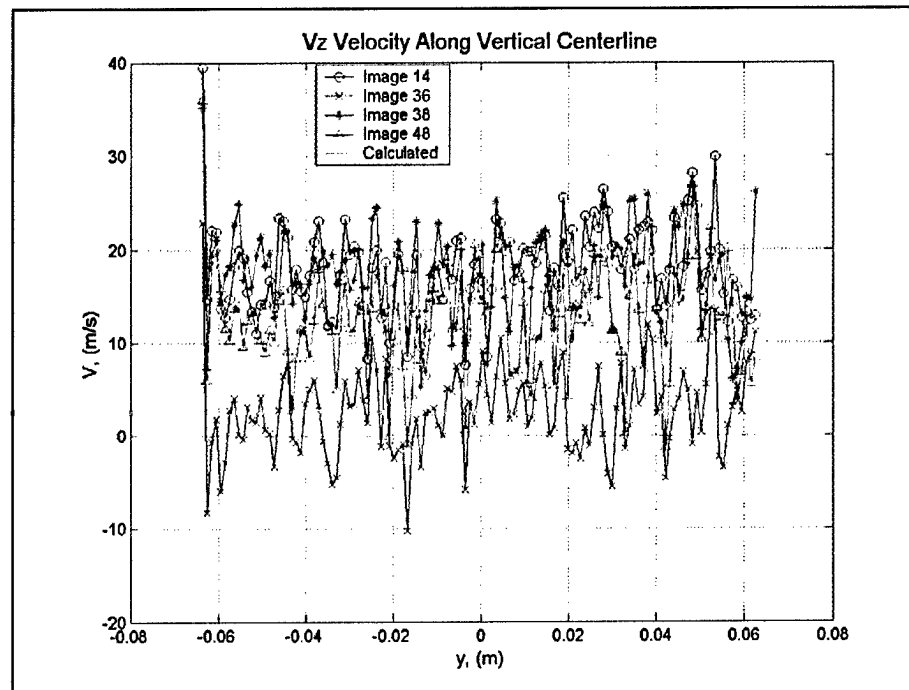

Figure B.12: z component of velocity along the vertical centerline of the calibration wheel for images 14, 36, 38, 48 and the values calculated from the angular velocity measured by the motor controller.